

NATIONAL AERONAUTICS AND SPACE ADMINISTRATION  
CONTRACT NO. NASw-6


**Research Summary No. 36-9, Volume I**  
*for the period April 1, 1961 to June 1, 1961*

JET PROPULSION LABORATORY  
CALIFORNIA INSTITUTE OF TECHNOLOGY  
PASADENA, CALIFORNIA

July 1, 1961

## Preface

The *Research Summary* is a bimonthly report of supporting research and development conducted at the Jet Propulsion Laboratory. This periodical is issued in two volumes. Volume I is unclassified, and Volume II is classified Confidential. Text outlines are developed under JPL Division and Section titles. Reports of advanced development projects and activities having specific application to space programs sponsored by the National Aeronautics and Space Administration are published in a companion periodical, the *Space Programs Summary*.



W. H. Pickering, Director  
Jet Propulsion Laboratory

Research Summary No. 36-9  
Volume I

Copyright © 1961  
Jet Propulsion Laboratory  
California Institute of Technology

## Contents

### SPACE SCIENCES DIVISION

<b>I. Space Instruments</b> . . . . .	<b>1</b>
A. Electronic Circuit Elements, by J. Stuart and H. Fujimoto . . . . .	1
B. Tunnel Diode High-Speed Data Automation System, by C. E. Smith . . . . .	4

### SYSTEMS DIVISION

<b>II. Systems Analysis</b> . . . . .	<b>10</b>
A. Trajectory Analysis, by V. C. Clarke . . . . .	10
B. Space Flight Studies, by E. Cutting . . . . .	12
C. Research Studies, by C. G. Sauer . . . . .	14
D. Powered Flight Studies, by C. E. Kohlhasse . . . . .	15
E. Systems Performance Study, by A. E. Dickinson . . . . .	20

### GUIDANCE AND CONTROL DIVISION

<b>III. Guidance and Control Research</b> . . . . .	<b>21</b>
A. Adaptive Systems, by R. A. Bruns . . . . .	21
B. Dual-Sphere Gas-Floated Gyro, by J. H. Laub . . . . .	22
C. Capillary Pumping for Closed-Cycle Gas System, by H. D. McGinness . . . . .	23

### TELECOMMUNICATIONS DIVISION

<b>IV. Communications Systems Research</b> . . . . .	<b>27</b>
A. Mathematical Research, by S. W. Golomb, L. D. Baumert, J. J. Stiffler, and R. C. Titsworth . . . . .	27
B. Communications Research, by R. Sydnor and D. R. Anderson . . . . .	32
<b>V. Communications Elements Research</b> . . . . .	<b>38</b>
A. Low-Noise Amplifiers, by W. H. Wells . . . . .	38
B. Antennas for Space Communication, by P. D. Potter, D. Schuster, and C. T. Stelzried . . . . .	39
C. Thin-Film Techniques, by J. Maserjian, H. Erpenbach, and R. Frazer . . . . .	43

## Contents (Cont'd)

<b>VI. Communication System Development</b> . . . . .	47
A. Experimental Ranging Transponder, by J. B. Briggs . . . . .	47
B. Communications Research, by C. E. Gilchrist . . . . .	51

### PHYSICAL SCIENCES DIVISION

<b>VII. Chemistry Research</b> . . . . .	55
A. Nuclear Magnetic Spectra for Three-Proton Nuclei, by S. L. Manatt . . . . .	55
B. Photolysis of Ozone, by W. DeMore and O. F. Raper . . . . .	57
C. The Use of a Proton-Proton Spin Decoupling Technique for the Determination of NMR Chemical Shifts, by S. L. Manatt and D. D. Elleman . . . . .	58
<b>VIII. Physics Research</b> . . . . .	61
A. Vortex Tube Parameters for Caseous Fission Reactors, by H. Stumpf . . . . .	61
B. Electron Exchange Correction to Phonon Dispersion Relation in Metals, by O. von Roos . . . . .	64
C. Rates of Recombination of Nitrogen and Oxygen Atoms, by C. A. Barth . . . . .	64
D. Plasma Theory of the Many-Electron Atom, by P. H. Levine . . . . .	65
<b>IX. Gas Dynamics Research</b> . . . . .	68
Laminar Boundary Layer on a Disk in a Rotating Flow, by L. Mack . . . . .	68

### ENGINEERING MECHANICS DIVISION

<b>X. Materials Research</b> . . . . .	71
A. Ceramics, by M. H. Leipold . . . . .	71
B. Endothermal Materials, by R. G. Nagler . . . . .	73
C. Materials in Space Environment, by J. B. Rittenhouse . . . . .	75
<b>XI. Engineering Research</b> . . . . .	77
Plasma Confinement, by D. F. Spencer . . . . .	77

### ENGINEERING FACILITIES DIVISION

<b>XII. Wind Tunnels</b> . . . . .	80
A. 21-Inch Hypersonic Tunnel, by E. H. Koester and R. C. Hiller . . . . .	80
B. Low-Density Wind Tunnels, by N. L. Fox . . . . .	81



## Contents (Cont'd)

### PROPULSION DIVISION

<b>XIII. Liquid Propellant Propulsion</b> . . . . .	82
A. Combustion and Injection, by J. H. Rupe and G. I. Jaivin . . . . .	82
B. Heat Transfer and Fluid Mechanics, by A. B. Witte . . . . .	85
<b>XIV. Solid Propellant Propulsion</b> . . . . .	88
A. Polymer Research, by A. J. Havlik and A. B. Magnusson . . . . .	88
B. Secondary Injection for Thrust Vector Control by J. Newton . . . . .	90
<b>References</b> . . . . .	97

# SPACE SCIENCES DIVISION

## I. Space Instruments

### A. Electronic Circuit Elements

J. Stuart and H. Fujimoto

#### 1. Data Compression

Two approaches have been tried in the area of data compression. One is the use of a logarithmic diode as a feedback element around a suitable operational amplifier. In this approach, two factors limiting ultimate sensitivity are (1) the input current requirement and input noise level of the amplifier and (2) the logarithmic characteristics of the feedback element. The other approach utilizes the line segment approximation to the logarithmic curve.

*a. Linear logarithmic compressional amplifier.* The line segment approach yielded the block diagram shown in Figure 1. Its output characteristics are related to the input characteristics by the relation

$$E_{out} = K \sum_{j=0}^n E_j \quad (1)$$

where  $E_j = A^j E_{in} \leq E_c$ ;  $A$  is the gain per amplifier stage = 10.0 for base-10 log;  $E_c$  is the diode clamping

level = 2.0 volts; and  $K$  is the gain constant of the  $\Sigma$  amplifier. For any  $j$  such that  $A^j E_{in} \geq E_c$ , the remaining terms in the series may be placed by  $[n - (j - 1)] E_c$  since all remaining amplifier outputs are  $> E_c$ . The theoretical curve is given in Figure 2 for  $n = 4$ . The dashed line indicates the experimental results. Lack of sharpness at the cusps of the experimental curve are attributed to the clamp circuit not maintaining a constant clamping voltage as a result of the clamping diode internal impedance.

The error of the approximation is inversely proportional to the number of stages used per decade, whereas the range of the compressor is limited to the input noise level, dynamic range, and overload characteristics of the amplifier used in each stage.

*b. Logarithmic feedback compressional amplifier.* The second approach uses an operational amplifier with a logarithmic diode as the feedback element. For semiconductor diodes, it is known that

$$I_d = I_s (e^{qV/kt} - 1) \quad (2)$$

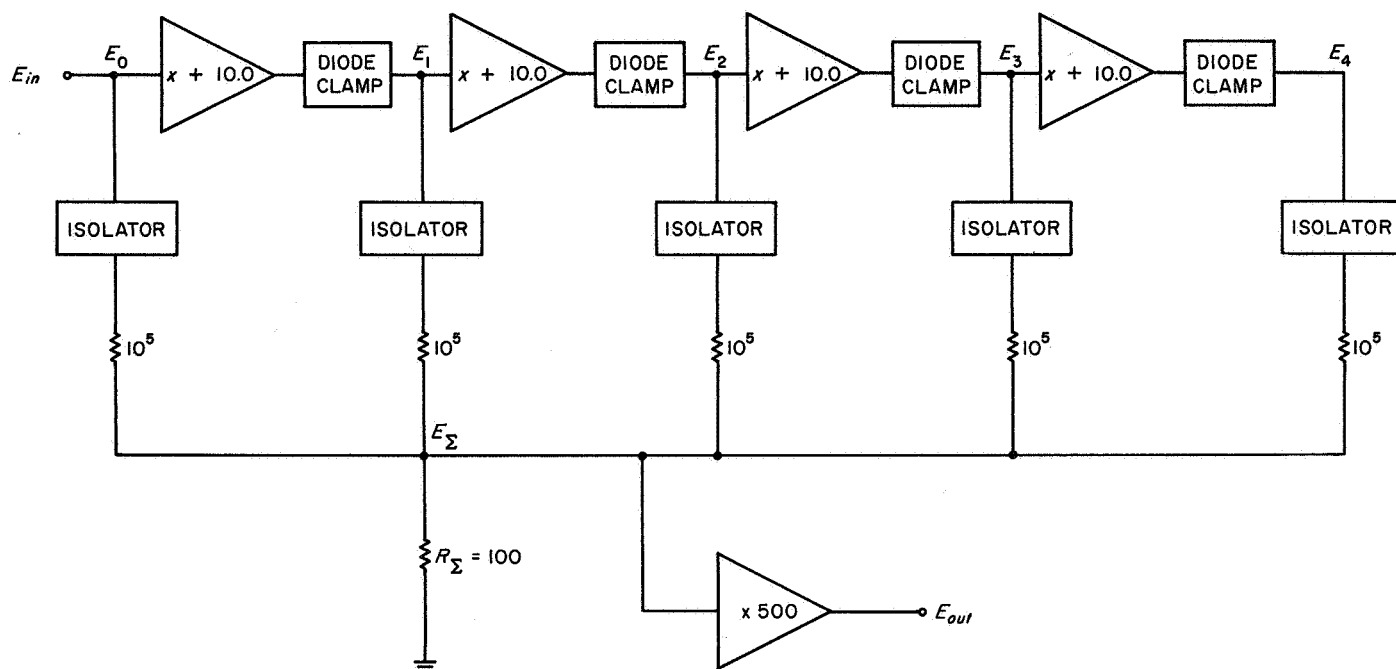


Figure 1. Linear logarithmic compressional amplifier

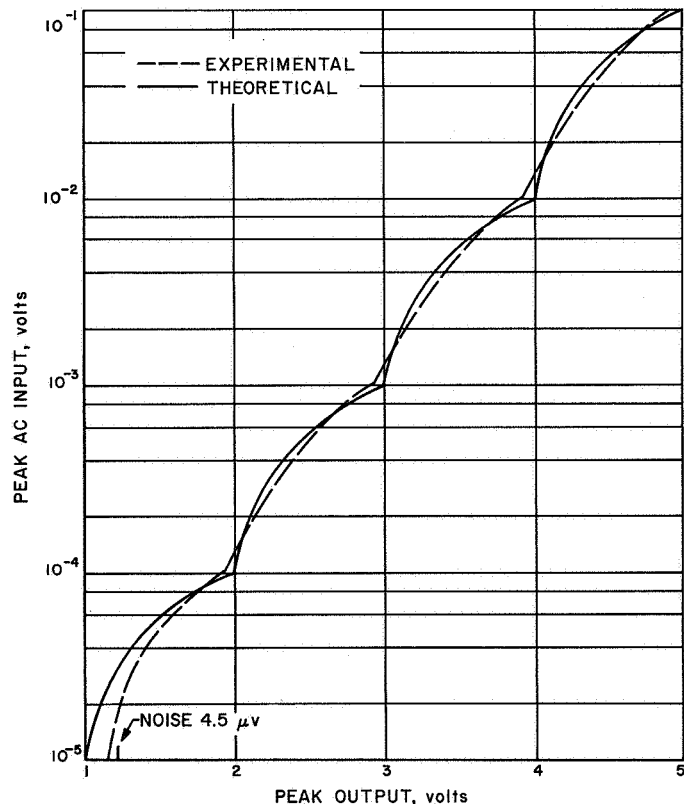


Figure 2. Output vs input of modified logarithmic compressor

is a valid expression relating the diode current  $I_d$  to the voltage drop  $V$  across the diode. If it is assumed that  $I_d > I_s$ , the leakage or reverse current, it may be shown that

$$V = \frac{kt}{q} \ln I_d - V_o \quad (3)$$

Here  $V_o$  is the offset voltage due to the reverse current  $I_s$ ;  $T$  is the absolute temperature in  $^{\circ}\text{K}$  and  $k/q$  is equal to  $86.2 \mu\text{v}/^{\circ}\text{K}$ . The circuit shown in Figure 3 utilizes two balanced differential amplifiers so chosen because of temperature stability.  $Q_1$ ,  $Q_2$  and  $Q_3$  form an operational amplifier capable of driving the variable feedback element  $D_1$ . The base of  $Q_2$  is maintained at 0 volt by comparison to the reference at the base of  $Q_1$ . The voltage developed across  $D_1$  will follow the relation in Equation (3). The temperature dependence shown in Equation (3) may be reduced by using a diode  $D_2$  having the same temperature coefficient as  $D_1$ . The input to  $Q_4$  now is only the logarithmic portion of the signal developed across  $D_1$ . This signal will be independent of temperature if both diodes have the same temperature coefficient. The second amplifier ( $Q_4$  and  $Q_5$ ) is a balanced differential amplifier designed with the provision for offsetting a difference in temperature effects due to slight differences between diodes.  $R_3$  is a similar adjustment for  $I_{co}$  present in  $Q_2$ . Typical values are shown in Figure 3. The varia-



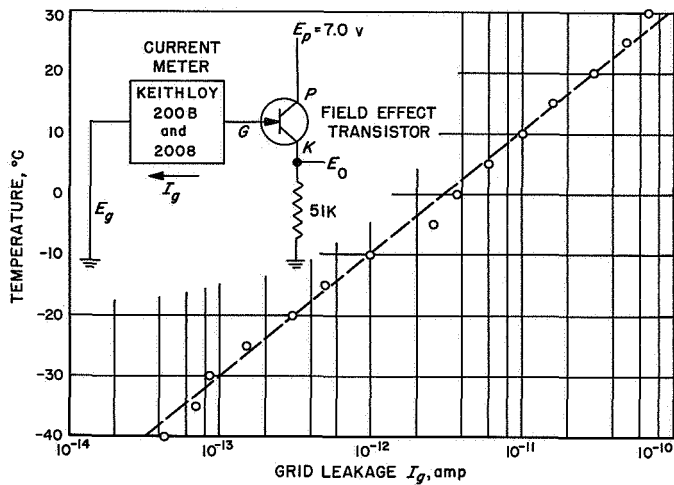


Figure 6. Grid leakage current vs temperature of C614 field effect transistor

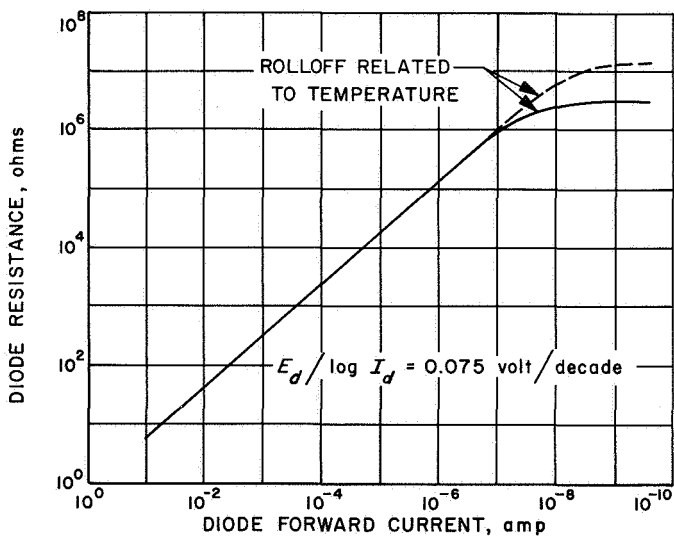


Figure 7. Forward impedance characteristics of logarithmic LF diode

ture for Type C-614. Additional tests made at room temperature indicate an input impedance greater than 1000 megohms without resorting to positive feedback or bootstrapping. Additional work is being done to determine the leakage current for the other types manufactured.

### 3. Wide Dynamic Range Logarithmic Diodes

In conjunction with the work being done with field-effect transistors, we are also examining various  $p$ - $n$  diodes

which may be used in logarithmic amplifiers of extended range (6 to 9 decades, bipolar). Some recently acquired large-area (0.20 in.<sup>2</sup>)  $p$ - $n$  junction diodes (Controls Co. of America, Tempe, Arizona) show promise of being logarithmic down to  $10^{-8}$  amperes at room temperature and  $10^{-12}$  amperes at  $-50^{\circ}\text{C}$ . The other unusual feature is a constant temperature coefficient over a wide range of current and temperature. Fabrication is underway on some dual bipolar units which will permit temperature compensation and bipolar compression. The logarithmic slope constant is 75 mv/decade of current. Figure 7 relates the diode resistance vs current over a 6.5-decade range at  $25^{\circ}\text{C}$ .

## B. Tunnel Diode High-Speed Data Automation System

C. E. Smith

### 1. Characteristics of Tunnel Diode Logic Circuits

The tunnel diode is a voltage-controlled, short-circuit stable, semiconductor device. Attention is now being devoted to the possibility of employing these relatively new devices in computer logic circuits (Refs 2 to 6). This application appears to be feasible since the tunnel diode is a negative resistance device capable of operating in two stable states when biased correctly. Another useful characteristic is the inherent gain property within its switching cycle from one state to another.

In spacecraft applications, tunnel diodes are demanding attention because of their relative insensitivity to large doses of nuclear radiation and to wide variations in temperature. This characteristic makes these diodes superior to many other solid-state devices for operation under adverse environmental conditions.

An outstanding feature of tunnel diodes is the short transient times encountered during switching from one voltage state to the other. Currently available tunnel diodes can switch in approximately 1 nanosecond ( $10^{-9}$  sec). In addition, the tunnel diode is a comparatively simple device, requiring only a single junction of  $p$ - $n$  material.

It has been demonstrated that simple logical operations can be performed using tunnel diode logic circuits. Ultimately, it is believed that a complete high-speed data

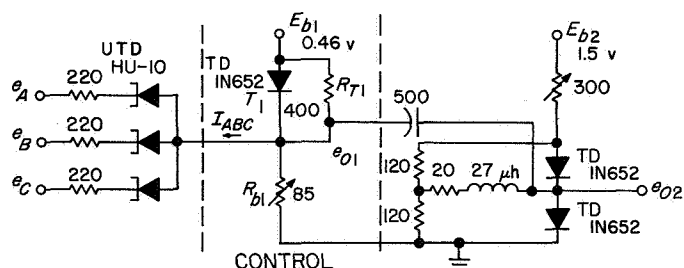
automation system could be constructed, containing exclusively tunnel diodes as the active elements in the logic circuitry. In this paper, the simple system selected to demonstrate the feasibility of tunnel diode logic circuits is the binary adder. The first steps in the fabrication of this adder were to construct basic logic building blocks to perform the necessary logical functions.

## 2. Design of Basic Logic Building Blocks

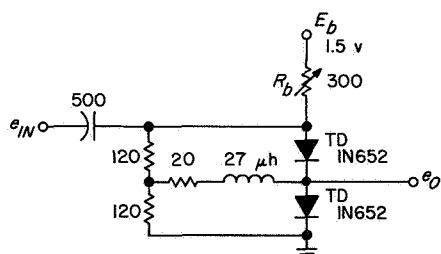
The building blocks needed to perform the necessary logical functions for the binary adder were the *and* gate, the *or* gate, and the *inverter* circuit.

**a. Design of *and* gate.** An *and* gate was designed, as shown in Figure 8a, to operate at the command of three simultaneous inputs. The gate was designed to operate on the low-level (approx 0.4 volt) positive output of a typical tunnel diode flip-flop driving unit, shown in Figure 8b. Since the inputs to the *and* gate were of such a low level, it was imperative to select logic diodes for the gate which would turn "on" at the lowest possible voltage. Hoffman HU-10 type silicon Uni-Tunnel Diodes (UTD, also called backward diodes) were selected for this purpose.

The state of the *and* gate is controlled by a tunnel diode  $T_1$  which has two possible levels of operation; i.e., a high-voltage state (0.4 volt) and a low-voltage state (0.08 volt). The circuit for the control tunnel diode  $T_1$  in parallel



a. THREE-INPUT *AND* GATE



b. TYPICAL DRIVER CIRCUIT

Figure 8. Three-input tunnel diode *and* gate and driver flip-flop circuit

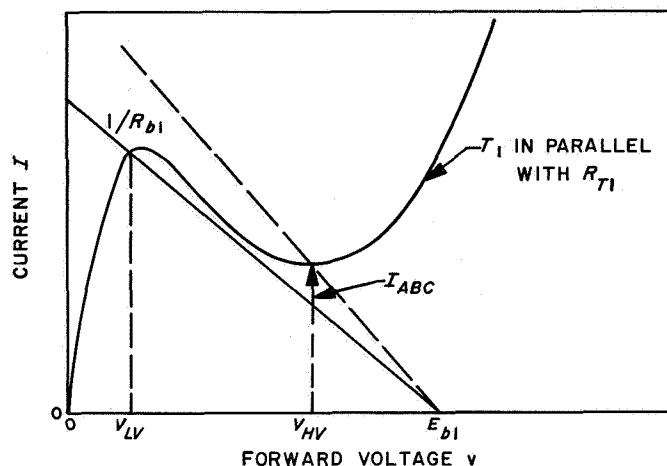


Figure 9. Modified tunnel diode characteristics

with resistor  $R_{T1}$  is shown within dashed lines in the center of Figure 8a. The electrical characteristic for the combination is shown in Figure 9. If any one of the three inputs to the *and* gate is held in the low-voltage state by a driving flip-flop, then the *and* gate tunnel diode  $T_1$  is clamped in the high-voltage state  $V_{HV}$ . In this case, the control current  $I_{ABC}$  is allowed to flow through any one or all of the logic diodes of the *and* gate, so that the apparent load line for the  $T_1$ - $R_{T1}$  combination appears as the broken line in Figure 9.

When all three inputs to the *and* gate are in the high-voltage state, the control current  $I_{ABC}$  is cut off, so that the apparent load line for the  $T_1$ - $R_{T1}$  combination appears as the solid line in Figure 9. The slope of the solid line is adjusted so that there is only one intersection of the characteristic curve, and this intersection occurs at the low-voltage point  $V_{LV}$ . When  $T_1$  is in this low-voltage state, the voltage across  $R_{b1}$  is by necessity in the high-voltage state. This high-voltage condition is subsequently coupled through the reshaping circuit to produce the output  $e_{o2}$ , thus completing the *anding* operation.

Electrical waveforms for the three-input *and* gate are shown in Figure 10. From this figure it is apparent that an assertion output  $e_{o2}$  occurs only when all three inputs are in the high-voltage state. The voltages shown in this figure have reference to the *and* circuit shown in Figure 8a.

**b. Design of *or* gate.** A four-input *or* gate is shown in Figure 11a. It was possible to use straightforward diode logic in the design of this gate, for no complications were involved. Again Hoffman Type HU-10 Uni-Tunnel Diodes were used for the logic diodes.

**c. Design of inverter circuit.** Another basic logic building block necessary for the fabrication of the tunnel

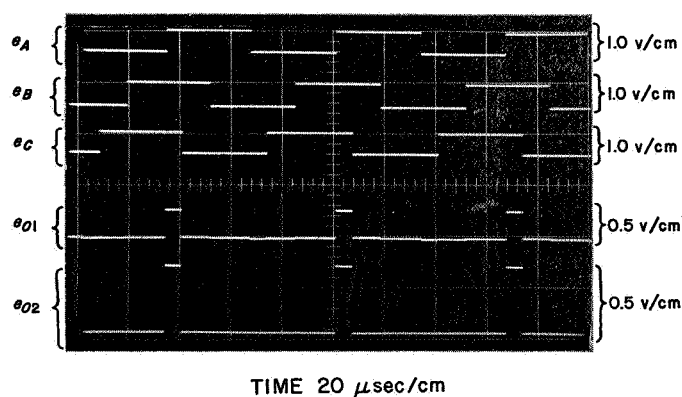


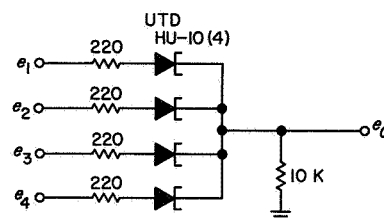
Figure 10. Waveforms for three-input and gate

diode binary adder is the *inverter* circuit. This circuit is shown in Figure 11b. The function of the first stage of the *inverter* circuit is to take the Boolean complement of the input voltage  $e_{IN}$ . The second stage is merely for the purpose of reshaping and amplifying the output  $e_{O1}$  of the first stage.

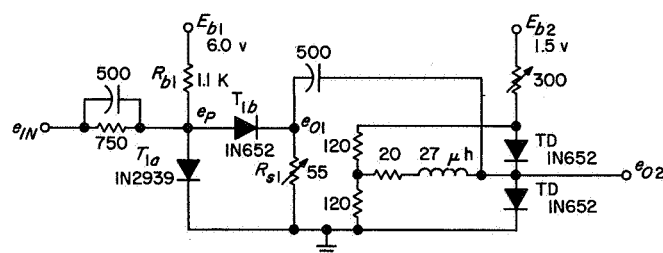
The characteristics for the tunnel diodes  $T_{1a}$  and  $T_{1b}$  (in parallel with  $R_{s1}$ ) are shown in Figure 12a. Diode  $T_{1a}$  was selected because its characteristic demonstrated a very low resistance in the forward voltage region, as well as the fact that this forward voltage region was found to be just slightly greater than the peak voltage for the  $T_{1b}$  and  $R_{s1}$  combination. This selection was desirable in order to realize maximum gain in the voltage  $e_{O1}$ . In reference to Figure 12b, maximum gain in  $e_{O1}$  is realized when the difference in voltage between  $e_{PHV}$  and  $e_{PLV}$  is a minimum. This is the same as stating that a minimum change in  $e_P$  will produce a maximum change in  $e_{O1}$ . Figure 12b represents the parallel summation of the tunnel diode characteristics of Figure 12a, thus demonstrating that there are only two possible states of operation for the first stage of the *inverter* circuit. The stable points of operation, designated at  $a$  and  $b$ , are determined by the intersection of the load line ( $1/R_{b1}$ ) with the summation curve. The resistance  $R_{b1}$  is adjusted so that the load line intersects the summation curve at the point where switching is most easily accomplished. The electrical waveforms describing the voltage variations at different points in the circuit are shown in Figure 13.

### 3. Assembly of Building Blocks into a Logical System

As a preliminary attempt to determine the usefulness of tunnel diode logic circuitry, it was decided to use the basic building blocks described above in the construction of a simple binary adder. In order to construct such a



a. FOUR-INPUT OR GATE



b. TUNNEL DIODE INVERTER CIRCUIT

Figure 11. Four-input tunnel diode or gate and inverter circuit

circuit, it is first necessary to examine the process of adding binary numbers and then to write the Boolean equations which describe the process.

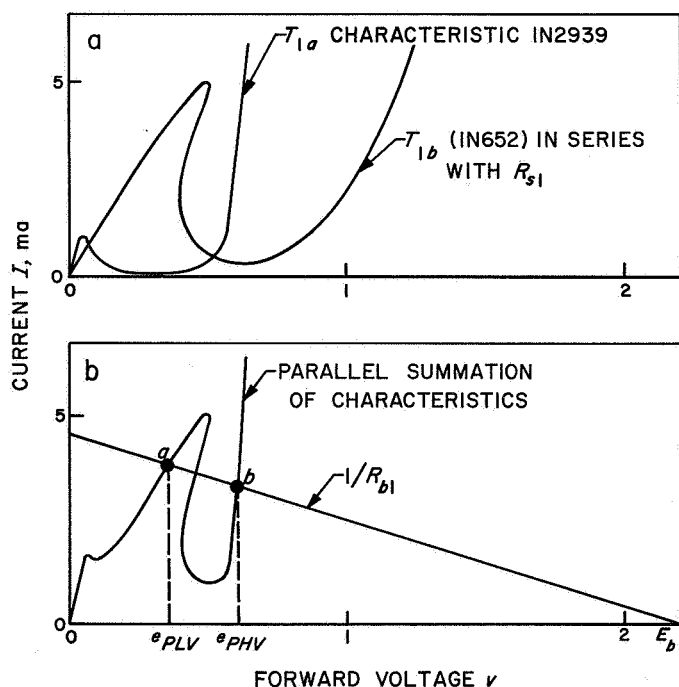


Figure 12. Tunnel diode characteristics

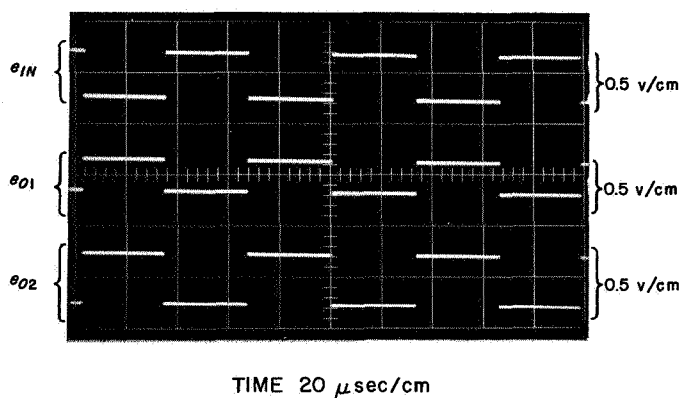


Figure 13. Waveforms for inverter circuit

Binary addition can be simulated in an electrical circuit by placing two binary flip-flop chains in parallel with outputs feeding into appropriate points in given logic blocks. A block diagram describing the general address logic for such binary addition with  $n + m$  flip-flops in the binary chain is shown in Figure 14.

Since the vertical sections of the address circuitry in Figure 14 are symmetrical, it is possible to describe this system by referring to just one section. Consider just the  $n$ th section of the address circuitry for future discussion. This section is marked off in the diagram with a broken line.

The present problem is to determine the proper circuit logic for the  $L_n$  logic block, so that the inputs ( $A_n$ ,  $B_n$ ,

and  $C_{n-1}$ ) to  $L_n$  might be combined logically to produce outputs  $S_n$  and  $C_n$ ;  $S_n$  and  $C_n$  represent, respectively, the *sum* and *carry* outputs from the  $L_n$  logic block. The problem can be solved by first setting up the logical truth table to describe the proper binary addition, and then proceeding with the writing of the logic equations from the directions given within the table.

From the results within the truth table it is possible to write the logic equations which express the outputs  $S_n$  and  $C_n$  in terms of the inputs  $A_n$ ,  $B_n$ , and  $C_{n-1}$  to the binary adder:

$$S_n = \bar{A}_n \bar{B}_n C_{n-1} + \bar{A}_n B_n \bar{C}_{n-1} + A_n \bar{B}_n \bar{C}_{n-1} + A_n B_n C_{n-1}$$

$$C_n = A_n B_n + B_n C_{n-1} + A_n C_{n-1}$$

These equations are the Boolean functions which describe the logic of the  $L_n$  logic block of the binary adder.

It would be cumbersome here to show the entire circuit for the complete binary adder or even for the  $L_n$  logic block. However, a representative portion of the circuitry for the  $L_n$  logic block is shown in Figure 15. This circuit demonstrates, in general, how the basic tunnel diode building blocks (*and* gate, *or* gate, and *inverter* circuit) may be combined in order to realize a logical function.

The electrical waveforms describing the voltages at various points in the segmented logic block are shown in Figure 16a. The waveforms which describe the voltages for the entire  $L_n$  logic block are shown in Figure 16b.

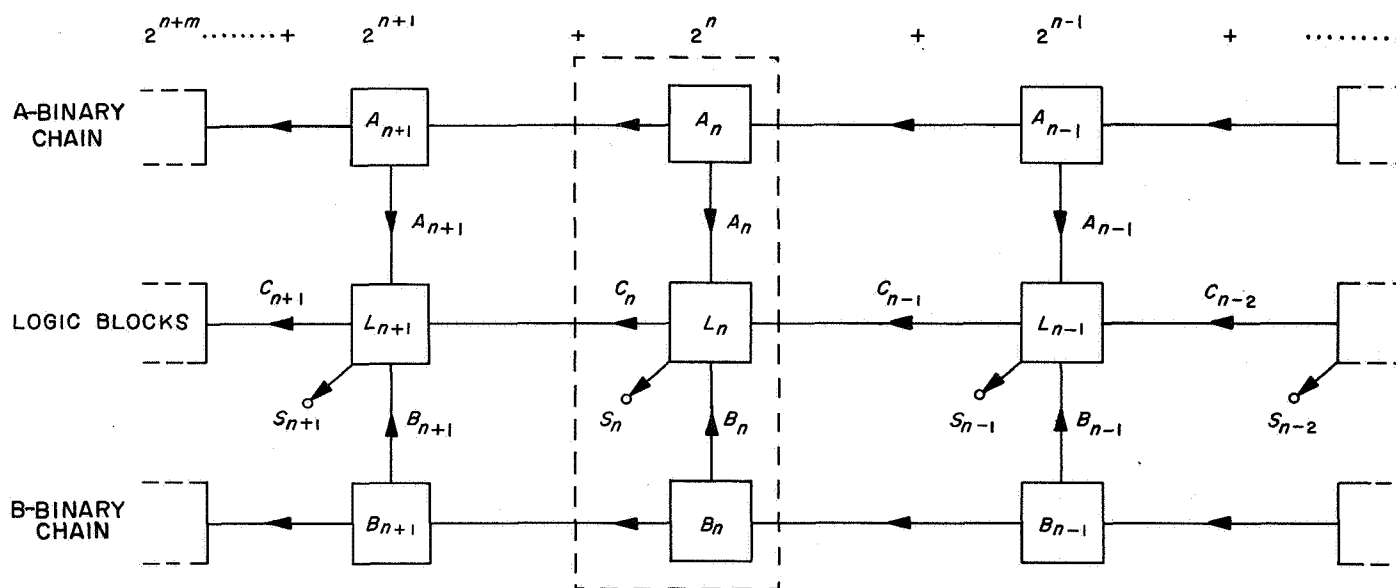


Figure 14. Address logic block diagram for binary adder



#### 4. Problems Inherent in Present System

Although the present tunnel diode logic system is operative, a few problems continue to plague the system due to inherent limitations of the tunnel diodes employed in the circuit. These problems are briefly discussed below:

*a. Low-level switching.* Due to the physical nature of the tunnel diode, it is limited to low-level voltage oper-

ation. When the tunnel diode switches from one voltage state to another, it produces a voltage swing of approximately 0.5 volt. This limitation presents a problem when one tries to use standard diodes in some of the basic logic blocks (*and* and *or* gates) when these blocks are triggered by the tunnel diode driving units shown in Figure 8b. The low-level output of the tunnel diode driver is hardly adequate to turn the logic diodes fully “on” or fully “off.”

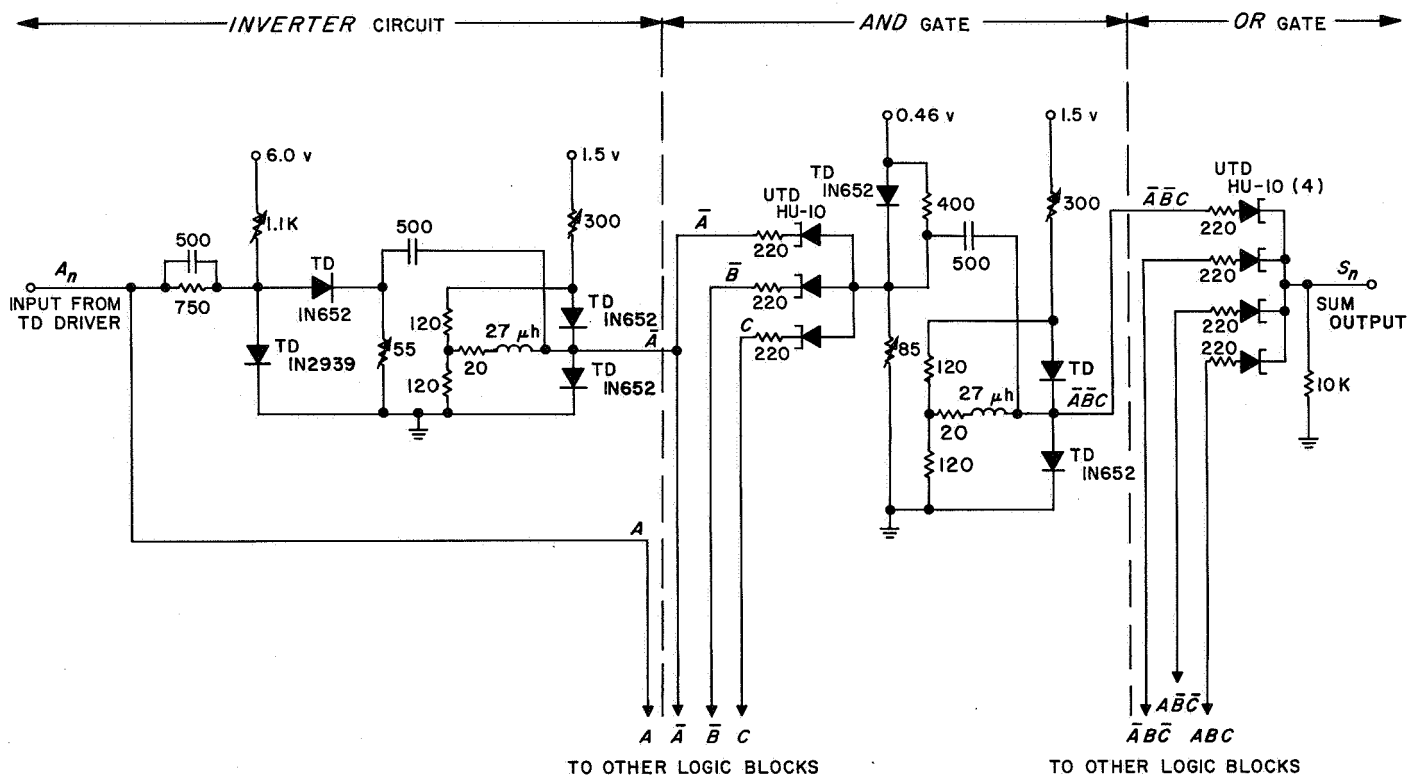


**Figure 15. Segment of logic circuit for  $L_n$  logic block**

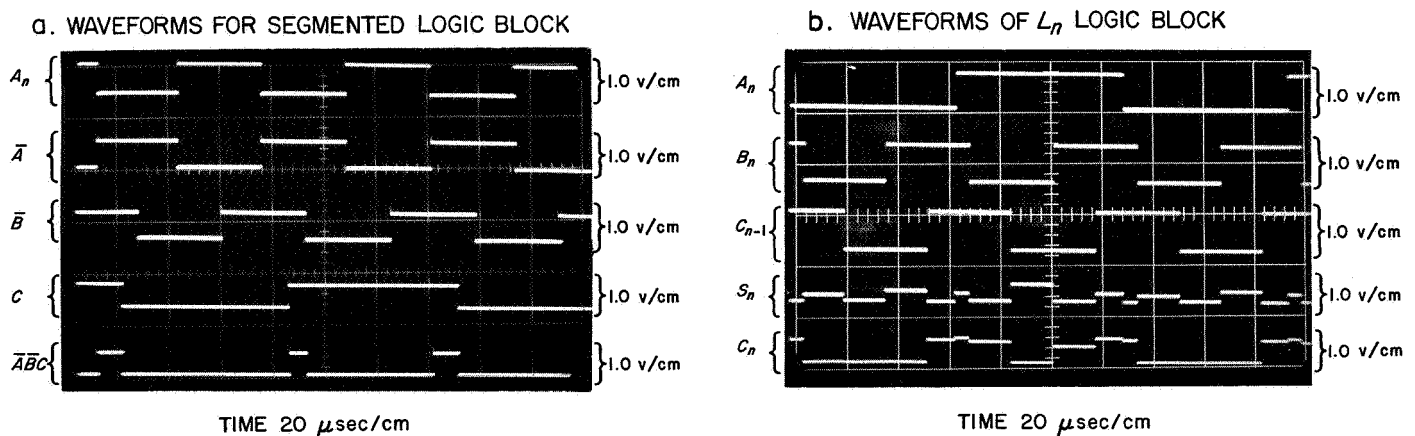


**Figure 16. Waveforms for segmented and  $L_n$  logic blocks**

The best attempt at solving this problem at present has been to employ diodes in the logic circuits which turn "on" at comparatively low voltage points. The Hoffman HU-10 Uni-Tunnel Diode is presently being used to perform this operation. These diodes turn "on" (conduct 1 ma) at approximately 0.2 volt, which was adequate for logical switching. However, if diodes could be found which begin to conduct at even lower voltages, the logic switching using tunnel diode driving units would be greatly improved. It is apparent that the low-level output of the tunnel diode driving unit in Figure 8b is definitely limited in its ability to drive other circuits, such as printers, recorders, and servos.

**b. Crosstalk.** Since the tunnel diode is a low-voltage, low-impedance, current-triggered device, it is susceptible to random triggering by noise and stray fields when the diode is in a critically biased condition. With the low-impedance circuitry associated with tunnel diodes, stray currents can be easily coupled into the system causing the tunnel diode to be triggered from one voltage state to another.

In the overall logic system discussed above, the problem of random triggering due to stray fields and noise was essentially eliminated when the power supply lines and main transmission lines from one part of the system to another were properly shielded.

**c. Critical bias voltage.** The parameters of the tunnel diode circuit may be adjusted to fit the individual tunnel diode characteristics. Once this adjustment has been made, however, a slight variation in supply voltage may

upset the critical bias of the tunnel diode. With some of the circuits in the  $L_n$  logic block described earlier, a variation in supply voltage by as much as 5% was able to upset the critical bias of the logic circuit. Obviously, power supply stability is an important factor to consider in the design of tunnel diode circuits.

**d. Variation of tunnel diode characteristics.** None of the tunnel diodes used in the overall logic system had identical  $I$ - $V$  characteristics. As a consequence of this nonuniformity in characteristics, it was necessary to adjust the parameters of each circuit individually in order to meet the bias condition for each tunnel diode used. The  $R_b$  of the circuit shown in Figure 8b was a typical parameter which required adjustment. It was found that it was necessary to vary  $R_b$  as much as 25% from one circuit to another to sustain operation. This necessity for individual circuit adjustment could be cumbersome in larger logical systems.

Two approaches are recommended for solving the problem of individual circuit adjustment in future tunnel diode systems. One approach is to select only those tunnel diodes for the system which have  $I$ - $V$  characteristics which are identical within strict tolerances. This might lead to considerable expense in the selection process. An alternate approach is to redesign the circuits themselves, so that they will depend little on the variation of tunnel diode characteristics. This is apparently the better approach; however, it is suspected that such a modification would require a sacrifice in gain and in the speed of switching.

## SYSTEMS DIVISION

### II. Systems Analysis

#### A. Trajectory Analysis

V. C. Clarke

##### 1. Interplanetary Trajectories

As reported in RS 36-8, a computer study is in progress to determine the characteristics of ballistic interplanetary trajectories from Earth to Mars, Venus, Mercury, and Jupiter. The computations for Venus from 1962 to 1970, for Mars from 1962 to 1977, for Mercury from October 1967 to January 1969, and for Jupiter from December 1969 to February 1970 are now complete. A table of minimum energy transfers was published in RS 36-8. Final additions to that table are given in Table 1. These trajectories have been computed using actual planet positions obtained from an ephemeris tape. Thus, inaccuracies arising from assuming coplanar, circular motions of the planets are nonexistent.

Selected parameters of the trajectories have been saved on magnetic tapes. These tapes are being used to generate graphs of the parameters on an automatic plotting machine. The results of this study, with about 200 graphs,

will be reported in Reference 7. Publication target date is September 1961.

A second phase of the study has begun with the computation of return ballistic trajectories from Mars and Venus to Earth. The results of these computations will also be saved on magnetic tape, and graphs will be prepared. In addition, the return trajectories will be combined with the Earth-to-target planet trajectories in a merging program to obtain round trip transfers. These transfers will include both ballistic flyby and stopovers of various duration at the planet. Completion of this phase of the study is projected to November 1961.

##### 2. Out-of-Ecliptic Trajectories

A study is nearing completion of a special class of trajectories in which a space probe is launched from Earth in a direction perpendicular to the ecliptic plane, flies above (or below) the plane for a period up to 6 months, and finally returns to Earth. A cursory look at such trajectories from two-body (Sun-probe) mechanics indicates that the distance above the ecliptic that can be

Table 1. Characteristics of minimum-energy transfer trajectories

Planet	Trajectory type	Launch date	Flight time, days	Geocentric injection energy, <sup>a</sup> $\text{m}^2/\text{s}^2 \times 10^3$	Heliocentric central angle, deg	Earth-planet distance at arrival, $10^6$ km	Celestial latitude of planet at arrival, deg
Mars	I	5/24/71	210	0.079	156.0	164	-0.352
	I	7/30/73	192	0.146	141.4	179	1.16
	I	9/15/75	206	0.187	144.7	221	1.85
	I	10/19/77	224	0.170	152.9	244	1.44
Jupiter	I	1/3/70	985	0.753	177.9	744	0.004
	II	12/30/69	995	0.754	182.5	757	-0.007

<sup>a</sup>Twice the total energy per unit mass, or the vis viva integral.

attained by a probe is directly proportional to the injection energy or hyperbolic-excess speed according to the relations

$$Z = R_E \tan \beta$$

and

$$\sin \frac{\beta}{2} = \frac{V_h}{2V_E}$$

where  $Z$  is the distance above the ecliptic,  $R_E$  is the Sun-Earth distance,  $\beta$  is the celestial latitude of the probe when it reaches its maximum distance above (or below) the ecliptic,  $V_h$  is the hyperbolic-excess velocity (directed normal to the ecliptic), and  $V_E$  is the heliocentric speed of the Earth.

In addition, for return to Earth, two-body mechanics dictates a 6-month flight time. A severe launch restriction is associated with this class of trajectories. For launchings from Cape Canaveral, it is found that launch azimuth is restricted to extreme northerly (<27 deg) or extreme southerly (>153 deg) azimuths. The reason for this is that the declination of the hyperbolic-excess velocity vector must be approximately 66.5 degrees or 90 degrees minus the obliquity of the ecliptic. The relation governing the limiting launch azimuths is

$$\sin \Sigma_L = \frac{\cos 66.5^\circ}{\cos \phi_L}$$

where  $\Sigma_L$  is the launch azimuth measured positive east of true north, and  $\phi_L$  is the launcher latitude. Because of the azimuth restriction, it is very likely that range safety considerations would prohibit launches from Cape Canaveral for this type of trajectory. However, launchings from the launch facilities of the Pacific Missile Range are feasible.

Departure from two-body mechanics to exact simulation of these trajectories reveals several interesting char-

acteristics. These are illustrated in Figures 17 and 18. Figure 17 is a plot of flight time vs injection energy. Here, it is seen that, as injection energy is decreased to zero, the flight time falls to just over 4 months, instead of 6 months. Any further decrease of energy would result in even lower flight times. This result cannot be predicted by two-body mechanics. In Figure 18, the plot of range from Earth center vs time shows that for a hyperbolic-excess speed of 3 km/sec (Venus-type speed) a height of almost 15 million kilometers above the ecliptic can be attained, in good agreement with two-body results.

Another property of this class of trajectories is that an approximate analytical solution to the four-body (Sun-Earth-Moon-probe) problem can be obtained. This solution is currently being evaluated and compared to the exact solution from the JPL six-body integrating trajectory program on the IBM 7090. Results of this comparison will be reported in the next *Research Summary*.

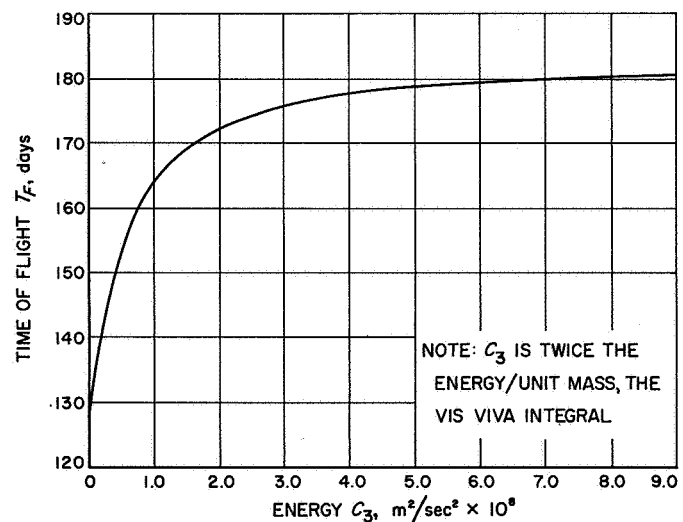


Figure 17. Time of flight vs injection energy

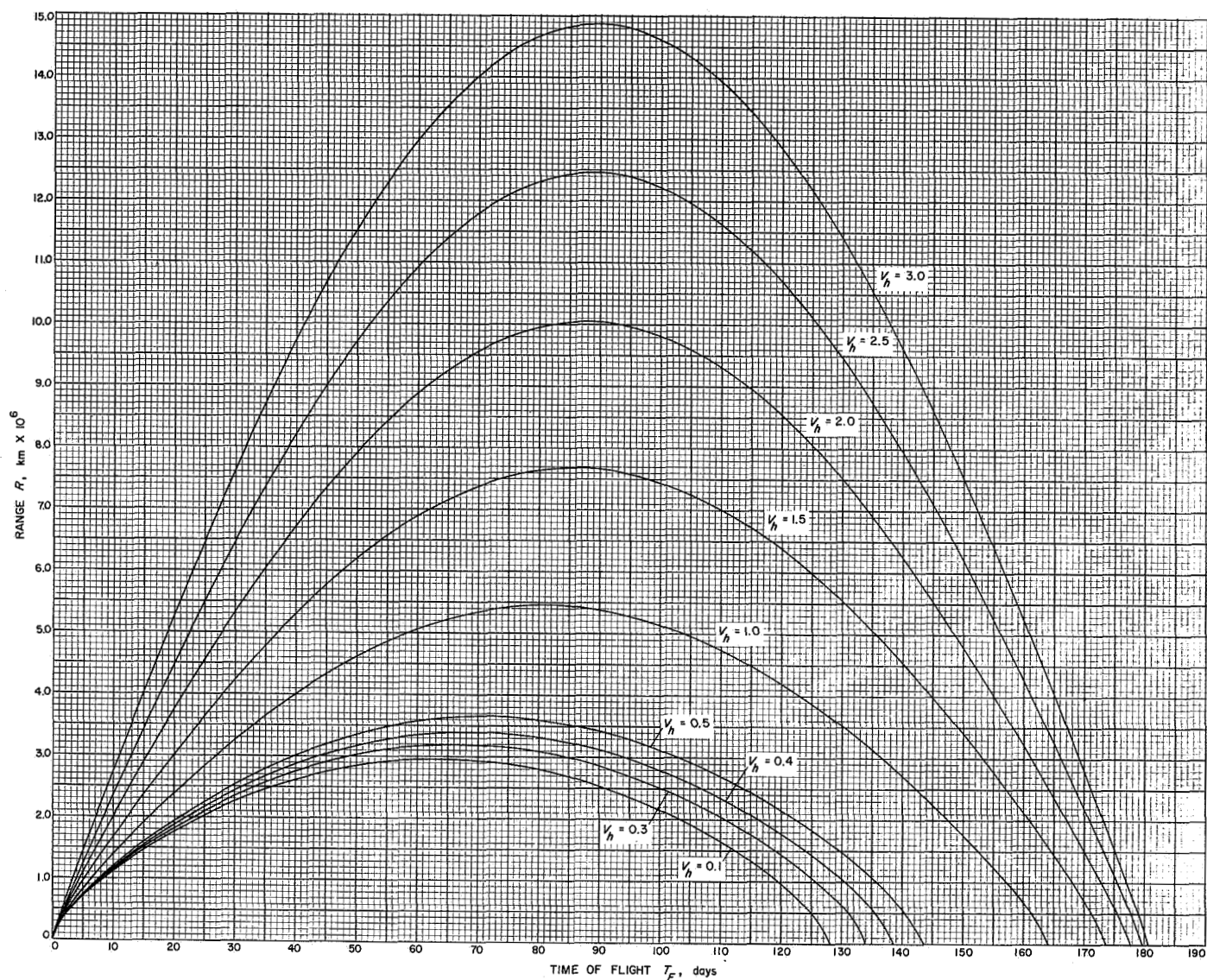


Figure 18. Range from Earth center vs time of flight for various hyperbolic excess speeds

## B. Space Flight Studies

E. Cutting

### 1. Program for Low-Thrust Correction of Circular Satellite Orbits

A spacecraft which uses low-thrust propulsion must first be boosted into orbit by a chemical rocket. The low-thrust motors then take over and cause the spacecraft to gradually spiral out to obtain the desired satellite orbit or to escape, depending on the mission. If the initial orbit is circular and if the propulsive acceleration is

small, each of the turns of the spiral is nearly circular (except for the last few before escape). Thus, it would be useful to know in what direction one should apply the thrusts and what magnitude the thrusts should have in order to make any desired changes or corrections in a nearly circular orbit.

Figure 19 shows the cylindrical coordinate system, and Figure 20 shows a thrust program which can be used to correct circular orbits. The program is resolved into three acceleration components which are radial, tangential, and normal to the standard orbit. The radial and tangential accelerations are each the sum of a constant and a square

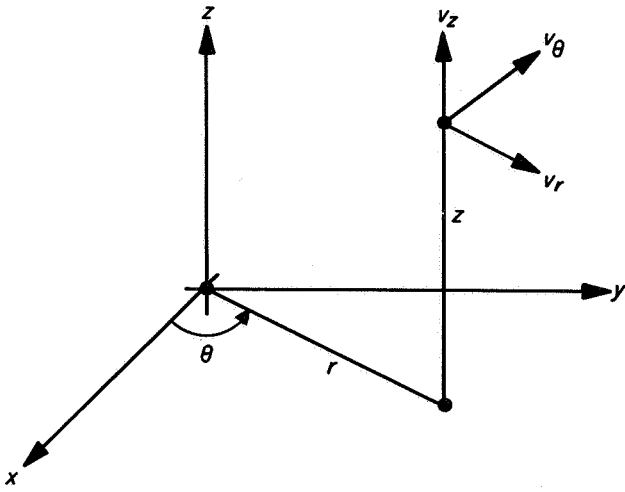


Figure 19. Coordinates of spacecraft motion

wave with a period equal to the orbital period. The transverse acceleration is the sum of two square waves which are out of phase by 0.25 orbital period. The magnitudes of each component are given by the equation in Figure 21. Although a number of different programs can be devised to correct a circular orbit, this particular one has several advantages. First, the equation in Figure 21 contains parameters which allow the duration of the thrust program to be adjusted so as to limit the peak

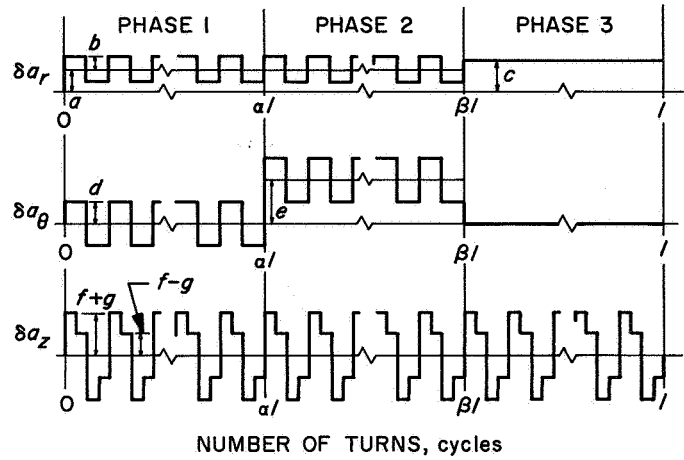


Figure 20. Orbit correction thrust programs

correcting acceleration to any desired value. Second, the program is of such a form that it can be easily generated in the guidance computer.

**a. Definitions.** In Figure 19,  $x, y, z$  is a space-fixed coordinate system centered at the attracting body;  $r, \theta, z$  are the cylindrical coordinates of the spacecraft. The velocity is measured by the three orthogonal components  $v_r = \dot{r}$ ,  $v_\theta = r\dot{\theta}$ , and  $v_z = \dot{z}$ . The components of the acceleration applied by the low-thrust motors are

$$\begin{bmatrix} a \\ b \\ c \\ d \\ e \\ f \\ g \end{bmatrix} = \begin{bmatrix} \frac{3}{4} \omega_0^2 \left( \frac{\beta - \alpha}{\beta} \right) & - \left( \frac{16 + 3\pi^2}{32\pi} \right) \omega_0 \frac{1}{\beta l} & 0 & \frac{3}{4} \omega_0 \left( \frac{\beta - \alpha}{\beta} \right) & 0 & 0 \\ \frac{1}{4} \omega_0^2 \frac{1}{\beta l} & 0 & 0 & - \frac{1}{2} \omega_0 \frac{1}{\beta l} & 0 & 0 \\ \frac{3}{2} \omega_0^2 \left( \frac{\beta}{1 - \beta} \right) & 0 & \frac{1}{4\pi} r_0 \omega_0^2 \frac{1}{l(1 - \beta)} & \frac{3}{2} \omega_0 \left( \frac{\beta}{1 - \beta} \right) & 0 & 0 \\ 0 & \frac{1}{8} \omega_0 \frac{1}{\beta l} & 0 & 0 & 0 & 0 \\ - \frac{1}{2\pi} \omega_0^2 \frac{1}{l(\beta - \alpha)} & 0 & 0 & - \frac{1}{2\pi} \omega_0 \frac{1}{l(\beta - \alpha)} & 0 & 0 \\ 0 & 0 & 0 & 0 & \frac{1}{4} \omega_0^2 \frac{1}{l} & 0 \\ 0 & 0 & 0 & 0 & 0 & - \frac{1}{4} \omega_0 \frac{1}{l} \end{bmatrix} \begin{bmatrix} \delta r_i \\ \delta v_{ri} \\ \delta \theta_i \\ \delta v_{\theta i} \\ \delta z_i \\ \delta v_{zi} \end{bmatrix}$$

Figure 21. Thrust amplitude equation

$\delta a_r, \delta a_\theta, \delta a_z$  measured in the same directions as  $v_r, v_\theta, v_z$ . The units are meters, radians, and seconds. The standard trajectory is defined by  $r = r_0$ ,  $\theta = \omega_0 t$ , and  $z = 0$ . It is assumed that the only forces on the spacecraft are the inverse-square gravitational attraction and the thrust of the low-thrust motors. Let the vector

$$\delta y_i^T = (\delta r_i, \delta v_{ri}, \delta \theta_i, \delta v_{\theta i}, \delta z_i, \delta v_{zi})$$

be the coordinate deviations which are to be corrected. These deviations could be measured in a number of ways; for example, by Earth-based radio tracking or by self-contained orbital rate measurements. The  $\delta y_i$  can be corrected by a thrust program of the type shown in Figure 20, where the amplitudes are defined by the equation in Figure 21. This equation is derived by means of linear perturbation theory. Actually, only six variables are needed to describe the thrust program since

$$a + \left( \frac{16 + 3\pi^2}{4\pi} \right) d + \left( \frac{3\pi}{2} \right) \frac{l(\beta - \alpha)^2}{\beta} e = 0$$

**b. Orbit correction program.** As shown in Figure 20, the total length of the program is  $l$  cycles. The length of Phase 1 is  $\alpha l$  cycles, and the length of Phase 2 is  $(\beta - \alpha)l$ , where  $\alpha < \beta < 1$ . In Phases 1 and 2,  $\delta a_r$  consists of a constant acceleration of magnitude  $a$  and a square wave with amplitude  $b$ . In Phase 3,  $\delta a_r$  becomes a constant with magnitude  $c$ . In Phase 1,  $\delta a_\theta$  is a square wave with amplitude  $d$ . In Phase 2, a constant  $e$  is added to the square wave. In Phase 3,  $\delta a_\theta = 0$ . The  $\delta a_z$  is the same for all three phases and is the sum of two square waves. The first square wave has amplitude  $f$  and is in phase with the square waves of  $\delta a_r$  and  $\delta a_\theta$ . The second square wave has amplitude  $g$  and leads the first by 0.25 cycle.

The parameters  $\alpha$ ,  $\beta$ , and  $l$  are useful since they can be adjusted to reduce the level of acceleration required. If it is not required to correct  $\delta \theta_i$ , as might be the case in some satellite applications, the program can be considerably simplified. The accelerations  $\delta a_r$ ,  $\delta a_\theta$ , and  $\delta a_z$  could be applied by maintaining a fixed spacecraft attitude and having a number of motors pointed in the proper directions. Alternatively, only one motor could be used, and the spacecraft itself would then have to be oriented to the proper direction angles. The attitude control system for a low-thrust vehicle will probably be designed to have a slow response because of the flimsy structure of the radiators. Thus, it might be desirable to use sine waves instead of square waves in the thrust program, which would entail minor changes in the matrix of Figure 21.

## C. Research Studies

C. G. Sauer

### 1. Hyperbolic Orbit Perturbation Study

Of particular interest in the design of lunar and interplanetary escape trajectories are the effects of the oblateness of the Earth on the escape hyperbola. In addition to the usual hyperbolic elements, it is also desirable to observe the effects of the oblateness on the magnitude and direction of the hyperbolic excess velocity vector.

The gravitational potential  $U$  of the Earth, expanded in terms of surface zonal harmonics and assuming axial symmetry, is

$$U = \frac{k^2}{r} \left[ 1 - \sum_{p=2}^{\infty} J_p r^{-p} P_p(\sin \phi) \right] \quad (1)$$

where the  $J_p$  are the coefficients of the zonal harmonics  $P_p(\sin \phi)$ ,  $k^2$  is the gravitational constant of the Earth,  $r$  the radial distance from gravicenter in equatorial radii, and  $\phi$  the geocentric latitude. Since the time spent in the vicinity of the Earth after injection is short, only the second harmonic of the potential function causes a significant perturbation of the orbital elements. Hence, the perturbative potential or disturbing function  $R$  may be expressed as

$$R = -J_2 \frac{k^2}{2r^3} (3 \sin^2 \phi - 1) \quad (2)$$

The solution of the differential equations representing the variations of the orbital elements with respect to the true anomaly was derived by a method analogous to that used by Kozai (Ref 8) in his investigations of elliptic motion. The solutions for the perturbations  $\delta$  of the orbital elements are

$$\delta E = R(T) - R(0) \quad (3)$$

$$\begin{aligned} \delta b = J_2 \frac{b \sin^2 i}{4p^2} [3e \cos(2\omega + \nu) + 3 \cos 2(\omega + \nu) \\ + e \cos(2\omega + 3\nu)]_0^T \end{aligned} \quad (4)$$

$$\begin{aligned} \delta \Omega = -J_2 \frac{\cos i}{4p^2} \{ 6(\nu + e \sin \nu) - [3e \sin(2\omega + \nu) \\ + 3 \sin 2(\omega + \nu) + e \sin(2\omega + 3\nu)] \}_0^T \end{aligned} \quad (5)$$

$$\delta\omega + \cos i \delta\Omega = J_2 \frac{3}{2p^2} \left\{ \left( 1 - \frac{3}{2} \sin^2 i \right) \left[ \nu + \frac{4 + 3e^2}{4e} \sin \nu \right. \right. \\ \left. \left. + \frac{1}{2} \sin 2\nu + \frac{e}{12} \sin 3\nu \right] - \frac{\sin^2 i}{48e} [3e^2 \sin(2\omega - \nu) \right. \\ \left. + (12 - 21e^2) \sin(2\omega + \nu) - 36e \sin 2(\omega + \nu) \right. \\ \left. - (28 + 11e^2) \sin(2\omega + 3\nu) - 18e \sin(2\omega + 4\nu) \right. \\ \left. \left. - 3e^2 \sin(2\omega + 5\nu) \right] \right\}_0^T \quad (6)$$

$$\delta\tau + \frac{(e^2 - 1)^{1/2}}{n} (\delta\omega + \cos i \delta\Omega) = J_2 \frac{3(e^2 - 1)^{1/2}}{2np^2} \\ \times \left\{ \left( 1 - \frac{3}{2} \sin^2 i \right) (\nu + e \sin \nu) + \frac{1}{4} \sin^2 i [3e \sin(2\omega + \nu) \right. \\ \left. + 3 \sin 2(\omega + \nu) + e \sin(2\omega + 3\nu)] + \frac{3MR}{n^3 a^2} \right\}_0^T \quad (7)$$

$$\delta h_z = 0 \quad (8)$$

The quantities appearing in the above equations are:  $E$  the energy,  $h$  the angular momentum,  $h_z = h \cos i$  the component of angular momentum along polar axis,  $\tau$  is the time of perifocal passage,  $\omega$  the argument of perigee,  $\Omega$  the longitude of the ascending node,  $i$  the inclination of orbit,  $p = h^2/k^2 = \text{semi-latus rectum}$ ,  $e = [1 - (2Eh^2/k^4)]^{0.5}$  the eccentricity,  $\nu$  the true anomaly,  $M$  the mean anomaly,  $n$  the mean motion, and  $a$  the semitransverse axis.

In addition, the perturbations of the magnitude  $V_H$ , right ascension  $\alpha_H$ , and declination  $\phi_H$  of the excess hyperbolic velocity vector are given by

$$\delta V_H = \frac{\delta E}{V_H}$$

$$\delta\alpha_H = \delta\Omega - \frac{\sin \phi_H \cos(\omega + \nu_H)}{\cos^2 \phi_H} \delta i + \frac{\cos i}{\cos^2 \phi_H} (\delta\omega + \delta\nu_H)$$

$$\delta\phi_H = \frac{\cos i \sin(\omega + \nu_H)}{\cos \phi_H} \delta i + \frac{\sin i \cos(\omega + \nu_H)}{\cos \phi_H} (\delta\omega + \delta\nu_H)$$

where

$$\delta\nu_H = - \frac{(e^2 - 1)^{0.5}}{2e^2} \left[ \frac{\delta E}{E} + 2 \frac{\delta b}{b} \right]$$

The constants and initial osculating elements shown in Table 2 were used as an example, and the resulting perturbations were calculated when the vehicle was a great distance from the Earth. The results are shown in Table 3.

Table 2. Initial values of elements

Element	Value
$E$ , megameters <sup>2</sup> /sec <sup>2</sup>	$7.811866 \times 10^{-6}$
$h$ , megameters <sup>2</sup> /sec	$7.563248 \times 10^{-2}$
$\tau$ , sec	0.0
$i$ , deg	30.0
$\omega$ , deg	306.87
$\Omega$ , deg	0.0
$k^2$ , megameters <sup>3</sup> /sec <sup>2</sup>	$0.398602 \times 10^{-3}$
$R_e$ , megameters	6.378150
$J_2$	$1.08228 \times 10^{-3}$

Table 3. Final values of perturbations

Element	Value
$\delta E$ , megameters <sup>2</sup> /sec <sup>2</sup>	$1.755 \times 10^{-8}$
$\delta h$ , megameters <sup>2</sup> /sec	$0.168 \times 10^{-6}$
$\delta\tau$ , sec	0.1607
$\delta i$ , deg	0.0043
$\delta\omega$ , deg	0.0696
$\delta\Omega$ , deg	-0.0273
$\delta V_H$ , megameters/sec	$4.449 \times 10^{-6}$
$\delta\alpha_H$ , deg	0.0888
$\delta\phi_H$ , deg	0.0043

## D. Powered Flight Studies

C. E. Kohlase

### 1. Terminal Mission Performance Studies

One of the most important factors in determining the selection of a particular terminal mission is the realizable payload which, of course, depends upon the terminal maneuver propellant and heat-shield requirements. Terminal maneuvers are defined as any maneuvers that result in the spacecraft being captured (either as a satellite or landing) by the destination body. The capture may be effected by utilizing chemical retro-thrust, low-thrust propulsion, atmospheric braking, or combinations of these. The purpose of this study is to determine the range



of final-to-initial-mass ratios that may be achieved for several different terminal missions to the Moon, Mars, and Venus.

**a. General formulas.** Consider the general situation of Figure 22, and suppose we want to determine the velocity decrement (instantaneous velocity addition is assumed) necessary to establish any desired ellipse at a distance  $R$  from the destination. (See Table 4 for nomenclature.)

It can be shown that the square of the required velocity decrement  $\Delta V$  is given by:

$$(\Delta V)^2 = V_\infty^2 + \frac{2\mu}{\lambda R_0} \left( \frac{2}{\xi_1} - \frac{1}{k+1} \right) - \frac{2}{(\lambda R_0)^{1/2} \xi_1^2} \left( \frac{2\mu}{k+1} \right)^{1/2} \\ \times \left\{ \left[ k \xi \xi_1 \left( \frac{2\mu}{\lambda R_0} + \xi \xi_1 V_\infty^2 \right) \right]^{1/2} + \delta \left[ \xi \xi_1 (1-k)^2 (1-\xi) \right. \right. \\ \left. \left. \times \left( \frac{2\mu}{\lambda R_0} (1-\xi) + \xi_1 V_\infty^2 (1-\xi^2) \right) \right]^{1/2} \right\} \quad (1)$$

where

$$\begin{aligned} R_a &= \lambda R_0, & \lambda &\geq 1 \\ R_p &= k R_a, & 0 &\leq k \leq 1 \\ R_{ca} &= \xi R, & 0 &\leq \xi \leq 1 \\ R &= R_a - \xi (R_a - R_p), & 0 &\leq \xi \leq 1 \\ \xi_1 &= 1 - \xi (1 - k) \\ \delta &= 1 \text{ for } \begin{cases} 0 \leq v_h, & 0 \leq v_e \leq \pi \\ v_h < 0, & \pi < v_e < 2\pi \end{cases} \\ \delta &= -1 \text{ for } \begin{cases} 0 \leq v_h, & \pi < v_e < 2\pi \\ v_h < 0, & 0 \leq v_e \leq \pi \end{cases} \end{aligned}$$

In order to limit the largest angle between  $V_h$  and  $V_e$  to  $\pi/2$ , we must choose  $\delta = 1$  and further assume that the two conics are never oppositely directed. It should be noted that  $\xi$  and  $\zeta$  are simply indicators which give the location along the approach and capture conics.

Neglecting gravity losses that accompany rocket burning against a gravitational field, for a constant-thrust rocket the ratio of final spacecraft mass to initial mass is given by

$$m_f/m_0 = e^{-\Delta V/c} \quad (2)$$

where  $c$  is the *effective* propellant exhaust velocity and is assumed equal to 3 km/sec whenever presenting typical values of  $m_f/m_0$  for various terminal retro-maneuvers. Figure 23 illustrates the surface of all possible retro-maneuvers that will establish an elliptic orbit about Mars ( $V_\infty = 4$  km/sec) with  $\lambda = 2$ ,  $k = 0.5$ . The ratio  $m_0/m_f$

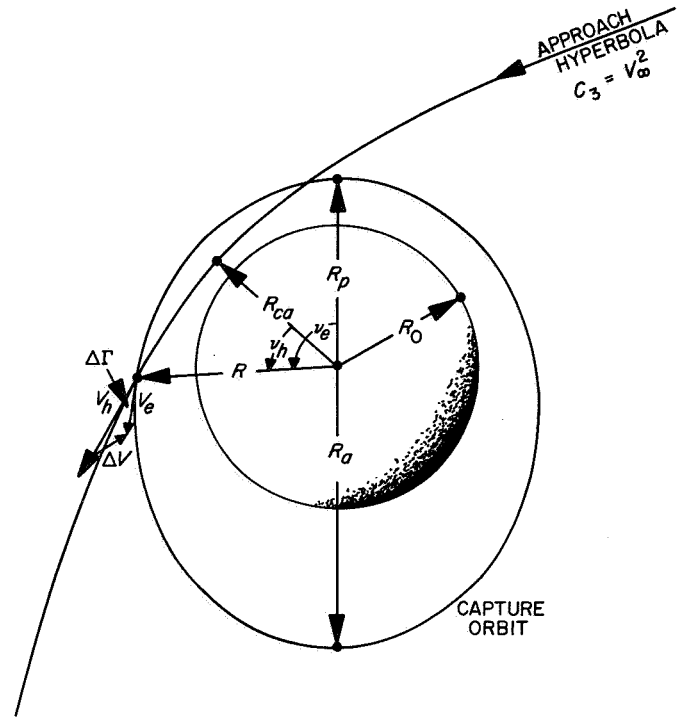


Figure 22. Terminal maneuver geometry

has been shown instead of its reciprocal in order that the surface might appear in its most lucid view. As expected, the minimum value of  $m_0/m_f$  occurs at (1,1) and the maximum value at (0,1). Curves A and B indicate the loci of  $\partial(m_0/m_f)/\partial\xi = 0$  and  $\partial(m_0/m_f)/\partial\xi = 0$ , respectively. These curves show clearly the interesting result that there is an optimum orientation of the approach and capture conics such that the required  $m_0/m_f$  will be a minimum, given any  $\xi$  or  $\zeta$ . It should be remembered that Figure 23 represents the maneuver surface for only one particular ellipse and that, in general, there are an infinite number of maneuver surfaces. For the special case of establishing a circular satellite orbit about the destination,  $m_0/m_f$  is independent of  $\zeta$  and the minimum  $m_0/m_f$  clearly occurs at  $\xi = 1$ . As the eccentricity of the capture ellipse is increased (without changing the periapsis distance), the troughs of A and B become more pronounced and significantly lower values of  $m_0/m_f$  are realized along Curve A. The corners of the maneuver-surface *curtain* at (0,0) and (1,1) are lowered with increasing eccentricity, while the corners at (0,1) and (1,0) are raised.

**b. Attaining a circular satellite orbit.** When the retro-maneuver is performed at the periapsis of the approach hyperbola in order to establish a circular satellite orbit about the destination, Equation (1) reduces to

$$\Delta V = [V_\infty^2 + 2\mu R_c^{-1}]^{1/2} - [\mu R_c^{-1}]^{1/2} \quad (3)$$

**Table 4. Nomenclature**

$C_3$	= twice total energy per unit mass
$c$	= effective exhaust velocity
$h$	= altitude above destination surface
$k$	= $R_p/R_a$
$m$	= vehicle mass
$R$	= distance from vehicle to center of attracting body
$V$	= vehicle inertial velocity
$\Gamma$	= path angle of inertial velocity vector
$\mu$	= gravitational parameter, equal to product of universal gravitational constant and mass of attracting body
$\nu$	= true anomaly
$\sigma$	= $V/V_{esc}$
$\xi$	= $R_{ca}/R$
$\zeta$	= $(R_a - R)/(R_a - R_p)$
$\lambda$	= $R_a/R_0$

**Subscripts**

$a$	= apoapsis
$c$	= circular conditions
$ca$	= closest approach distance of approach hyperbola
$e$	= ellipse
$esc$	= escape
$E$	= entry conditions
$f$	= final value
$h$	= hyperbola
$p$	= periapsis
$P$	= payload
$0$	= reference value
$\infty$	= value at infinite distance from destination body

where  $R_c$  is the distance of the circular orbit from the center of the destination. It can be shown that there exists an optimum distance (designated  $R_c^*$ ) for which  $\Delta V$  given by Equation (3) is a minimum.

$$R_c^* = \frac{2\mu}{V_\infty^2} \quad (4)$$

At this value of  $R_c$ ,  $\Delta V = V_\infty/(2)^{1/2}$ , which represents the minimum required  $\Delta V$  for a given value of  $V_\infty$ . Figure 24 illustrates the values of  $h_c^*$  (altitude above destination surface) for a range of  $V_\infty$  relative to the Moon, Mars, and Venus. Typical  $V_\infty$  relative to Mars and Venus (for chemical-propulsion trajectories from Earth) fall in the region from about 4.5 to 7.5 km/sec. Mars is especially interesting as small  $h_c^*$  are available. For the Moon and Venus, however, small  $h_c^*$  can only be realized by using higher  $V_\infty$  which would, of course, result in smaller  $m_f/m_0$ .

In order to obtain a feel for how much is lost by establishing a circular satellite orbit at an altitude other than

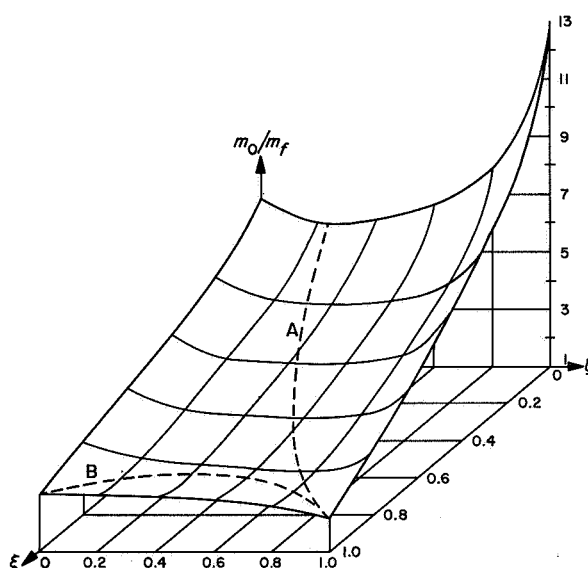


**Figure 23. Burnout mass-ratio surface of all possible retro-maneuvers to establish elliptical orbit, with  $\lambda = 2$ ,  $k = 0.5$ , about Mars for  $V_\infty = 4$  km/sec**

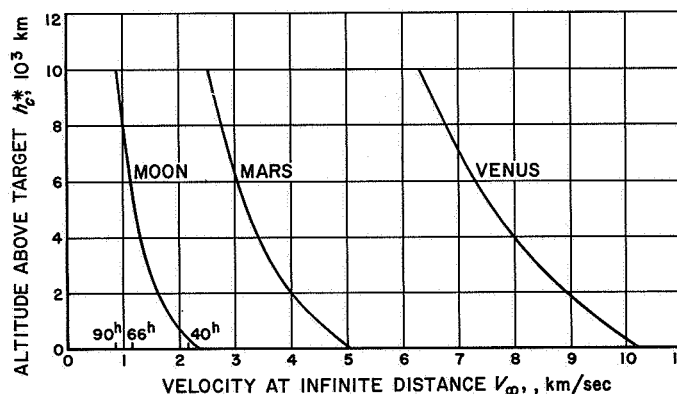


**Figure 24. Altitude above destination surface for minimum velocity decrement necessary to establish circularity for given value of  $V_\infty$  relative to destination**

$h_c^*$ , Table 5 gives the approximate percentage losses in  $m_f$  per 1000 km of deviation from the optimum altitude  $h_c^*$ .

*c. Descent along capture orbit.* Consider Figure 25, and suppose we wish to determine  $R_a$  and  $R_p$  such that a preselected velocity  $V$  and path angle  $\Gamma$  may be obtained at some given distance  $R$ . The following expressions have been obtained from the general conic formulas:

$$\frac{R_p}{R} = \frac{R_a - R}{R_a \sec^2 \Gamma - R} \quad (5)$$

Table 5. Mass loss per 1000 km deviation from  $h_c^*$

Parameter	Moon		Mars		Venus	
$V_\infty$ , km/sec	1.0	2.0	4.0	5.0	4.0	8.0
$\Delta m_f/m_f$ , %	0.1	0.5	0.5	1.0	NIL	0.3

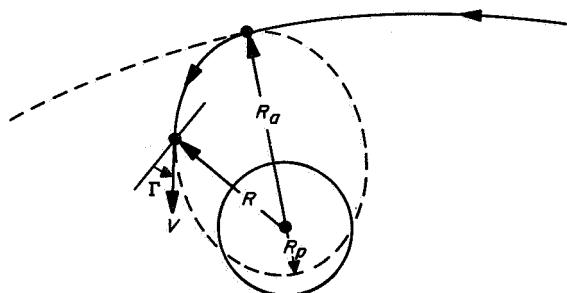


Figure 25. Elliptical descent geometry

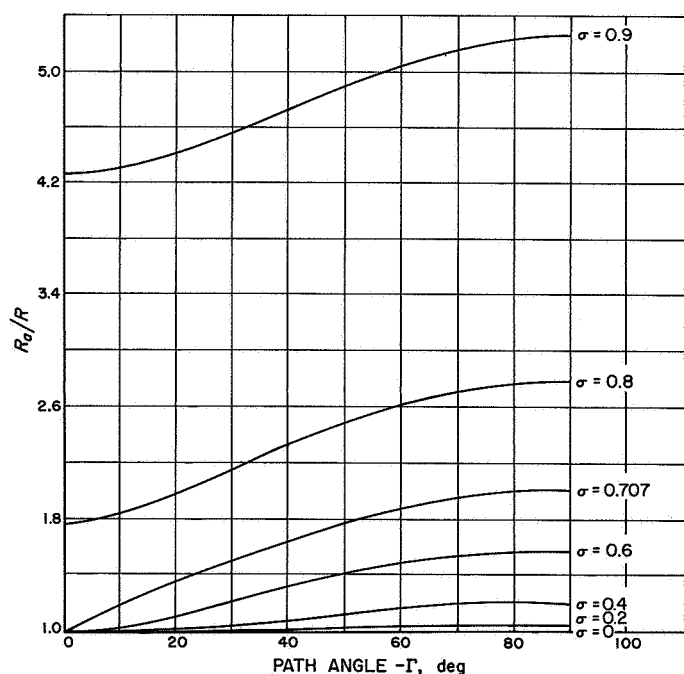


Figure 26. Apoapsis behavior with path angle,

$$\frac{R_p}{R} = \frac{1}{1 - \sigma^2} - \frac{R_a}{R} \quad (6)$$

where  $\sigma = V/V_{esc}$ , and  $V_{esc} = (2\mu/R)^{1/2}$ . Equations (5) and (6) may be solved to yield:

$$\frac{R_a}{R} = \frac{1}{2(1 - \sigma^2)} \{1 + [1 - 4\sigma^2(1 - \sigma^2)\cos^2 \Gamma]^{1/2}\} \quad (7)$$

Figure 26 illustrates the behavior of  $R_a/R$  with  $\Gamma$ , for curves of constant  $\sigma$ . Once  $R_a/R$  has been determined,  $R_p/R$  may be obtained from Equation (6). In specifying

Table 6. Terminal missions resulting in capture

Terminal maneuver	Braking technique	Landing technique	Table 7 Mission No.
Direct descent from approach hyperbola	Rocket braking only, for bodies that do not possess an atmosphere	Retro-rocket	1
	Atmospheric braking only	Parachute	2
		Retro-rocket	3
	Combination of rocket and atmospheric braking	Parachute	4
		Retro-rocket	5
Retro-thrust <sup>a</sup> application to establish capture orbit, beginning either at periapsis or at a given altitude	Orbit not adjusted or improved	Observe planet without landing	6
		Descent or entry along capture orbit	7
		Eject capsule from orbiting spacecraft to transit atmosphere	8
	Orbit improved by determining orbital elements and performing adjustive maneuver	Observe without landing	9
		Descent along capture orbit	10
		Ejected capsule landing	11
Advanced terminal missions	Capture and entry achieved by gasdynamic lift	Gasdynamic lift till touchdown	12
	Satellite orbit established by using low thrust, with gas dynamic lift during entry	Gasdynamic lift till touchdown	13
	High, controllable thrust that enables efficient descent	Fully controlled thrust till touchdown	14

<sup>a</sup>The establishment of a satellite orbit by successive passes through the atmosphere will not be considered since advanced guidance system would be required to control such a sensitive series of maneuvers.

conditions for atmospheric entry, it is quite common to prescribe some preselected entry velocity  $V_E$  and entry angle  $\Gamma_E$  which are desired at some given entry distance  $R_E$ . Once these quantities have been selected, Equations (6) and (7) may be used to obtain the required  $R_a$  and  $R_p$  of the capture ellipse.

**d. Terminal mission mass-loss requirements.** Finally, we come to the mass-loss requirements for various terminal mission schemes. Table 6 outlines many of the possible missions, and Table 7 summarizes the approximate range of burnout and payload mass ratios that may be realized. Several assumptions were necessary in order to complete Table 7. The following definitions and assumptions are relevant to the data in the tables:

$m_0$  = initial or gross spacecraft (entry vehicle) mass before terminal maneuvers; for chemical-propulsion trajectories,  $m_0$  is the spacecraft mass after mid-course and approach guidance corrections have been made

$m_1$  = propellant mass

$m_2$  = ablation mass

$m_3$  = propulsion system mass

$m_4$  = heat shield structure mass

$m_f$  = final spacecraft (entry vehicle) mass after maneuvers

$m_p$  = payload mass, including any structure other than  $m_4$

where

$$m_f = m_0 - (m_1 + m_2)$$

$$m_p = m_f - (m_3 + m_4)$$

It can be shown that

$$m_f/m_0 = e^{-\Delta V_2/c} (e^{-\Delta V_1/c} - m_2/m_0)$$

where  $\Delta V_1$  is the sum of all velocity decrements prior to atmospheric entry, and  $\Delta V_2$  is the velocity decrement just prior to landing. If it is assumed that  $m_3 \approx 0.1m_1$ , then it follows that

$$m_p/m_0 = 1.1m_f/m_0 - 0.1(1 - m_2/m_0) - m_4/m_0$$

Table 7. Space vehicle mass remaining upon completion of various terminal missions,  $c = 3$  km/sec

Table 6 Terminal Mission No.	Moon		Mars		Venus	
	$m_f/m_0$	$m_p/m_0$	$m_f/m_0$	$m_p/m_0$	$m_f/m_0$	$m_p/m_0$
1	0.35 to 0.40	0.30 to 0.35	0.08 to 0.12 <sup>a</sup>	0 to 0.03 <sup>a</sup>	0.01 to 0.03 <sup>a</sup>	0 <sup>a</sup>
2	—	—	0.95 to 0.97	0.90 to 0.95	0.70 to 0.80	0.40 to 0.70
3	—	—	0.92 to 0.94 <sup>b</sup>	0.86 to 0.91 <sup>b</sup>	0.68 to 0.77 <sup>b</sup>	0.38 to 0.67 <sup>b</sup>
4	—	—	0.26 to 0.36 <sup>c</sup>	0.15 to 0.30 <sup>c</sup>	0.05 to 0.20 <sup>c</sup>	0 to 0.10 <sup>c</sup>
5	—	—	0.25 to 0.35 <sup>d</sup>	0.14 to 0.27 <sup>d</sup>	0.05 to 0.19 <sup>d</sup>	0 to 0.08 <sup>d</sup>
6	0.60 to 0.75	0.55 to 0.72	0.15 to 0.50	0.10 to 0.45	0.20 to 0.45	0.10 to 0.40
7	0.30 to 0.35	0.25 to 0.30	0.26 to 0.36 <sup>e</sup>	0.15 to 0.30 <sup>e</sup>	0.05 to 0.20 <sup>e</sup>	0 to 0.10 <sup>e</sup>
8	—	—	— <sup>f</sup>	0.08 to 0.40 <sup>f</sup>	— <sup>f</sup>	0.07 to 0.33 <sup>f</sup>
9	0.58 to 0.72 <sup>g</sup>	0.54 to 0.69 <sup>g</sup>	0.14 to 0.48 <sup>h</sup>	0.05 to 0.43 <sup>h</sup>	0.19 to 0.43 <sup>h</sup>	0.10 to 0.37 <sup>h</sup>
10	0.28 to 0.33	0.21 to 0.26	—	0.14 to 0.28	—	0 to 0.08
11	—	—	—	0.08 to 0.40 <sup>i</sup>	—	0.07 to 0.33 <sup>i</sup>
12	—	—	—	0.90 to 1.0 <sup>j</sup>	—	0.90 to 1.0 <sup>j</sup>
13	—	—	—	0.90 to 1.0 <sup>j</sup>	—	0.90 to 1.0 <sup>j</sup>
14	—	0.90 to ? <sup>j</sup>	—	0.80 to ? <sup>j</sup>	—	0.80 to ? <sup>j</sup>

<sup>a</sup>Neglecting atmosphere.

<sup>b</sup>Based upon 100 m/sec impulse prior to landing.

<sup>c</sup>Preliminary rocket braking to reduce entry velocity from hyperbolic to orbital, with no change in entry angle.

<sup>d</sup>Same as Footnote c plus 100 m/sec impulse prior to landing.

<sup>e</sup>Approximately the same as Terminal Mission 4, but assumes heat protection by ablation.

<sup>f</sup>Total mass of orbital craft plus landed capsule, where the initial capsule mass is assumed equal to 20% of the total mass in orbit before capsule ejection; initial  $\Delta V$  of 2 km/sec applied by capsule propulsion system.

<sup>g</sup>Based upon adjustive maneuver of 100 m/sec.

<sup>h</sup>Based upon adjustive maneuver of 200 m/sec.

<sup>i</sup>A few percent less than Terminal Scheme 8.

<sup>j</sup>Author's opinion; may not be realized for several years. Schemes 12 and 13 could only achieve mass ratios of unity by dissipating the heat input entirely by radiation and by maneuvering with the aid of control surfaces only.

It has been assumed that for passage through the Martian atmosphere with no preliminary rocket braking, the ablation shield requirements fall approximately in the range

$$0.03 < m_2/m_0 < 0.05$$

$$0.02 < m_4/m_0 < 0.05$$

and, for passage through the Cytherean atmosphere

$$0.20 < m_2/m_0 < 0.30$$

$$0.10 < m_4/m_0 < 0.30$$

**e. Conclusions.** For the type of terminal systems that will be developed and in use over the next decade, the fraction of space vehicle mass which can be landed upon the destination can be maximized by utilizing the atmosphere in order to brake the descent of the space vehicle. As elegant guidance and control techniques are developed, a more gradual form of descent (achieved through gasdynamic lift) will permit the use of radiative or internal cooling systems. These lifting entry vehicles will, of course, realize larger values of  $m_p/m_0$ . If the destination does not possess any appreciable atmosphere, then the most economical landing can be realized by descending directly (under power) rather than via intermediate transfer paths.

Studies are currently underway to determine suitable guidance techniques for terminal missions. The results of these studies will be made available in succeeding *Research Summaries*.

## E. Systems Performance Study

A. E. Dickinson

### 1. Data Processing for Near Real Time Engineering Evaluation of RA-1 and -2

Evaluation of spacecraft performance during flight operations will be done by members of the Spacecraft Data Analysis Team (SDAT) in session at the JPL Central Computing Facility. Some aspects of providing the RA-1 and -2 SDAT with the telemetry data required to perform this function are discussed here.

The telemetered analog engineering measurement data is received at the stations of the Deep Space Instrumentation Facility (DSIF) in the form of modulated subcarriers in the spacecraft RF signal. This telemetry data is auto-

matically detected and decommutated, appearing at a continuous sequence of 11-digit sample points on the decommutator output tape. Under normal operating conditions, the decommutator tape will print out a sample point each time a commutator segment in the spacecraft data encoder is sampled, at the nominal rate of one measurement sample per second.

At the South Africa and Goldstone DSIF stations there will be one man assigned the task of sampling the decommutator output and preparing the selected samples for teletype transmission to JPL. For this purpose a sampling schedule will be provided by the SDAT before the mission. Such a schedule must take into account the fact that if the space-to-ground communication link performs according to design, engineering telemetry data will be received at the DSIF much faster than it can be transmitted to JPL. In this situation, the amount of data which can be provided to the SDAT is limited by the following factors: (1) availability of TWX lines, where orbit determination data has priority, (2) the rate at which data can be sampled and manually punched (and checked for accuracy when required) for TWX transmission, (3) TWX transmission of about 60 words per minute, and (4) the rate at which the encoded TWX data can be reduced at JPL for evaluation by the SDAT.

The Central Computing Facility will have a 7090 program for converting the teletype tape data into a form suitable for use by the SDAT. This program identifies each sample point by its two-digit address, converts the corresponding three-digit frequency value into engineering units calibrated for center frequency drift, and tags those samples containing a nonstandard data condition indicator. The program also uses the address digits, which occur in time-correlated sequence, to compute the time of each sample with reference to the initial time of a continuous data sequence. This reduces the required word length of teletyped samples from 11 to 6 digits, thereby increasing the number of samples which can be transmitted in a given period.

The program produces a tabular printout of time-correlated samples in engineering units for each spacecraft parameter being measured. The various measurements are grouped according to subsystem, such as communications, power, attitude control, and temperature. This information is used by the SDAT to keep the Test Director informed of the spacecraft status and as the basis for periodic technical reports until more extensive data records are available. Some of this data is also used by the Command Group to determine what, if any, commands are to be transmitted to the spacecraft during flight.

# GUIDANCE AND CONTROL DIVISION

## III. Guidance and Control Research

### A. Adaptive Systems

R. A. Bruns

A combination of logic and control appears to be required for future spacecraft attitude control systems. These systems must be able to perform not only mid-course and terminal maneuvers in space but must also carry out exacting guidance and control functions while in an unknown planetary environment. Since a digital computer is carried on board for terminal guidance, it is advantageous to determine what functions it might perform in landing control systems. Adaptive systems will also be required in roving vehicles which must operate in unpredictable planetary environments. Such machines must adapt themselves to strange climates, unknown planetary terrains, outputs of sensory instruments, and even unreliable component operations.

The broad field known as *artificial intelligence* is also being investigated since this is related to the study of adaptive control systems. As the term is used here, an adaptive system is one in which the control system is automatically adjusted to achieve a given performance

criterion in the face of a widely varying environment, disturbances in instrument output, conflicting input signals, and noise. Artificial intelligence is more difficult to define, but it encompasses adaptive control systems as well as many aspects of information processing.

A survey of the fields of artificial intelligence and adaptive control systems has been made by this Laboratory in order to determine the activity to date and to list important applicable references (Refs 9 to 23). Artificial intelligence, or machine learning, is being considered both from the computer simulation standpoint and from the implementation standpoint. Adaptive control systems are divided into three groups depending on the nature of the computer carrying out the adjustment processes; i.e., systems in which (1) a digital computer makes numerous calculations, (2) a hybrid computer generates simple input functions, or (3) various self-adaptive processes take place in an analog fashion within the main control loop.

#### 1. Artificial Intelligence

The concepts of artificial intelligence from a computer simulation standpoint involve the programming of a

general-purpose digital computer to suggest new methods of machine learning. In addition, methods of communicating with the computer are developed to enhance the man-machine relationship in the learning process. It would appear that this is a step which should be taken before the implementation of the process is actually carried out on a specially designed digital computer. At least four organizations (Refs 19, 21, 22) are presently involved in this type of work.

Artificial intelligence from the implementation standpoint involves the building of a computer with neuron-like components, thus providing it with learning characteristics when subjected to input signals and the proper reinforcements or inhibitions. Evidently, such a machine can produce nothing of itself, but it might have the property of adjusting itself to inputs if there is stored within the machine sufficient information to recognize the proper solutions. At least seven organizations, including four private companies, are engaged in this type of endeavor (Refs 16, 18, 23).

## **2. Adaptive Control Systems**

The most elaborate adaptive control system is one in which a digital computer determines performance and generates corrective measures to achieve a performance criterion stored in the machine. Measurements of important system variables are made and processed in the computer. Comparisons are made between actual and required performance such as the minimum-integral error-squared criterion. The computer then calculates the necessary changes in the control system characteristics to obtain the proper outputs. Four companies and two universities are known to be working in this field (Refs 10, 14, 15).

Since the computer becomes such a large portion of the control system when it has to perform detailed calculations, a simplified approach is often taken which involves the use of a hybrid computer. Proponents of this scheme claim a more practical solution to the control problem where environments cover ranges too broad for ordinary compensation. Certain simplifying assumptions are necessary in the theoretical considerations in order that only simple arithmetic operations and a small memory are required for the computer. One method utilizes a staircase forcing function, generated by the computer to obtain the required response (Ref 20). Some suggest applying white noise to the system, take cross correlations between input and output, determine the transfer function of the system, and make necessary adjustments in parameters (Ref 12). Others would include digital com-

pensators or adjust sampling frequency for adaptive sampled-data systems (Refs 13, 17).

Finally, there are those adaptive systems in which the adaptive process takes place without the use of a digital computer but by analog methods. The dividing line between this type of system and a nonlinear compensated feedback control system is very hazy. Active or passive adaption may be used, components or gains may be varied, and switches may be closed as a function of certain system variables. This approach seems most practical for spacecraft control systems since fewer components are required than for those requiring a special computer. There has been considerable effort in this aspect of control system theory over the past 5 years (Refs 9, 11). The survey of important literature in these two fields of artificial intelligence and adaptive control systems is continuing.

More specifically, an attempt is being made to state in a clear and concise manner the types of Laboratory control problems which might be solved by adaptive methods. Some simplified models of adaptive control systems and roving vehicles have been set up on the analog computer, and attempts have been made to improve performance by elementary adaptive techniques. Several linear third-order systems have been studied and comparisons made between usual methods of compensation and adaptive methods in an effort to determine when the adaptive approach is justified. It is planned to extend this activity to relay systems, sampled data systems, and nonlinear control systems.

## **B. Dual-Sphere Gas-Floated Gyro**

*J. H. Laub*

Space missions of the future, in particular planetary and orbiting expeditions extending over long periods of time, require for the guidance and control of the space vehicle inertial references of greater accuracy and reliability than are now available in conventional instruments. The accumulation of errors over many thousand hours of operation makes it mandatory to reduce drift rates to extremely small values, of the order of 0.001 deg/hr. Of equal importance is the need for utmost reliability and freedom from wear.

The search for improved techniques of inertial references which promise to meet these future needs has

prompted the Laboratory to investigate several promising parallel approaches and advanced concepts. A research project of studying the suspension of superconductive sensing masses and the feasibility of a cryogenic gyro is in progress (RS 36-5, Vol I). In addition, an outside project involving suspension by electrostatic forces in a vacuum is being supported. Furthermore, research on mass suspension by gas flotation has been in progress for some time. (See previous issues of RS and CBS.) It has lately been extended to gas-floated spinning spheres (RS 36-8, Ref 24), motivated in part by considerable interest in the concept and potential of the dual-sphere gas-floated gyro. Figure 27 shows in schematic form the basic idea underlying this gyro, which was first published in 1949 (Ref 25). Two concentric masses of spherical configuration are separated by a thin film of compressed gas which supports the inner rotor. The outer rotor is supported by gas bearings, which may be of the hydrodynamic type or hydrostatic type, and is driven either by an electric motor or mechanically by turbine action of gas jets. The gyro is spun up with the inner rotor caged mechanically. When operational speed is reached, the inner mass is uncaged and continues to spin at the same speed and around the same axis as the outer rotor. This virtually eliminates any viscous drag as well as wear by metal-to-metal friction. Angular motion of the outer rotor with respect to the inner inertial reference is read out optically, as shown schematically (Fig 27), or by electrical pickups.

There are a number of significant advantages of this system over conventional gyros. The life expectancy is greatly increased due to the absence of metal-to-metal contact of rotating surfaces. The load-carrying capacity is limited only by the available gas pressure. High-g capability and stiffness can be obtained with moderate pressures. In low-g environments, the pressure can be still further reduced with attendant savings in power. Effects of mass shifts due to anisotropy and other causes are either eliminated or substantially reduced. The rotation of both the outer and inner rotor cancels the drift-producing effects of certain disturbing torques. Temperature effects due to motor losses are greatly reduced since the rotor is effectively isolated thermally.

In the past, the major obstacle to the use of externally pressurized components on long missions has been the expenditure of gas. However, closed-cycle gas systems which recirculate a small quantity of gas or vapor are practical for use on-board of space vehicles. For example, it has been shown that a two-phase Rankine cycle using Freon or a fluid with similar thermodynamic properties is feasible; *thermal pumping* of the fluid requires

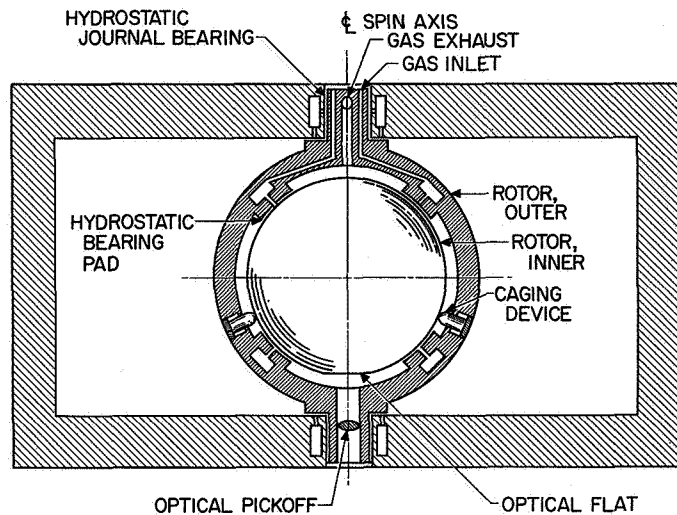


Figure 27. Dual-sphere gas-floated gyro

a small amount of power only, available from solar or nuclear sources and eliminating conversion losses from thermal to electrical and mechanical energies (Ref 26).

As a result of these investigations, the Laboratory has decided to support further research on various phases of this concept. This includes studies of the design and performance characteristics of the dual-sphere gas-supported gyro and its overall feasibility for spacecraft applications by two outside organizations as well as further in-house research.

## C. Capillary Pumping for Closed-Cycle Gas System

H. D. McGinness

In *Research Summaries 36-1, 36-2, 36-4, and 36-7*, a closed-cycle gas supply system for gas bearing instruments was described which employs thermal power from solar or nuclear energy sources to pump a two-phase fluid from the evaporator through the gas bearing to the condenser. The cycle is completed by pumping the liquid back into the evaporator. This can be accomplished by a small mechanical pump. However, it appears desirable to eliminate moving or rotating elements from the system altogether and to employ a technique such as capillary



action which can be used in the zero-g environment of a spacecraft.

The following is a preliminary report on a project which has been initiated to study the feasibility of utilizing the capillary action of a wick for returning the condensate to the evaporator.

The manner in which a wick can permit a pressure difference across its ends may be understood by the following considerations. (A wick is defined here to be a group of capillary tubes in parallel.) It is well known that liquids which wet the walls of a capillary rise above the free surface of the liquid. For the case where the meniscus makes a contact angle  $\theta$  with a circular cross section capillary, the liquid rise  $z$  is given approximately by the following equation:

$$z = \frac{4\sigma \cos \theta}{\gamma d} \quad (1)$$

where  $\sigma$  is the surface tension,  $\gamma$  is the weight density of the liquid, and  $d$  is the capillary diameter. Since ambient pressure exists on the top surface of the meniscus and also at the free surface of the liquid, the pressure on the bottom surface of the meniscus must be less than ambient by the amount of the elevation pressure  $\gamma z$ . The pressure on the bottom of the meniscus,  $P_{bm}$ , is

$$P_{bm} = P_{ambient} - \gamma z = P_{ambient} - \frac{4\sigma \cos \theta}{d} \quad (2)$$

The pressure difference  $\Delta P$  across the meniscus surface is

$$\Delta P = P_{ambient} - \left( P_{ambient} - \frac{4\sigma \cos \theta}{d} \right) = \frac{4\sigma \cos \theta}{d} \quad (3)$$

Equation (3) shows that the pressure difference which may be obtained with a given liquid and given capillary material, varies inversely with the capillary diameter  $d$ .

A few simple experiments were made in order to determine the liquid rise in wicks made of different materials. Of those tested, the wicks composed of a bundle of glass fibers caused the liquid to rise considerably higher than it did in the other wicks. The glass fibers used were measured with an optical comparator and found to be circular in cross section with a diameter of 0.0005 inch. When a group of such fibers is perfectly compacted, each capillary cross section is formed by three mutually tangent fibers as shown in Figure 28. In order to learn the characteristics of capillaries of this shape, the following experiments were conducted.

First, the rises of both distilled water and liquid Freon 113 were measured in round glass capillary tubes having the following inside diameters: 0.010, 0.026, 0.039, and

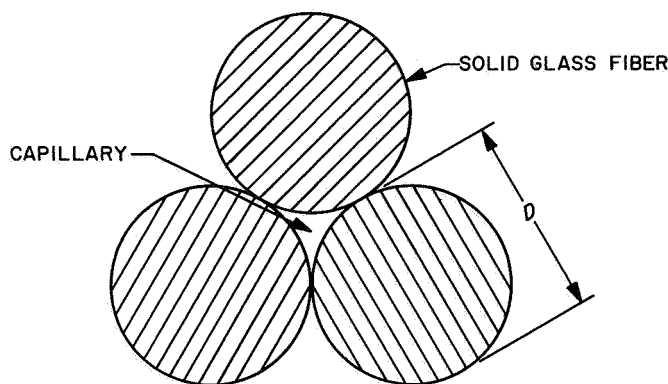


Figure 28. Capillary formed by perfectly packed glass fibers

0.044 inch. Knowing the weight densities of the liquids and the measured rises, the products  $\sigma \cos \theta$  were computed by using Equation (1). As expected, these product values were essentially independent of the tube size. Next, a series of capillaries were formed by binding together solid glass rods of diameter  $D$  (Fig 28). The effective diameter  $d_e$  of a capillary is here defined as

$$d_e = \frac{4\sigma \cos \theta}{\gamma z} \quad (4)$$

By making use of the previously established values of  $\sigma \cos \theta$  and the known weight densities  $\gamma$ , the following formulas obtain for the three-glass-rod capillary:

for distilled water

$$d_e = \frac{0.0441}{z} \quad (5)$$

for liquid Freon 113

$$d_e = \frac{0.0065}{z} \quad (6)$$

In Table 8 are listed the results of the experiments with the three-glass-rod capillaries. It may be seen that the ratio  $d_e/D$  for water varies from 0.258 to 0.317, whereas  $d_e/D$  for Freon 113 varies from 0.159 to 0.172. The variation in values for either liquid is probably due to experimental errors. The average values for water and Freon 113 are 0.292 and 0.166, respectively. Why this factor is so different for the two liquids remains to be studied. If  $d_e$  is assumed to be the diameter of a circle having the same area as the cross section of a capillary formed by three mutually tangent circles of diameters  $D$ , then  $d_e/D$  is 0.226. (It is curious that this value is the average of 0.166 and 0.292.) If the  $d_e/D$  value of 0.166 is tentatively accepted for the liquid Freon-glass fiber wick

**Table 8. Three-glass-rod capillaries**

Liquid	Rod diameter $D$ , in.	Measured liquid rise $z_m$ , in.	Effective diameter $d_e$ , in.	$\frac{d_e}{D}$
Distilled water	0.036	4.76	0.00927	0.258
	0.041	3.78	0.01165	0.284
	0.081	1.75	0.0252	0.311
	0.193	0.72	0.0612	0.317
Liquid Freon 113	0.036	1.05	0.00619	0.172
	0.041	1.00	0.0065	0.159
	0.081	0.48	0.01355	0.167
	0.193	0.20	0.0325	0.168

combination, then the following formula may be derived which pertains to the perfectly packed wick:

$$\Delta P = \frac{4\sigma}{0.166D} \quad (7)$$

A closed-cycle system was constructed as is shown schematically in Figure 29. The wick consists of a  $\frac{3}{8}$ -inch-ID by 12-inch-long glass tube compactly filled with

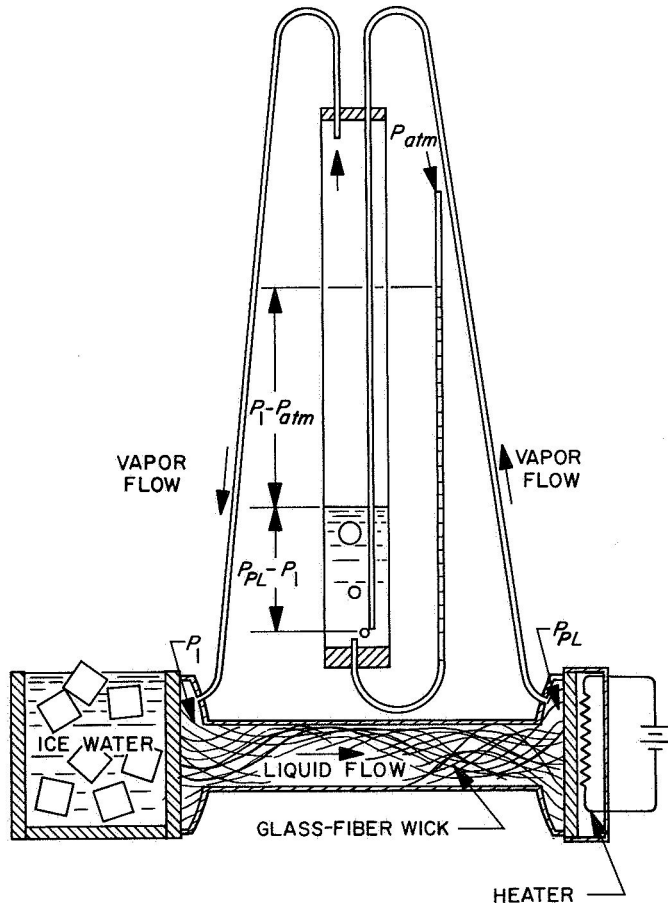


**Figure 29. Single element of experimental two-phase closed-cycle gas system**

0.0005-inch-D glass fibers. The fibers flare out at each end and partially fill bell-shaped cavities (Fig 30). One end is connected to a wall of an ice box, and the other end is connected to a glass plate containing a heating element. The pressure drop through a gas bearing,  $P_{PL} - P_1$ , is simulated by the elevation pressure of a mercury column. The principle of operation is as follows: Assume that a liquid is in the cavity next to the ice box. The liquid will flow by capillarity to the opposite free end, even though the pressure at the free end is somewhat greater than the pressure at the cold cavity. If heat is applied, there will be evaporation from the menisci at the hot end and vapor will flow upward through the mercury column, thus undergoing a pressure reduction of  $\Delta P$ . The vapor then returns to the cold cavity and condenses.

The apparatus was charged with Freon 114 vapor. (The boiling point of Freon 114 at atmospheric pressure is 38°F). Liquid was soon observed in the cold end cavity. No current was applied to the heating element as the room temperature was 75.5°F. After a few minutes, the mercury level was set 0.40 inch above the bottom of the inlet tube, creating a  $\Delta P$  of 0.20 psi. The system pressure was 19.8 psia. Vapor bubbles rose at the rate of 49 per

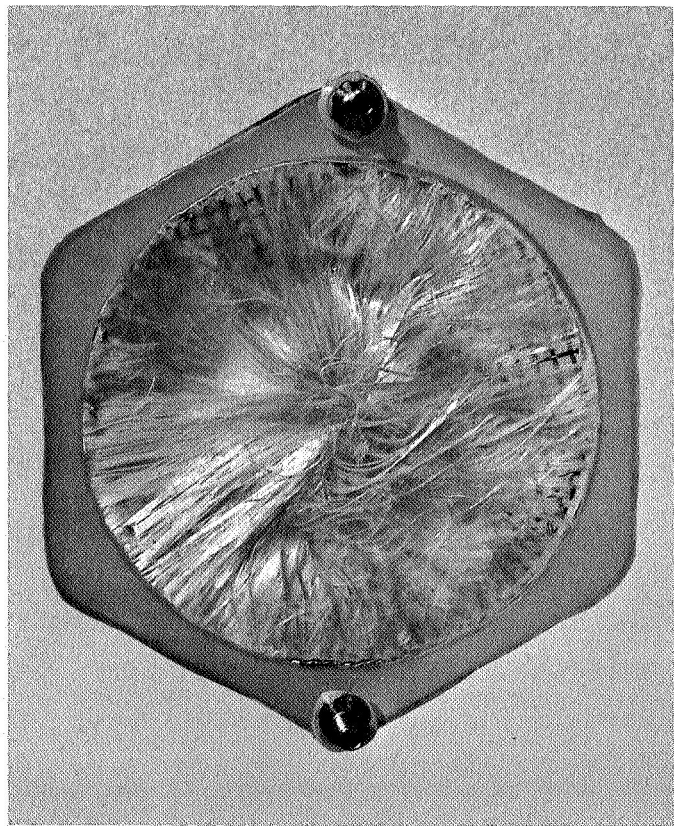


**Figure 30. Glass fibers partially filling end cavity of wick**

minute which corresponds, at this pressure, to a weight flow of approximately 0.01 gm/min. After 15 hours, the same values were observed. Then the mercury level was slowly raised until the flow stopped. At this point the mercury level was 1.20 inches above the bottom of the inlet tube which corresponds to a  $\Delta P$  of 0.60 psi. The maximum  $\Delta P$ , given by Equation (7), applied to Freon 114, is 3.50 psi. The large difference between the theoretical maximum  $\Delta P$  and that experimentally observed is probably due to imperfect packing of the fibers.

Further experiments and an analysis of the thermodynamic cycle will be reported later. These first results are encouraging. If it is assumed that the flow rate is proportional to the cross sectional area of the wick, a flow of 0.5 gm/min (which is adequate for certain single-orifice-fed bearings) could be obtained with a 2.65-inch-D wick. It is to be expected that improved wick designs would appreciably increase the  $\Delta P$  value. An important advantage of this liquid pump is that it will operate under zero-g conditions.

# TELECOMMUNICATIONS DIVISION

## IV. Communications Systems Research

### A. Mathematical Research

S. W. Golomb, L. D. Baumert,  
J. J. Stiffler, and R. C. Titsworth

#### 1. Divisibility Property of Enumerating Functions

Let  $\{b_i\}_{i=1}^{\infty}$  be a sub-sequence of the positive integers. Let  $\beta(x)$  denote the number of terms in this sequence which do not exceed  $x$ .

**Lemma.** Given integers  $m$  and  $n$ , if  $m < n$  and

$$\frac{m}{\beta(m)} < \frac{n}{\beta(n)}$$

then every integer  $k$  with

$$\frac{m}{\beta(m)} \leq k \leq \frac{n}{\beta(n)}$$

occurs as a ratio of the form  $a/\beta(a)$ .

*Proof.* Let  $k$  be any fixed integer between  $m/\beta(m)$  and  $n/\beta(n)$ . Let  $r$  be the largest integer on the interval  $[m, n]$  with  $r/\beta(r) \leq k$ . (The integer  $m$  satisfies this inequality, and there may be others.) If  $r = n$ , then

$$\frac{r}{\beta(r)} \leq k \leq \frac{r}{\beta(r)}$$

and  $k = r/\beta(r)$  as required. Otherwise,  $r < n$ , so that

$$r + 1 \leq n$$

and

$$\frac{r+1}{\beta(r+1)} > k$$

by the choice of  $r$ . Thus

$$\frac{r}{\beta(r)} \leq k < \frac{r+1}{\beta(r+1)}$$

If  $r/\beta(r) = k$ , there is nothing further to prove. Otherwise,

$$\frac{r}{\beta(r)} < k < \frac{r+1}{\beta(r+1)}$$

Because  $\beta$  is an enumerating function  $\beta(r) \leq r$ , and either

$$\beta(r+1) = \beta(r) \quad \text{or} \quad \beta(r+1) = \beta(r) + 1$$

In the latter case

$$\frac{r+1}{\beta(r+1)} = \frac{r+1}{\beta(r)+1} \leq \frac{r}{\beta(r)}$$

contradicting

$$\frac{r}{\beta(r)} < k < \frac{r+1}{\beta(r+1)}$$

Hence

$$\beta(r+1) = \beta(r)$$

and

$$\frac{r}{\beta(r)} < k < \frac{r+1}{\beta(r)}$$

so that

$$r < k\beta(r) < r+1$$

Since  $k$  and  $\beta(r)$  are both integers,  $k\beta(r)$  would be an integer strictly between  $r$  and  $r+1$ , which is impossible. Hence, every integer between  $m/\beta(m)$  and  $n/\beta(n)$  has a representation in the form  $a/\beta(a)$  where, moreover,  $m \leq a \leq n$ .

**Theorem 1.** The intersection of the set of rational numbers  $\{n/\beta(n)\}$  with the positive integers consists of a semi-infinite interval, i.e., all integers  $\geq g_0$  for some  $g_0$ , if and only if

$$\lim_{n \rightarrow \infty} \frac{\beta(n)}{n} = 0$$

When this condition is satisfied

$$1 \leq g_0 \leq b_1$$

with  $g_0 = 1$  if and only if  $b_1 = 1$ .

*Proof.* If

$$\lim_{n \rightarrow \infty} \frac{\beta(n)}{n} \neq 0$$

then  $n/\beta(n)$  is *bounded*, and no sufficiently large integer can be represented in the form  $n/\beta(n)$ . Of course, the values of  $n$  less than  $b_1$ , for which  $\beta(n) = 0$ , are discarded when looking at  $\{n/\beta(n)\}$ .

If

$$\lim_{n \rightarrow \infty} \frac{\beta(n)}{n} = 0$$

then arbitrarily large values of  $n/\beta(n)$  occur for arbitrarily large values of  $n$ . Since  $\beta(n) \leq n$  for all  $n$ , let

$$\text{glb}_{n \rightarrow \infty} \frac{n}{\beta(n)} = \alpha \geq 1$$

For any integer  $k > \alpha$ , it is then possible to find an integer  $m$  with  $m/\beta(m) < k$ , and an integer  $n > m$  with  $n/\beta(n) > k$ . Hence, by the Lemma,  $k = a/\beta(a)$  for some  $a$  between  $m$  and  $n$ . However, for  $k < \alpha$ , all terms of  $n/\beta(n)$  exceed  $k$ . If  $\alpha$  is not an integer, then precisely those integers  $\geq g_0 = [\alpha + 1]$  are of the form  $n/\beta(n)$ . If  $\alpha$  is an integer, the same result holds with  $g_0 = \alpha$  or  $g_0 = \alpha + 1$ , according to whether  $\alpha$  is *attained* as the minimum value of  $n/\beta(n)$  or not, respectively.

Since  $n = b_1$  gives  $n/\beta(n) = b_1$ , clearly  $g_0 \leq b_1$ . Since  $\beta(n) \leq n$  for all  $n$ ,  $g_0 \geq 1$ ; and since  $\beta(n) < n$  for all  $n$  unless  $b_1 = 1$ ,  $g_0 = 1$  only if  $b_1 = 1$ . In view of  $1 \leq g_0 \leq b_1$ ,  $g_0 = 1$  if and only if  $b_1 = 1$ .

**Corollary.** If  $\pi(x)$  denotes the number of primes not exceeding  $x$ , then every integer  $m \geq 2$  occurs as a ratio of the form  $n/\pi(n)$ .

*Proof.* Since  $\pi(x) = o(x)$ , Theorem 1 surely applies. Moreover,  $b_1 = 2$ , so that  $1 < g_0 \leq 2$ , whence  $g_0 = 2$ , and every integer  $\geq 2$  has at least one representation of the form  $n/\pi(n)$ .

A plausible generalization of Theorem 1 would be that, with  $\{b_i\}$  and  $\beta(n)$  as before, but without the assumption that

$$\lim_{n \rightarrow \infty} \frac{\beta(n)}{n} = 0$$

the integer values of  $n/\beta(n)$  still fill up an interval, although possibly a *finite* interval. The incorrectness of this conjecture is shown by the following counter-example.

**Theorem 2.** There exist infinite sub-sequences  $\{b_i\}_{i=1}^{\infty}$  of the integers for which the integer values of  $n/\beta(n)$  do not fill an interval, where  $\beta(x)$  is the number of terms of  $\{b_i\}$  which do not exceed  $x$ .

*Proof.* Consider the sequence  $b_i = i + 15$ . Thus,  $\beta(n) = 0$  for  $n < 16$ , and  $\beta(n) = n - 15$  for  $n \geq 16$ . The meaningful values of  $n/\beta(n)$  are thus of the form  $n/(n - 15)$  for  $n \geq 16$ . The only integers obtained in this way are  $16/(16 - 15) = 16$ ,  $18/(18 - 15) = 6$ ,  $20/(20 - 15) = 4$ , and  $30/(30 - 15) = 2$ . In particular,  $1 < n/(n - 15) < 2$  for all  $n > 30$ ; and the integers 2, 4, 6, 16 do not fill an interval.

**Comment.** The significance of the Lemma is that when it is *increasing*,  $\{n/\beta(n)\}$  skips no integers. However, when it is *decreasing*,  $\{n/\beta(n)\}$  may skip many integers, as in the example of Theorem 2.

It is a simple exercise for the reader to show that the *plausible generalization* disproved by Theorem 2 is in fact true under the further constraint that  $b_1 < 4$ . Another simple exercise is to show that if  $n/\beta(n)$  takes on values both larger and smaller than 2, it must also assume the value 2.

## 2. Inequivalent Hadamard Matrices

A *Hadamard matrix* is a matrix of *ones* and *minus ones* whose row (column) vectors are orthogonal. The order

of a Hadamard matrix is necessarily 1, 2 or  $4t$  with  $t = 1, 2, 3, \dots$ . Two  $n \times n$  Hadamard matrices are called *equivalent* ( $\sim$ ) if one can be formed from the other by permutation and complementation ( $h_{ij} \rightarrow -h_{ij}$ ) of rows and columns. There is only one equivalence class of Hadamard matrices for  $n = 1, 2, 4, 8, 12$ . A Hadamard matrix is said to be in *normal form* (or normalized) if its first row and first column are 1. Clearly every Hadamard matrix is equivalent to a Hadamard matrix in normal form. A Hadamard matrix is called a group if its rows form a group with respect to multiplication of components.

Consider the group of row (column) permutations and complementations. The set of complementations forms a normal subgroup of this group. Thus, the equivalence of  $H_1, H_2$  implies

$$P_1 C_1 H_1 C_2 P_2 = H_2$$

where the  $C_i$  are complementation matrices and the  $P_i$  are permutation matrices.

Suppose  $H_1, H_2$  are to be tested for equivalence. Then transitivity of equivalence insures that the test may be performed on  $H'_1, H'_2$ , where  $H_i \sim H'_i$ , and  $H'_i$  is in normal form.

**Theorem.** If  $H_1, H_2$  are two equivalent Hadamard matrices,  $H_1$  is normalized, and  $H_2$  is a group, then  $H_1$  is a group.

*Proof.* Since  $H_1, H_2$  are equivalent, there exist permutation matrices  $P_i$  and complementation matrices  $C_i$  such that

$$P_1 C_1 H_1 C_2 P_2 = H_2$$

Since  $H_2$  is a group

$$P_1 C_1 H_1 = H_2 P_2^{-1} C_2^{-1}$$

is a coset of a group  $G$ , and so  $C_1 H_1$  is a coset of  $G$ . Since  $H_1$  is in normal form

$$C_1 H_1 = G \text{ or } -G$$

Thus, the set of rows of  $H_1 U - H_1$  is the same as the set of rows of  $G U - G$ , and so  $x, y$  in  $H_1$  implies  $xy$  is a row of  $H_1$  or  $-H_1$ . But  $H_1$  is normalized, so  $xy$  is in  $H_1$ .

In the matrices listed below, 1,  $-1$  correspond to 1,  $-$ , respectively. Notice that the product of rows 4 and 5 of the first matrix is  $11-1-1-1-111-$ . By the theorem above, therefore, (1) cannot be equivalent to any group, and in particular it is not equivalent to (2).

<p>(1)</p> <table style="width: 100%; border-collapse: collapse;"> <tr><td>1111</td><td>1111</td><td>1111</td><td>1111</td></tr> <tr><td>1111</td><td>1111</td><td>—</td><td>—</td></tr> <tr><td>1111</td><td>—</td><td>1111</td><td>—</td></tr> <tr><td>111-</td><td>1—</td><td>1—</td><td>11-</td></tr> <tr><td>11-1</td><td>-1-</td><td>-1-</td><td>11-1</td></tr> <tr><td>11—</td><td>11—</td><td>-1-1</td><td>1-1</td></tr> <tr><td>11—</td><td>-11</td><td>-1-1</td><td>-11-</td></tr> <tr><td>11—</td><td>-1-1</td><td>1-1-</td><td>-11</td></tr> <tr><td>1-11</td><td>-1—</td><td>-1—</td><td>-111</td></tr> <tr><td>1-1-</td><td>-1-1</td><td>-11</td><td>11—</td></tr> <tr><td>1-1-</td><td>1-1-</td><td>-11</td><td>-11</td></tr> <tr><td>1-1-</td><td>-11</td><td>11—</td><td>1-1</td></tr> <tr><td>1-1</td><td>-11-</td><td>1-1</td><td>1-1-</td></tr> <tr><td>1-1</td><td>1-1</td><td>-11-</td><td>1-1-</td></tr> <tr><td>1-1</td><td>1-1</td><td>1-1</td><td>-1-1</td></tr> <tr><td>1—</td><td>111-</td><td>111-</td><td>-1—</td></tr> </table>	1111	1111	1111	1111	1111	1111	—	—	1111	—	1111	—	111-	1—	1—	11-	11-1	-1-	-1-	11-1	11—	11—	-1-1	1-1	11—	-11	-1-1	-11-	11—	-1-1	1-1-	-11	1-11	-1—	-1—	-111	1-1-	-1-1	-11	11—	1-1-	1-1-	-11	-11	1-1-	-11	11—	1-1	1-1	-11-	1-1	1-1-	1-1	1-1	-11-	1-1-	1-1	1-1	1-1	-1-1	1—	111-	111-	-1—	<p>(2)</p> <table style="width: 100%; border-collapse: collapse;"> <tr><td>1111</td><td>1111</td><td>1111</td><td>1111</td></tr> <tr><td>1111</td><td>1111</td><td>—</td><td>—</td></tr> <tr><td>1111</td><td>—</td><td>1111</td><td>—</td></tr> <tr><td>1111</td><td>—</td><td>—</td><td>1111</td></tr> <tr><td>11—</td><td>11—</td><td>11—</td><td>11—</td></tr> <tr><td>11—</td><td>11—</td><td>-11</td><td>-11</td></tr> <tr><td>11—</td><td>-11</td><td>11—</td><td>-11</td></tr> <tr><td>11—</td><td>-11</td><td>-11</td><td>11—</td></tr> <tr><td>1-1-</td><td>1-1-</td><td>1-1-</td><td>1-1-</td></tr> <tr><td>1-1-</td><td>1-1-</td><td>-1-1</td><td>-1-1</td></tr> <tr><td>1-1-</td><td>-1-1</td><td>1-1-</td><td>-1-1</td></tr> <tr><td>1-1-</td><td>-1-1</td><td>-1-1</td><td>1-1-</td></tr> <tr><td>1-1</td><td>1-1</td><td>1-1</td><td>1-1</td></tr> <tr><td>1-1</td><td>1-1</td><td>-11-</td><td>-11-</td></tr> <tr><td>1-1</td><td>-11-</td><td>1-1</td><td>-11-</td></tr> <tr><td>1-1</td><td>-11-</td><td>-11-</td><td>1-1</td></tr> </table>	1111	1111	1111	1111	1111	1111	—	—	1111	—	1111	—	1111	—	—	1111	11—	11—	11—	11—	11—	11—	-11	-11	11—	-11	11—	-11	11—	-11	-11	11—	1-1-	1-1-	1-1-	1-1-	1-1-	1-1-	-1-1	-1-1	1-1-	-1-1	1-1-	-1-1	1-1-	-1-1	-1-1	1-1-	1-1	1-1	1-1	1-1	1-1	1-1	-11-	-11-	1-1	-11-	1-1	-11-	1-1	-11-	-11-	1-1
1111	1111	1111	1111																																																																																																																														
1111	1111	—	—																																																																																																																														
1111	—	1111	—																																																																																																																														
111-	1—	1—	11-																																																																																																																														
11-1	-1-	-1-	11-1																																																																																																																														
11—	11—	-1-1	1-1																																																																																																																														
11—	-11	-1-1	-11-																																																																																																																														
11—	-1-1	1-1-	-11																																																																																																																														
1-11	-1—	-1—	-111																																																																																																																														
1-1-	-1-1	-11	11—																																																																																																																														
1-1-	1-1-	-11	-11																																																																																																																														
1-1-	-11	11—	1-1																																																																																																																														
1-1	-11-	1-1	1-1-																																																																																																																														
1-1	1-1	-11-	1-1-																																																																																																																														
1-1	1-1	1-1	-1-1																																																																																																																														
1—	111-	111-	-1—																																																																																																																														
1111	1111	1111	1111																																																																																																																														
1111	1111	—	—																																																																																																																														
1111	—	1111	—																																																																																																																														
1111	—	—	1111																																																																																																																														
11—	11—	11—	11—																																																																																																																														
11—	11—	-11	-11																																																																																																																														
11—	-11	11—	-11																																																																																																																														
11—	-11	-11	11—																																																																																																																														
1-1-	1-1-	1-1-	1-1-																																																																																																																														
1-1-	1-1-	-1-1	-1-1																																																																																																																														
1-1-	-1-1	1-1-	-1-1																																																																																																																														
1-1-	-1-1	-1-1	1-1-																																																																																																																														
1-1	1-1	1-1	1-1																																																																																																																														
1-1	1-1	-11-	-11-																																																																																																																														
1-1	-11-	1-1	-11-																																																																																																																														
1-1	-11-	-11-	1-1																																																																																																																														

Thus, there are at least two equivalence classes of Hadamard matrices of order 16.

A *difference set*  $D = (d_1, d_2, \dots, d_k)$  is a subset of the integers modulo  $v$  for which  $d_i - d_j \pmod{v}$ ,  $i \neq j$ , assumes each value  $1, 2, \dots, v-1$  exactly  $\lambda$  times. Define a sequence  $\{a_r\}$  by

$$a_r = \begin{cases} 1 & \text{if } r \text{ belongs to } D \\ -1 & \text{otherwise} \end{cases}$$

If  $v = 4t - 1$ ,  $k = 2t - 1$ ,  $\lambda = t - 1$  and a 1 is added to the beginning of each cyclic shift of  $\{a_r\}$ , then the resulting sequences together with the sequence of all 1's form the rows of a Hadamard matrix of order  $4t$ . Such a Hadamard matrix can be referred to as being generated by the difference set  $D$ . Letting  $\{b_r\}$  be the sequence derived from  $\{a_r\}$  by replacing  $-1$  with 0, it can be shown (Ref 27) that the Hadamard matrix generated by a difference set  $D$  is a group if and only if (1) the order of  $H$  is  $2^j$ , and (2)  $\{b_r\}$  satisfies a linear recursion relation

$$b_r = \sum_{i=1}^j c_i b_{r-i}$$

where the summation is modulo 2, the subscripts are considered modulo  $2^j - 1$  and the coefficients  $c_i$  are 0 and 1. Thus, the first theorem implies:

**Theorem.** If  $D$  is a difference set with parameters

$$v = 4t - 1 = 2^j - 1$$

$k = 2t - 1$ ,  $\lambda = t - 1$  whose associated sequence  $\{b_r\}$  does not satisfy (2), then the Hadamard matrix generated by  $D$  is not equivalent to a group.

This shows, for example, that the quadratic residue difference set for  $v = 31$  generates a Hadamard matrix which is not equivalent to the group of order 32.

### 3. Nonexistence of Certain Perfect Sequences

This note is intended to stress certain properties of sequences with two-level autocorrelation functions. Such sequences are called *perfect*. The theorem to be proved is the following:

**Theorem.** Let  $\{\alpha(i)\}$  be a nontrivial binary  $(0, 1)$  cyclic sequence with perfect autocorrelation, period  $L$ , and symmetry about  $\alpha(0)$ . Let the sequence have exactly  $k$  terms equal to  $\alpha(1)$  per period. Then it is necessary that  $L$  be even and the ratio  $r = k/L$  be bounded below by

$$r \geq \frac{1}{1 + \frac{(2^s + 1)^2}{(L - 1)}}$$

where  $L$  is divisible by  $s$  distinct primes. An approximation to this bound is given, for large  $s$ , by

$$r_1 \geq 1 - \frac{(4e)^s}{(2\pi s)^{0.5} s^s}$$

**Proof.** Let a sequence  $\{\alpha(i)\}$  of *zeros* and *ones* with period  $L$  be represented by an element of  $F_x$ , the group ring of a cyclic group  $(x)$  over the rational field  $F$ .

$$\alpha = \alpha(0) + \alpha(1)x + \cdots + \alpha(L-1)x^{L-1}$$

If  $\{\alpha(i)\}$  has a point of symmetry, then let  $\alpha(0)$  be this point: The correlation function  $\rho$  is independent of the starting point, in any case. However, by choosing this starting point,  $\alpha$  is equal to its reverse  $\alpha^*$ .

$$\alpha\alpha^* = \alpha^2 = \rho$$

**Case I (odd  $L$ ).** Let  $L$  be odd, and assume that a nontrivial perfect sequence  $\alpha$  exists. One may reduce both  $\alpha^2$  and  $\rho$  modulo 2 and equate coefficients of corresponding powers of  $x$ .

$$\alpha(n) = \rho(2n)$$

But  $\rho$  has only two distinguishable coefficients,  $\rho(0)$  and  $\rho(1) = \rho(2) = \cdots = \rho(L-1)$ . Reduction, modulo 2, of  $\rho$  reveals that  $\alpha$  would be one of the trivial sequences: all-zeros, all-ones, all-zeros with a one, or all-ones with a zero, contrary to the assumption that  $\alpha$  is nontrivial. Therefore, if  $\alpha$  is a nontrivial reversible perfect sequence, then  $L$  may not be odd.

**Case II (even  $L$ ).** Let  $L$  be even, and assume that  $\alpha$  is a nontrivial reversible perfect sequence. By the relations  $\rho(0) = k$  and

$$\sum_{n=0}^{L-1} \rho(n) = k^2$$

the form for  $\rho$  is found,

$$\begin{aligned} \alpha^2 &= k + \frac{k(k-1)}{L-1}(x + x^2 + \cdots + x^{L-1}) \\ &= \frac{k(L-k)}{L-1} + \left[ \frac{k(k-1)L}{L-1} \right] \left( \frac{1}{L} \right) \sum_{i=0}^{L-1} x^i \end{aligned}$$

The latter term is recognized to be a multiple of  $\eta_1$ , the idempotent of the minimal ideal field  $F_1$  having period one in  $F_x$ . Let  $n = k(L-k)/L-1$ .

$$\begin{aligned} \alpha^2 &= n + \left( \frac{k(k-1)L}{L-1} \right) \eta_1 \\ &= k^2\eta_1 + n\eta_2 + \cdots + n\eta_L \end{aligned}$$

The subscripts  $i$  on  $\eta_i$  refer to the period of  $F_i$ . One, therefore, seeks solutions to the equations

$$\begin{aligned} \alpha_1^2 &= k^2\eta_1 \\ \alpha_2^2 &= n\eta_2 \\ &\vdots \\ \alpha_L^2 &= n\eta_L \end{aligned}$$

These are equations in fields and, hence,  $(n)^{0.5}$  must be in  $F$  if there is to be *any* solution  $\alpha$ .

$$\begin{aligned} \alpha_1 &= \pm k\eta_1 \\ \alpha_2 &= \pm (n)^{0.5}\eta_2 \\ &\vdots \\ \alpha_L &= \pm (n)^{0.5}\eta_L \end{aligned}$$

Clearly, the  $(+)$  sign must be affixed to  $\alpha_1$  since multiplication of  $\alpha$  by  $\eta_1$  merely computes its coefficient sum.

If a binary sequence has two-level autocorrelation, then so does its complement. Choosing  $\alpha$  to be the one such that  $\alpha(1) = 1$ ,

$$\alpha_1(1) + \alpha_2(1) + \cdots + \alpha_L(1) = 1$$

It is known that only those idempotents in fields of period  $d$  having

$$d = p_1^{m_1} p_2^{m_2} \cdots p_s^{m_s}$$

where  $m_i = 0$  or 1, have non-zero  $\eta_d(1)$ . All those non-zero  $\eta_d(1)$  are equal to  $1/L$ . If it is assumed that  $s$  is the number of distinct primes which divide  $L$ , then there are  $2^s$  non-zero  $\eta_d(1)$ .

$$\alpha(1) = 1 = \frac{1}{L} [k + (n)^{0.5} (a_1 + \cdots + a_t)]$$

The  $(2^s - 1)$  numbers  $a_i$  above may be plus or minus one. Applying the triangle inequality

$$k + (n)^{0.5} (2^s - 1) \geq L$$

Therefore, subtracting  $k$  from both sides, dividing by  $(n)^{0.5}$  and squaring, the following is obtained.

$$(2^s - 1)^2 \geq \frac{(L - k)(L - 1)}{k}$$

Denote by  $r$  the ratio of  $k$  to  $L$ :

$$r = k/L$$

Substitution and rearrangement in the inequality gives the expression as stated in the theorem. The inequality obtained above is least stringent for  $L = \pi_s$ , the product of the first  $s$  primes.

$$(2^s - 1)^2 \geq \left( \frac{1 - r}{r} \right) (\pi_s - 1)$$

For any specified value of  $r$ , as  $s$  increases,  $\pi_s$  increases much faster than  $2^{2s}$ . For any given  $s$ , the limiting value of  $r$  is given by

$$r_0 = \frac{1}{1 + \frac{(2^s - 1)^2}{\pi_s - 1}}$$

For any ratio  $r < r_0$ , no sequences may exist with perfect autocorrelation. It is proper to speak only about integer values of  $s$ . However, for visual facility, Figure 31 shows  $r_0$  as a function of  $s$  with points connected by a smooth curve. For  $s = 7$ ,  $r$  is within 2% of unity; and at  $s = 8$ , within 0.7%. (See Table 9.) Hence, sequences of length  $L$  with a large number of prime divisors must have a large number of ones.

For large  $s$  (say  $s \geq 7$ ), it is possible to approximate  $r_0$  by

$$r_0 = 1 - \frac{2^{2s}}{\pi_s}$$

One may further approximate  $\pi_s$  by  $s!$  although this will underestimate  $\pi_s$  severely for large  $s$ . (A better estimate

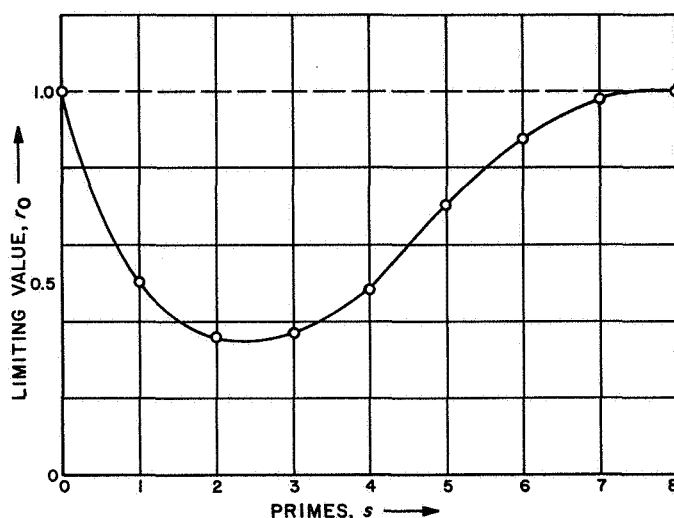


Figure 31. Lower bound  $r_0$  on ratio  $k/L$  as a function of  $s$ , the number of primes dividing  $L$

is  $s^s$ .) However, as a trend, it is sufficient to provide a fair lower bound on  $r_0$  for large  $s$ . Applying Stirling's formula, this lower bound, call it  $r_1$ , is given by

$$r_1 = 1 - \frac{(4e)^s}{(2\pi s)^{0.5} s^s}$$

This completes the proof of the theorem.

It may be noted, upon reviewing the proof, that nowhere in Case II (even  $L$ ) was use actually made of the evenness of  $L$ , except perhaps in the statement that  $\pi_s \leq L$ . Prior to that statement, however, the argument is general. From this argument the following conditions on  $k$  and  $L$  may be extracted: (1)  $k(k-1)/L - 1$  is a rational integer, (2)  $k(L-k)/L - 1$  is the square of a rational integer. It may be possible, by consideration of such divisibility properties as implied by (1) and (2), to show that no even-length reversible perfect sequences exist.

Table 9. Tabulation of lower bound  $r_0$  on  $k/L$

$s$	$\pi_s$	$r_0$
0	1	1.000
1	2	0.500
2	6	0.357
3	30	0.371
4	210	0.481
5	2,310	0.706
6	30,030	0.881
7	510,510	0.981
8	9,699,690	0.993



## B. Communications Research

R. Sydnor and D. R. Anderson

### 1. Investigation of an FM Demodulator with Negative Feedback

An *improvement factor* can be realized in signal-to-noise ratio at the demodulated output of the receiver in communication systems when the total received RF power is significantly above the receiver threshold. In FM systems, an *FM improvement factor* can be obtained by transmitting at high modulation indices and detecting the modulation in a frequency discriminator which employs negative feedback (Refs 28 and 29). Analysis of a PM communication system has demonstrated that a similar *PM improvement factor* can be obtained with transmission at high modulation indices and detection in a properly designed phase-locked demodulator (Ref 30). A research effort has been initiated to investigate the problems associated with designing communication systems which provide signal enhancement in the detection process. This report presents some preliminary experimental data for a FM communication system which employs negative feedback in the frequency discriminator.

The equipment used for this investigation is the Bell Telephone Laboratory's FM modulator and demodulator which was used at the Goldstone tracking and communications station for the *Echo I* experiment. A block diagram of the FM feedback demodulator is shown in Figure 32. Figure 33 is a block diagram of the experimental test setup used to obtain the data. In this setup, the input carrier power to the demodulator was maintained constant for convenience and the input noise power was varied in order to adjust the input ratio of RF carrier to RF noise. The carrier power was measured at the output of the FM

oscillator and corrected by the known amount of attenuation to obtain the FM demodulator signal input. The RF noise power was measured in the known noise bandwidth of the noise source, corrected for the known attenuation, and referred to a 6-kc bandwidth.

The output ratio of AF signal to AF noise was obtained by measuring the output signal level across a known resistance with the narrow-band audio wave analyzer, in the presence of noise. The audio noise power output was obtained in the absence of modulation by means of the rms meter. For low ratios of RF carrier to RF noise, the audio noise was not gaussian but had superimposed on the ordinary gaussian noise a random high-amplitude, low-duty-cycle, pulse type of disturbance. To eliminate difficulties due to this characteristic (erratic meter readings, high peak-to-rms ratios), the meter detector was followed by an integrator and a calibrated dc voltmeter, and an attenuator was inserted ahead of the rms detector to adjust the noise level so that the detector was operating in the proper range for true rms indication. It was determined experimentally that the measurement of audio noise in the absence of modulation was a valid means of measuring the audio noise in the presence of modulation. This was accomplished by scanning the spectrum of the audio output noise with a narrow-band tunable audio wave analyzer both with and without modulation on the RF carrier. No change in the audio noise spectrum due to modulation could be measured for any given feedback and input carrier-to-noise ratio. The noise bandwidths of the critical components in the system were measured and are indicated on Figures 32 and 33. The output noise spectrum depends on the adjustment of the discriminator circuits. The following data was all taken with a discriminator adjustment which produced a linear characteristic over a range of  $\pm 100$  kc from the center frequency.

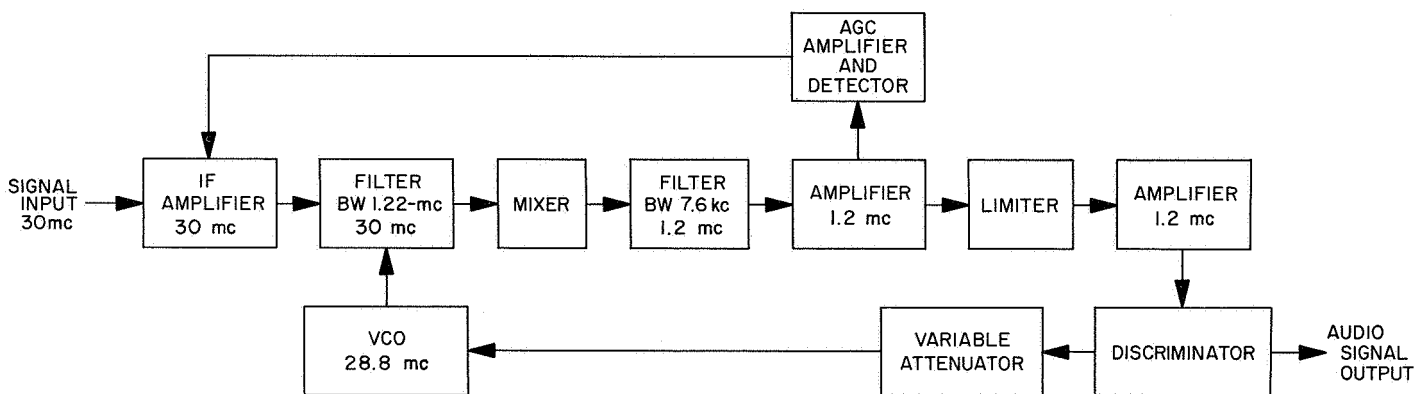


Figure 32. Block diagram of FM demodulator with negative feedback

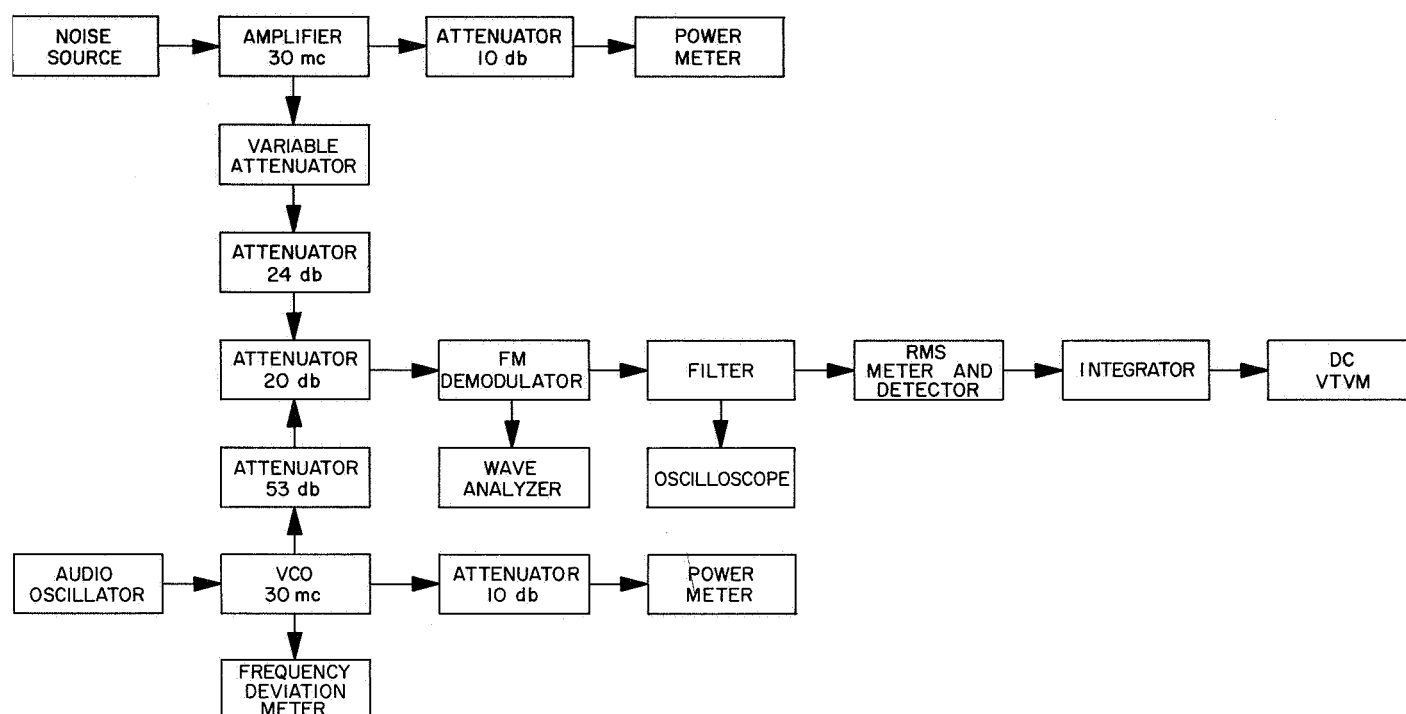


Figure 33. Test setup for FM demodulator with negative feedback

Figure 34 shows curves of output audio-signal-to-audio-noise ratio vs input carrier-to-RF-noise ratio ( $C/N$ ), both referred to a 6-kc bandwidth, for various modulation indices and amounts of feedback. Feedback is defined here as the ratio of the input frequency deviation to the error frequency deviation, or as the loop gain plus one. In obtaining these curves, the modulation index was set, and the feedback was adjusted to a value which produced an error frequency deviation of  $\pm 2.5$  kc. The upper limit on the modulation index was determined by the amount of feedback available from the loop gain of the system. These curves demonstrate that the FM improvement factor and the position of the knee of the curve depend on the amount of feedback used. The improvement factor increases from 7 to 29.5 db as the feedback increases from 9.8 to 33.5 db while the threshold is reduced by 12 db [from 6 to 18 db input ( $C/N$ )]. The decrease in the improvement factor at high input  $C/N$  was due to the system internal noise. The shape of these experimental curves is similar to the theoretical curves (Fig 9 of Ref 30) for a PM demodulator.

In the curves of Figure 34, there is some uncertainty below the knee of the curves partly due to the pulse-type noise and the characteristics of the rms meter and partly due to the action of the 30-mc amplifier and its associated AGC detector. The curves are probably somewhat opti-

mistic in this region. Further experimental work will be done to separate the effects due to this amplifier and the effects due to the demodulator itself.

Output signal-to-noise ratio vs modulation frequency is shown in Figure 35 for the system with a 2.94-kc output filter noise bandwidth (2.4-kc 3-db bandwidth) and for various input carrier-to-noise ratios. The curves of Figure 35 extend to dc on the low-frequency end. The maximum FM improvement factor is 12.3 db referred to a 6-kc bandwidth (15.4 db for the 2.94-kc bandwidth) for the conditions of Figure 35. Threshold for the amount of feedback used (26 db) occurs at approximately 15-db input  $C/N$ , interpolated from Figure 34a. It should be noted that the input frequency deviation ( $\pm 30$  kc) in Figure 35 was the same as that used in Project Echo.

Experimental investigation of a PM system is planned as a continuation of this evaluation of communication systems providing signal enhancement.

## 2. Mutually Distinguishable Self-Synchronizing Continuous Codes

*a. Continuous codes and synchronization.* In almost all coding problems studied to date, the codes used have been digital. However, in the problem of self-synchronous

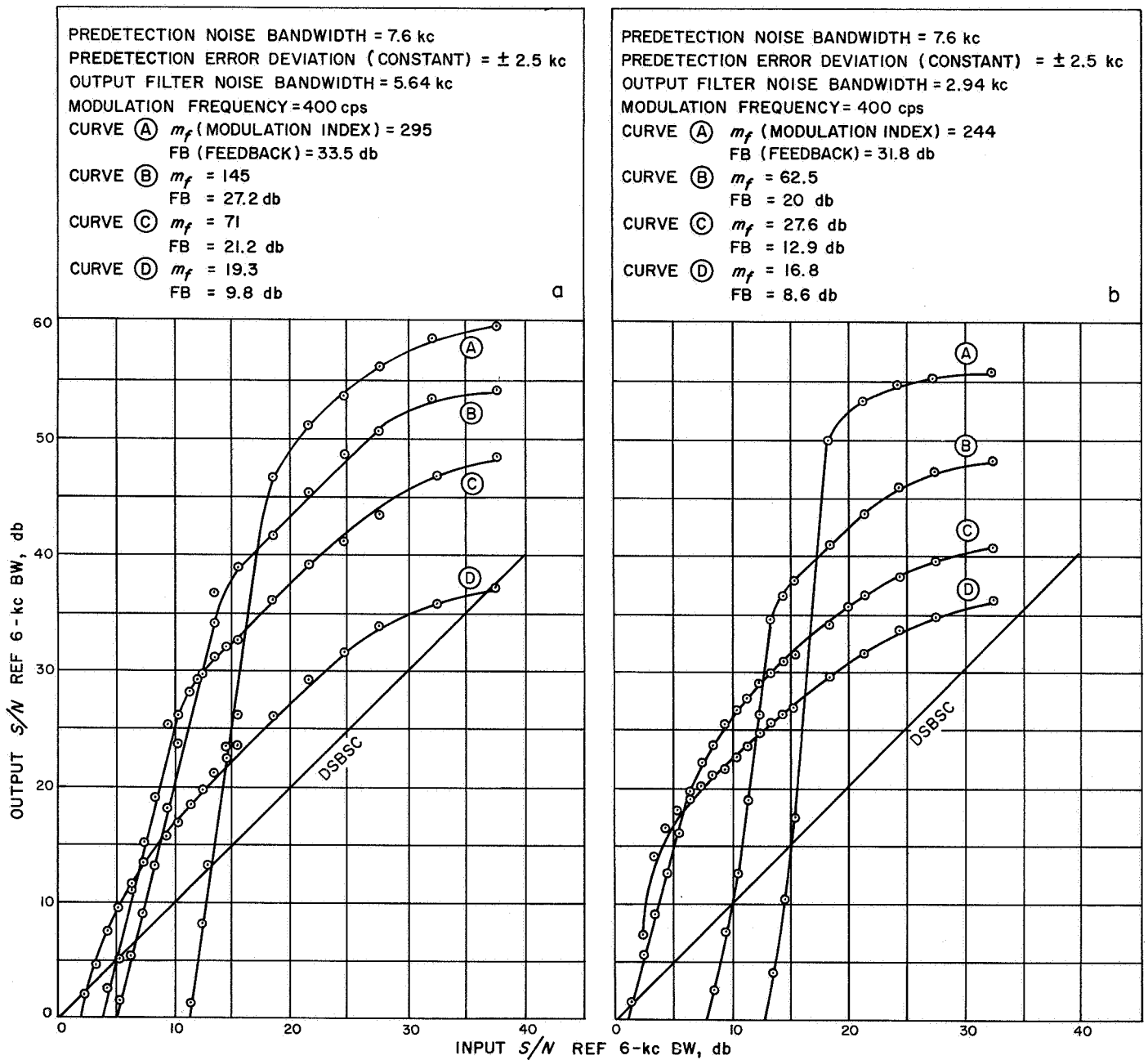


Figure 34. Output  $S/N$  vs input  $S/N$  of FM demodulator with negative feedback

codes the use of *continuous codes* becomes possible; i.e., we can employ continuous waveforms with the same finite time duration, the same bandwidth, and the same total energy. We can obtain the self-synchronizing property by requiring of every pair of members of a continuous code,  $v(t)$  and  $w(t)$ , that the cross-correlation  $C[v(t), w(t + \tau)]$  should be small, independent both of the choice of  $\tau$  and the choice of pair.

To deal with self-synchronization more explicitly, we make the following observations: Suppose the code is the sequence of waveforms  $[v_2(t), \dots, v_N(t)]$ , where

$$\int_{-\infty}^{+\infty} v_k^2(t) dt = V^2 \quad (1)$$

for all  $k$  and, if  $k$  is unequal to  $l$ ,

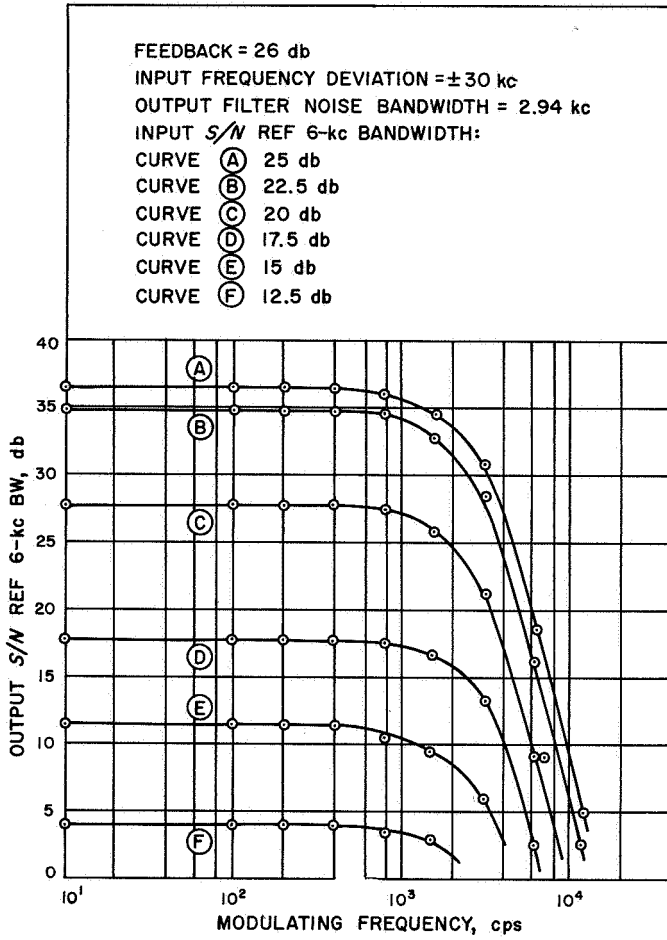


Figure 35. Output  $S/N$  vs modulating frequency for FM demodulator with negative feedback

$$\left| \int_{-\infty}^{+\infty} v_k(t) v_l(t + \tau) dt \right| < \varepsilon \quad (2)$$

for all choices of  $k$ ,  $l$ , and  $\tau$ . Suppose that to each  $v_k(t)$  we add a white gaussian noise signal  $N(t)$ ,  $N(t)$  having standard deviation  $\sigma$ . Then let us consider  $C[v_k(t) + N(t), v_l(t + \tau)]$ , and let us note how and when we can use it to distinguish  $v_k(t) + N(t)$  from  $v_m(t) + N(t)$  if  $m$  is different from  $k$ .

We have two significant inequalities

$$P \left\{ \int_{-\infty}^{+\infty} v_k(t) [v_k(t) + N(t)] dt \geq V^2 - 10V\sigma \right\} \geq 0.99 \quad (3)$$

if  $k \neq l$

$$P \left\{ \int_{-\infty}^{+\infty} v_l(t + \tau) [v_k(t) + N(t)] dt \leq \varepsilon + 10V\sigma \right\} \geq 0.99 \quad (4)$$

While the results are obviously very rough, they still indicate that for a sufficiently small signal-to-noise ratio it is possible to detect any signal consisting of a single  $v_k(t)$  without even knowing the time of arrival.

Further, with the same restriction on the signal-to-noise ratio, one can detect and perform a synchronization process on a signal consisting of a finite sequence of waveforms, each of which is some  $v_k(t)$ . For if we write the signal as

$$s(t) = \sum_{r=0}^M v_{k_r}(t - rT) + N(t)$$

$T$  being the common duration of  $v_k(t)$ 's, then for all  $l$

$$\int_{-\infty}^{+\infty} v_l(t + \tau) s(t) dt$$

has one of three forms:

$$\begin{aligned} & \int_{-\tau}^{-\tau+T} v_l(t + \tau) [v_{k_0}(t) + N(t)] dt \\ & \int_{-\tau}^{-\tau+T} v_l(t + \tau) \{ v_{k_r}(t - rT) \\ & \quad + v_{k_{r+1}}[t - (r+1)T] + N(t) \} dt \end{aligned}$$

or

$$\int_{-\tau}^{-\tau+T} v_l(t + \tau) [v_{k_M}(t) + N(t)] dt$$

Then from Equation (3) it follows that we have for  $l = k_r$ :

$$P \left[ \int_{-\infty}^{+\infty} v_{k_r}(t - rT) s(t) dt \geq V^2 - 10V\sigma \right] \geq 0.99 \quad (5)$$

And from Equation (4) it follows that for  $-(r-1)T < \tau \leq -rT$  and for  $l \neq k_{r-1}, k_r$ , and  $k_{r+1}$  we have:

$$P \left[ \int_{-\infty}^{+\infty} v_l(t + \tau) s(t) dt \leq \varepsilon + 10V\sigma \right] \geq 0.99 \quad (6)$$

Thus, at intervals of length  $T$

$$\int_{-\infty}^{+\infty} v_k(t + \tau) s(t) dt$$

will have a significant peak for exactly one value of  $k$ , and this event will occur with probability 0.99.

**b. Construction of continuous codes.** The continuous codes which we shall discuss are most simply defined by means of Fourier transforms. Let us look at a sequence of waveforms with the following transforms:

$$\begin{aligned} & \phi(\omega) e^{j(\text{sgn } \omega) |K\omega|^{1+\alpha}}, \quad \phi(\omega) e^{2j(\text{sgn } \omega) |K\omega|^{1+\alpha}}, \dots, \\ & \phi(\omega) e^{nj(\text{sgn } \omega) |K\omega|^{1+\alpha}}, \dots \end{aligned}$$

[sgn  $\omega$  is the function which is 1 for  $\omega > 0$ , 0 for  $\omega = 0$ , and  $-1$  for  $\omega < 0$ .] Here  $\alpha$  and  $K$  are positive, while  $\phi(\omega)$  must be such that (a)

$$\int_{-\infty}^{+\infty} |\phi(\omega)|^2 d\omega$$

is finite, (b)  $\phi(\omega)$  is a conjugate symmetric function of  $\omega$ . It is easy to see that every one of these waveforms has the same total energy and the same bandwidth (regardless of definition). It can be shown, calling the bandwidth  $B$ , that the cross-correlation function of any two of these waveforms tends uniformly to zero with the order of  $1/BK$ ; i.e., it is bounded uniformly by a constant divided by  $BK$ . Further, if the first  $N$  of these waveforms are truncated outside the interval

$$-N^{1/(1+\alpha)}K \leq t \leq N^{1/(1+\alpha)}K$$

it can be shown that their cross-correlations are uniformly less than any preassigned small number when  $B [2N^{1/(1+\alpha)}K]$  is large enough, and it can be shown that these truncated waveforms all have time-bandwidth products which are approximately equal to  $B [2N^{1/(1+\alpha)}K]$ . In fact, given a maximum cross-correlation  $\epsilon$ , a time-width  $T$ , and a bandwidth  $B$ , then for  $TB$  sufficiently large and a suitable choice of  $\alpha$  one can construct approximately  $(\epsilon TB)^{2+\alpha}$  waveforms with maximum cross-correlation  $\epsilon$ , time-width  $T$ , and approximate bandwidth  $B$ .

We shall now discuss in detail a particular case of the general construction process in order to provide some understanding of the methods actually used. Suppose that

$$\phi(\omega) = B^{-0.5} e^{-\frac{1}{8\pi} \left(\frac{\omega}{B}\right)^2}$$

and that  $\alpha = 1$ . Then  $B$  is the bandwidth in the sense that

$$B = \frac{1}{2\pi} \int_{-\infty}^{+\infty} |\phi(\omega)|^2 d\omega / [\max |\phi(\omega)|]^2$$

and the  $n$ th untruncated waveform  $f_n(t)$  obeys the following relation:

$$f_n(t) = \frac{1}{(2\pi)^{0.5}} \int_{-\infty}^{+\infty} e^{j\omega t} \left[ B^{-0.5} e^{-\frac{1}{8\pi} \left(\frac{\omega}{B}\right)^2} e^{jn(K\omega)^2} \right] d\omega \quad (7)$$

From Equation (7), straight-forward calculations lead to a formula in terms of the complex error function:

$$f_n(t) = \left(\frac{\pi}{2} B\right)^{-0.5} \operatorname{Re} \left[ \left( \frac{1}{8\pi B^2} - jnK^2 \right)^{-0.5} e^{-t^2/4 \left( \frac{1}{8\pi B^2} - jnK^2 \right)} \times \left\{ \frac{\pi^{0.5}}{2} + \int_0^{j/2} \left( \frac{1}{8\pi B^2} - jnK^2 \right)^{-0.5} t e^{-\omega^2} d\omega \right\} \right] \quad (8)$$

We can obtain a form of  $f_n(t)$  useful for small values of  $t$  by using the series expansion of the error function;

$$f_n(t) = \left(\frac{\pi}{2} B\right)^{-0.5} \operatorname{Re} \left[ \left( \frac{1}{8\pi B^2} - jnK^2 \right)^{-0.5} e^{-t^2/4 \left( \frac{1}{8\pi B^2} - jnK^2 \right)} \times \left\{ \frac{\pi^{0.5}}{2} + \sum_{m=0}^{\infty} \frac{\left[ \frac{j}{2} \left( \frac{1}{8\pi B^2} - jnK^2 \right)^{-0.5} t \right]^{2m+1}}{(2m+1)m!} \right\} \right] \quad (9)$$

Using the asymptotic expansion of the error function we have an asymptotic expression for  $f_n(t)$  when  $t > 0$ :

$$f_n(t) \approx \left(\frac{\pi}{2} B\right)^{-0.5} \operatorname{Re} \left[ \sum_{m=1}^{\infty} \frac{1.3 \cdots (2m-1)}{2^{3m+2}} \times \left( \frac{1}{8\pi B^2} - jnK^2 \right)^m t^{-(2m+1)} \right] \quad (10)$$

If  $t < 0$ , one can subtract the asymptotic series of (10) from

$$\pi^{0.5} e^{-t^2/4 \left( \frac{1}{8\pi B^2} - jnK^2 \right)}$$

to obtain an asymptotic expression for  $f_n(t)$ . Also, the correlation function of  $f_m(t)$  and  $f_n(t)$  for  $m < n$  is given by:

$$\begin{aligned} \int_{-\infty}^{+\infty} f_m(t) f_n(t+\tau) dt = \\ (B/2)^{-1} \operatorname{Re} \left[ \left[ \frac{1}{4\pi B^2} - j(n-m)K^2 \right]^{-0.5} e^{-\tau^2/4 \left[ \frac{1}{4\pi B^2} - j(n-m)K^2 \right]} \times \left\{ \frac{(\pi)^{0.5}}{2} + \int_0^{j/2} \left[ \frac{1}{4\pi B^2} - j(n-m)K^2 \right]^{-0.5} \tau e^{-\omega^2} d\omega \right\} \right] \end{aligned} \quad (11)$$

Expressions similar to Equations (9) and (10) hold:

$$\begin{aligned} \int_{-\infty}^{+\infty} f_m(t) f_n(t+\tau) dt = \\ (B/2)^{-1} \operatorname{Re} \left[ \left[ \frac{1}{4\pi B^2} - j(n-m)K^2 \right]^{-0.5} e^{-\tau^2/4 \left[ \frac{1}{4\pi B^2} - j(n-m)K^2 \right]} \times \left\{ \frac{\pi^{0.5}}{2} + \sum_{m=0}^{\infty} \frac{\left\{ \frac{j}{2} \left[ \frac{1}{4\pi B^2} - j(n-m)K^2 \right]^{-0.5} \tau \right\}^{2m+1}}{(2m+1)m!} \right\} \right] \end{aligned} \quad (12)$$

$$(\tau > 0) \int_{-\infty}^{+\infty} f_m(t) f_n(t + \tau) dt \approx$$

$$(B/2)^{-1} \operatorname{Re} \left[ \sum_{m=1}^{\infty} \frac{1}{2^{3m+2}} \frac{3 \cdots (2m-1)}{4\pi B^2} \left[ \frac{1}{4\pi B^2} - j(n-m)K^2 \right]^m \tau^{-(2m+1)} \right] \quad (13)$$

(If  $\tau < 0$ , one can subtract the asymptotic series of (13) from

$$\pi^{0.5} e^{-\tau^2/4} \left[ \frac{1}{4\pi B^2} - j(n-m)K^2 \right] \quad (13)$$

to obtain an asymptotic expression for  $C[f_m(t), f_n(t + \tau)]$ .

We can estimate the cross-correlations of the truncated  $f_n(t)$ 's. Suppose we truncate  $f_1(t)$ ,  $\dots$ , and  $f_N(t)$  outside the interval  $-N^{0.5}K \leq t \leq N^{0.5}K$ , and suppose we call the truncated functions, respectively,  $\bar{f}_1(t)$ ,  $\dots$ , and  $\bar{f}_N(t)$ . An estimate of the cross-correlation of  $\bar{f}_m(t)$  and  $\bar{f}_n(t)$  is:

$$\int_{-\infty}^{+\infty} \bar{f}_m(t) \bar{f}_n(t + \tau) dt \leq 14N^{0.5}/B(2N^{0.5}K) + 16\pi^{0.5}/[B(2N^{0.5}K)]^{0.5} \quad (14)$$

[Note that  $2N^{0.5}K$  is the common time-width of  $\bar{f}_1(t)$ ,  $\dots$ , and  $\bar{f}_N(t)$ .]

Finally  $B_n$ , the bandwidth of every  $\bar{f}_n(t)$ , is asymptotic to  $B$  as the latter tends to  $+\infty$ . In fact:

$$B_n \leq B \left\{ 1 - \left\langle \frac{1}{3} \left( \frac{2}{\pi} \right)^{0.5} / [B(2N^{0.5}K)]^2 \right\rangle \right\}^{-2} \quad (15)$$

$$B_n \geq B \left\{ 1 - \left\langle \frac{8}{2^{0.5}\pi} / [B(2N^{0.5}K)]^{0.5} \right\rangle \right\} \times \left\{ 1 + \left\langle \frac{1}{3} \left( \frac{2}{\pi} \right)^{0.5} / [B(2N^{0.5}K)]^2 \right\rangle \right\}^{-2} \quad (16)$$

[It is of course assumed that  $B(2N^{0.5}K) > (2^{0.5}8)^2$ .] Thus,  $B_n$  is asymptotic to  $B$  as  $B(2N^{0.5}K)$  tends to  $+\infty$ , and, since  $B_n(2N^{0.5}K)$  is the time-bandwidth product of  $\bar{f}_n(t)$ , it is immediate that the time-bandwidth product of  $\bar{f}_n(t)$  is asymptotic to  $B(2N^{0.5}K)$  as the latter tends to  $+\infty$ .

And now we have reached the point where we have the desired information about the sequence of  $\bar{f}_1(t)$ ,  $\dots$ ,  $\bar{f}_N(t)$ ; i.e., we can find a significant value of  $N$  such that given a bandwidth  $\bar{B}$ , a time-width  $\bar{T}$ , and a maximum cross-correlation  $\epsilon$ , the  $\bar{f}_n(t)$ 's have  $\epsilon$  as a maximum cross-correlation,  $\bar{T}$  as time-width, and, asymptotically with  $\bar{T}\bar{B}$ ,  $\bar{B}$  as bandwidth. For let us set  $\bar{T} = 2N^{0.5}K$ ,  $\bar{B} = B$ , and set  $N$  equal to the largest integer less than or equal to  $\{1/14[\epsilon - 16\pi^{0.5}/(\bar{T}\bar{B})^{0.5}] \bar{T}\bar{B}\}^2$ . Clearly, the  $\bar{f}_n(t)$ 's have time-width  $\bar{T}$ . By Equations (15) and (16), the bandwidth of every  $\bar{f}_n(t)$  is asymptotic to  $\bar{B}$  as  $\bar{T}\bar{B}$  tends to  $+\infty$ . Lastly, the choice of  $N$  and Equation (14) make it apparent that the cross-correlation of any two distinct  $\bar{f}_n(t)$ 's has  $\epsilon$  as upper bound.

## V. Communications Elements Research

### A. Low-Noise Amplifiers

W. H. Wells

#### 1. Three-Level Mixer

It is well known that a three-level quantum mechanical system functions as a mixer for radiation at its three resonant frequencies. That is, when radiated with two of the frequencies, it produces an oscillating polarization at the third.

A mixer composed of many such systems can have the low noise characteristics of a maser. It is conceptually applicable to the usual heterodyne problems that occur in communications work. If lasers (optical masers) become practical in communications work, then this form of mixer is available for modulating light with a microwave frequency, or for mixing light with light to obtain a microwave IF in a heterodyne receiver.

A theoretical analysis is underway to determine the detailed response and noise characteristics of a three-level system. The theory is valid when the radiation field is so weak that it must be quantized. Work so far in this area at JPL has provided the techniques for treating the quantized case within the formalism of classified linear

networks (Ref 31). The three-level system is presumed to be embedded in a molecular environment (or crystal lattice) at a fixed temperature. The tendency of the three-level system to relax to thermal equilibrium with the environment will be described by the usual set of phenomenological relaxation rates.

The results will be expressed in convenient form by analogy to a three-terminal-pair circuit element, one pair for each resonant frequency. To one pair, fixed power is applied from the local oscillator, or in maser language, the pump.

The other two pairs are for input and output signals, and it is for these pairs that the transfer characteristics are desired. Seven functions will be derived: the self-impedance at each pair (2), the signal transfer characteristics both ways (2), the autocorrelation function for the noise at each pair (2), and finally the cross-correlation function (1) for the correlation between the noise at one pair and the noise at the other.

#### 2. Solid State Maser

Reporting on the Venus project cavity maser has been transferred to the *Space Programs Summary*, a companion periodical.

## B. Antennas for Space Communication

P. D. Potter, D. Schuster, and C. T. Stelzried

### 1. Antenna Feed Research

The widespread use of large paraboloidal reflector ground antennas for space communications and for radio and radar astronomy lends new importance to the problem of optimum feed system design. For receiving applications where the critical system criterion is the signal-to-noise ratio, a figure of merit for the antenna system, defined as the ratio of the antenna effective area to the receiving system noise temperature, is a useful concept. Since a significant contribution to system noise may be introduced by the antenna, an optimum feed system would not only result in a high aperture efficiency but would also result in low effective antenna noise temperature.

At the Jet Propulsion Laboratory, a program exists to develop practical feed systems which realize a close approximation to the optimum. In addition, work is being carried out on an 85-foot paraboloid at the Goldstone Tracking Station to develop improved techniques for measurement of both aperture efficiency (i.e., gain) and effective antenna noise temperature.

*a. Cassegrainian feed system studies.* It appears that a cassegrainian feed system may be designed to produce a relatively low effective antenna noise temperature, while at the same time providing a relatively high aperture efficiency. Preliminary work in this direction has been performed under subcontract to JPL by the RCA Victor Company of Montreal, Canada. As an extension to this contract, work has been initiated at JPL to study, both analytically and experimentally, certain problems inherent in cassegrainian design.

The basic properties of the cassegrainian system have been described in the literature (Refs 32, 33). The geometry is shown in Figure 36a. It can be seen that simple ray tracing techniques would indicate no spillover of energy beyond the edge of the paraboloid and, hence, a low effective noise temperature. Practically, even for antenna systems which are very large in terms of the operating wavelength, this situation can only be approximated; fortunately, however, to a rather high degree.

As shown in Reference 33, many properties of the cassegrainian system may be described in terms of an equivalent focal point feed paraboloidal antenna whose focal length is equal to the magnification factor,  $M$ , times

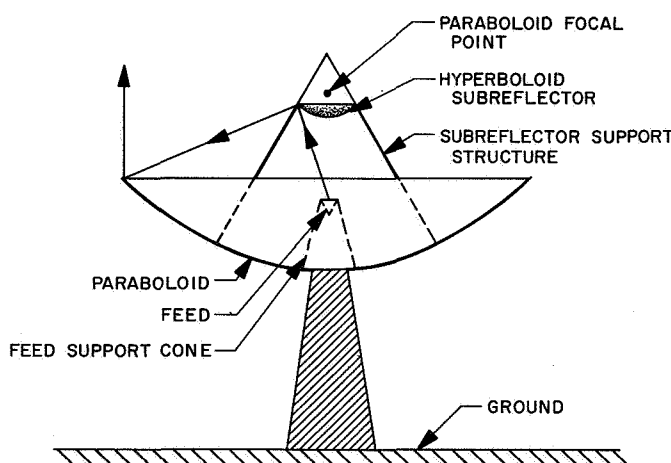
the real focal length. This concept is depicted in Figure 36b. Several consequences of this equivalence are evident. The first is that for normal values of  $M$  (usually about 10), uniform illumination of the subreflector will result in near uniform illumination of the paraboloid, even for very deep paraboloids. A second important consequence is that the large cross polarization loss normally associated with deep paraboloids (Refs 34, 35) is practically absent in cassegrainian systems. This fact may be rigorously proved without aid of the equivalent paraboloid concept.

An important feature of the cassegrainian system relates to its performance in the monopulse tracking mode. It is well known that for focal point feed systems the wavelength separation  $S_\lambda$  between feed elements (for half-power crossover level) is given approximately by

$$S_\lambda \simeq f/D \quad (1)$$

where  $f$  is the focal length of the paraboloid, and  $D$  is its diameter. For focal point feed systems, a higher crossover level (and, hence, higher reference channel efficiency) is

a. CASSEGRAINIAN ANTENNA



b. EQUIVALENT PARABOLOID

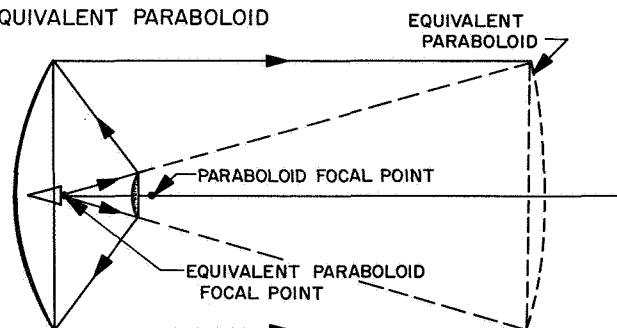


Figure 36. Cassegrainian antenna and equivalent paraboloid



not achieved without great difficulty because of the necessarily close spacing of feed elements. In a cassegrainian system, however, Equation (1) is modified to the following:

$$S_{\lambda} \simeq M f/D \quad (2)$$

In general,  $M$  is a sufficiently large number (usually about 10) so that practical monopulse feeds with high crossover levels and, hence, high efficiencies may be designed. Experimentally, Hannon (Ref 33) has reported an overall aperture efficiency of 54% for a monopulse system. It appears that by further sacrifice of error channel sensitivity it is possible to achieve even higher efficiencies. In addition, the high error channel dish spillover which is associated with a high-crossover, focal point feed is largely eliminated in a cassegrainian system. One would, therefore, expect an error channel noise temperature comparable to that in the reference channel.

One of the major problems associated with the cassegrainian system is that of spillover around the subreflector. This effect not only reduces the aperture efficiency but drastically affects the noise temperature performance when the antenna is pointed close to the Sun. The effect will be particularly evident in the error channels of a high-crossover monopulse feed.

Particular emphasis at JPL is being directed to two areas. The first area involves the synthesis of subreflector illuminator devices which approximate the ideal sector beamshape. Both shaped reflector and modified horn antennas are being investigated as possible solutions.

The second area of investigation involves optimization of the  $f/D$  ratio. The dish illumination function and spillover characteristics are a function of the subreflector size in wavelengths. The larger the subreflector is, the more nearly the ideal optical spillover situation will be approximated. There is some experimental data to indicate, however, that the  $f/D$  ratio is involved in the rapidity of the cutoff and, hence, the noise temperature performance of the system. This effect is being investigated.

**b. Shaped beam feed studies for focal point feeds.** Since one of the objectives of modern feed design is to reduce the antenna temperature, a value for the minimum possible antenna temperature is needed. Bell Telephone Laboratories has reported a low of about 4.5°K at 5650 mc with a special low-noise horn antenna (Ref 36). At JPL, analytical and experimental work has been in progress for some time to determine the minimum antenna temperature for a large paraboloidal reflector antenna.

The antenna temperature has thermal noise contributions due to the following: (1) black-body radiation from the ground with a brightness temperature assumed to be  $T_0 [1 - |R(\theta)|^2]$ ; where  $T_0$  is the effective ambient temperature,  $\theta$  the angle from the vertical, and  $|R(\theta)|^2$  the power reflection coefficient of the ground; (2) atmospheric absorption, primarily due to oxygen and water vapor with a minimum effective temperature of about 2 or 3°K at 1000 to 2000 mc; this will increase as the elevation angle decreases (Ref 37); (3) radiation from discrete sources such as the Sun, Moon, and radio stars and from the broad region of the Milky Way; (4) radiation from the sky background; average brightness temperatures for the quiet regions of space are probably less than 3°K at 1000 mc and less than 1°K at 2400 mc; (5) resistive losses in the reflector, feed support structure, antenna feed, and transmission line; reflector and structure losses may contribute less than 1°K.

For a highly directive antenna, the minimum antenna temperature will be achieved with the antenna beam aimed at a quiet region in the sky. Then ground radiation usually will be the largest contributor to antenna temperature.

The excess antenna temperature  $T_a$ , exclusive of resistive loss and reflector emission contributions, may be calculated by the equation

$$T_a = \frac{\int_{4\pi} T_b(\Omega) G(\Omega) d\Omega}{\int_{4\pi} G(\Omega) d\Omega} \quad (1)$$

or

$$T_a = \frac{1}{4\pi} \int_{4\pi} T_b(\Omega) G(\Omega) d\Omega \quad (2)$$

where  $T_b(\Omega)$  is the brightness temperature in the direction of  $d\Omega$  and  $G(\Omega)$  is the antenna gain in the direction of  $d\Omega$ .

If the antenna gain could be measured accurately enough in all directions, and if  $T_b(\Omega)$  is known or can be calculated, the calculation of  $T_a$  would be straightforward. However, for low-noise antennas  $G(\Omega)$  will be very small in the direction of the ground and, hence, difficult to measure.

The above procedure may be modified by writing

$$T_a = \frac{1}{4\pi} \int_{\Omega_0} T_b(\Omega) G(\Omega) d\Omega + \frac{1}{4\pi} \sum_{n=1}^N \int_{\Omega_n} T_b(\Omega) G(\Omega) d\Omega \quad (3)$$

where the  $\Omega_n$  are independent,  $\Omega_0$  covers the region where  $G(\Omega)$  may be measured accurately (including the main beam), and

$$\Omega_0 + \sum_{n=1}^N \Omega_n = 4\pi$$

Assume the antenna is pointed at the zenith. Then for the back hemisphere of the antenna, an average ground temperature may be calculated ( $T_{G, avg}$ ). For this region we have as a first approximation

$$T_{a, g} = T_{G, avg} \cdot \frac{\int_{\Omega_g} G(\Omega) d\Omega}{4\pi} \quad (4)$$

The factor on the right is the fraction of the antenna pattern power contained in the back hemisphere. This will be caused by primary feed pattern spillover, diffraction at the dish edge, and leakage, if the reflector has a mesh surface. A conventional feed horn will have a primary pattern tapered to about  $-10$  db at the edge illumination angle of the reflector, with reference to the center of the reflector. Usually spillover into the ground for this type of horn will amount to 8 to 10% of the total pattern power. Normally, this will be the largest contributor to Equation (4). For example, we may have  $T_{G, avg} \approx 200^\circ\text{K}$ , for desert ground. If we take

$$\frac{\int_{\Omega_g} G(\Omega) d\Omega}{4\pi} \approx 0.09$$

then the spillover into ground of  $T_a \approx 18^\circ\text{K}$ . The value of primary pattern spillover may be found by simple pattern integration for any feed horn.

To test the influence of primary pattern spillover, feed horns with different pattern tapers were evaluated on the Goldstone 85-foot receiver antenna in September 1960. The results in terms of spillover contribution to the antenna temperature are presented in Table 10 and compared to the simple calculated values. Similar experiments have been conducted with the 2388-mc feeds tested for the Venus Radar Project. The results are also shown in Table 10.

The change  $\Delta T_{ag}$  in antenna temperature due to changing the percentage of spillover power can be measured quite accurately. The agreement between the measured and calculated values of  $\Delta T_{ag}$  is quite good and indicates that the average effective ground temperature at Goldstone for the spillover region is indeed close to  $200^\circ\text{K}$ .

The last feed (No. 5) mentioned in Table 10 was designed with minimum spillover (Fig 37) only for the purpose of measuring minimum antenna temperature. This was completed and tested during the last week of the Venus Radar Experiment. Ordinary high-gain horns available at JPL did not have sufficiently low spillover. The special horn was developed using a combination of *tunneling* and the previous JPL techniques. Figure 38 shows the E- and H-plane patterns which indicate the extremely small spillover and low backlobes. The E-plane pattern includes out-of-phase sidelobes which reduce the secondary antenna gain. This was measured and found to be 3 db less than with the shaped beam feed normally used. The measured value of antenna temperature for this

Table 10. Spillover contribution to antenna temperature<sup>a</sup>

No.	Type of feed	Average pattern taper, db	Measured spillover for ground region, %	Calculated temperature due to ground $T_{AG}$ , °K	Calculated $\Delta T_{AG}$ , °K	Measured antenna temperature minus feed losses, °K	Measured <sup>b</sup> $\Delta T_{AG}$ , °K
1	960-mc horn	-10	9	18	9	25 ± 4	8 ± 2
2	960-mc horn	-14	4.5	9		17 ± 4	
3	2388-mc horn	-10	About 10 to 12 (to be remeasured)	20 to 24	11 to 15	30 ± 4	15 ± 2
4	2388-mc shaped beam feed	-9.5	4.5	9		15 ± 4	
5	2388-mc low-spillover shaped beam feed	-32	<0.5	<1	8 to 9	8 ± 4	7 ± 2

<sup>a</sup>Tolerances indicate estimated measurement accuracies.  
<sup>b</sup>Relative measurement accuracy is better.

low-spillover feed was about  $8^\circ\text{K}$ . A reasonable accounting of the contributions to this  $8^\circ\text{K}$  is shown on the next page in the list, which includes a probable leakage power of 1 or 2%, based on the mesh surface of the reflector.

Spillover	$1^\circ\text{K}$
Atmosphere	$3^\circ\text{K}$
Sky background	$0^\circ\text{K}$
Reflector absorption	$1^\circ\text{K}$
Reflector leakage	$3^\circ\text{K}$
Total	$T_a \approx 8 \pm 4^\circ\text{K}$

## 2. Noise Temperature Measurements

An important part of the antenna temperature and radiometer instrumentation used at Goldstone is a high-

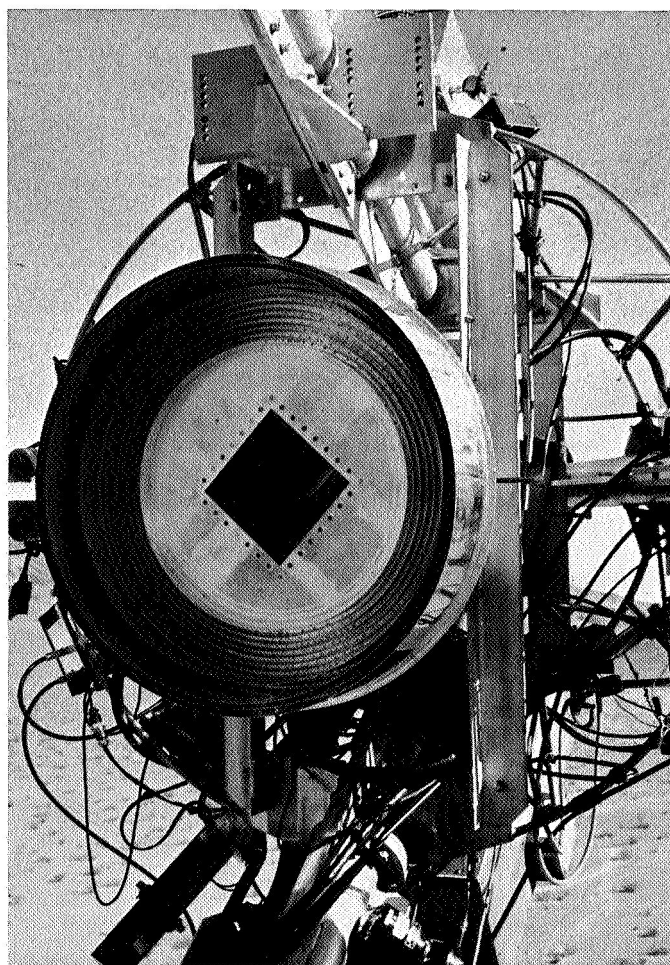


Figure 37. Low-spillover feed

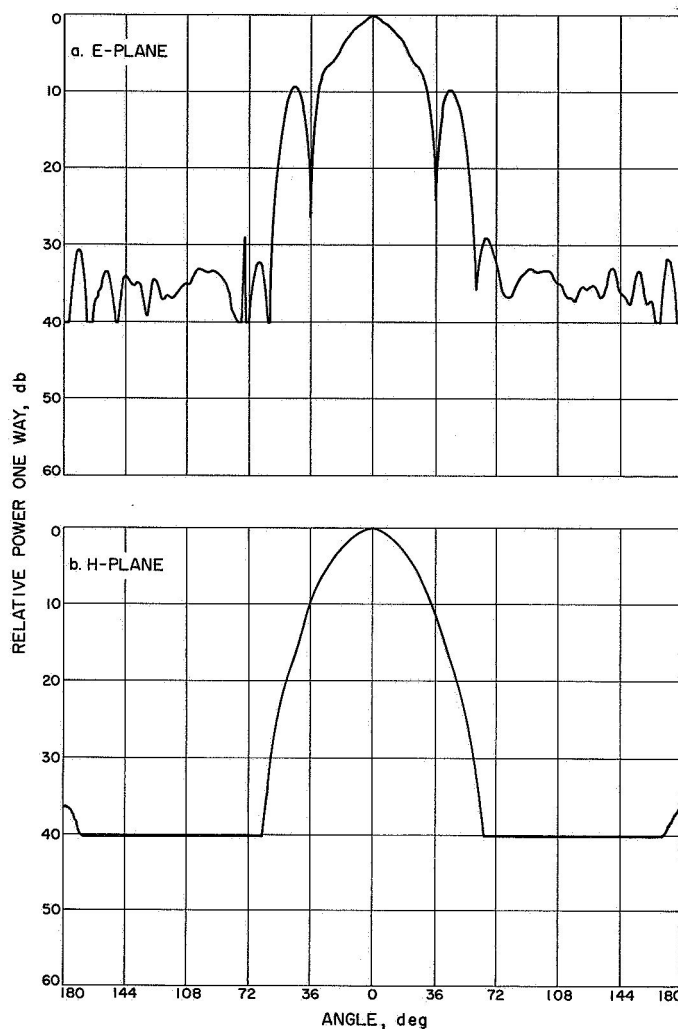


Figure 38. Antenna E- and H-plane patterns

stability 2388-mc mixer and IF amplifier. This equipment is described in RS 36-8. It has also been used for antenna gain and pattern measurements.

An important model of the IF amplifier is under construction utilizing aluminum channel for mechanical rigidity. Figure 39 shows the constructional details and assembled view of the amplifier and a typical mixer section (2388 mc). Various mixers and IF frequency combinations can be obtained. Amplifiers with center frequencies of 10 and 30 mc have been constructed using a cascode input stage followed by four stages of conventional grounded cathode configuration. The tube types used are Western Electric 437A, 417A, 436A, and Amperex 6688, all selected for high reliability and gain stability.

The last three stages of the 30-mc amplifier were stagger-tuned for additional bandwidth. Figure 40 shows

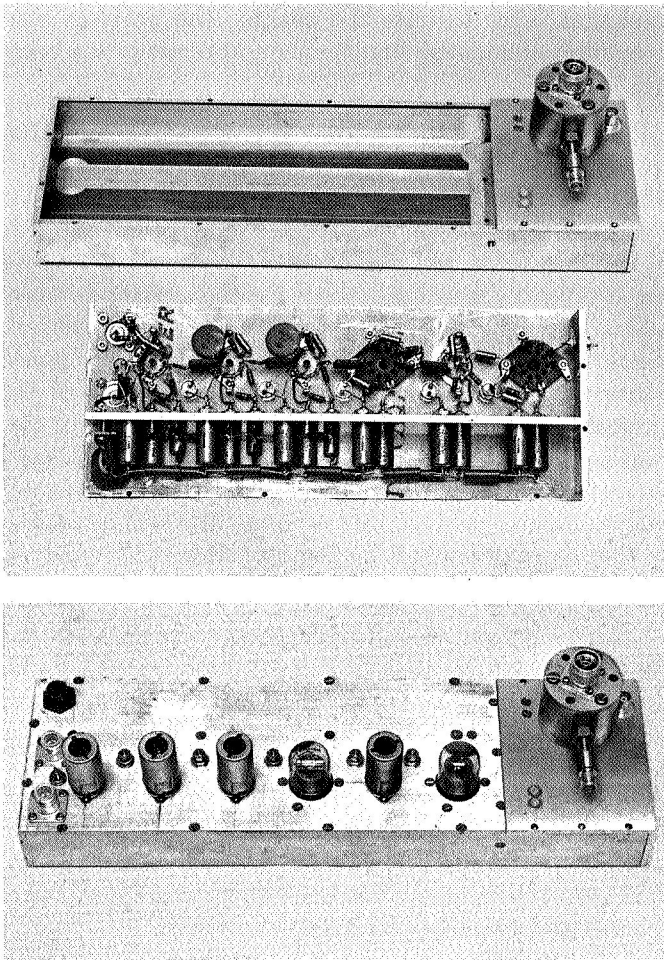


Figure 39. Construction details of 30-mc IF amplifier and typical 2388-mc mixer

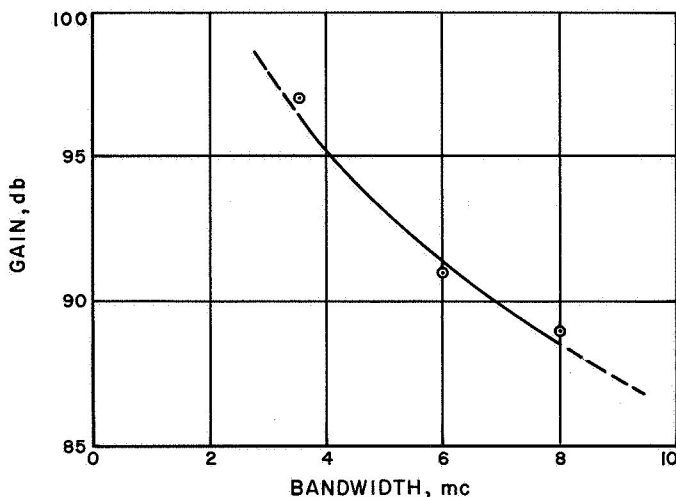


Figure 40. Effect of stagger tuning of 30-mc amplifier on gain

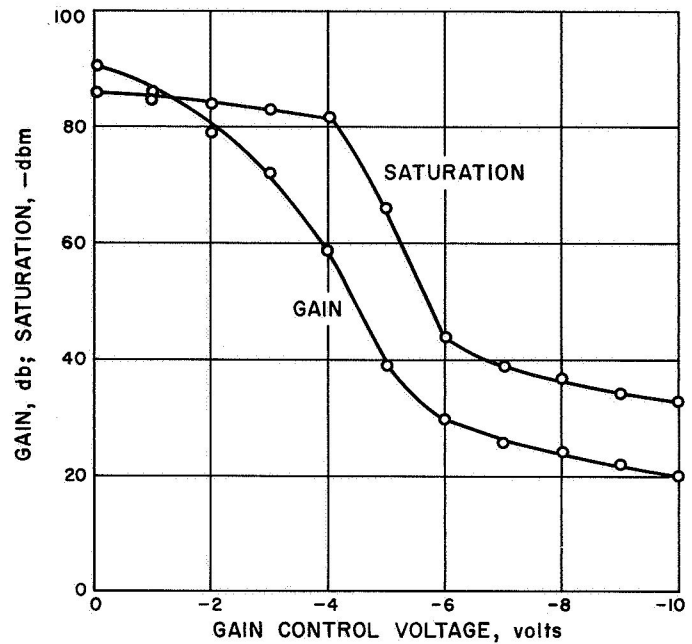


Figure 41. Gain and saturation vs gain-control voltage for 30-mc amplifier

the reduction in amplifier gain with increased bandwidth. Normal operation of this amplifier will probably be at 6-mc bandwidth.

Gain control of the amplifier is obtained by varying the bias voltage to the last three stages. Figure 41 shows a plot of amplifier gain and saturation with input signal level as a function of gain control voltage.

## C. Thin-Film Techniques

J. Maserjian, H. Erpenbach, and R. Frazer

### 1. Thin-Film Single Crystal

The investigation of microzone growing of single crystal films has continued (RS 36-4 to 36-8, TR 34-206). A new electron-visual optical system introduced just prior to the last reporting period has required some modifications in order to provide the desired performance.

Sporadic deflections of the electron beam occurred in the new electron-visual optical system. This effect was attributed to charge accumulation on some insulating material located near the electron beam. Careful cleaning

of the column and apertures was ineffective in reducing the deflections. The stainless tube was then suspected because of the large surface immediately adjacent to the beam; it was, therefore, removed. The tube was replaced by a beam-defining aperture, a lens shield in the hole of the visual objective lens, and a suitable support for the lens (Fig 42). When this failed to eliminate the problem, it was reasoned that a sufficient number of secondary electrons were reaching the objective lens from the target even though the intervening electron lens should trap out most of them. It was calculated that a current of a few  $\mu\mu$ amperes reaching the lens surface might be sufficient to cause the observed deflections. Since the beam current was 6  $\mu$ amp, the argument was considered reasonable. To eliminate this problem, a conducting film of gold about 100 Å thick was deposited on both surfaces of the lens. This thickness permits good transmission of light while providing adequate surface

conductance to dissipate the charge. The problem was completely eliminated after these improvements had been completed.

The pole configuration of the electron lens was modified to optimize the electron optics under the constraints of the existing physical arrangement. According to Liebmann's data (Ref 38), the spherical aberration could become appreciable with improper design. The spherical aberration is given by  $\delta = C_s \alpha^3$ , where  $\delta$  is the deviation in the gaussian image plane,  $C_s$  is the coefficient of spherical aberration determined by the lens, and  $\alpha$  is the angular aperture of the rays at the image point. Values of  $C_s$  increase rapidly with the ratio  $f/(S + D)$ , where  $f$  is the focal length,  $S$  the pole gap, and  $D$  the diameter. Because the focal length is predetermined by the working distance, only the sum  $S + D$  could be adjusted. This was increased to the limit permitted by the existing field winding arrangement (Fig 42).

With the present overall arrangement, at peak intensity the total demagnification of the source is 1/10, giving a final image size of less than 10  $\mu$ . The disk of least confusion due to spherical aberration should be about 2.5  $\mu$  under these conditions. At a sacrifice in beam intensity (increasing condenser lens current), it is possible to obtain greater demagnification and reduced aberration. For example, at 8% maximum intensity, the demagnification is 1/50, giving an image size of less than 2  $\mu$  and the effective aberration is calculated at 1.8  $\mu$ .

Because the available maximum beam power is more than adequate (0.35 watt) and the electron gun can be improved to give considerably better performance (Ref 39), it should be possible to operate at the minimum image size if it proves advantageous.

The previous experimental work on microzone melting indicates that a scanning device is needed in the electron optics. This would permit the zone to scan back and forth, while traversing the film in the perpendicular direction. In this way, it should be possible to microzone-grow over a much wider area of the film and, consequently, permit more reasonable techniques of analysis.

## 2. Niobium Superconducting Thin Films

Work has continued on the problem of depositing thin films of niobium which are superconducting. Since the last report (RS 36-8), thin films of niobium have been deposited on a sapphire substrate by "cathodic sputtering." These films were tested for superconductivity, but the

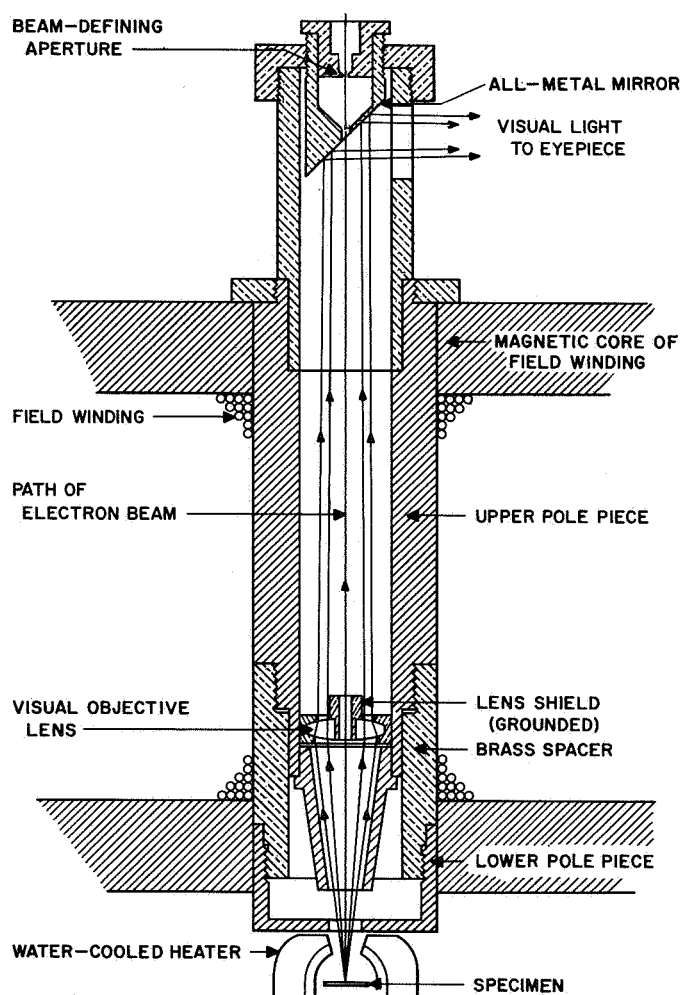


Figure 42. Arrangement of visual electron optics

results were negative. Figure 43 shows the apparatus used for the deposition of the thin films.

When an electrical discharge is passed between the niobium cathode (Fig 43) and the anode at a low gas pressure, the cathode is slowly disintegrated under the bombardment of the ionized gas molecules. The disintegrated material leaves the electrode surface either as free atoms or in chemical combination with the residual gas molecules. Some of the liberated atoms are condensed on surfaces surrounding the cathode, while the remainder are returned to the cathode by collision with gas molecules. Tank argon was used for the sputtering gas; it was introduced through a needle valve to the ionization chamber at a pressure of  $150 \mu$ .

The disintegration rate increases with the atomic weight of the gas; it is greatest with argon and least with helium. Thus, for rapid film deposition and the prevention of undesirable chemical reactions between the sputtered deposit and the residual gas, the sputtering should be carried out in an argon atmosphere.

The deposition rate of niobium for a 1000 Å film was about 5 minutes; the adherence to the substrate was very good. Aside from the fact that the sputtered film was not superconducting (for reasons not yet understood), two unusual differences between a sputtered film and an evaporated one were noted: (1) The electrical

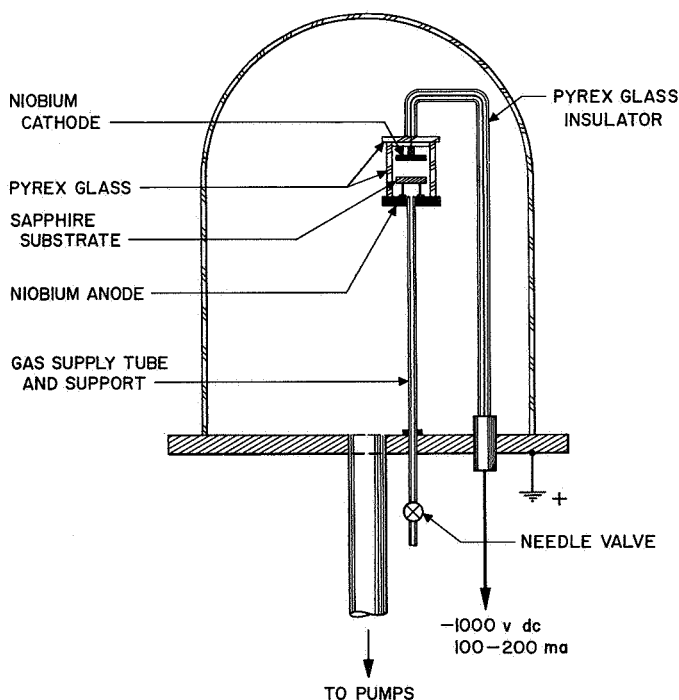


Figure 43. Apparatus for deposition of thin films

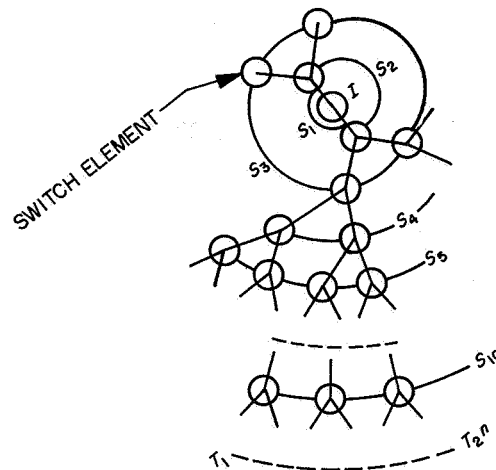


Figure 44. Branching switch array

resistivity of the sputtered film was negative versus temperature change. (2) The resistivity was about twice that of bulk niobium.

### 3. Advanced Digital Techniques

As part of the JPL research activity in coding and communications applicable to space communication, an effort has been initiated to study applications of thin-film device techniques to advanced digital concepts. Known physical phenomena are used to create switching paths necessary to implement boolean algebraic processes. The basic element of such networks is a single-pole double-throw electronic switch capable of operation at rates in excess of 1 mc. To perform the desired range of operations, a branching array terminating in up to  $2^{10}$  (1024) such switch elements is required.

Thin-film deposition techniques seem to offer the greatest promise of achieving the necessary component density with the required reliability. These film techniques also imply the use of stripline interconnections with the possibility of greatly increased speed as a major growth potential.

Initial considerations have served to define a planar geometry as most attractive. The branching nature of the necessary array now serves to further define the geometry as a circle (Fig 44) with the origin at the center and ten concentric rings of switch elements. The  $2^n$  terminations  $T$  occupy the periphery of the disk where they can be most easily interconnected. The only remaining connections are the central input  $I$  and the ten switching bus connections partially shown as  $S_1, S_2, \dots, S_{10}$ .

Various phenomena are under study as possible switching mechanisms. These include but are not yet limited to (1) cryogenic switching and tunneling; (2) field effect, thin film; (3) field emission, by micromachining; (4) photoconductive, coupled to various photon sources, and (5) dielectric tunneling, voltage-induced and photon-induced. The planar geometry and the dictates of thin-

film techniques tend to eliminate several otherwise interesting possibilities based on the Hall effect and on various magneto-optic effects.

In making a decision on which concepts to pursue, emphasis will be placed on simplicity, reliability, growth potential, and minimum associated hardware.



## VI. Communication System Development

### A. Experimental Ranging Transponder

*J. B. Briggs*

Ranging research has been underway for some time, as reported in previous issues of this summary (*RS 36-1* to *36-7*). For the most part, this work has been oriented either toward (1) the general ranging problem, or (2) the mechanization of a ranging ground station. An experimental ranging transponder has now been built for the purpose of investigating the technique and equipment problems associated with the airborne end of a ranging link, including the determination of a desirable block diagram, functional circuits, and proper values for gains and bandwidths. Equally important is the research on coding techniques, ranging code acquisition, and digital mechanization.

A generalized block diagram of a ranging receiver was shown in *RS 36-7*. This receiver uses a balanced-modulator pseudonoise code correlation technique. The ranging transponder to be described here uses essentially that technique. In this report, the RF, or analog, part of the transponder is described.

The main part of the ranging transponder (Fig 45) is the 890/960-mc transponder as used on the *Ranger* spacecraft. This furnishes the basic receiver and transmitter, to which are added the components necessary for coherent detection of the pseudonoise-modulated ranging sub-

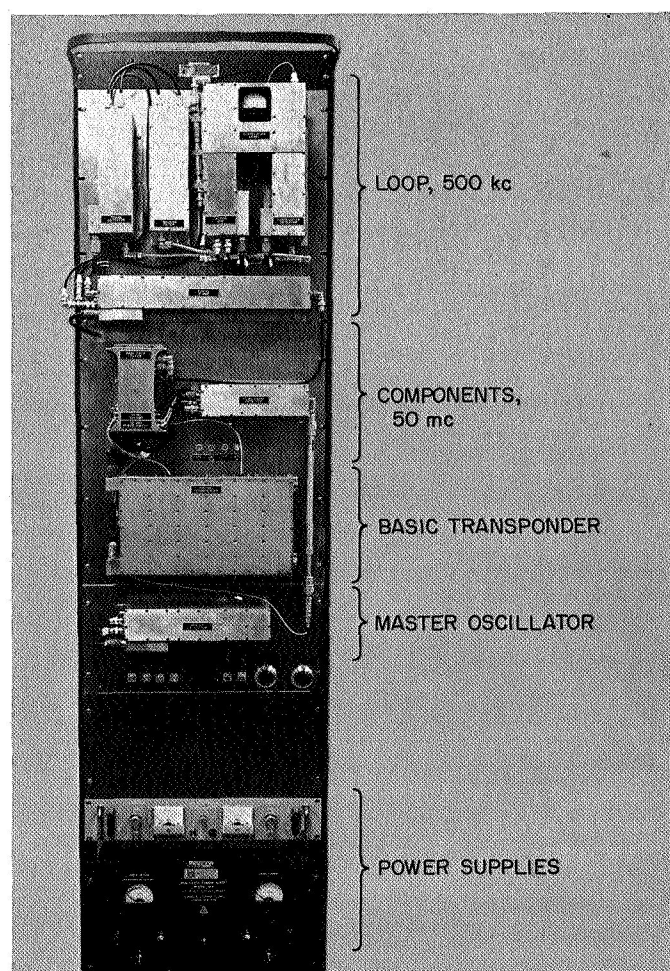


**Figure 45. Experimental ranging transponder**



carrier. The block diagram (Fig 46) shows the blocks which are elements of the basic transponder and also those which were added to adapt it for ranging. The experimental ranging transponder is a laboratory type item; however, many of the modules are essentially the same design as would be used for flight in a spacecraft. This includes all of the modules in the basic transponder and, in addition, the 50-mc isolation amplifier,  $\times 5$  frequency multiplier, and 50-mc phase switch.

The nominal characteristics of the ranging transponder, including those of the basic receiver, are summarized in Table 11. The modulation index is an assumption which is discussed below.

### 1. Changes to Basic Transponder

The basic transponder was modified to provide a signal output to the ranging loop at 50 mc. This output was taken at the last stage of the 50-mc IF amplifier, just ahead of the 10-mc mixer stage. The original transponder provided for AGC of both 50- and 10-mc IF amplifiers. It has been found that the gain variation necessary to accommodate a signal range from  $-50$  to  $-139$  dbm can be attained by providing AGC to the 50-mc amplifier alone, and operating the 10-mc amplifier at fixed gain. Thus, the 500-kc amplifier can also be operated at fixed gain, and the problem of gain and phase tracking between the 10-mc and 500-kc amplifiers is eliminated. With this mode of operation, the 50-mc amplifier gain varies from  $+32$  db at threshold to  $-57$  db at the strong signal condition, and the signal to the ranging loop is maintained at an approximately constant level of  $-97$  dbm.

**Table 11. Experimental ranging transponder characteristics**

Parameter	Units	Value
Receiver input frequency	mc	890.046
Receiver noise figure	db	15
Receiver noise bandwidth ( $2B_{LO}$ )	cps	100
Receiver threshold	dbm	$-139$
Ranging noise bandwidth ( $2B_{LO}$ )	cps	1 or 10
Ranging threshold	dbm	$-139$ or $-129$
Ranging modulation index	radians	0.14
Ranging bandwidth to ranging modulation detector	mc	3.9
Ranging clock frequency	kc	500
Transmitter frequency	mc	960.05
Transmitter output level	dbm	7
Transmitter modulation bandwidth	mc	0 to 5
Transmitter modulation sensitivity	rad/volt	2.0

In order to accomplish synchronous detection of the 500-kc ranging subcarrier, a 50-mc reference is necessary. For this purpose, the transponder was modified to provide an output from the RF frequency divider in the transponder at 10 mc, which is then multiplied by 5 to give the desired reference.

The basic transponder, due to a filter in the 50-mc IF preamplifier, has a signal bandwidth of 1.0 mc. Although this has been adequate for initial, low modulation index experiments, this will not, in general, be true. Therefore, this filter is being removed, which will result in an overall 50-mc bandwidth of 3.9 mc. Thus, no significant sideband power will be lost for any reasonable ranging modulation index.

### 2. Ranging Loop Design

The 50-mc signal from the receiver IF output is taken through the isolation amplifier to the 50-mc phase detector, which detects the phase modulated subcarrier by means of the coherent 50-mc reference. This subcarrier is then tracked by the 500-kc phase locked loop. Signal levels throughout the loop are as shown on the block diagram, Figure 46.

The 50-mc isolation amplifier is essentially the same unit as the 50-mc IF amplifier in the basic transponder. It is needed to provide gain ahead of the 50-mc detector, and also to provide reverse isolation between the 10-mc signal, which is present at the reference side of the ranging 50-mc phase detector, and the input of the 10-mc mixer. The 50-mc amplifier used has 110-db isolation in this direction, thus assuring RF loop stability.

The 50-mc phase detector, 500-kc IF amplifier, phase and correlation detectors, tracking filter, and VCO were formerly CODORAC components, and have been converted for the present use. This entailed minor changes such as retuning and minor component changes for circuit modernization.

The 1400-cps bandpass filter at the input to the 500-kc IF amplifier serves to reduce the noise power accompanying the 500-kc signal, and it thus reduces the signal suppression by the phase detector limiter. It is planned to change the 1400-cps bandwidth to 300 cps, and thus reduce the suppression still further. The gain of the 500-kc amplifier is ordinarily fixed; however, during the testing phase a manual gain control is provided which may be used, if necessary, to accommodate changes in the modulation index.

The ranging loop threshold is dependent upon the loop noise bandwidth and is related to the RF loop threshold

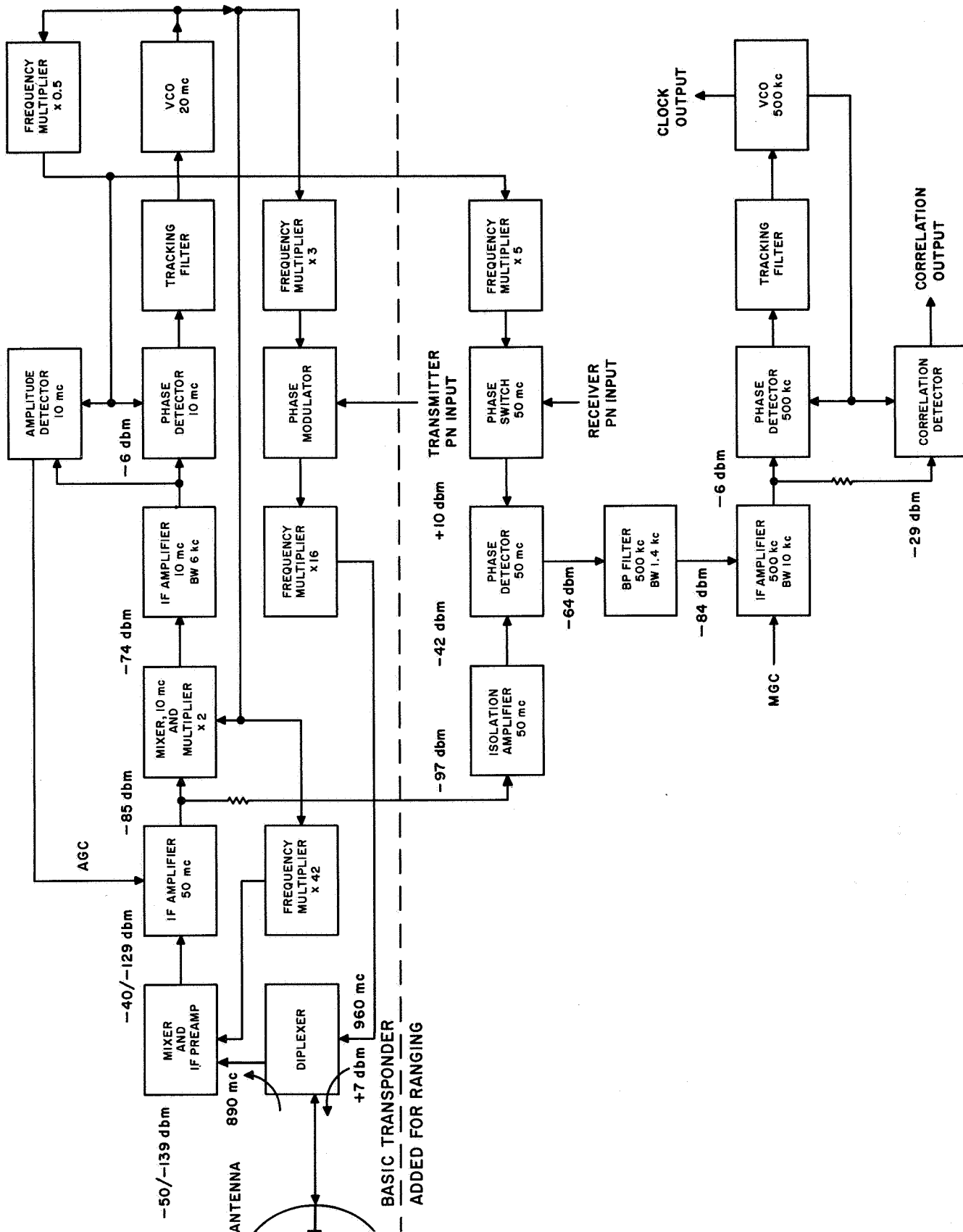


Figure 46. Block diagram of ranging transponder

by the ratio of the ranging sideband power to the RF carrier power and the ratio of the ranging and RF loop bandwidths. Consideration of the doppler rates which might be encountered in some hypothetical deep space ranging experiment suggests that a loop bandwidth ( $2B_{Lo}$ ) of 1 cps would be adequate for tracking purposes (Ref 40). Since the RF loop has a noise bandwidth  $2B_{Lo}$  equal to 100 cps, this represents a noise power reduction of 20 db. Thus, the ranging loop should have a threshold equal to the RF loop if the ranging sideband power were 20 db below the carrier power. This corresponds to a modulation index of 0.14 radian.

A switch has been provided in the tracking filter so that the bandwidth may be changed from 1 cps to 10 cps when this may be desirable for easier acquisition. The threshold is, of course, degraded by 10 db in this mode of operation.

The  $\times 5$  frequency multiplier in the 50-mc phase detector reference line consists of a 10-mc amplifier stage which drives a varicap multiplier. A filter selects the fifth harmonic, at 50 mc. This is then applied to the phase switch, before being used as the phase detector reference. It was convenient to build the  $\times 5$  and phase switch on the same module, as shown in Figure 47. This type of module construction is the same as that used in the basic transponder.

The circuit of the 50-mc phase switch is shown in Figure 48. It is seen to consist of two parallel 50-mc amplifiers with a common load which are driven by signals of opposite phase. The direct-coupled driver amplifiers alternately switch off one 50-mc amplifier and then the other, as controlled by the pseudonoise (PN) ranging code at the PN input, thus producing phase shifts of 0 or  $\pi$  for the binary conditions of zero or one. Figure 49 shows the output waveform and spectrum when driven by a square wave and by a PN code of length 7. The phase switch is seen to be a special case of a balanced modulator which is designed for a binary code input and has modulation input bandwidth extending from dc to about 4 mc.

### 3. Conclusions

The ranging transponder has recently been mated with the digital code generating equipment. Except for some initial minor interface problems, the integration has proceeded smoothly. Both RF and ranging phase lock have been achieved and maintained as the RF signal level was lowered to the nominal threshold value. A strip chart recorder is being used to record ranging loop phase error and correlation output signals, with a PN modulated

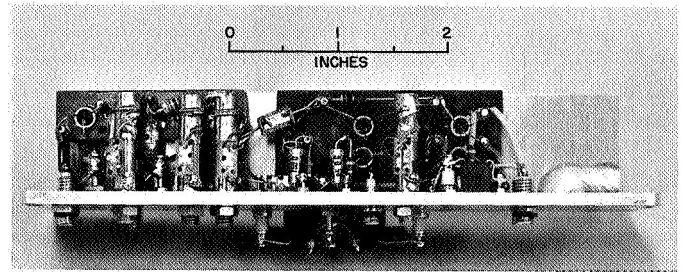


Figure 47. Multiplier  $\times 5$  and phase switch module

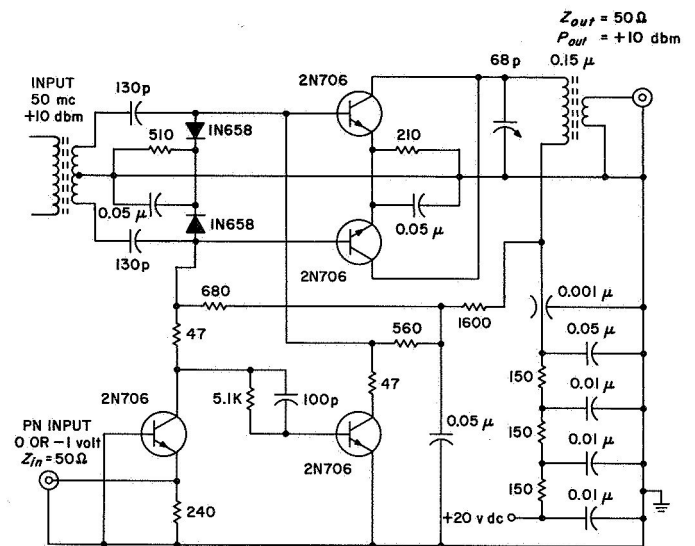


Figure 48. Circuit of phase switch

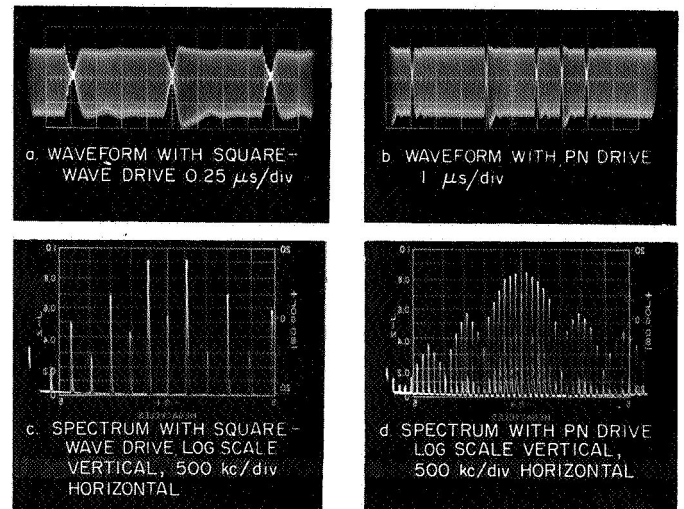


Figure 49. Output waveforms and spectra of phase switch

890-mc signal supplied to the receiver input, and a corresponding PN code driving the phase switch. The signals are then recorded as the relative phase of the two codes is varied. Various code lengths and combinations are being investigated. Experiments to date have consisted of one-way range locks only. However, future plans call for supplying the PN code to the phase modulator in the transmitter and establishing a round-trip lock. This will then allow actual (short distance) range measurements to be made.

## B. Communications Research

C. E. Gilchrist

### 1. Pseudonoise System Lock-In

A class of systems used in the past by JPL and used extensively now in JPL spacecraft communication systems comes under the generic name Pseudonoise Systems. (See RS 36-3, 36-5, 36-6, SPS 37-9 for current usage in spacecraft communication systems.) In the latter usages, the pseudonoise (PN) systems are utilized in obtaining bit and word sync and a phase reference for demodulation. These systems are of the digital type embracing bit-by-bit detection, phase shift keying modulation (PSK), and matched filtering. As in all synchronization schemes, there is an associated lock-in problem which is the subject of this discussion.

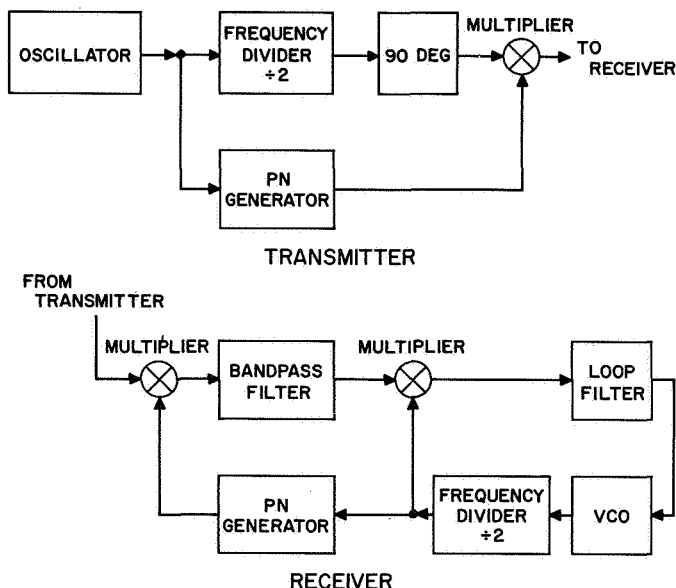


Figure 50. Basic pseudonoise sync system

Figure 50 shows the block diagram of the essential elements of the system to be considered. In determining the lock-in characteristics, the error function of the loop (output of the second multiplier of the receiver section) must be known. Its characteristics are a function of the specific mechanization.

Two mechanizations were considered for this study in which the second multiplier signal channel inputs were sine waves (possibly a limiter followed by a bandpass filter) for Case I and square waves (possibly a limiter only) for Case II. The error functions for these mechanizations are shown in Figure 51. Figure 51a illustrates

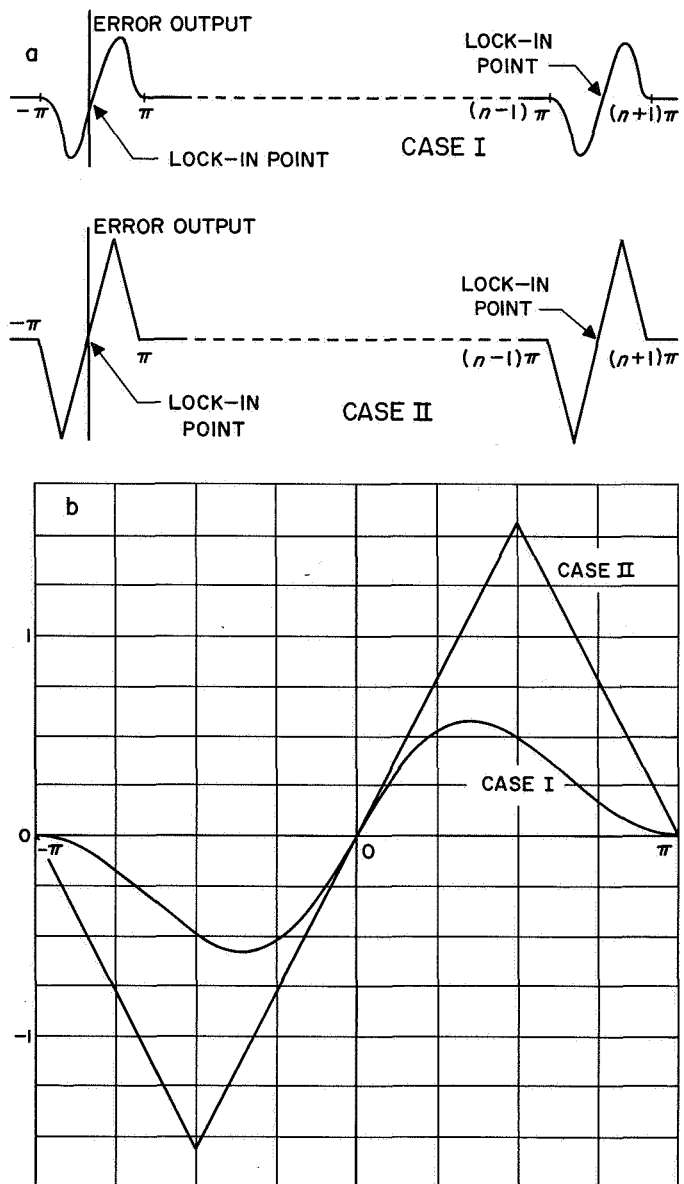
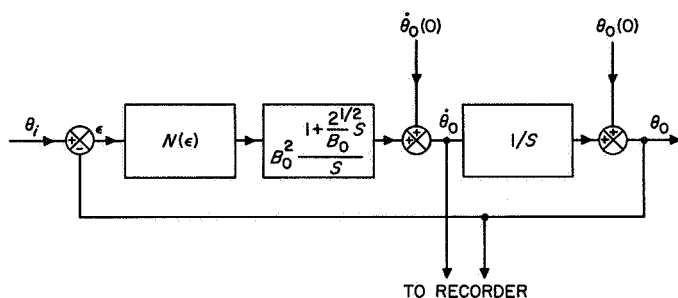


Figure 51. Pseudonoise system error functions

the fact that in between the stable lock-in points the gain is essentially zero, which is not strictly true in that small spurious S-curves can exist in this region.

In order to achieve satisfactory lock-in performance, the following conditions must be satisfied: (1) There must be an initial frequency offset in the VCO to drive the system to a stable point. (2) The frequency offset must



## CASE I

$$\begin{aligned} N(\epsilon) &= K\epsilon, \quad \epsilon < -\pi \\ &= \frac{K}{\pi}(\epsilon + \pi) \sin \epsilon, \quad -\pi \leq \epsilon \leq 0 \\ &= -\frac{K}{\pi}(\epsilon - \pi) \sin \epsilon, \quad 0 \leq \epsilon \leq \pi \\ &= K\epsilon, \quad \pi < \epsilon \end{aligned}$$

## CASE II

$$\begin{aligned} N(\epsilon) &= K\epsilon, \quad \epsilon < -\pi \\ &= -K(\epsilon + \pi), \quad -\pi \leq \epsilon \leq -\frac{\pi}{2} \\ &= K\epsilon, \quad -\frac{\pi}{2} \leq \epsilon \leq \frac{\pi}{2} \\ &= -K(\epsilon - \pi), \quad \frac{\pi}{2} \leq \epsilon \leq \pi \end{aligned}$$

WHERE  $K=10, (10)^{2/3}, (10)^{1/3}, 1, (1/10)^{2/3}, (1/10)^{1/3}, 1/10$  A GAIN FACTOR

$\theta_0(0) = -\pi$  WHEN  $\dot{\theta}_0 > 0$

$\theta_0(0) = \pi$  WHEN  $\dot{\theta}_0 < 0$

$\theta_i = 0$

Figure 52. Pseudonoise system simulation

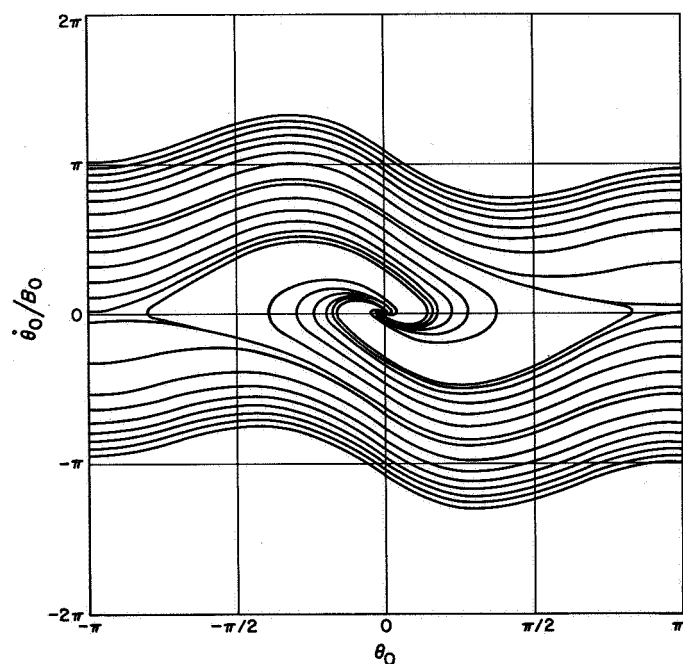


Figure 53. Phase plane plot, unity gain, Case I

be within prescribed limits to keep the search time at a minimum and to arrive at the proper stable point. Practical experience shows that, if the frequency offset is too small, the system could lock up on the spurious S-curves; and if the frequency offset is too large, it would not lock up when it passed through the proper S-curve. Since the values of the offset limits are a function of the loop bandwidth, the variable gain effects of the bandpass limiters under variable S/N conditions must also be con-

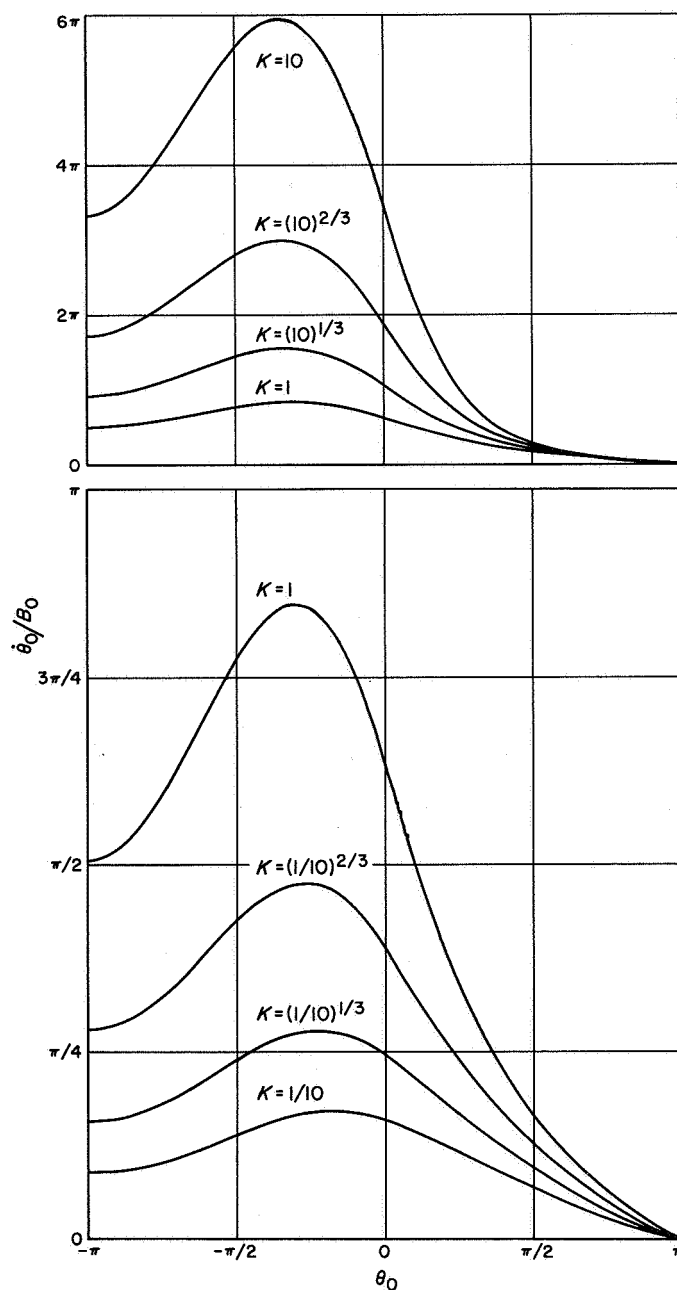


Figure 54. Phase plane plot, critical  $\dot{\theta}/B_0$ , for various gains, Case I

sidered. The estimated maximum allowable offset for phase-locked loops, whose error function is  $\sin \theta$ , as determined experimentally is  $\dot{\theta}_0/B_0 = 6$ , where  $B_0$  is the natural angular frequency (measured in rad/sec) of the loop. This type of loop may utilize several cycles to lock in without appreciably affecting lock-in time, while the pseudonoise systems must lock in upon reaching the first lock-in point or appreciable time is wasted until the next one is reached. These factors indicate that a complete knowledge about the pseudonoise system lock-in is needed. Since explicit solutions of the nonlinear differential equations are difficult, if not impossible, an analog computer simulation program was initiated.

The equivalent system simulated is shown in Figure 52. It should be noted that the variables to be plotted are  $\theta_0$  and  $\dot{\theta}_0$ , which is the familiar phase plane plot (Ref 41). Phase plane plots are much more useful than time plots since the lock-in time is determined largely by the probability of being at any particular  $\theta_0$  when lock-in is initiated and by  $\dot{\theta}_0$ . The gain values  $K$  were chosen as indicated

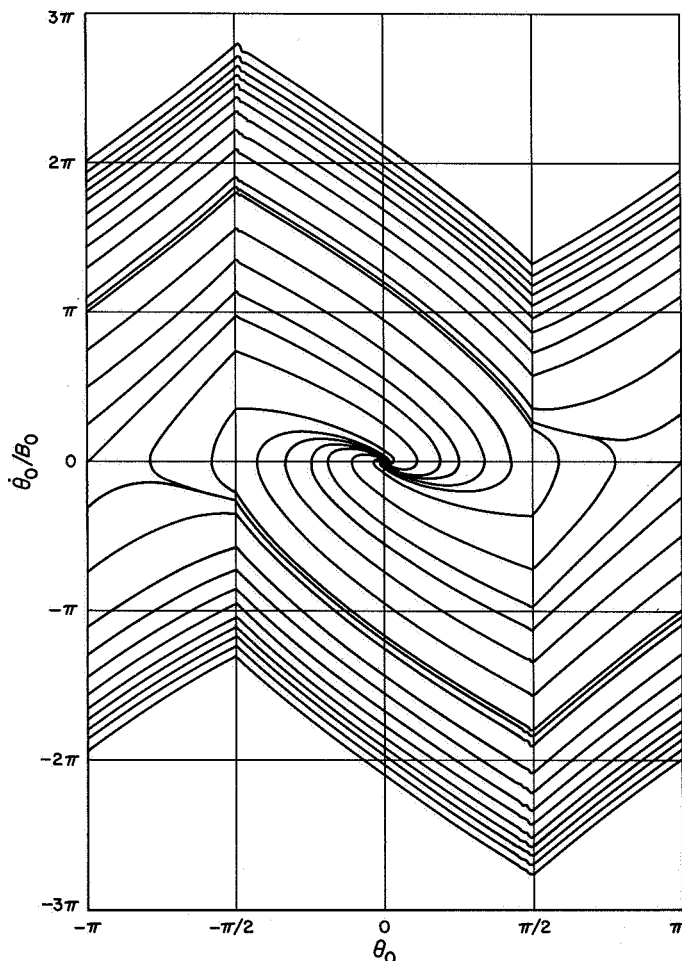


Figure 55. Phase plane plot, unity gain, Case II

because a system would normally be designed so that the bandwidth and transfer function were specified near threshold, where the suppression factor  $\alpha$  due to a bandpass limiter would be less than 1 ( $K$  is taken as 1 at this value of  $\alpha$ ). At high  $S/N$ , the gain  $K$  would then be larger and the system should be studied under these circumstances. On the other hand, the small-gain  $S$ -curves between the wanted lock-in points should also be studied, hence the small values of  $K$ . Only the values of  $K$  between 0.1 and 10 are taken since the simulation problem becomes more difficult for a wider range of values; yet these values are sufficient to determine an empirical law for estimations.

Figure 53 shows the phase plane plot for Case I for which  $K = 1$ . For a particular large value of  $|\dot{\theta}_i(0)/B_0|$ , it should be noticed that the plane is traversed from one side to the other and that the value upon reaching the other side is  $< |\dot{\theta}_i(0)/B_0|$ . This indicates that, although the system does not lock on this passage of the lock point, it tends toward lock. After passing the lock point a finite number of times, it can pass a saddle point (or critical value) at which time it will lock in. For this particular case, the critical value for  $|\dot{\theta}_i(0)/B_0|$  is about  $\pi/2$ . Figure 54 shows only the critical values (obtained by changing the sign of the integrators of the computer and running backward from  $\dot{\theta}_0/B = 0 + \zeta$ ;  $\zeta$  is a small value  $> 0$ ) for various gains (Case I). Figure 55 shows the phase plane plot for Case II for which  $K = 1$ . Similar remarks can be made as in Figure 53. The critical value for this case is about  $\pi$ , or more than twice that of Case I and a value about  $1/2$  that estimated from experience on ordinary locked loops, which means that Case II will be the best system for fastest lock-in. It was also noted that after the system gets into the region of finite gain,  $-\pi < \theta_0 < \pi$ , the system proceeds toward the lock-in point much faster. This is because  $\dot{\theta}_0/B_0$  becomes quite large during this time. Figure 56 shows only the critical values for  $|\dot{\theta}_i(0)/B_0|$  for various gains (Case II). A summary of the critical values of  $|\dot{\theta}_i(0)/B_0|$  is shown in Figure 57. These values follow nearly a 1.78 power law.

Enough knowledge has now been obtained to estimate the values of the offset frequency used to search for the lock-in point. The method is shown in Figure 58. One area is left to study before complete knowledge is obtained. In some mechanizations there are unstable  $S$ -curves of equal magnitude to the proper lock-in points. In the current systems, lock-on to these unstable points has been circumvented by a method called code switching, which inverts their correlation function making them stable points. Further study in this area should be made to complete the knowledge.

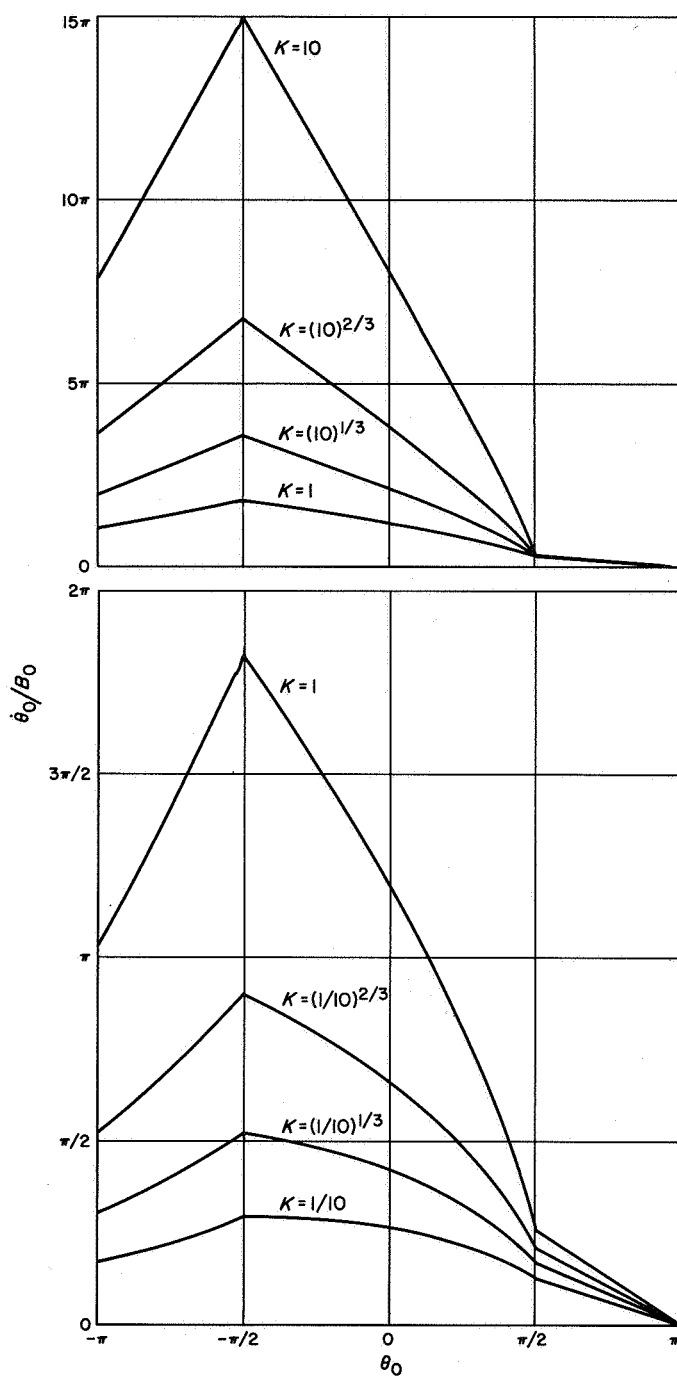


Figure 56. Phase plane plot, critical  $\dot{\theta}/B_0$ , for various gains, Case II

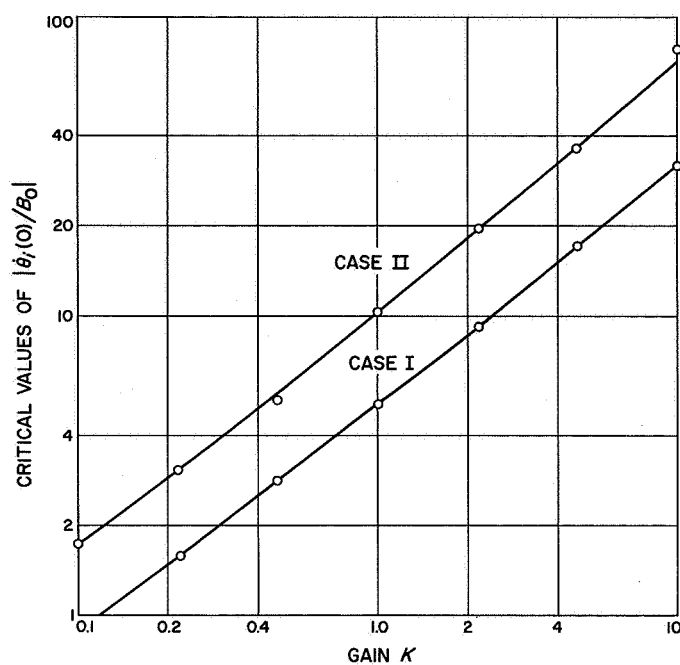


Figure 57. Critical values of  $|\dot{\theta}_i(0)/B_0|$ , for various gains, pseudonoise systems

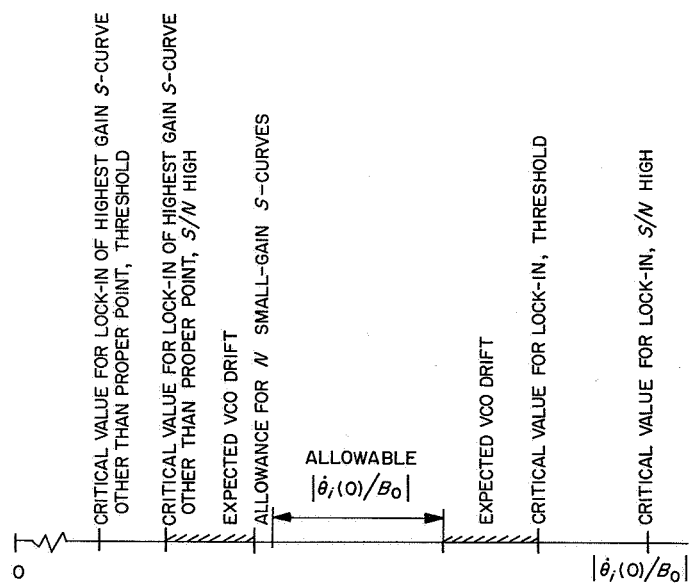


Figure 58. Allowable  $|\dot{\theta}_i(0)/B_0|$  offset frequency, pseudonoise systems

# PHYSICAL SCIENCES DIVISION

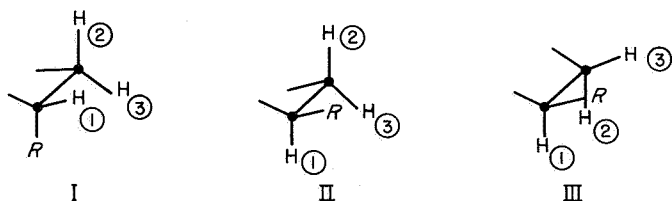
## VII. Chemistry Research

### A. Nuclear Magnetic Spectra for Three-Proton Nuclei

S. L. Manatt

#### 1. Three-Proton Nuclei in Transition from $A_2B$ System to ABC System

Three important three-proton systems whose nuclear magnetic resonance (NMR) spectra have not, in general, been completely analyzed are the following:



These particular conformations occur in many stereochemical and structural problems, especially where these groups of protons are part of a rigid system or a system where rotational conformers can be distinguished.

If  $R$  is an electronegative group, the resonance lines of the 1-proton will be shifted considerably downfield from those of the 2- and 3-protons. This is true if  $R$  is a halogen (F, Cl, Br, I),

or  $-OH$ ,  $-OCR'$ ,  
or  $-OR''$ . There are other groups which will give smaller downfield shifts, such as

or  $-C \equiv N$ ,  $-CR''$ ,  $-aryl$ ,  $-alkyl$   
or  $-COR'''$

For  $sp^3$  bonded systems such as I, II, and III, most of the spectra to date have been analyzed in terms of phenomenological arguments, and the true relationships between the various coupling constants and chemical shifts have not been heeded, especially by organic chemists. In most cases for systems like those described above, the 1-proton was the only proton whose spectral lines could be cleanly accounted for. The true pattern of the spectral lines of the upfield 2- and 3-protons was usually masked by the overlap of the lines from the other protons in the molecule. This results in a complex fingerprint



region. The 1-proton signal at low field is usually observed to be a triplet or a quartet. For the triplet structure, it has been customary to assume that the two coupling constants ( $J_{12}$  and  $J_{13}$ ) between the 2-proton and the other two protons are the same and equal to the triplet spacing (Ref 42). For the quartet structure, the smaller of the two coupling constants has been assumed to be nearly the spacings between either of the outer lines and the adjacent inner line; the larger coupling constant has been assumed to be the distance between either of the outer lines and the second-line over (Ref 42). Using this phenomenological treatment, the 1-proton region of the spectra of several borneol and isborneol derivatives and that of 2 $\beta$ -bromolanostan-3-one were analyzed some time ago (Ref 43). From the triplet structure, one coupling constant in the range 4.5 to 5.8 cps was obtained for the borneol and isborneol derivatives. This would suggest that the conformations of these systems are somewhat different than had heretofore been assumed (Ref 44). If the conformations of those systems were what had been assumed previously, a quartet would have been observed for the 1-proton, and the two coupling constants of about 8.2 and 2.2 cps would have been obtained by the phenomenological treatment described above. Barton (Ref 45) has shown from spectral and chemical studies that the A-ring of 2 $\beta$ -bromolanostan-3-one has a "boat" conformation. It was expected that the two  $\alpha$ -proton would show a quartet structure with two apparent coupling constants of about 8.2 and 2.2 cps (Ref 46). Instead, a triplet structure with separation of about 10.1 cps was observed (Ref 43). This result could not be satisfactorily explained on the basis of Barton's conformational studies (Ref 45).

We have made some theoretical calculations of the NMR spectra for the proton systems I, II, and III which explain the apparently anomalous triplet structures for the one-protons of the compounds discussed above. These molecules are all Type III systems. The calculations were made using the following sets of coupling constants for Systems I, II, and III:

Coupling constant	Type I, cps	Type II, cps	Type III, cps
$J_{12}$	1.7	9.2	8.2
$J_{13}$	1.7	1.7	2.2
$J_{23}$	12.5	12.5	12.5

These coupling constants are taken from the theoretical calculations of the dependence of coupling constants on

angular configuration (Ref 46) and include a number of experimental values from systems of known conformations (Ref 47). For each case, the chemical shifts between the 1-proton and the 2- and 3-protons were varied from 1 to 300 cps, while the chemical shift between the 2- and 3-protons was varied from 0 to 25 cps. The results of these calculations show that in many cases where the chemical shift between the 2- and 3-protons is zero or small (only a few cps), a triplet structure will be observed for the 1-proton. The spacing of this triplet *will not* be the coupling constants  $J_{12}$  and  $J_{13}$ , but the spacing of the two outer lines will equal  $J_{12} + J_{13}$ . The spacing between two adjacent lines will usually be several cps less than the larger of  $J_{12}$  and  $J_{13}$ .

The present theoretical study has shown that extreme caution must be exercised in applying the common phenomenological analysis described above for the analysis of the NMR spectra of quite simple systems where the chemical shift between the proton being observed and the other two protons is of the order of 50 to 300 cps.

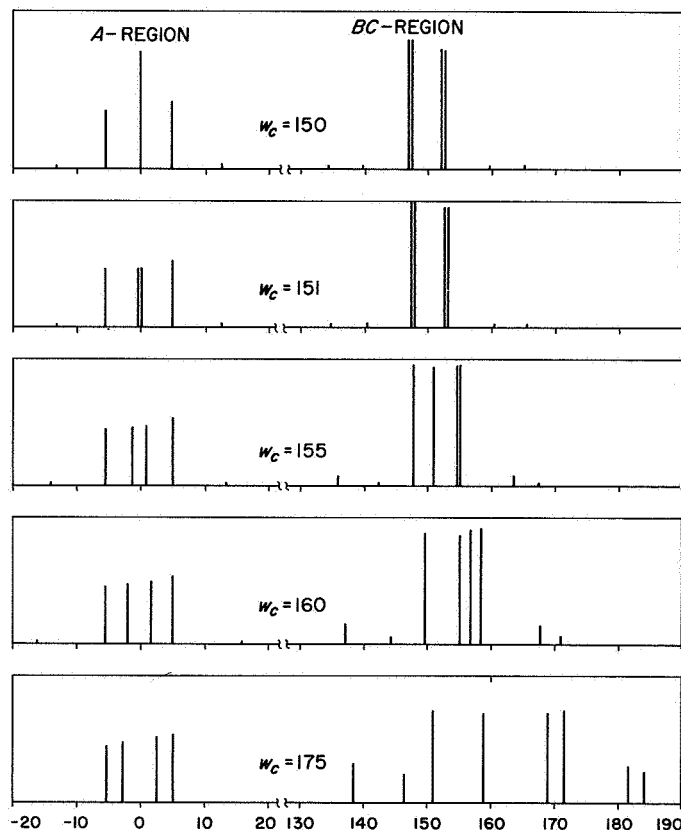


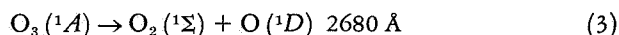
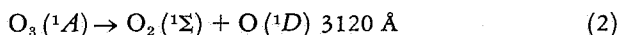
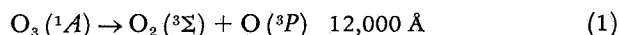
Figure 59. Calculated NMR spectra for ABC system, where  $J_{AB} = 8.20$  cps,  $J_{AC} = 2.20$ ,  $J_{BC} = 12.5$ ;  $w_A = 0.0$  cps,  $w_B = 150.0$

The results from these calculations for one set of parameters for System III are shown in Figure 59; the transition from a triplet structure to a quartet structure is obvious. A more detailed report of these calculations will be given later.

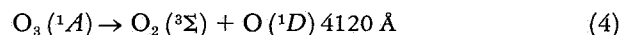
## B. Photolysis of Ozone

W. DeMore and O. F. Raper

Photolysis of ozone may occur by several paths. Those which obey the spin conservation rules are the following, along with the wavelength limits corresponding to the required energies:



According to this scheme, the longest wavelength at which  $\text{O}(^1D)$  may be produced with conservation of spin is 3120 Å. The process



can produce  $\text{O}(^1D)$  at longer wavelengths, but spin is not conserved.

In a previous study (Ref 48), it was shown that oxygen atoms produced by photolysis of ozone at 2537 Å react efficiently with nitrogen, in liquid nitrogen solution, to form nitrous oxide, and that oxygen atoms produced by photolysis of molecular oxygen at 1849 Å react slowly with nitrogen. The interpretation was that the former process involves  $\text{O}(^1D)$  and that the latter involves  $\text{O}(^3P)$ .

It is often assumed that  $\text{O}(^1D)$  is formed in ozone photolysis at all wavelengths in the near ultraviolet below about 3100 Å. If this is the case, then  $\text{N}_2\text{O}$  formation should be observed at all wavelengths in this region, since the reaction



is believed to have zero energy of activation (Ref 49). We have irradiated solutions of ozone in liquid nitrogen at several wavelengths from 2700 to 3130 Å and have found that the quantum yield of  $\text{N}_2\text{O}$  falls sharply near the theoretical limit for Reaction (2).

### 1. Experimental Method

The apparatus, shown in Figure 60, consists of a vacuum-jacketed 1-cm optical cell to contain the ozone-

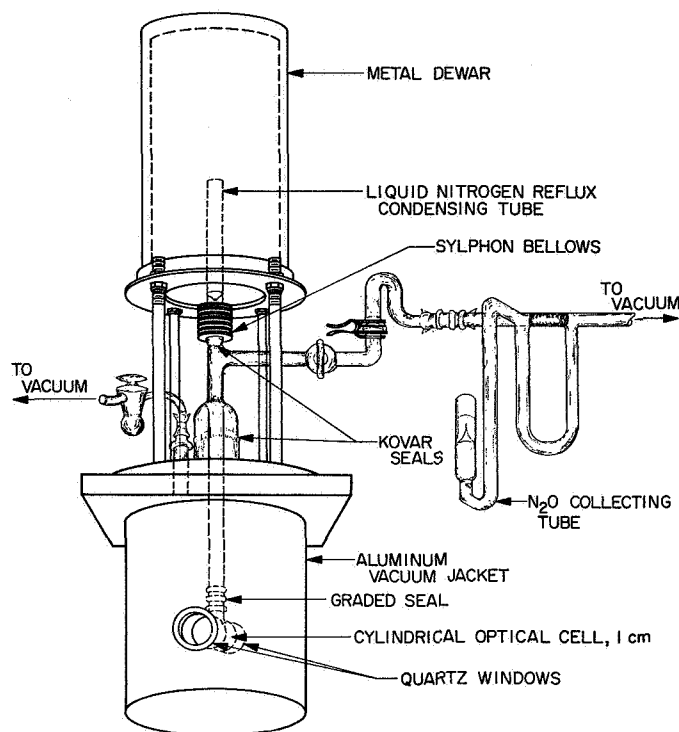


Figure 60. Cell for irradiation of ozone solution in liquid nitrogen

nitrogen solution (approx 0.01 to 0.02 M) with a liquid nitrogen reflux condenser attached above. The solutions were irradiated with light from a Bausch and Lomb Monochromator ( $f/4.4$ , dispersion 33 Å/mm), using a BH6 mercury lamp as source. A slit width of 0.5 mm was used at both entrance and exit slits. The output of the monochromator was measured as a function of wavelength with an Eppley thermopile. The results are shown in Figure 61, along with the bandpass of the monochromator and a typical absorption curve of the ozone solution.

To make a run, ozone is first condensed in the reflux tube, and nitrogen is then admitted under pressure. The nitrogen condenses and falls into the optical cell, washing the ozone down with it. When the cell is full, the apparatus is closed off from the vacuum system. An absorption spectrum of the ozone solution is then taken by placing the apparatus in a Cary Model 11 recording spectrophotometer. The solution is then irradiated for about 4 hours, after which a second absorption spectrum is taken. The apparatus is then returned to the vacuum system. The contents of the optical cell are pumped out, and  $\text{N}_2\text{O}$  is separated and collected by fractionation. The amount of  $\text{N}_2\text{O}$  is determined mass spectrometrically. A quantum yield of  $\text{N}_2\text{O}$  is then calculated, using the data of Figure 61. Although absolute accuracy of the quantum yields is not high, the relative values are accurate within 20%.

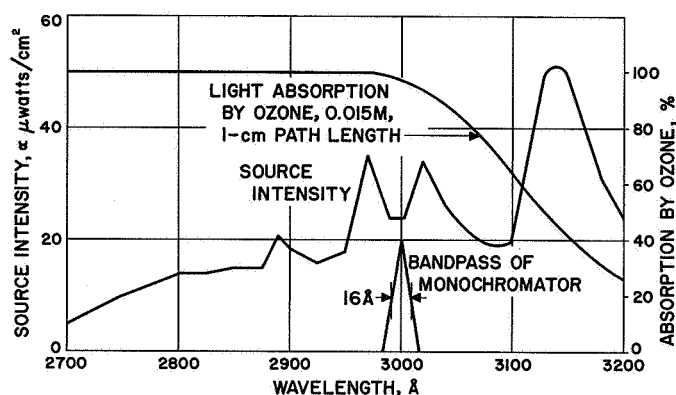


Figure 61. Intensity distribution of light source, bandpass of monochromator, and percentage absorption by ozone

In a typical run, the number of ozone molecules present is about  $5 \times 10^{19}$ , and the number of quanta absorbed is of the order of  $10^{19}$ . However, the quantum yield of ozone dissociation is very low in liquid nitrogen; as a result, the amount of ozone decomposed is less than can be detected within the accuracy of the spectrophotometric analysis.

## 2. Results and Discussion

The quantum yield,  $\Phi$ , for  $N_2O$  formation as a function of wavelength is shown in Figure 62. It is seen to be fairly constant in the region 2700 to 3000 Å, and it falls to a minimum at about 3090 Å. Failure of  $\Phi$  to fall completely to zero may indicate a significant  $O(^1D)$  contribution by the spin forbidden Reaction (4).

The results of this study provide strong evidence that  $O(^1D)$  is produced according to Reaction (2) when ozone

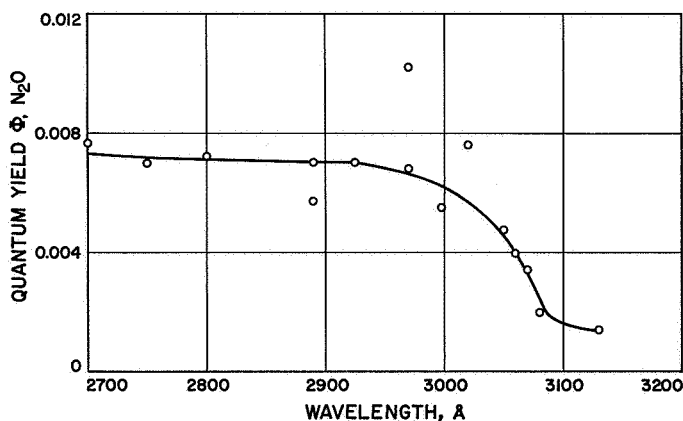


Figure 62. Quantum yield of  $N_2O$  formation

is photolyzed in the region from 2680 to 3120 Å. There appears to be a discrepancy between the observed change in  $\Phi$  and the predicted limit of 3120 Å. This difference, which corresponds to about 1 kcal, may be due to the cage effect, since the probability of recombination of  $O_2$  and  $O$  may be very high when little excess photochemical energy is available to separate them, as is the case near the wavelength limit.

## C. The Use of a Proton-Proton Spin Decoupling Technique for the Determination of NMR Chemical Shifts

S. L. Manatt and D. D. Elleman

In a previous *Summary* (RS 36-8), the audio sideband phase detection method for proton-proton spin decoupling was described. In this report, a new technique is described for the determination of certain proton chemical shifts which were heretofore unattainable; this technique also utilizes the audio sideband phase detection decoupling method.

There are many molecules whose NMR spectra have one proton or a group of equivalent protons which are chemically shifted considerably downfield from most of the other protons or, as is usually the case for only moderately complex molecules, from a complex fingerprint region. Any multiplet structure of the downfield signals can not generally be completely analyzed to give the relevant coupling constants.

In order to spin-decouple two groups of chemically shifted protons, it has been shown (Ref 50) that the following condition must be met:

$$\gamma H_1 > \pi J$$

where  $\gamma$  is the gyromagnetic ratio,  $H_1$  the rotating magnetic RF field, and  $J$  the spin-spin coupling constant in cycles per second. If a resonance signal occurs at frequency  $\nu$  and a weak audio frequency  $\Omega$  (in angular units) is applied to the sweep coils of the spectrometer, the first sidebands will occur at  $\nu \pm \Omega$ , if  $H_1$  is very small. However, for large  $H_1$ , as required in spin decoupling of

two groups of chemically shifted protons, the first sidebands do not occur at  $\nu \pm \Omega$  (Ref 51). If  $\delta$  is the position of the first sidebands (measured in parts per million from the centerband) then

$$\delta = \pm \frac{10^6}{w} (\Omega^2 - \gamma^2 H_1^2)^{1/2}$$

where  $w$  is the resonance frequency of the nuclei ( $w = 2\pi f$ ,  $f$  being the radiofrequency of the spectrometer, i.e., 60 mc.). In the audio sideband phase detection method for proton-proton spin decoupling,  $\delta$  is just the chemical shift between the two groups of protons being decoupled. Since in a decoupling experiment all the parameters on the right side of the expression given above are known, the chemical shift can easily be computed. This technique will be an extremely valuable means for the analysis of the NMR spectra of many molecules where it was heretofore impossible to obtain chemical shift and coupling

constant data between the type of proton groups discussed above.

To test this technique, we have studied the acetaldehyde NMR spectrum at 60 mc. This molecule is simple from an NMR standpoint since it has only two types of protons whose chemical shift can be directly measured. The two types of protons were decoupled; an  $H_1$  was chosen such that  $\gamma H_1 > \pi J$ , and  $\Omega$  was varied until the best singlet structure was obtained for either of the decoupled signals. Figure 63 shows our results. The agreement of the directly measured value and spin-decoupled value of the chemical shift was excellent. This technique was applied to  $\alpha$ -bromocamphor in order to determine the chemical shift between the three- and four-protons. The results are shown in Figure 64.

This new technique will be applied to more complicated systems. We will also determine the smallest chemical shift difference for which this technique will work.

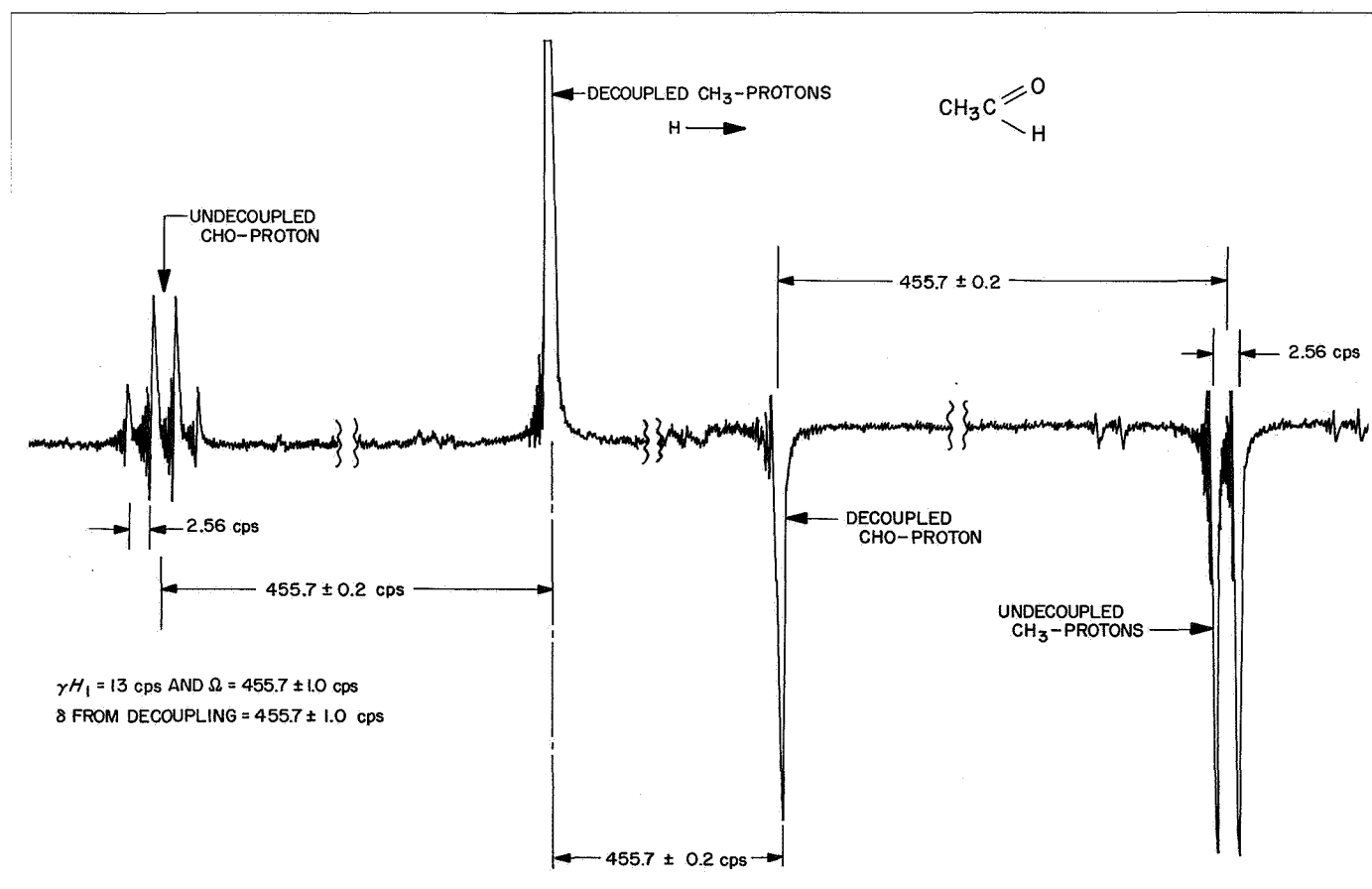


Figure 63. Audio-sideband phase detection proton decoupled NMR spectrum of acetaldehyde at 60 mc;  $J = 2.56$  cps,  $\delta = 455.7 \pm 0.2$ , determined by sideband method

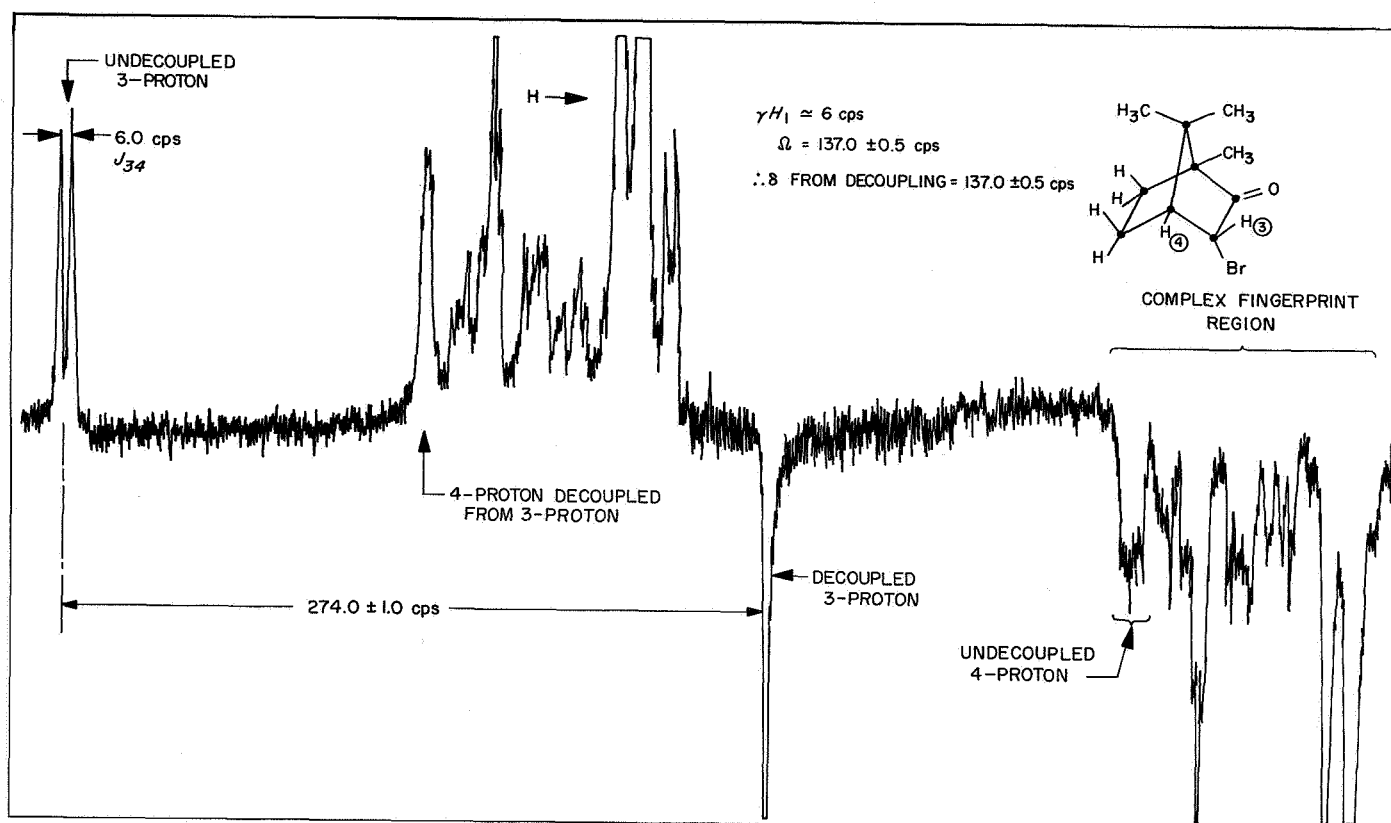


Figure 64. Audio-sideband phase detection proton decoupled NMR spectrum of  $\alpha$ -bromocamphor at 60 mc; spectrum of nearly saturated solution in  $\text{CDCl}_3$

## VIII. Physics Research

### A. Vortex Tube Parameters for Gaseous Fission Reactors

H. Stumpf

#### 1. Introduction

One concept of gaseous core reactors for propulsion employs vortex containment of the fuel, and so allows intimate mixing of the propellant gas and fissionable species. The gas-phase separation may be accomplished by a system of cylindrical cavities in the reactor core, each of which contains a vortex flow field. Since the performance of the system is governed to a large extent by the mass flow rate and the radius and number of these vortex tubes, a simple analysis was carried out to define the range of the variables for which the system performance is attractive. The following simplifications in the analysis were made: (1) The performance calculations were based upon simple "burnout velocities" of single-staged vehicles in vertical, drag-free flight in a constant gravitational field. (2) The gross weight of the vehicle consists of the payload, propellant, tanks, and reactor. (3) The vortex flow is two-dimensional, laminar, and inviscid.

#### 2. Calculations

The performance potential of the system may be obtained in terms of the specific impulse  $I_c$ . If the propellant at stagnation enthalpy  $h_c$  is completely expanded in a de

Laval nozzle, then  $I_c = h_c^{0.5}/g$ . A power balance for the system (Ref 52) then yields

$$(\tilde{I})^3 + \left[ \frac{f + \zeta(1-f)}{\beta} \right] (\tilde{I})^2 - \left( \frac{\beta+1}{\beta} \right) = 0 \quad (1)$$

where  $\tilde{I}$  is the impulse ratio  $I_c/I_s$ ,  $\zeta$  denotes the fraction of the fission energy that appears as nuclear radiation and is attenuated in the solid region,  $f$  is the fraction of the total fission power released in the solid region, and

$$\beta \equiv \frac{\sigma \epsilon_c A_s T_s^4}{\dot{m} h_s} \quad (2)$$

In Equation (2),  $\sigma$  is the Stefan-Boltzmann constant,  $\epsilon_c$  the emissivity,  $\dot{m}$  the propellant mass flow rate, and  $A_s$  the surface area of the vortex tubes.

For a particular mission (velocity increment  $\Delta V$  and payload  $W_{pl}$  known), the weights of the various components and the power level of the system may be computed, starting with Equation (1) and given the radiation parameters  $\beta$  and  $\epsilon_c$ , the vortex tube void fraction  $\chi$ , the regenerative tube void fraction  $\kappa$ , the allowable power density  $p_s$  and allowable temperature  $T_s$  of the solid region, and  $f$ . It is then easy to show (Ref 53) that the vortex tube radius  $r_r$ , the number of vortex tubes  $N_v$ , and the propellant mass flow rate per unit length of vortex tube  $M$  are given by

$$r_r = \frac{2\chi V_R}{A_c} \sim \left( \frac{\epsilon_c}{\beta} \right) \left( \frac{\chi}{1-\chi-\kappa} \right) \quad (3)$$

$$N_v = \frac{A_r}{2\pi l_R I_r} \sim \left(\frac{\beta}{\epsilon_c}\right)^2 \left(\frac{1-\chi-\kappa}{\chi}\right) \left(\frac{P}{l_R I^2}\right) \quad (4)$$

and

$$M = \left(\frac{2}{c_s^2}\right) \left(\frac{P}{l_R N_v I^2}\right) \sim \left(\frac{\epsilon_c}{\beta}\right)^2 \left(\frac{\chi}{1-\chi-\kappa}\right) \quad (5)$$

where  $V_R$  is the reactor volume,  $l_R$  is the length of the reactor,  $P$  is the reactor power, and  $c_s$  is the exhaust velocity corresponding to the solid temperature  $T_s$ .

Relations (3), (4), and (5) have been solved for a series of values of  $f$ ,  $\beta$ ,  $\epsilon_c$ ,  $\chi$ , and  $\kappa$  for an Earth satellite mission and an Earth escape mission. For all the calculations,  $\zeta = 0.1$ ,  $p_s = 1 \text{ kw/cm}^2$ ,  $c_s = 22,400 \text{ ft/sec}$ ,  $T_s = 2000^\circ\text{K}$ , and  $I_s = 700 \text{ seconds}$ .

### 3. Discussion

**a. Vortex tube mass flow rate.** It is clear from Equation (5) that the propellant mass flow rate per unit length of vortex tube depends only on the ratio of the radiation parameters and the cavity-to-solid volume fraction ratio. Fluid dynamic considerations (Ref 54) require that  $M \sim 0.01$  to  $0.02 \text{ lb/ft-sec}$ , if an adequate separation process is to result. From Figure 65a, it can be seen that this implies  $\epsilon_c/\beta \sim 20$  for void fractions of  $\sim 0.1$ , and  $\epsilon_c/\beta \sim 5$  for void fractions of  $\sim 0.6$ . The performance of the system is rapidly degraded as  $\beta$  increases, and past analyses (Ref 55) have shown that for the high acceleration systems a  $\beta$  of  $10^{-2}$  is a reasonable value. This, of course, implies that  $\epsilon_c$  will range from 0.05

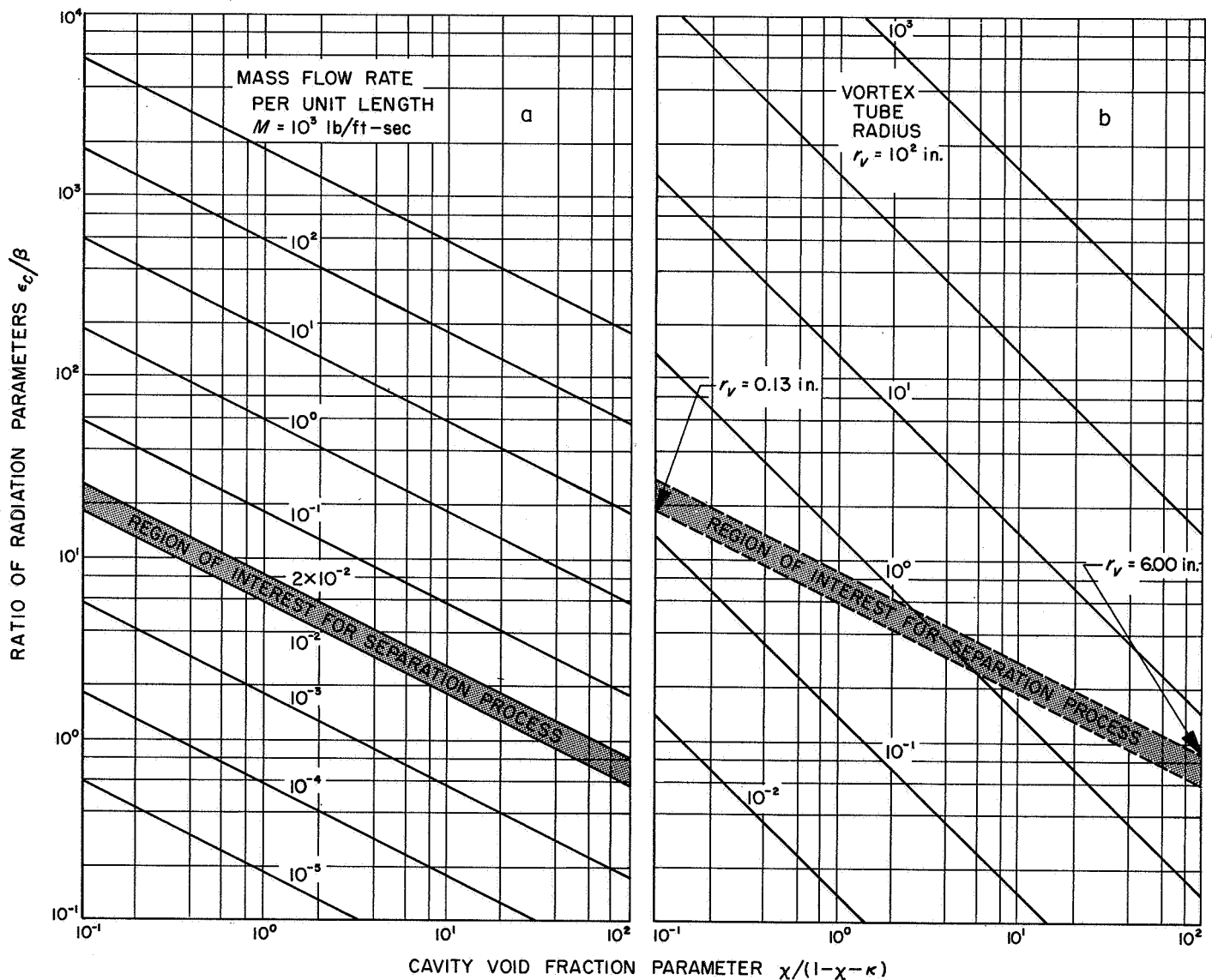


Figure 65. Ratio of radiation parameters vs cavity void fraction parameter

to 0.20. Whether these values of  $\epsilon_c/\beta$  can be achieved without greatly degrading system capabilities is dependent upon the resolution of the thermal radiation problem, that is, the calculation of the numerical value of  $\epsilon_c$ .

**b. Vortex tube radius.** As before, only the radiation parameters and void fractions are important. From Figure 65b, the vortex tube radii  $r_v$  corresponding to the required mass flow rates are in the range 0.25 to 6.00 inches.

**c. Number of vortex tubes.** The parameter  $P/l_r \bar{T}^2$  appearing in the expression for the number of vortex tubes  $N_v$  depends upon the variables  $f$ ,  $\chi$ ,  $\kappa$ , and  $\beta$  in a complex fashion; hence, it is not expected that  $N_v$  can be adequately represented graphically with the two groups of variables

$\epsilon_c/\beta$  and  $\chi/(1-\chi-\kappa)$ . An examination of Figure 66 reveals that (1)  $N_v$  increases as  $\alpha$  increases, the effect being more pronounced for small values of  $\alpha$ ;  $\alpha$  is the ratio of the power generation per unit volume in the solid region to that in the cavity region; and (2)  $N_v$  increases as  $\beta$  increases, the effect being more pronounced at large cavity fractions.

In order to obtain the proper mass flow rates, the required number of vortex tubes will be of the order of 3,000 to 20,000 for the Earth satellite mission and may increase to as much as 100,000 for the higher performance Earth escape mission. It is evident from the curves that small  $\beta$  ( $< 10^{-3}$ ), large cavity fractions ( $\chi > 0.6$ ), and large fractions of fuel in the gas phase ( $\alpha < 1$ ) are

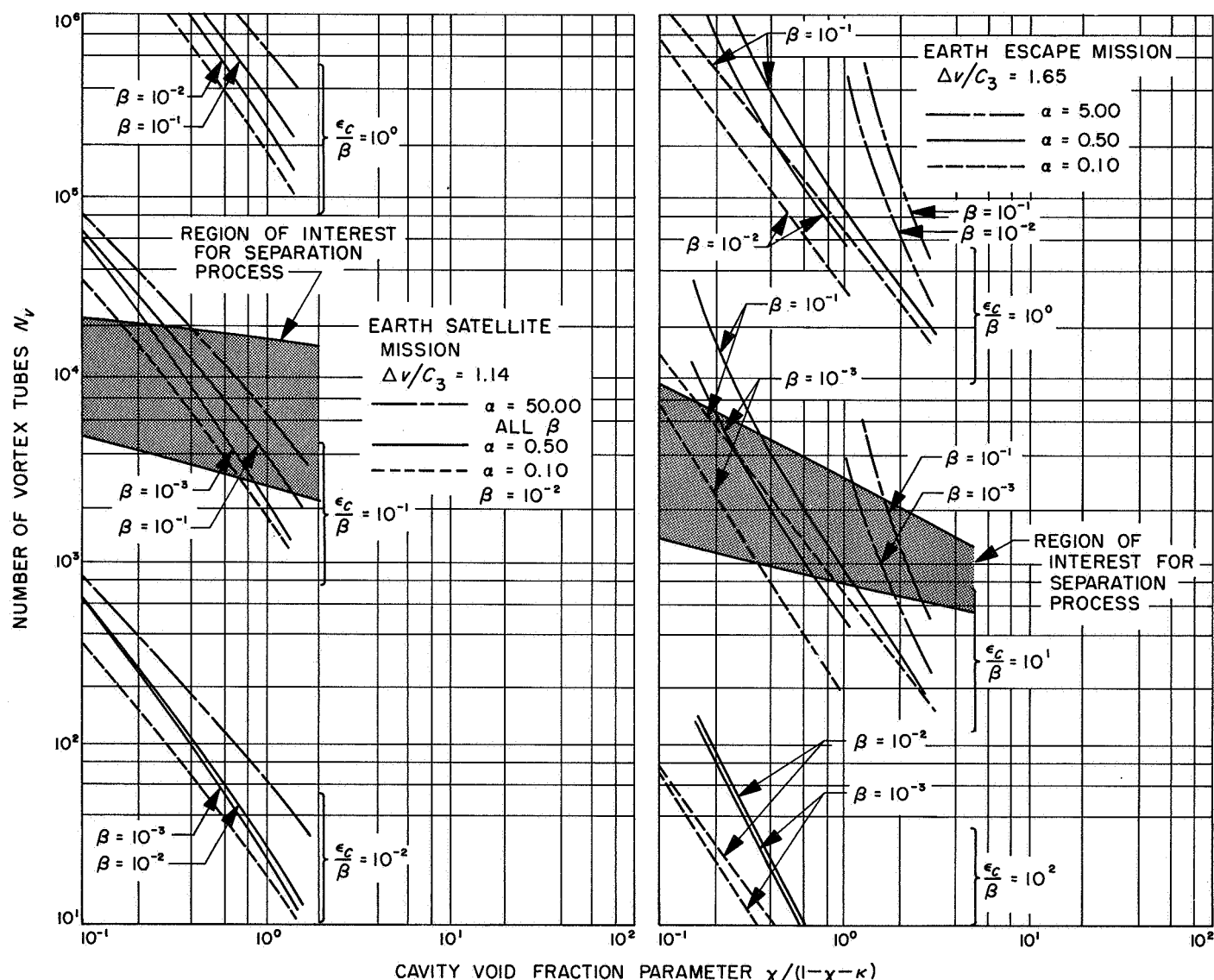


Figure 66. Number of vortex tubes vs cavity void fraction parameter



desirable if the number of vortex tubes is to be substantially decreased. These last two requirements lead to increased reactor volumes.

## B. Electron Exchange Correction to Phonon Dispersion Relation in Metals

O. von Roos

The kinetic equations of the electron-phonon system derived earlier (Ref 56) have been applied to a determination of the sound frequencies in monovalent metals. Particular attention has been devoted to the effect of electron exchange on the screening mechanism between a lattice ion and the surrounding electrons. Contrary to current belief (Ref 57), it is found that electron exchange is not negligible in the long wavelength limit. The physical situation may be pictured as follows. In 0th order, the ions and electrons of the metal are treated as a plasma in which the coulomb forces between electrons and ions are neglected. Of course, the ions interact among themselves. The electrons constitute, therefore, the necessary negative charge background so as to prevent the system from exploding. It can be shown that in the limit of long wavelengths the ions perform longitudinal oscillations with a "bare" phonon frequency  $\omega_1$ , very closely equal to the ionic plasma frequency

$$\omega_p = \left( \frac{4\pi e^2 N}{M} \right)^{0.5}$$

where  $N$  is the density, and  $M$  the mass of an ion. The picture entirely changes when the coulomb forces between electrons and ions are switched on. Then the ions surround themselves with a polarization cloud of electrons, screening takes place, and the coupling constant  $e^2$  is effectively reduced (coupling constant renormalization). The eigen frequencies of the ions go over into the (observable) frequencies of sound, so in the long wavelength limit

$$\omega_1 \rightarrow c_L K$$

where  $c_L$  is the longitudinal velocity of sound, and  $K$  the wave vector. That exchange effects do play a role is now easily understood. In fact, the interaction between adjacent ions is very sensitive to an overlap of the electronic wave functions, and this overlap tends to be suppressed

by the exclusion principle. Hence, it is expected that the velocity of sound will be lowered.

It is not intended here to display the mathematical details of the calculations which confirm the intuitive picture given above; however, the final result will be quoted. The renormalized sound frequency  $\omega$  is connected with the bare phonon frequency  $\omega_1(K)$  in the following way:

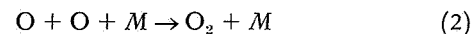
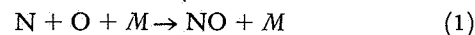
$$\omega^2 = [\omega_1(K)]^2 - \frac{N^2}{mM\omega_p^2} [K^2 \phi(K)]^2 \left\{ 1 - \frac{v_F^2 K^2}{3\omega_p^2} + \frac{K^2}{4k_F^2} \right\} \quad (1)$$

where  $v_F$  and  $k_F$  are the velocity and wave vectors of an electron at the Fermi surface,  $\phi(K)$  is the Fourier transform of the unrenormalized electron-ion interaction energy, and  $\omega_p$  the electronic plasma frequency. The last term within braces is due to exchange. If it is omitted, Equation (1) becomes identical with the dispersion relation of Bardeen and Pines (Ref 57). As an example, numerical calculations show that the exchange correction lowers the velocity of sound (in sodium) by 10%.

## C. Rates of Recombination of Nitrogen and Oxygen Atoms

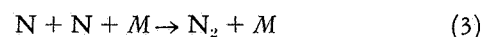
C. A. Barth

Laboratory measurements of the rate coefficients of reactions between the various atomic and molecular species of atmospheric oxygen and nitrogen are of interest in the calculation of the composition of the upper atmosphere of the Earth and other planets. There has been much recent experimental work on the reactions between oxygen atoms, nitrogen atoms, and molecules containing these atoms (Refs 58 to 65). In the present experiment, rate coefficients were measured for the following three-body recombinations:



where the third-body  $M$  was, in this case, molecular nitrogen  $N_2$ .

The experimental technique was essentially a modification of the equipment used by Harteck et al (Ref 60) to measure the three-body recombination of nitrogen atoms.



Nitrogen atoms were produced by pumping nitrogen gas at low pressure through a 2450-mc electrodeless discharge. The afterglow tube where the reaction rates were measured was 4 cm OD and 1 meter long. The pressure in this tube was 5 mm Hg, and the flow velocity was 50 cm/sec. The density of nitrogen atoms at the upstream end of the reaction tube was measured by means of the NO titration (Refs 58 to 60). The nitric oxide flow rate was then adjusted to produce a deep blue afterglow where the number of oxygen atoms present is much greater than the number of nitrogen atoms. The density of nitrogen and oxygen atoms down the tube was determined by measuring the light intensity of the orange afterglow ( $N_2$  first positive bands) and the blue afterglow (NO beta bands). The orange light intensity is proportional to the square of the nitrogen atom density (Ref 66); the blue light intensity is proportional to the product of the nitrogen atom and oxygen atom densities (Ref 67). The ratio of the orange to blue light intensity gives the ratio of nitrogen atom density to oxygen atom density. The atom densities along the tube may be calculated since, at the titration nozzle, the sum of oxygen and nitrogen atoms is equal to the original density of nitrogen atoms that were present before the nitric oxide was added; i.e., to the number of nitrogen atoms measured by the NO titration (RS 36-3).

A set of six differential equations was written describing the reaction rates of Reactions (1), (2), and (3) and six other reactions involving atomic oxygen, atomic nitrogen, molecular oxygen, molecular nitrogen, ozone, nitric oxide, and nitrogen dioxide. The rate coefficients for the latter seven reactions are available in the literature (Refs 58 to 65). The measured atom densities and approximate rate coefficients for Reactions (1) and (2) were substituted into the differential equations, and the set was numerically integrated on an IBM 704 digital computer for the conditions present in the experiment (RS 36-2). An analysis of the computer results led to the following approximate analytical solutions for the nitrogen and oxygen atom densities:

$$\begin{aligned} (N) = & \frac{(N)_0(O)_0(M)(k_2 - k_1)[1 + 2k_2(O)_0(M)t]^{-k_1/k_2}}{(O)_0(M)(k_2 - k_1) + k_3(N)_0(M)\{[1 + 2k_2(O)_0(M)t]^{1-k_1/k_2} - 1\}} \\ & (4) \end{aligned}$$

$$(O) = (O)_0 [1 + 2k_2(O)_0(M)t]^{-1} \quad (5)$$

where  $k_1$ ,  $k_2$ , and  $k_3$  are the rate coefficients for Reactions (1), (2), and (3), respectively;  $(N)_0$  and  $(O)_0$  are the initial atom density,  $(M)$  the third-body density, and  $t$  the time (Ref 68). These equations neglect the effect of diffusion in the direction of the flow stream (Ref 63).

The analysis of data taken for atom concentrations of approximately 0.5%, a pressure of 5 mm Hg, and a flow velocity of 50 cm/sec gave the following rate coefficients:

$$k_1 = 1.6 \times 10^{-32} \text{ cm}^6 \text{ molecule}^{-2} \text{ sec}^{-1}$$

$$k_2 = 8.2 \times 10^{-33} \text{ cm}^6 \text{ molecule}^{-2} \text{ sec}^{-1}$$

The three-body recombination of atomic nitrogen was also remeasured in this apparatus and found to be:

$$k_3 = 7.0 \times 10^{-33} \text{ cm}^6 \text{ molecule}^{-2} \text{ sec}^{-1}$$

For all three coefficients, the third body was molecular nitrogen. The ratio of the coefficients of Reactions (1) and (2) to Reaction (3) should be free of any systematic errors that may have been present in this experiment.

## D. Plasma Theory of the Many-Electron Atom

P. H. Levine

### 1. Introduction

Atoms containing more than one electron are generally treated (in the approximation to the many-body problem in which correlations are neglected) either by the Hartree-Fock method or, in the case of many electrons, by the Thomas-Fermi statistical approach. Within the framework of the neglect of correlations, the Hartree-Fock equations are exact and, consequently, in the limit of infinite atomic number, should approach the Thomas-Fermi equations. The formal connection between the two approaches, which must be established if the Thomas-Fermi equations are to be improved, has therefore been recently under investigation by several authors (Refs 69 to 72). These investigations have traditionally involved quasi-classical approximations to the Dirac density matrix obtained from the Hartree-Fock equations, although recently a more ambitious program based on the Schwinger Green's Function formalism has been published (Ref 72). In this note, we outline a new approach to the problem which is felt to have the advantage of analytical simplicity and physical lucidity. This approach is based on the observation by von Roos (Ref 73) that the Hartree-Fock equations are formally equivalent to a new equation (to be exhibited later) for a certain quantum-mechanical phase space density function,  $\tilde{F}(\mathbf{r}, \mathbf{v})$ . The equation determining  $\tilde{F}$  becomes, in the classical limit ( $\hbar \rightarrow 0$ ), just the "collisionless" Boltzmann equation or the

Vlasov equation familiar to plasma physicists, so that  $\tilde{F}$  approaches the classical phase space density function. This correspondence allows us to view the Hartree-Fock equations as the extreme quantum limit of the von Roos quantum equation and, consequently, to treat many-electron atoms just as we would a plasma, only using the von Roos equation in place of the Vlasov equation. The difference is more than semantic for the following two reasons: (1) The simple Thomas-Fermi atom is, in fact, a classical plasma of particles obeying Fermi statistics; consequently, in correcting the Thomas-Fermi equation, we *begin* at the classical end. (2) The von Roos equation is of a form which admits a natural expansion of  $\tilde{F}$  in powers of  $\hbar$ ; it has the further advantage over the more commonly used Wigner density (Ref 74) that exchange is included in a tractable fashion. In view of (1), it is perhaps not surprising that the method should be far simpler than those which begin at the quantum extreme of the Hartree-Fock equation.

## 2. Classical Plasma

We begin by treating the steady-state problem of a classical plasma of  $N$  identical particles of charge  $-|e|$  and mass  $m$ , which interact electrostatically with each other and with a fixed-point charge  $Z|e|$ . We assume further that the total energy of the system is negative, so that we have a bound system.

In the usual fashion, we ignore correlations (i.e., "collisions") at first and require that the singlet time-independent phase space density function,  $F_0(\mathbf{r}, \mathbf{v})$ , satisfy the Vlasov equation:

$$\mathbf{v} \cdot \nabla_{\mathbf{r}} F_0(\mathbf{r}, \mathbf{v}) - \frac{1}{m} \nabla_{\mathbf{r}} U_0 \cdot \nabla_{\mathbf{v}} F_0(\mathbf{r}, \mathbf{v}) = 0 \quad (1)$$

where

$$U_0 = -\frac{Ze^2}{r} + \left(\frac{N-1}{N}\right) e^2 \phi_0 \quad (2)$$

and

$$\begin{aligned} \nabla_{\mathbf{r}}^2 \phi_0 &= -4\pi \int d^3v F_0(\mathbf{r}, \mathbf{v}) \\ \iint d^3r d^3v F_0 &\equiv N \end{aligned} \quad (3)$$

If we restrict ourselves to zero total angular momentum, it is clear that  $F_0$ , a scalar, can only be a function of the three variables:

$$\mathbf{r} \cdot \mathbf{r}, \mathbf{r} \cdot \mathbf{v}, \mathbf{v} \cdot \mathbf{v}$$

Consequently, Equation (1) has two independent characteristics which turn out to be the energy and the magnitude of the orbital angular momentum. That is, the general solution to (1) is any functional of the form

$$F_0 = F_0 \left[ \frac{1}{2} m v^2 + U_0(\mathbf{r}); |\mathbf{r} \times \mathbf{v}| \right] \quad (4)$$

Since we ultimately will want that  $F_0$  which corresponds to the lowest energy of the system at a given temperature, it is clear that  $F_0$  must be spherically symmetric in  $\mathbf{v}$  space. We, therefore, suppress the dependence on  $|\mathbf{r} \times \mathbf{v}|$ . Thus, any distribution function of the form

$$F_0 = F_0 \left[ \frac{1}{2} m v^2 + U_0(r) \right] \equiv F_0(\epsilon) \quad (5)$$

will satisfy the Vlasov Equations (1) to (3), and correspond to minimum energy (ground state) at a given temperature.

Again, in the usual fashion, the otherwise neglected "collision" term of the Boltzmann equation (corresponding to the neglect of correlations) is now taken into account by choosing that  $F_0$  of the set (5) which maximizes the entropy; consistent, of course, with the statistics of the particle. We choose Fermi statistics, so that

$$F_0(\epsilon) = 2 \left( \frac{m}{h} \right)^3 \left[ \exp \left( \frac{\epsilon + \lambda}{KT} \right) + 1 \right]^{-1} \quad (6)$$

Introducing (6) into Equations (1) to (3) yields the Thomas-Fermi equations generalized to arbitrary temperature in a natural fashion.

## 3. Quantum Plasma

To proceed further, we wish to compute corrections to  $F_0$  due to quantum *mechanics* (as opposed to the quantum *statistics* which is introduced at the start). We, therefore replace Equations (1) to (3) by the von Roos equation (Ref 73) for  $\tilde{F}$  (of which  $F_0$  is the classical limit), which can be written in the form:

$$\begin{aligned} \mathbf{v} \cdot \nabla_{\mathbf{r}} \tilde{F} - \frac{1}{m} \nabla_{\mathbf{r}} U \cdot \nabla_{\mathbf{v}} \tilde{F} &= \frac{i\hbar}{2m} \\ &\times \left[ \nabla_{\mathbf{r}}^2 \tilde{F} - \frac{1}{m} \sum_{n=0}^{\infty} \left( -\frac{i\hbar}{m} \right)^n \frac{2}{(n+2)!} (\nabla_{\mathbf{r}} \cdot \nabla_{\mathbf{v}})^{n+2} U \tilde{F} \right] \\ &+ \frac{ie^2(N-1)\hbar}{2m^2} \int d^3l e^{i\mathbf{l} \cdot \mathbf{v}} \tilde{f}(\mathbf{r}, \mathbf{l}) \left[ \frac{1}{l} \tilde{F} \left( \mathbf{r} + \frac{\hbar}{m} \mathbf{l}, \mathbf{v} \right) \right. \\ &\left. - \frac{P}{2\pi^2} \int \frac{d^3v'}{|\mathbf{v} - \mathbf{v}'|^2} \tilde{F} \left( \mathbf{r} + \frac{\hbar}{m} \mathbf{l}, \mathbf{v}' \right) \right] \end{aligned} \quad (7)$$

$$U = -\frac{Ze^2}{r} + \left(\frac{N-1}{N}\right) e^2 \phi \quad (8)$$

$$\nabla_r^2 \phi = -4\pi \int d^3v \widetilde{F}(\mathbf{r}, \mathbf{v}) \quad (9)$$

where the notation is defined in von Roos' paper (Ref 73). The second term on the right of (7) is the effect of exchange. The first term generates the "inhomogeneity" corrections. We now expand  $\widetilde{F}$  and  $U$  powers of  $\hbar$ :

$$\begin{aligned} \widetilde{F} &\equiv \sum_{n=0}^{\infty} \hbar^n F_n \\ U &\equiv \sum_{n=0}^{\infty} \hbar^n U_n \end{aligned} \quad (10)$$

and match coefficients of similar powers of  $\hbar$  on both sides of (7). The 0th order equation is just the Vlasov equation for  $F_0$ , Equations (1) to (3). The equation for  $F_1$  is

$$\begin{aligned} \mathbf{v} \cdot \nabla_r F_1 - \frac{1}{m} \nabla_r U_0 \cdot \nabla_v F_1 = \\ \frac{i}{2m} \left[ \nabla_r^2 F_0 - \frac{1}{m} (\nabla_r \cdot \nabla_v)^2 U_0 F_0 \right] \end{aligned} \quad (11)$$

which has the immediate solution:

$$F_1 = -\frac{i}{2m} \nabla_r \cdot \nabla_v F_0 \quad (12)$$

and carrying through the program one step further, one finds  $F_2$  after a mild amount of algebra:

$$\begin{aligned} F_2 = U_2 \frac{dF_0}{d\epsilon} - \frac{1}{4m} (\nabla^2 U_0) \frac{d^2 F_0}{d\epsilon^2} - \frac{1}{6} \left\{ \left( \frac{d^2 U_0}{dr^2} - \frac{1}{r} \frac{dU_0}{dr} \right) \left( \frac{\mathbf{v} \cdot \mathbf{r}}{r} \right)^2 \right. \\ \left. + \frac{1}{r} \frac{dU_0}{dr} v^2 + \frac{1}{m} \left( \frac{dU_0}{dr} \right)^2 \right\} \frac{d^3 F_0}{d\epsilon^3} - \frac{1}{8} \left( \frac{\mathbf{v} \cdot \mathbf{r}}{r} \right)^2 \left( \frac{dU_0}{dr} \right)^2 \frac{d^4 F_0}{d\epsilon^4} \\ - \frac{2\pi e^2 (N-1)}{m^2 N} \frac{dF_0}{d\epsilon} \int \frac{d^3 v'}{|\mathbf{v} - \mathbf{v}'|^2} F_0(\mathbf{r}, \mathbf{v}') \end{aligned} \quad (13)$$

The spatial density  $\rho$  is recovered from  $\widetilde{F}$  by integration over velocity space. Carrying this out, we find that the

first corrections  $\rho_2$  and  $U_2$  to the Thomas-Fermi density and potential are of order  $\hbar^2$  and are given by:

$$\begin{aligned} \rho_2 = \pi \left( \frac{2}{m} \right)^{3/2} \int_0^\infty \frac{dw}{w^{0.5}} \left[ -U_2 F_0(w + U_0) \right. \\ \left. + \frac{\nabla_r^2 U_0}{12m} F_0'(w + U_0) + \frac{1}{24m} \left( \frac{dU_0}{dr} \right)^2 F_0''(w + U_0) \right] \\ \left. + \frac{8\pi^3 e^2 (N-1)}{m^2 N} \left[ \int_0^\infty \frac{dw}{w^{0.5}} F_0(w + U_0) \right]^2 \right] \end{aligned} \quad (14)$$

$$\nabla_r^2 U_2 = -4\pi \rho_2 \left( \frac{N-1}{N} \right) e^2$$

where  $F_0$  is defined in Equation (6), and primes indicate differentiation of  $F_0$  with reference to its argument. If we pass to the limit of zero temperature, Equation (14) reduces to that found by Kompaneets and Pavlovskii (Ref 70). The advantage of the present approach is that the result (14), which is valid at any temperature, was obtained without additional effort. A more detailed exposition of this work, as well as its extension to the case of an atom (or ion) with non-zero total angular momentum will be published later.

#### 4. Conclusions

The plasma theory of many-electron atoms leads in a straightforward and relatively painless fashion to the quantum and exchange corrections to the Thomas-Fermi model at arbitrary temperatures. Aside from the generalization to non-zero total angular momentum and perhaps an extension to include spin-orbit forces, it appears that the "correlationless" Thomas-Fermi model has been pushed to the limit. The inclusion of correlations will be a difficult task since they first appear in the 0th order equation. That is, one must first be able to handle correlations in a classical inhomogeneous plasma, a problem which is still unsolved.

It should finally be mentioned in this summary, that the Thomas-Fermi model finds application in several fields of more than theoretical interest, such as in calculations of the state of matter at extreme pressures, in the medium energy electron physics of gases, and (generally) in all problems related to the gross features of many-electron atoms.

## IX. Gas Dynamics Research

### Laminar Boundary Layer on a Disk in a Rotating Flow

*L. Mack*

The experimental work of J. M. Kendall (Ref 75) on the vortex chamber has demonstrated the importance of the secondary-flow boundary layer that develops on the closed end wall of the chamber. The inward pressure gradient of the rotating flow, acting on fluid of reduced velocity near the end wall, causes an inward radial flow. The mass carried by this inward flow must eventually be discharged in some manner back into the main flow. The question of interest is whether this discharge takes place in a smooth manner over a considerable portion of the end wall or whether there is a sudden eruption of the boundary layer near the center, similar to separation.

In order to investigate this question theoretically, the laminar boundary layer on a finite stationary disk above which the fluid is in rotation has been studied by means of the Kármán-Pohlhausen momentum-integral method. The boundary layer is considered to start at the edge of the disk with zero thickness and with the flow direction tangential. It is subject to the pressure gradient of a specified external flow.

There are two important limiting cases for this problem. In the first, the outer fluid is in solid-body rotation

( $w_\infty \sim r$ , where  $w_\infty$  is the tangential velocity of the external flow, and  $r$  is the radius), and in the second, it is in free-vortex motion ( $w_\infty \sim 1/r$ ). The first case has been treated by Schultz-Grunow (Ref 76), and the second by Taylor (Ref 77) and Cooke (Ref 78). All three authors used the momentum-integral method. Schultz-Grunow solved the resultant two first-order ordinary differential equations by a four-term power series that is valid only near the edge of the disk. Taylor and Cooke both integrated the equations numerically.

The experiments have shown that the external velocity over a large portion of the disk can be approximated by  $w_\infty \sim 1/r^n$ , where  $n \approx 0.75$ . Therefore, it was necessary to generalize the preceding analyses to cover this type of flow. Both Schultz-Grunow and Taylor used essentially the method developed by von Kármán for the turbulent boundary layer on a rotating disk with stationary outer flow (Ref 79). In this method, the compatibility condition at the wall,

$$\frac{dp}{dr} = \mu \frac{\partial^2 u}{\partial z^2} \quad (1)$$

is not satisfied. In Equation (1),  $p$  is the pressure,  $\mu$  the viscosity coefficient,  $u$  the radial velocity,  $r$  the radius, and  $z$  the coordinate normal to the disk. The two unknowns for the two momentum equations are the boundary-layer thickness  $\delta(r)$ , and the amplitude function of the radial velocity  $E(r)$ . Actually, the radial and

tangential velocities reach their free-stream values at different distances from the disk and, consequently, there are two boundary-layer thicknesses. Cooke used these two thicknesses as his two unknowns and was, therefore, able to satisfy Equation (1). However, in the Pohlhausen method it is not certain whether or not this boundary condition should be satisfied. To ignore it removes one of the chief influences of the pressure gradient on the flow, but to satisfy it tends to overly restrict the type of solution possible. In view of this uncertainty, the method of Taylor was selected on the basis of its simplicity.

The laminar boundary layer equations for an incompressible fluid in cylindrical coordinates with axial symmetry are

$$u \frac{\partial u}{\partial r} + v \frac{\partial u}{\partial z} - \frac{\omega^2}{r} = -\frac{\omega_\infty^2}{r} + \nu \frac{\partial^2 u}{\partial z^2} \quad (2)$$

$$u \frac{\partial w}{\partial r} + v \frac{\partial w}{\partial z} + \frac{uw}{r} = \nu \frac{\partial^2 w}{\partial z^2} \quad (3)$$

$$\frac{\partial}{\partial r}(ru) + \frac{\partial}{\partial z}(rv) = 0 \quad (4)$$

where  $v$  is the velocity in the  $z$  direction, and  $\nu$  is the kinematic viscosity coefficient ( $\mu/\rho$ ). The subscript  $\infty$  refers to the specified outer flow, which is here considered to be of the form

$$w_\infty = w_0 \left( \frac{r_0}{r} \right)^n \quad (5)$$

where the subscript 0 refers to conditions at the edge of the disk.

The radial and tangential velocities are written in the form

$$u = w_0 \left( \frac{r_0}{r} \right)^n E(r) f(\xi) \quad (6)$$

$$w = w_0 \left( \frac{r_0}{r} \right)^n \phi(\xi) \quad (7)$$

where  $\xi$  is the dimensionless variable  $z/\delta(r)$ . The quantity  $E(r)$  in addition to its meaning as the amplitude function of  $u$  is also related to the direction of the limiting streamline at the surface of the disk. The functions  $f(\xi)$  and  $\phi(\xi)$  are polynomials which are determined by the boundary conditions applied to the velocity profiles at the disk surface and the edge of the boundary layer.

If now the dimensionless variables

$$u^* = u/w_0, w^* = w/w_0, r^* = r/r_0, \delta^* = \delta(\omega_0/r_0 \nu)^{0.5}$$

and  $\xi$  are introduced, and Equations (2), (3), and (4) are integrated in the usual manner from  $z = 0$  to  $z = \delta$ , the

following two ordinary differential equations are obtained for the variables  $E^2$  and  $E\delta^{*2}$ .

$$\frac{dE^2}{dr^*} = 2[n - (1-n)(1-B)] \frac{E^2}{r^*} - 2 \frac{A}{r^*} - 2(C-D) \frac{E^2}{E\delta^{*2}} r^{*n} \quad (8)$$

$$\begin{aligned} \frac{d(E\delta^{*2})}{dr^*} = & -[n + (1-n)(3B-1)] \frac{E\delta^{*2}}{r^*} \\ & + \frac{A}{r^*} \frac{E\delta^{*2}}{E^*} + (C-3D)r^{*n} \end{aligned} \quad (9)$$

The quantities  $A$ ,  $B$ ,  $C$ , and  $D$  are velocity-profile constants given by

$$\begin{aligned} A &= \frac{1 - \int_0^1 \phi^2 d\xi}{\int_0^1 f^2 d\xi}, \quad B = \frac{2 \int_0^1 f\phi' d\xi - \int_0^1 f d\xi}{\int_0^1 f\phi d\xi - \int_0^1 f d\xi} \\ C &= \frac{f'(0)}{\int_0^1 f^2 d\xi}, \quad D = \frac{\phi'(0)}{\int_0^1 f\phi d\xi - \int_0^1 f d\xi} \end{aligned} \quad (10)$$

The initial conditions are  $E^2 = 0$ ,  $E\delta^{*2} = 0$ . The variables  $E^2$  and  $E\delta^{*2}$  were chosen in order to have finite derivatives at  $r^* = 1$ . As Schultz-Grunow first pointed out, near  $r^* = 1$ ,  $\delta^* \sim (1-r^*)^{1/4}$  and  $E \sim (1-r^*)^{1/2}$ .

The quantity of primary interest is the radial mass flow,  $m$ , as a function of  $r$ . The radius where  $m$  reaches its maximum, if any, is the radius where mass is first ejected from the boundary layer. The mass flow in dimensionless form, and in terms of  $E$  and  $\delta^*$ , is given by

$$M = \frac{m(\omega_0 r_0/\nu)^{0.5}}{2\pi\rho r_0^2 w_0} = E\delta^{*1-n} \int_0^1 f d\xi \quad (11)$$

The IBM 7090 computer was used to solve Equations (8) and (9) by the Runge-Kutta method from  $r^* = 1$  to  $r^* = 0.001$ . The program was set up for arbitrary  $f(\xi)$ ,  $\phi(\xi)$ , and  $n$ . In addition to  $E$  and  $\delta^*$ , the mass flow, outflow velocity, and torque were also computed. The computations were performed for eleven different combinations of  $f(\xi)$  and  $\phi(\xi)$  and for various values of  $n$ . All of the profiles satisfied the boundary conditions  $u = w = 0$  at  $z = 0$ , and  $u = 0$ ,  $w = w_\infty$  at  $z = \delta$ . Other boundary conditions satisfied were  $u'' = 0$  at  $z = 0$ , and first, second, and third derivatives of  $u$  and  $w$  equal to zero at  $z = \delta$ .

As is usual with the momentum-integral method, large numerical differences were obtained with the different degree polynomials for  $f(\xi)$  and  $\phi(\xi)$ . The magnitude of  $\delta$  and quantities proportional to it increased with increases in the degree of the polynomials. Although there is no

exact solution available with which to compare the results, Stewartson (Ref 80) has given an exact solution valid near  $r^* = 1$ . By comparing the momentum-integral results with this solution it was found that the profiles used by Taylor provide the closest agreement. These profiles are

$$f(\xi) = \xi - 2\xi^2 + \xi^3 \quad (12)$$

$$\phi(\xi) = 2\xi - \xi^2 \quad (13)$$

which satisfy the boundary conditions  $u = 0$ ,  $w = 0$  at  $z = 0$ , and  $u = 0$ ,  $u' = 0$ ;  $w = w_\infty$ ,  $w' = 0$  at  $z = \delta$ .

In Figure 67 are shown the mass-flow results obtained for these profiles for various values of  $n$ . For  $n = 1$  (free-vortex), the maximum of  $M$  occurs at  $r^* = 0$ , and there is inflow over the entire disk. However, for  $n < 1$ , there is always a maximum away from the origin which moves gradually outward until for  $n = -1$  (solid-body rotation) it is at  $r^* = 0.72$ , so that there is outflow over half the area of the disk. For the experimentally observed tangential velocity distribution ( $n = 0.75$ ), the maximum is at  $r^* = 0.45$ . Therefore, the question posed at the start of the investigation has been answered. Mass is ejected smoothly from the boundary layer over a considerable portion of the disk and not by a sudden eruption of the boundary layer close to the origin. This result is in accord with the experimental findings of Kendall.

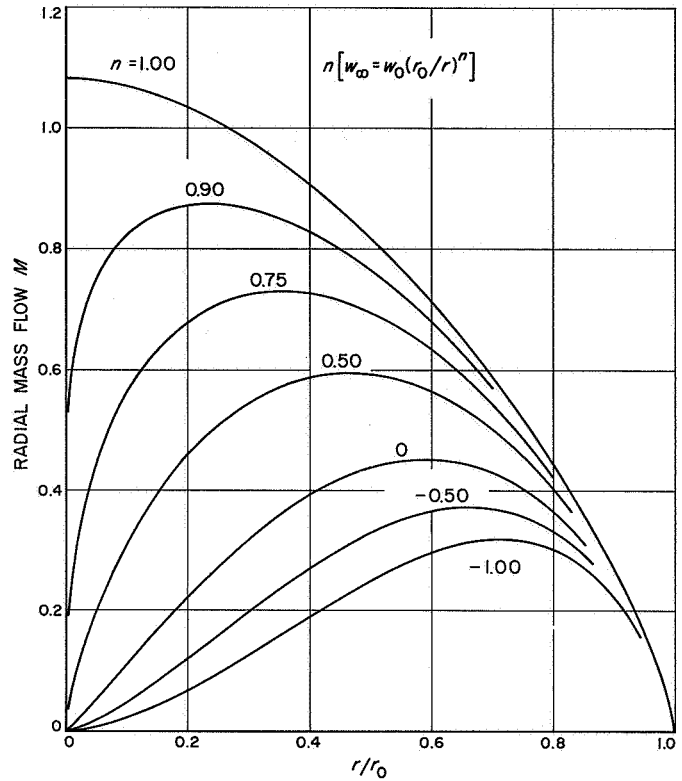


Figure 67. Radial mass flow distribution for different values of external tangential velocity parameter

# ENGINEERING MECHANICS DIVISION

## X. Materials Research

### A. Ceramics

M. H. Leipold

#### 1. Thermal Conductivity of Magnesium Oxide

The investigation of heat transfer mechanisms in refractory oxides by means of thermal conductivity measurements, described previously in RS-6 and RS 36-2, has continued. To clarify the subsequent analysis of the data, a brief review will be given of the pertinent theories of thermal conductivity as applied to this material.

Magnesium oxide belongs to the class of insulating solids in which thermal conductivity is attributed to the movement of phonons through the crystal lattice, otherwise known as lattice conductivity. Debye (Ref 81) and later Peierls (Ref 82) developed the theory for this phenomenon, in which they state that the thermal conductivity  $k$  is proportional to  $C_v V l_p$ , where  $C_v$  is the specific heat per unit volume,  $V$  the phonon velocity, and  $l_p$  the mean free path of the phonons. For solid insulators at temperatures above the Debye temperature, only  $l_p$  varies markedly with temperature and bears the relationship  $l_p \propto 1/T$ , where  $T$  is the absolute temperature. Thus,

according to this theory, at temperatures above 200°C the thermal conductivity for solid MgO varies as the reciprocal of the absolute temperature; or conversely, thermal resistivity is proportional to the absolute temperature.

Experimentally (Refs 83, 84), in this type of solid, this relationship is found to exist until temperatures of 1200 to 1500°C are reached. In this range, thermal resistivity begins to deviate from that predicted by theory, showing a less-than-proportional rate of increase with temperature. From the magnitude of the deviation of observed thermal resistivity from theoretical resistivity, an additional mechanism of thermal conduction may be postulated. Kingery and others (Refs 84, 85) have suggested a mechanism based on the transmission of energy by radiation. Their analysis, supported by limited data, concludes that the transfer of energy by radiation in an insulating solid should vary as the third power of absolute temperature.

During this investigation, sufficient data for an analysis of heat transfer mechanisms have been obtained on porous specimens of MgO of a composition designated as FPM-1. The composition and purity data are given



in Table 12. The specimens were fabricated by cold-pressing at 30 kpsi, drilling sight holes, and firing to 1510°C in air for 3 hours. A 6% addition of chemically pure  $\text{MgCl}_2$  water solution (density = 1.2 gm/cc) was used as a binder.

Photomicrographs of the MgO body as-sintered and after ten heatings to temperatures up to 1700°C showed no apparent change in microstructure (Fig 68). The typical structures exhibited in these photomicrographs contain torn-out areas resulting from mechanical polishing. This is apparently due to the relatively low cohesion of the material. For this reason, a careful structure analysis in terms of grain size and pore size and shape has not been undertaken.

Thermal conductivity data for this material under 1 atmosphere of argon have been obtained on each of four specimens of composition FPM-1. The specimen numbers and densities, along with the number of runs for each and the total number of data points obtained during these runs, are listed in Table 13. In all cases, data were obtained and reduced using procedures outlined in RS-6 and RS 36-5.

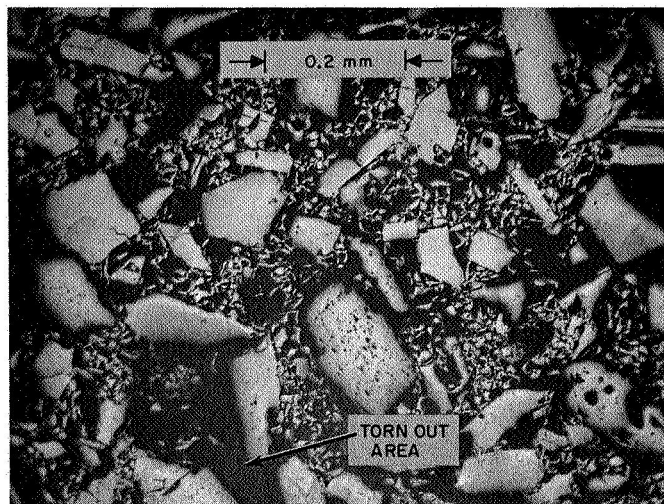
The thermal conductivity data are presented in Figure 69. These curves represent smooth approximations to the large number of data points obtained. The standard deviations of the actual data points are given in Table 13. This approximate standard deviation was obtained by the following method. All the data points for each specimen were enclosed by two curves drawn parallel to the smooth approximation. From this envelope, a range was obtained and, by using a statistical conversion factor (Ref 86), the standard deviation was approximated.

Note that, in Figure 69, the data for specimen MS-18 are slightly anomalous although the specimen is of the same composition as the others. A slightly lower value of density as given in Table 13 does not appear to be sufficient to cause the observed difference in thermal conductivity. However, it is felt that the difference in thermal

**Table 12. Composition of FPM-1 MgO thermal conductivity specimens**

Material	Quantity, wt %	Purity, wt %	Grain size
Fused MgO	45	99.0	—40 +60 mesh
Fused MgO	15	99.0	—80 +100 mesh
Fused MgO	35	98.5	—325 mesh
Precipitated MgO	5	99.5	0.02 —0.03 $\mu$

**a. AS SINTERED**



**b. AFTER TEN HEATINGS TO 1700°C**

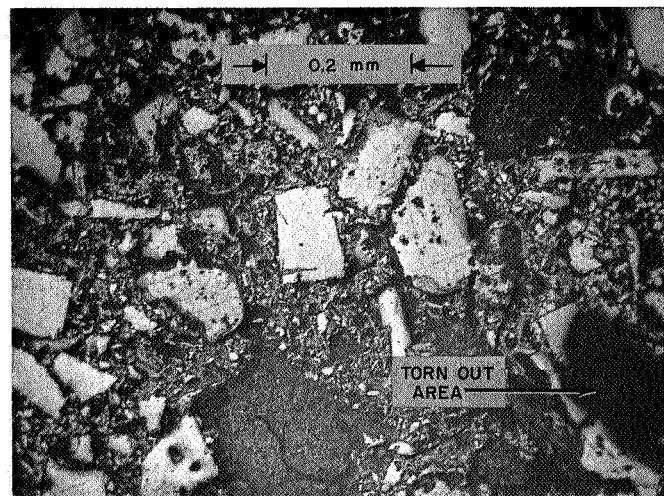


**Figure 68. Microstructure of FPM-1 magnesium oxide specimen MS-7**

conductivity and density both arise from the same unknown fabrication variable. However, since the data follow a smooth curve and no inherent error was noted in the testing procedure, the data are included in the investigation of heat transfer mechanisms.

The data in Figure 69, when plotted as thermal resistivity vs temperature, indicate that the deviation of thermal resistivity from that calculated from lattice conductivity as discussed previously becomes significant at approximately 1300°C. To ascertain the applicability of the radiant mechanism as proposed by Kingery and others, the deviation in thermal resistivity

$$\Delta R = R_{\text{lattice}} - R_{\text{exp}}$$

**Table 13. Summary of determination on FPM-1 MgO composition**

Specimen No.	Apparent density, <sup>a</sup> gm/cc	No. of runs	No. of data points	Std deviation cal/cm sec °C × 10 <sup>-3</sup>
MS-6	2.88	3	14	± 0.70
MS-7	2.90	4	14	± 0.73
MS-8	2.90	5	26	± 1.00
MS-18	2.78	4	17	± 0.45

<sup>a</sup>Theoretical density is 3.58.

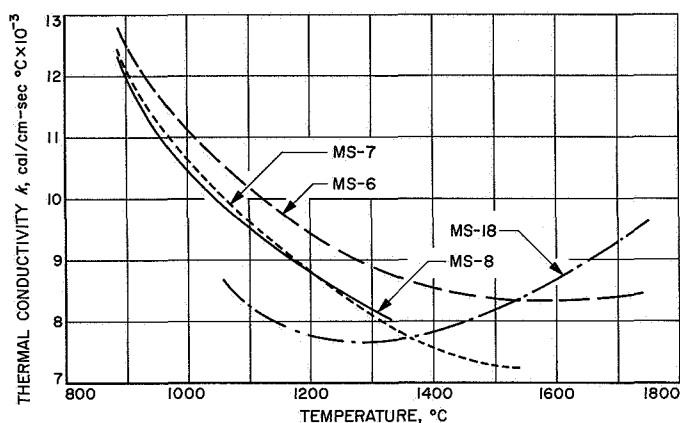


**Figure 69. Thermal conductivity vs temperature for MgO, FPM-1**

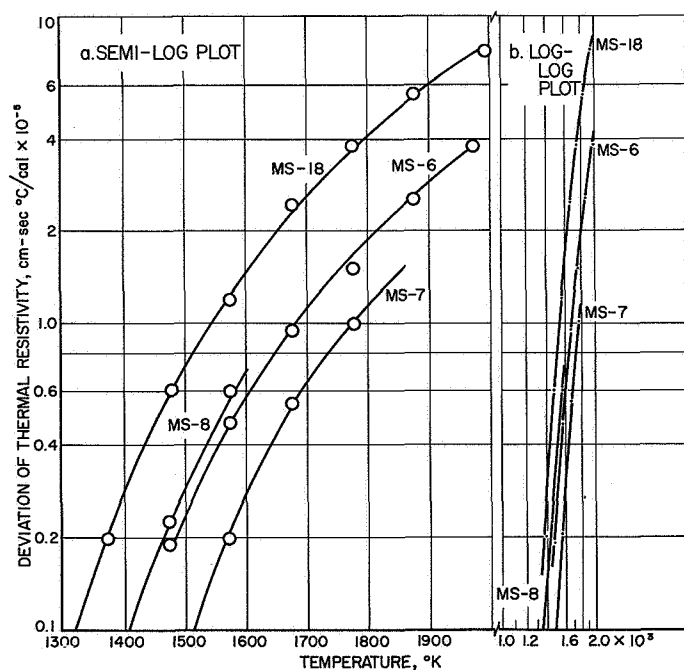


**Figure 70. Deviation of thermal resistivity vs temperature for MgO, FPM-1**

was plotted versus absolute temperature, as shown in Figure 70. Although a fair straight-line relationship is obtained on log-log paper (Fig 70b), from the slope of this best-fit straight line it is found that the deviation in thermal resistivity varies as nearly the tenth power of absolute temperature. Because of the disagreement with a  $T^3$  relationship, as required by Kingery's analysis, the radiation mechanism appears to be unsatisfactory.

Since this theory does not satisfactorily predict the physical process producing the deviation in observed thermal conductivity from that predicted by the Debye theory, some further explanation must be evolved. A significant step in the determination of this explanation would be a knowledge of the mathematical relationship which such experimentally determined deviations obey. Consequently, plots were prepared of various functions of  $\Delta R$  versus various functions of  $\Delta T$  to determine if any such dependency exists, but all results were similar in form to those in Figure 70. Additional data are now being obtained on MgO specimens having different grain size, densities, and pore structure.

## B. Endothermal Materials

R. G. Nagler

### 1. Arc-Imaging Furnace

Calibration of the arc-imaging furnace facility described in RS 36-8 has continued, using improved measuring techniques. Operation of the furnace at 150 amperes of current, with the optical axis in the horizontal position, gives the irregular heat flux distribution shown in Figure 71. Curves representing a manufacturer's (Arthur D. Little, Inc., Cambridge, Mass.) typical calibration from measurements on similar furnaces are shown for comparison. The flux distribution found by this Laboratory and that of the manufacturer were determined with similar 1-mm-D Gardon foil type radiometers. The irregular flux distribution shown by the JPL data is a characteristic of a specific furnace and is probably due to optical misalignment and imperfections in the ellipsoidal mirrors.

A comparison of manufacturer's typical heat flux data and JPL data is shown in Table 14. The maximum heat fluxes were determined with similar radiometers. The average heat fluxes were determined with two cold-wall calorimeters, one furnished by the manufacturer having

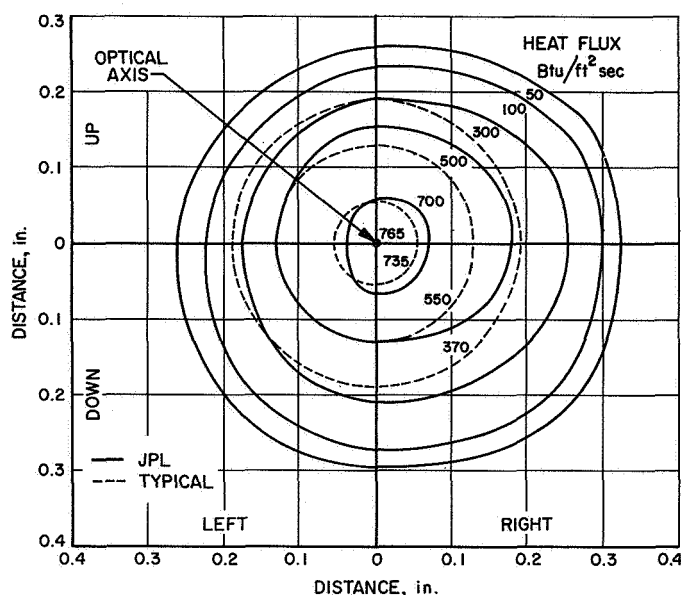


Figure 71. Heat flux distribution in arc-imaging furnace, horizontal position

0.111-in.<sup>2</sup> area, and the other made at JPL having 0.250-in.<sup>2</sup> area. The maximum heat flux and the average heat flux determined by this Laboratory with the calorimeter furnished by the manufacturer are both slightly low when compared with the manufacturer's data. It is believed that this behavior is a result of normal instrumentation variations, optical misalignment, and the pitting of the first mirror of the furnace because of anode splattering during stop-start operation. The average flux determined by the JPL 0.250-in.<sup>2</sup> calorimeter is high in comparison with the value reported by the manufacturer (Table 14).

The effect of the position of the temperature modulator on average heat flux is shown in Figure 72. The tempera-

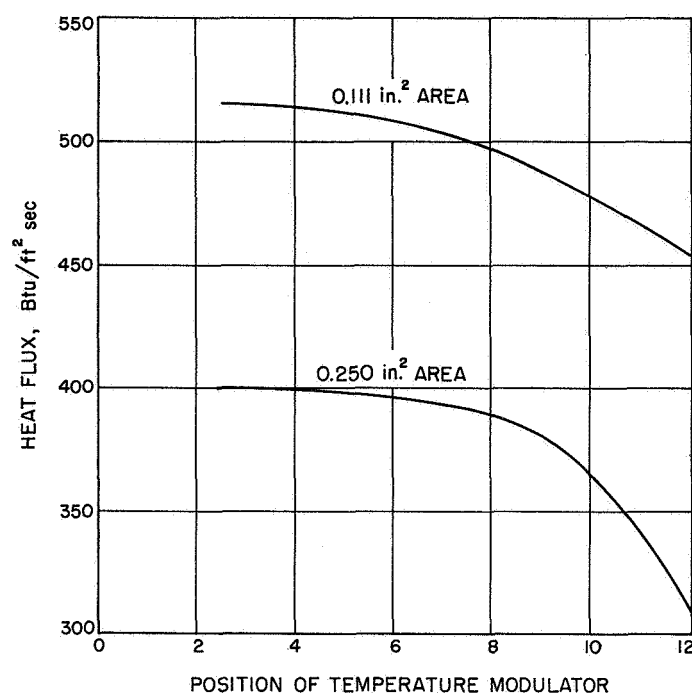


Figure 72. Effect of temperature modulator position on average heat flux

ture modulator is a plate which blocks portions of the total flux by positioning its circular opening at different locations along the optical axis. The average heat flux

Table 14. Arc-imaging furnace heat flux measurements, comparison of manufacturer's and JPL data<sup>a</sup>

Test method	Heat flux, Btu/ft <sup>2</sup> sec		Heat flux deviation, %
	Manufacturer's data	JPL data	
Maximum, 1-mm-D radiometer	789	765	3
Average, 0.111-in. <sup>2</sup> area cold-wall calorimeter	553	520	6
Average, 0.250-in. <sup>2</sup> area cold-wall calorimeter	360 <sup>b</sup>	420	17

<sup>a</sup>Furnace operating at 150 amps, horizontal optical axis.  
<sup>b</sup>From a curve extrapolated by the manufacturer.

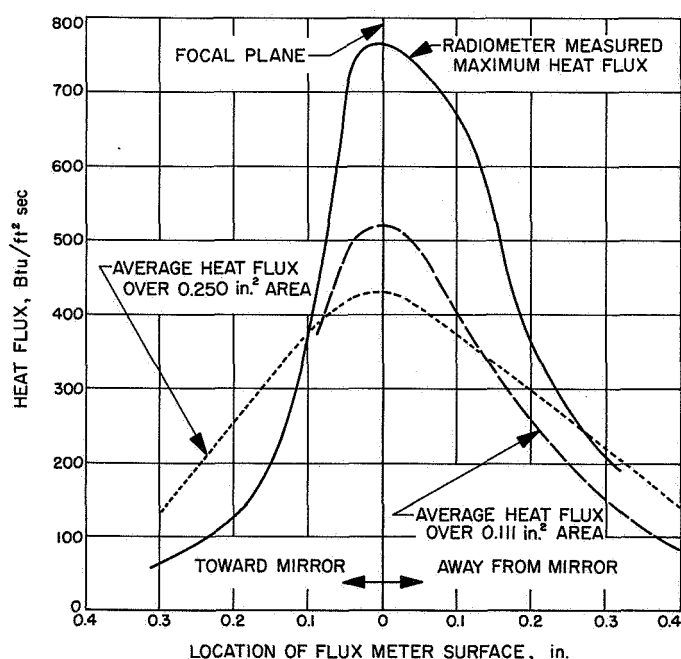


Figure 73. Effect of axial position of flux meter on maximum and average heat flux

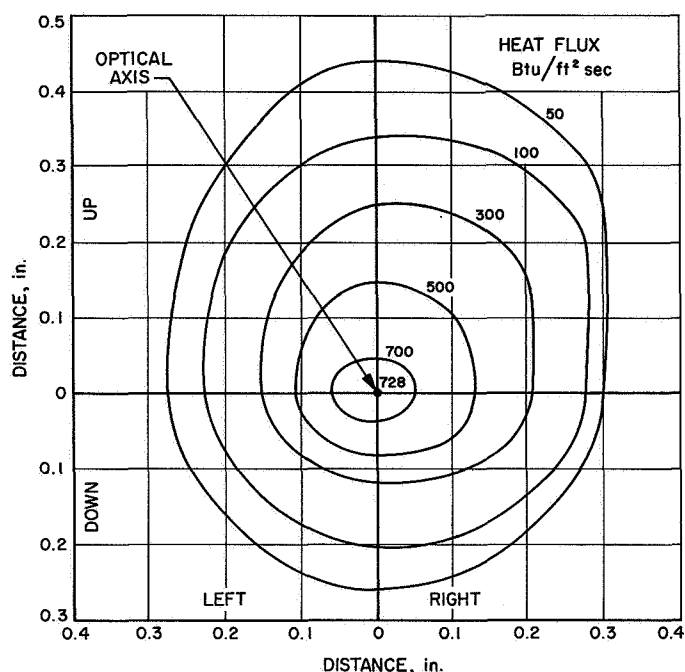


Figure 74. Heat flux distribution in arc-imaging furnace, vertical position

incident on the 0.111-in.<sup>2</sup> calorimeter is reduced as much as 11% while that incident on the 0.250-in.<sup>2</sup> calorimeter is reduced as much as 22%. The temperature modulator plate interrupts that portion of the flux which is subject to the greatest optical aberrations. Therefore, the position of the temperature modulator will have a greater influence on the flux incident upon the calorimeter with the larger area. The position of the temperature modulator did not affect the maximum flux value measured with the radiometer.

The effect of position of the radiometer or calorimeter surface along the optical axis on the maximum or average heat flux is shown in Figure 73. In all cases the heat flux

Table 15. Arc-imaging furnace heat flux measurements, difference between horizontal and vertical operation<sup>a</sup>

Test method	Heat flux, Btu/ft <sup>2</sup> sec		Heat flux reduction, %
	Optical axis horizontal	Optical axis vertical	
Maximum, 1-mm-D radiometer	765	728	5
Average, 0.111-in. <sup>2</sup> area cold-wall calorimeter	520	450	13
Average, 0.250-in. <sup>2</sup> area cold-wall calorimeter	420	360	14

<sup>a</sup> Furnace operating at 150-amp operation.

drops off from the maximum value more rapidly toward the mirror than away from it.

Figure 74 is a plot similar to Figure 71 for operation of the arc-imaging furnace in the vertical position at 150 amperes. The plot has the same general distribution as Figure 71 except for an elongation in the up-down direction. Vertical operation is accomplished by insertion of a 45-degree mirror in the optical path between the ellipsoidal mirrors. This mirror is rated for 95% reflection. Table 15 shows the effect of the 45-degree mirror on reducing the maximum and average heat fluxes.

## C. Materials in Space Environment

J. B. Rittenhouse

### 1. Thermal Degradation of Polytetrafluoroethylene in Vacuum

There are a number of conflicting reports of the thermal degradation of polytetrafluoroethylene (PTFE) in high vacuum ( $10^{-6}$  mm Hg). A literature study (RS 4) of polymer degradation mechanisms has shown that it is inaccurate to use kinetic theory to calculate evaporation rates of polymers because the degradation mechanisms are, in general, complex. These complexities in degradation mechanisms do not permit an accurate determination of the overall molecular weight of degradation species and thus result in inaccurate determinations of vapor pressures of polymers. Furthermore, plasticizers and stabilizers are used in many polymers to aid in fabrication. These additives have different compositions than the basic polymer and can influence evaporation rates when estimated by kinetic theory.

Packard (Ref 87) used kinetic theory to calculate an evaporation rate for PTFE of  $7 \times 10^{-4}$  gm/cm<sup>2</sup>-hr. He assumed a molecular weight of the evaporating species of 1000, a temperature of 170°F (77°C), and used a value for the polymer vapor pressure of  $10^{-7}$  mm Hg obtained from the work of Jensen (Ref 88).

Jensen (Ref 88) used hot filament ionization gages to measure the difference in pressure between an oven with a small orifice, containing the heated PTFE, in a vacuum bell jar and the vacuum pressure in the bell jar. The PTFE vapor pressure thus determined by Jensen was a nitrogen equivalent pressure because ionization gages are calibrated to measure the nitrogen (mol wt 28) partial

pressure in a vacuum system. It is believed that Jensen's value of the PTFE vapor pressure is in error. Consequently, Packard's calculated evaporation rate may be wrong.

It is believed that Madorsky et al. (Ref 89) have used the best experimental techniques to study polymer thermal degradation mechanisms in high vacuum. He used a wire spring balance to measure the weight loss of pure PTFE ribbons at about  $10^{-6}$  mm Hg. The temperature ranged from 480 to 520°C (896 to 932°F). Degradation rates calculated from Madorsky's data were extrapolated to 170°F (77°C) to obtain  $10^{-7}$  gm/cm<sup>2</sup>-hr. Madorsky analyzed the degradation products and found, for the lower temperatures of his work, 97% C<sub>2</sub>F<sub>4</sub> (mol wt 100), which is the tetrafluoroethylene monomer. Therefore, Packard's assumption of 1000 for the molecular weight of the evaporating species may be too high.

The equipment shown in Figure 75 was used at this Laboratory in preliminary experiments in the thermal degradation of polymers in simulated space vacuum; it is a liquid nitrogen trapped vacuum bell jar with high pumping capacity. Inside the bell jar, a spirally wound tungsten wire heating element on a stainless steel frame surrounds the specimen; this assembly is surrounded by a cylindrical stainless steel liquid nitrogen cooled surface.

Commercial PTFE specimens 1 inch square and 0.125 inch thick were thoroughly cleaned in warm distilled water and detergent, rinsed in cold distilled water, dried with a lintless cloth, and stored in a desiccator prior to exposure to vacuum. Each of the four specimens was weighed to the closest milligram on an analytical balance before and after exposure to vacuum of  $5 \times 10^{-7}$  to  $2 \times 10^{-6}$  mm Hg. Exposure times were 24, 47, and 72 hours, with a duplicate experiment at 24 hours. The specimens were impaled upon the stainless steel sheath of a copper-constantan thermocouple. Thus, the hot junction of the thermocouple was at the geometrical center of the specimen. The bulb of a mercury-in-glass thermometer was in contact with one surface of the specimen. The maximum temperature measured at the specimen thermocouple was from 168 to 180°F, that at the thermometer was from 163 to 190°F. The arithmetical average thermal degradation rate of the four specimens was  $1 \times 10^{-6}$  gm/cm<sup>2</sup> hr. The weight loss and temperature data for these experiments are shown in Table 16.

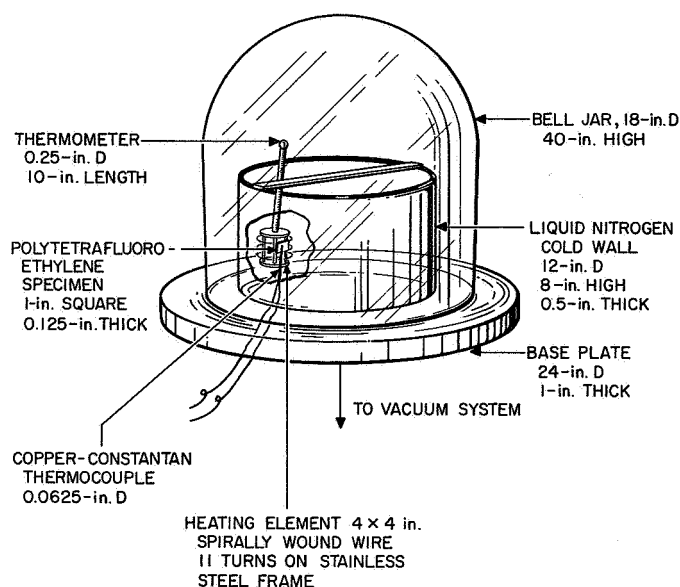


**Figure 75. Equipment for preliminary studies of thermal degradation of polytetrafluoroethylene in vacuum**

It is believed that this experimental value for commercial PTFE compares favorably with that for the pure material extrapolated from Madorsky's data. This result further indicates that Packard's calculated evaporation rate may be in error.

It is planned to install a recording semimicro balance in the vacuum system of Figure 75. With this apparatus, continuous weight loss data of pure polymers will be obtained in high vacuum ( $10^{-6}$  mm Hg) at temperatures from ambient to 400°C (750°F). Pure polymers as free of plasticizers and stabilizers as practicable will be used.

**Table 16. Thermal degradation of commercial polytetrafluoroethylene in vacuum<sup>a</sup>**

Specimen No.	Exposure time, hr	Maximum temperature range, °F	Weight loss rate, gm/cm <sup>2</sup> hr
1	24	168 to 180	$1.6 \times 10^{-6}$
2	24	163 to 174	$6.8 \times 10^{-7}$
3	72	168 to 190	$8.4 \times 10^{-7}$
4	47	168 to 174	$1.1 \times 10^{-6}$
			Avg rate $1.1 \times 10^{-6}$
<sup>a</sup> Vacuum $5 \times 10^{-7}$ to $2 \times 10^{-6}$ mm Hg.			

## XI. Engineering Research

### Plasma Confinement

D. F. Spencer

In order that a plasma might be confined within particular geometrical bounds, it is necessary that a state of equilibrium be maintained throughout the plasma. In the case of an infinitely long cylindrical plasma, this requires that

$$\nabla (B_z^2/8\pi + p) = 0 \quad (1)$$

in the radial direction, where  $B_z$  is the uniform axial magnetic field, and  $p$  the kinetic pressure of plasma. For a dense plasma, the kinetic pressure is given by

$$p = \frac{3}{2} nkT_p \quad (2)$$

where  $n$  is the total particle concentration,  $k$  is Boltzmann's constant, and  $T_p$  the plasma temperature. Thus, we require that

$$\frac{B_z^2}{8\pi} + \frac{3}{2} nkT_p = \text{const} \quad (3)$$

at each instant of time at each radial coordinate.

The induced magnetic field,  $B_z$ , does not penetrate into the plasma immediately, due to its diamagnetic nature. Thus, at  $t = 0$ , the induced field is restricted to the surface and has a value which just balances the interior

kinetic pressure. In the case to be discussed later, the initial magnetic field is  $1.66 \times 10^4$  gauss corresponding to a uniform plasma temperature of  $10,000^\circ\text{K}$  and a concentration of  $5.4 \times 10^{17}$  particles/cc.

In time, due to the finite electrical conductivity of the plasma, the magnetic field begins to leak into the plasma (RS 36-7, Vol II). In order that Equation (1) may hold at all times, the plasma must now diffuse out across the magnetic field lines.

If, however, the surface magnetic field strength is continually increased (by increasing an external current in a solenoidal winding and inducing an emf through Faraday's Law), it is possible to maintain equilibrium conditions for appreciable periods of time, thereby increasing the relaxation time of the plasma.

The time-dependent partial differential equation governing the diffusion of the magnetic field into the plasma is

$$\frac{\partial^2 B_z}{\partial r^2} + \frac{1}{r} \frac{\partial B_z}{\partial r} = \frac{1}{\eta} \frac{\partial B_z}{\partial t} \quad (4)$$

where  $r$  is the radial coordinate,  $t$  the time, and  $\eta$  the magnetic field diffusion coefficient. This relation is subject to the boundary conditions that the magnetic field must be finite at  $r = 0$  for all times and at  $r = r_p$

$$B_z = B_{z0} + Kt \quad (5)$$

where  $B_{z0} = B_z(t=0)$ , and  $K$  is the constant rate of increase of the surface magnetic field. More explicitly, it is assumed that the plasma boundary remains fixed. This condition would not be realized in a practical application; however, it offers a means of obtaining some insight into the problem.

Equation (4) may be solved by using the Laplace transform technique to obtain

$$B_z(r, t) = B_{z0} - \frac{2B_{z0}}{r_p} \sum_{n=1}^{\infty} e^{-\eta \alpha_n^2 t} \frac{J_0(\alpha_n r)}{\alpha_n J_1(\alpha_n r_p)} + K \left[ t - \frac{(r_p^2 - r^2)}{4\eta} \right] + \frac{2K}{\eta r_p} \sum_{n=1}^{\infty} e^{-\eta \alpha_n^2 t} \frac{J_0(\alpha_n r)}{\alpha_n^3 J_1(\alpha_n r_p)} \quad (6)$$

The roots  $\alpha_n$  are obtained from

$$J_0(\alpha_n r_p) = 0 \quad (7)$$

For a constant plasma temperature of  $10,000^\circ\text{K}$ ,  $\eta = 1.55 \text{ m}^2/\text{sec}$ . Based on a plasma radius of 2 meters, the required plasma concentration as a function of radial

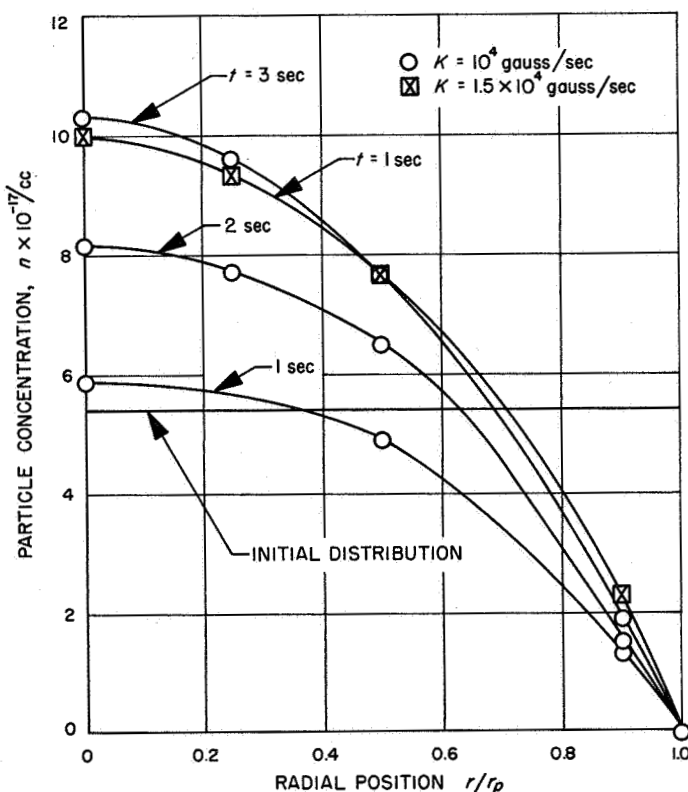


Figure 76. Required total concentration to maintain equilibrium as a function of radial position and time

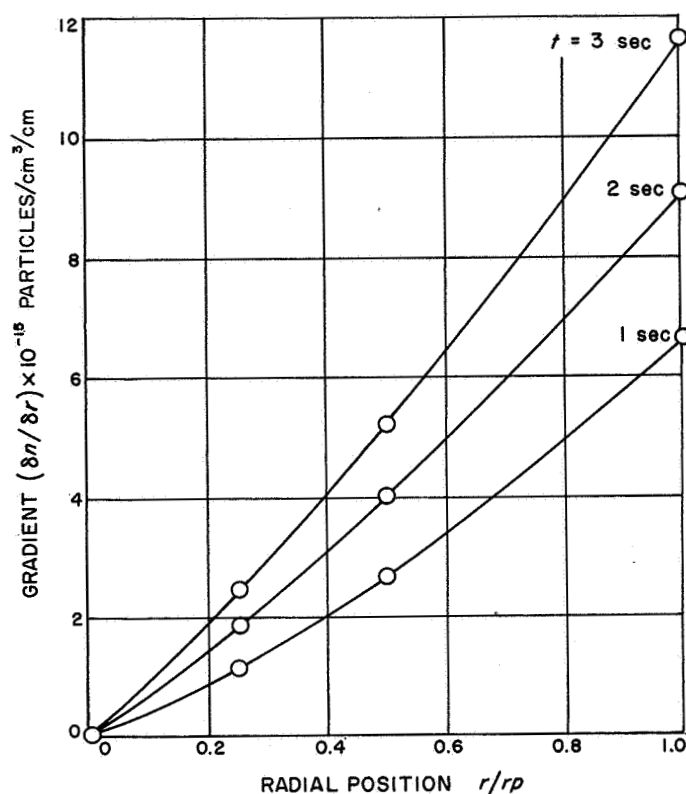


Figure 77. Radial concentration gradient as a function of radial position and time for  $K = 10^4 \text{ gauss/sec}$

position and time is shown in Figure 76 for  $K = 10^4 \text{ gauss/sec}$  after  $t = 1, 2$ , and 3 seconds and  $K = 1.5 \times 10^4 \text{ gauss/sec}$  after 1 second.

It may be seen that for  $K = 10^4 \text{ gauss/sec}$ , approximately  $\frac{1}{2}$  the original number of particles within the plasma are lost after 1 second. For longer times, it is necessary to supply additional plasma material near the axis in order to maintain equilibrium. For  $K = 1.5 \times 10^4 \text{ gauss/sec}$ , the total number of particles required for equilibrium is approximately the same as the original total number present. This suggests that the magnetic field may be used to force the particles near the plasma surface into the inner volume. If this could be effected, the plasma would have minimal losses during this time. Of course, for longer times, additional plasma must be supplied from some exterior source.

It is interesting to note that the diffusion of the magnetic field into the plasma forces the original uniform profile into a nearly parabolic distribution. This distribution tends to produce greater diffusion of the particles across the magnetic field due to the continually increasing concentration gradient at  $r = r_p$  for times greater than

1 second (Fig 77). This effect tends to increase losses from the plasma but, to first order, does not appear to grow as rapidly as the enhancement effect.

Returning to the assumption that the plasma boundary remains fixed, it should be stressed that the actual case will find the plasma being compressed with a higher average concentration. If the plasma material is fissionable, as in the case of the plasma core reactor (Ref 90), the system could conceivably be maintained just critical

since the critical concentration increases with decreasing radius. Further, it may be possible to control the system by varying the poison concentration in the propellant.

Thus, it appears that plasma confinement times in the plasma core reactor may be increased by continually raising the induced magnetic field at the plasma surface if (1) continuous plasma injection can be effected and (2) the system can be maintained critical and dynamically stable.



## ENGINEERING FACILITIES DIVISION

### XII. Wind Tunnels

#### A. 21-Inch Hypersonic Tunnel

*E. H. Koester and R. C. Hiller*

##### 1. Tunnel Development Program

A preliminary investigation (Test 21-C11B) to extend the Mach number range of the hypersonic wind tunnel above  $M = 10.1$  has been conducted.

Prior to the test, several new high Mach number nozzle contours had been computed on the ElectroData Computer using different throat and test section heights. Due to tunnel mechanical limitations, the largest throat height possible for  $M = 10.7$  with the inflection point of the nozzle contour at its normal location was 0.030 inch. The tunnel started and ran easily with the  $M = 10.7$  nozzle contour. The average Mach number recorded in the test section was  $M = 10.70$ . The value of  $P_0$  was 3000 cm Hg abs, and  $T_0$  was 900°F. No time was available to smooth out minor pressure variations. This will be done later during a scheduled flow calibration. The nozzle was subsequently adjusted to the  $M = 11.0$  shape and, again, there was no trouble in starting or running the tunnel. At  $P_0 = 3000$  cm Hg and  $T_0 = 900^\circ\text{F}$ , the average Mach

number was 11.1. Liquefaction may account for the Mach number difference of 0.1 from the calculated value. Temporary restrictions on the maximum heater tube-wall temperature limited  $T_0$  to 900°F. This preliminary investigation shows conclusively that the tunnel is operational at Mach numbers up through  $M = 11.0$ . However, in all cases where the desired Mach number is above 10.0, Compressors A and B must be added to the standard four-stage hypersonic tunnel plant. This presents a scheduling problem because of interference with the 20-inch supersonic wind tunnel.

A test (21-C16) to briefly assess the effects of tunnel flow angularity and Mach number variation on model aerodynamic data was performed in the 21-inch hypersonic wind tunnel. Data was gathered at a nominal Mach number of 9 for two different stagnation pressures since the quality of the tunnel flow varies with the stagnation pressure. In order to properly relate the investigation to typical aerodynamic tests, it was necessary to inspect the air flow at a number of stations ranging from the centerline to 5 inches above and below the tunnel centerline.

The effect of variations in Mach number above and below the centerline was measured by noting the variation in chord force on a 4-inch diameter sphere. The

chord force varied from the centerline value by as much as 2% and was practically the same as the variation in pitot pressure.

The effective flow angularity was deduced from forces resulting on a  $6 \times 8 \times 0.5$ -inch thick flat plate with a sharp leading edge placed at a 15-degree angle of attack. Variations in normal force above and below the tunnel centerline indicated that the maximum flow inclination was 0.5 degree in the 10-inch height which was inspected. It is planned to verify and extend the flow angularity measurements with another more rigorous technique in a future nozzle air-flow calibration.

Although the detailed analysis of the test results has not been completed, it appears that there is no practical difference in the results obtained at stagnation pressures of 2000 and 3200 cm Hg abs at  $M = 9$ .

## B. Low-Density Wind Tunnels

N. L. Fox

The low-density wind tunnel (RS 5), until recently located in extremely crowded quarters, has been moved to a more adequate location formerly occupied by the 12-inch supersonic wind tunnel. Check calibrations of the test-section air flow are underway, and initial inspection of the data shows that the quality of the air flow is essentially unchanged, as expected. It is expected that the sphere drag studies (RS 36-2 and 36-5) will be resumed shortly in this tunnel.

In coordination with this move, a new low-density wind tunnel, designated as Leg II, has been designed, fabricated by an outside vendor, and installed. This new tunnel is about 50% larger than the existing Leg I mentioned above, both in geometric size and volume flow capability. Flow calibrations in Leg II are expected to start soon. The equipment for providing ionized flow, built by Vidya, Incorporated, is on hand and will be installed in this tunnel after completion of the initial shakedown. The Vidya equipment will also provide flow at 4000°F (inert gas only) without ionization, when desired.

In contrast to the earlier installation, the new installation features controls for most of the pumps and valves located in a centralized area, as shown in Figure 78. This centralization of controls has made possible sufficient safety interlocks to make feasible unattended operation at night. The elimination of morning startup and afternoon shutdown periods should appreciably increase the available first-shift useful time.

In connection with these low-density wind tunnels, a low-pressure calibration laboratory has been put into operation. A long existing discrepancy of about 6% (at the 100-micron level) between supposedly primary pressure-measuring instruments is currently being resolved.

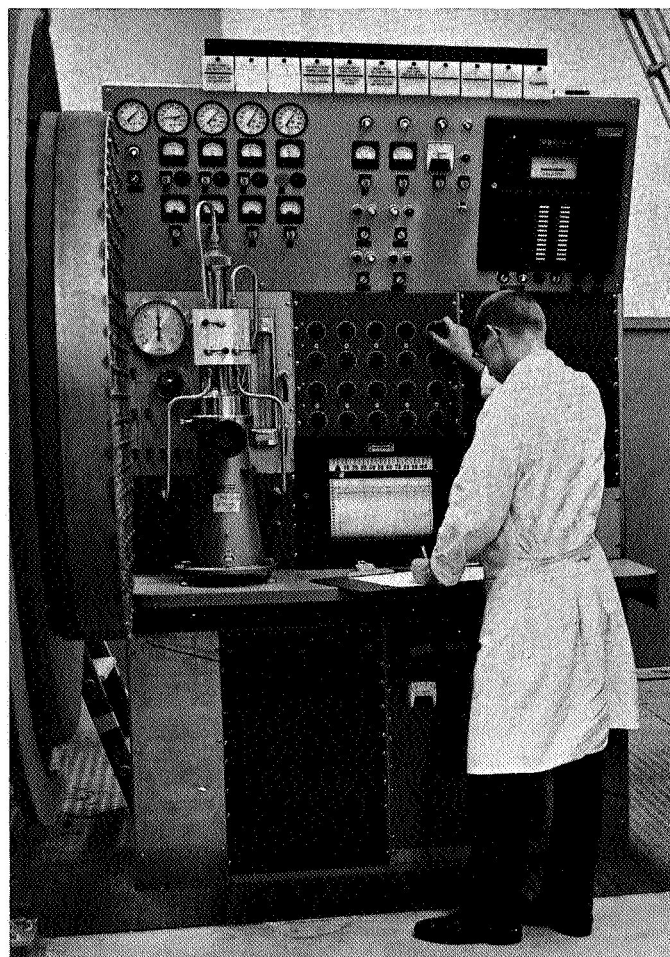


Figure 78. Control console for low-density wind tunnels

# PROPULSION DIVISION

## XIII. Liquid Propellant Propulsion

### A. Combustion and Injection

*J. H. Rupe and G. I. Jaivin*

#### 1. Rocket Motor Injection Research

The pressure that exists within an operating combustion chamber—particularly in rocket engines—is usually inferred from experimental measurements made at one (or a few) points on the chamber boundary. Further, it is customary to relate these measurements to the entire combustion volume by assuming that the measurement represents a static pressure that has a constant value (i.e., uniform) at any instant in time and is characteristic of the particular axial station of a one-dimensional steady flow system with which it is associated. Thus, if it is further assumed that the observed pressure is steady in time, or that the time-average value is equivalent to a steady one, then such measurements together with some additional, nontrivial assumptions and an analysis of a one-dimensional flow system can be combined to yield a value for the stagnation pressure at that particular station. This value can then be used in the calculation of an index of performance such as the calculation of  $c^*$  for a rocket engine (Ref 91).

It is well known, however, that such pressure measurements are in fact not steady in time. And it is pertinent to question the validity of the steady-state assumption

and, in particular, to consider the significance of the observed pressure fluctuations insofar as they may independently influence the critical combustion processes. It can be argued, for example, that the nonsteady part of the measurement must reflect local pressure gradients and/or velocity variations that can be an important part of the mass transport and mixing processes that are essential to a complete reaction. Also, the relative contribution of these disturbances must be a function of their scale and intensity. Obviously if the scale of the disturbance is quite large so that its  $\frac{1}{4}$  period would approach the residence time for the chamber, the effect should be interpreted as a gross change which has little effect on the macroscale mixing and/or transport processes. (Note that residence times of interest in this concept are associated with typical chamber velocities of 100 to 300 ft/sec for chamber lengths of 1 to 2 feet, so that variations at frequencies in the order of 100 cps or less—depending on a particular geometry—can be considered as gross variations.) On the other hand, when the scale of the disturbance is small, then it seems probable that its effect on the combustion process must increase as the intensity of the disturbance increases.

It is obviously impossible with a single measurement to determine the origin of the disturbance, or whether it represents simply a change in the form of the available energy—i.e., from potential energy to velocity energy—or the consequence of a change in total energy—i.e., in local

reaction rates. However, in each case it does represent a disturbance that is potentially capable of contributing to the combustion processes.

Thus, it can be postulated that (1) the contribution to the combustion processes associated with a particular frequency (i.e., a component of a complex disturbance) is proportional to the apparent change in specific energy which is associated with that component (as previously noted, it is assumed that this change in energy can be inferred from the change in pressure alone); (2) that the rms value of the departure from a mean pressure of an arbitrary pressure fluctuation over a time interval  $2T$  can be used to characterize the intensity of the fluctuations; and (3) that "... the mean square of a complex wave is just the sum of the mean square of its constituents ..." (Ref 92, pp 1-10).

Then, utilizing the sketch of Figure 79 and the assumptions outlined above, it may be concluded that the pertinent portion of the energy changes—relative to the mean level—are simply related to  $(p - p_{avg})$  and the rms value of this perturbation over a time interval  $2T$  is by definition

$$\phi = \left[ \frac{1}{2T} \int_{-T}^{+T} (p - p_{avg})^2 dT \right]^{1/2}$$

so that this quantity can then be utilized to characterize the fluctuation insofar as its effect on the combustion processes is concerned.

In the course of some recent experiments on a large-thrust, liquid-propellant uncooled rocket engine, utilizing  $N_2O_4 + N_2H_4$  as propellants, it was observed that the

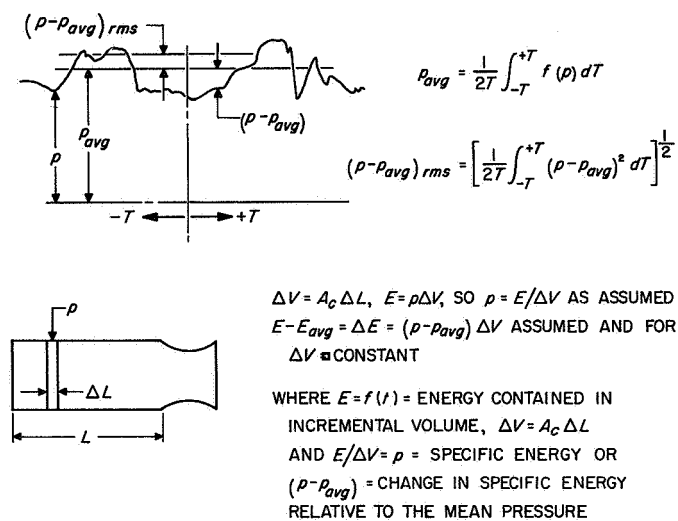


Figure 79. Typical record of pressure-time history at a single point on combustion chamber boundary

level of combustion noise was unusually high. An attempt was made to correlate a measured value of  $\phi$ , i.e., the rms value of the observed pressure fluctuation, with the gross combustion properties. For this purpose, the electrical output of a Photocon pressure transducer was first passed through a wide-band sharp cutoff filter and then monitored with an rms converter. The Photocon has near flat response from dc to about 10 kc, beyond which the output of the oscillator-detector is rapidly attenuated. The filter has zero gain and cuts off at the high-frequency limit at 8.0 kc with attenuation of 40 db at 10 kc. At the low-frequency limit, it cuts off at 10 cps with attenuation at 24 db per octave. Although the use of the filter does impose a boundary condition on the interpretation of  $\phi$ , i.e., a finite bandwidth, it is essential in order to restrict the data to the usable portion of the Photocon spectrum, and hence provide comparative information from measurement to measurement. As yet, there is no basis for stating that the effects are frequency dependent—so it is presumed that a symmetrical, repetitive disturbance would have the same influence on combustion phenomena as a noiselike disturbance having the same value for  $\phi$ . It is noted, however, that the information that has been obtained to date has been limited to disturbances that were predominantly noiselike in character.

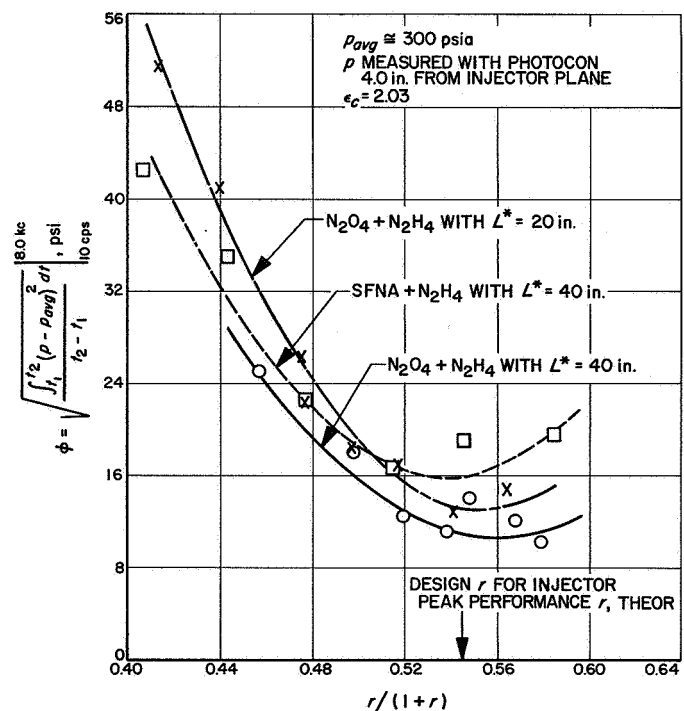


Figure 80. Correlation between combustion roughness and mixture ratio for several engine propellant configurations

Figure 80 presents a correlation between  $\phi$  and mixture ratio for three different engine propellant combinations. Although there is some scatter of the experimental points, it is certain that  $\phi$  increases as the mass fraction ratio decreases, and though some imagination is necessary, it would appear that a minimum exists at or near the design mixture ratio for the injector—which is also the peak performance mixture ratio (theoretical) for the  $\text{N}_2\text{O}_4$ - $\text{N}_2\text{H}_4$  propellant combination. It is interesting to note that at least for one system that was evaluated, a decrease in  $L^*$  produced a small increase in the level of roughness.

It is obvious that these correlations in themselves do not relate  $\phi$  to the combustion process. However, when considered together with the gross performance characteristics of these several configurations as presented in Figure 81, it can be seen that there is justification for arguing that combustion noise can supplement the essen-

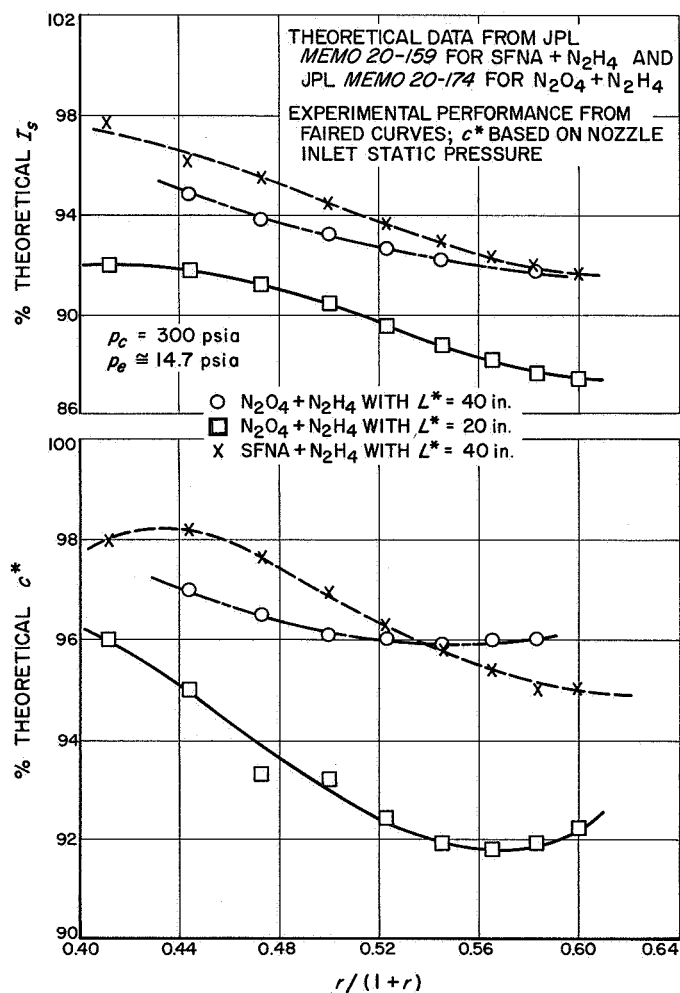


Figure 81. Relative performance of injector D-9111607 (Mod 1) (i.e., Inj No. 7) for different propellant-chamber configurations

tial combustion processes. This argument is supported by the fact that the relative performance of each of these three configurations as characterized by either  $c^*$  or specific impulse increases as the mass fraction ratio decreases so that these changes are correlated with roughness.

It is, therefore, possible to make the tentative conclusions that (1) the rms value of the pressure fluctuations observed at a single point on a combustion chamber can be correlated with gross combustion properties, and (2) increasing the observed intensity of roughness can increase the overall combustion efficiency.

## 2. Atomization and Injection Hydraulics

A technique for determining the local thickness and average velocity of a liquid sheet from momentum and flow rate measurements was discussed in RS 36-5, Vol II. The apparatus discussed therein has been built and calibrated, and the data obtained to date are presented in Figure 82.

The flow geometry employed to produce the liquid sheet under investigation (Fig 83) is essentially a sharp-edged annular slit (RS 36-4, Vol II). In the current test series, the diameter of the annulus is 1.00 inch, and the slit width is maintained at 0.018 inch. The data shown were obtained with a probe having a 2.00-inch radius as measured from the sheet centerline. The probe intercepted a 60-degree segment of the axially symmetric sheet.

It is of interest to note the apparent decrease in sheet thickness at increasing sheet velocities. Although one would expect *vena contracta* effects to modify the sheet thickness to a small degree as a function of flow velocity, the marked change observed cannot be completely ration-

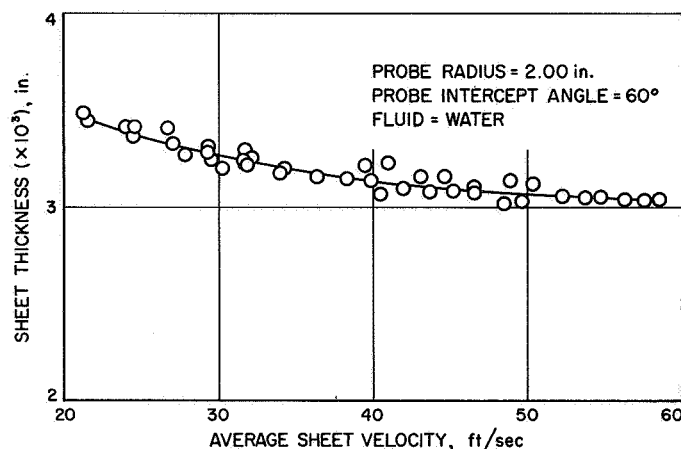


Figure 82. Sheet thickness as a function of average sheet velocity

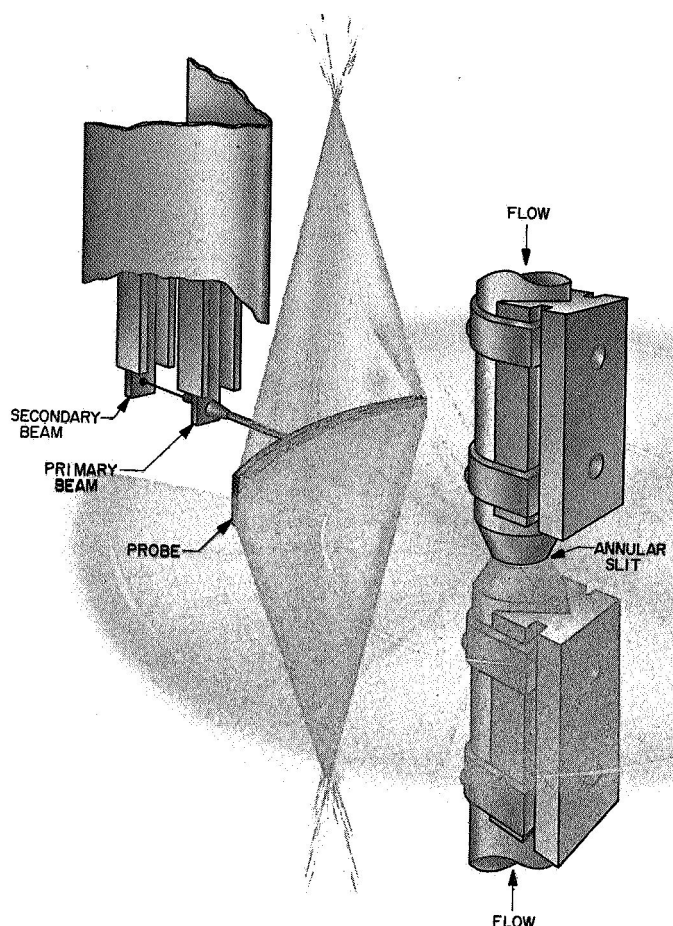


Figure 83. Configuration of liquid sheet test hardware

alized solely by this hypothesis. It is believed that the angle at which the fluid leaves the probe surface may be other than the assumed 90 degrees at the lower flow velocities, thus contributing to the effect shown.

This work is continuing, and tests have been planned to investigate the fluid separation angle from the probe as well as to extend the data to larger radii.

## B. Heat Transfer and Fluid Mechanics

A. B. Witte

### 1. Heat Transfer in Rocket Motors

An experimental investigation of heat transfer in rocket engines is being conducted to determine the effect of

injector configuration, thrust-chamber geometry, and operating conditions on the axial heat flux distribution. These tests are being made at chamber pressures between 100 and 300 psia, with nitrogen tetroxide ( $N_2O_4$ ) and hydrazine ( $N_2H_4$ ) as bipropellants at a nominal mixture ratio of 1.0. Steady-state values of heat flux have been measured calorimetrically by passing cooling water through axially short, circumferential cooling passages which form the thrust-chamber walls. Comparisons between the analytical and experimental values of local heat flux were made with 1.64-to-1, 4-to-1, and 8-to-1 contraction-area-ratio nozzles and reported in References 93 and 94; RS 36-7, Vol II; and RS 36-8, Vol I. Analytical values of heat transfer coefficient were calculated by the method proposed in Reference 95. As suggested in Reference 96, enthalpy difference between the free stream and the wall temperature condition was used as the driving potential in calculating predicted values of local heat flux. A detailed development showing how the enthalpy potential and the heat-transfer coefficient are combined to evaluate the axial heat flux distribution is given in the appendix of Reference 94.

Recently, a 1.64-to-1 contraction-area-ratio uncooled nozzle, which has the same inner contour as the 1.64-to-1 calorimetrically cooled nozzle described in References 93 and 94, was designed, fabricated, and instrumented with circumferentially, axially, and radially spaced thermocouples to deduce local values of heat flux. These local heat-transfer rates will be compared to the semilocal heat-transfer rates obtained with the calorimetric, 1.64-to-1 contraction-area-ratio nozzle (Refs 93 and 94). In addition, a limited number of tests will be conducted to determine circumferential variations of heat-transfer rates produced by various injector types. Computation of test results has not been completed; consequently, no results are reported. However, a description of this nozzle and the instrumentation is presented.

The uncooled nozzle, shown in Figure 84, was fabricated from Type 1020 steel, and has an 0.625-inch wall thickness and a 3.90-inch diameter throat. The nozzle is nominally rated at 5000-pound thrust while operating at 300 psia chamber pressure with nitrogen tetroxide and hydrazine at a mixture ratio of 1.0.

In order to deduce local values of heat flux in the uncooled nozzle, knowledge of the temperature distribution in the nozzle wall as a function of the time and space coordinate is required. Having two temperature boundary conditions provided by radially spaced thermocouples, and prescribing the variation of physical properties of the wall material with temperature, allows solution of the heat-conduction equation in finite-difference form



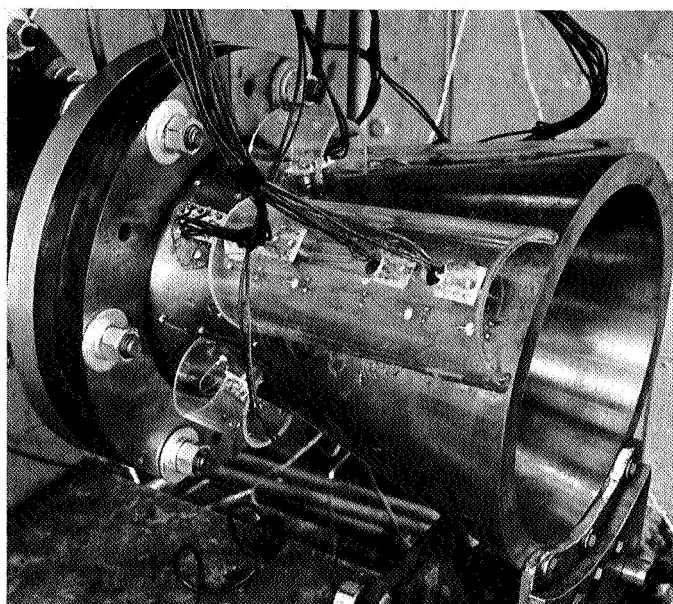


**Figure 84. Uncooled 1.64-to-1 contraction-area-ratio nozzle**

which yields the temperature distribution. The heat flux is then calculated by evaluating Fourier's equation at the gas-side surface. One thermocouple was resistance-welded to the outer surface of the nozzle; however, due to the practical limitations of locating a reliable thermocouple junction at the gas-side surface, the second thermocouple was imbedded 0.020-inch from the gas-side surface. The temperature distribution was then calculated between these two boundary conditions, and a

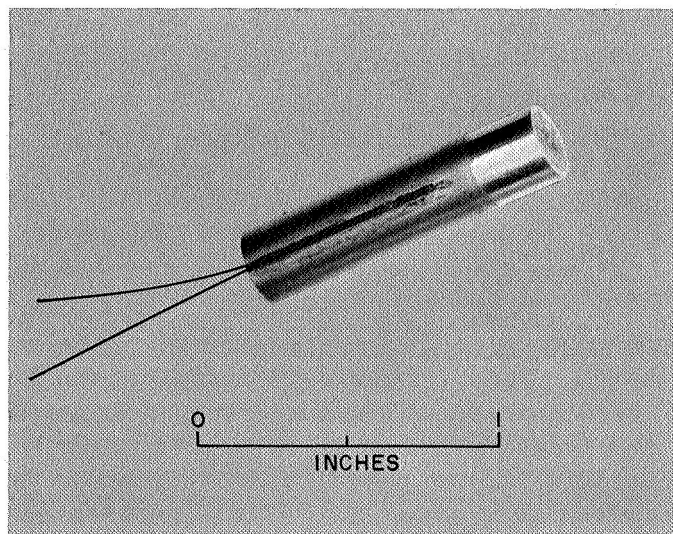


**Figure 85. Transient thermocouple plug**

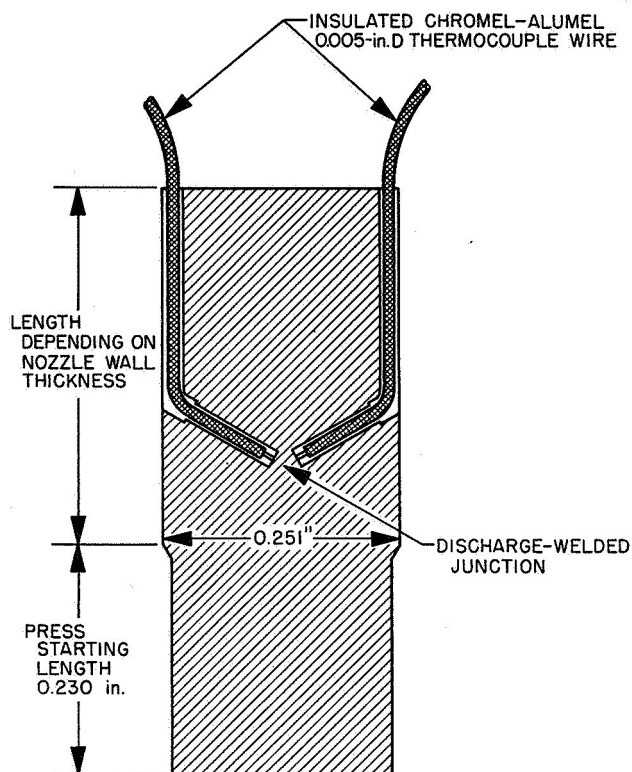


**Figure 86. Schematic of transient thermocouple plug**

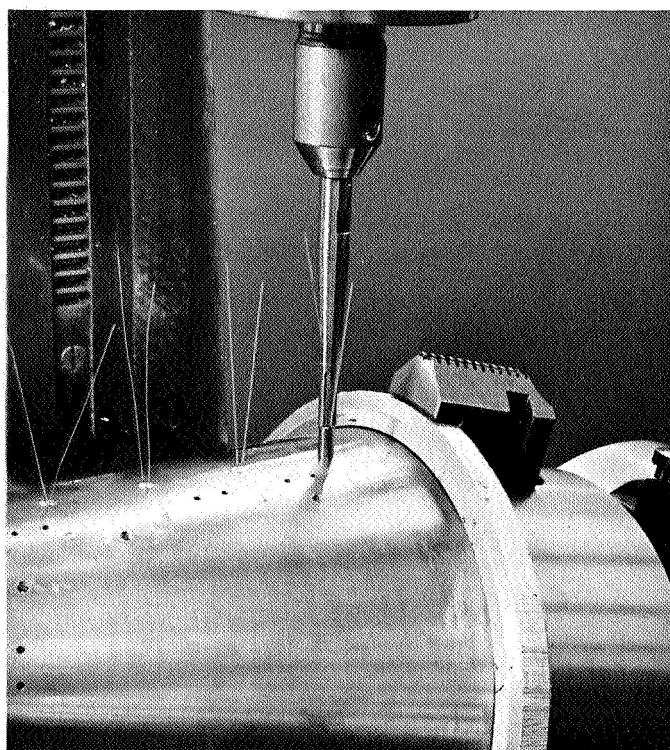


**Figure 87. Transient thermocouple plug pressing operation**

fifth-order polynomial was used to fit and extrapolate the calculated temperature distribution to the gas-side wall.

The imbedded thermocouple was fabricated by discharge-welding the thermocouple junction in a Type 1020 steel, 0.250-inch diameter plug (plug material taken from same billet as nozzle), shown in Figures 85 and 86. Chromel-Alumel thermocouples were used. The fabrication and installation specifications of the transient heat transfer thermocouple, called the thermocouple plug, are found in Reference 97. The thickness of the nozzle wall at each thermocouple position was measured so that the thermocouple plug could be precut and pressed in flush with the nozzle outer surface as shown in Figure 87. After the plugs were pressed in place, the portions of the thermocouple plugs protruding beyond the gas-side surface were cut off by machining to the inner contour of the nozzle. The final thermocouple plug length was then measured to obtain the exact location of the thermo-

couple junction from the gas-side surface (nominally 0.020 inch).

Seventeen positions in the nozzle were instrumented for transient temperature measurements in this manner. Two axial rows of seven positions each were spaced circumferentially 120 degrees apart; in addition, three positions with 120-degree circumferential spacing were located at the nozzle throat. The axial location of each position was chosen to correspond to each cooling passage location of the 1.64-to-1 calorimetric nozzle (Refs 93 and 94).

Each thermocouple is sampled every 50 ms (0.050 sec) of test duration by use of a digital recording system (RS 4 and RS 36-6, Vol II). The data are recorded on magnetic tape in a format suitable for digital computing on the IBM 7090.



## XIV. Solid Propellant Propulsion

### A. Polymer Research

A. J. Havlik and A. B. Magnusson

#### 1. Polyoxyalkylenes Terminated with Different Functional Groups

The objectives and proposed plan of research on the end-group modification of the polyoxyalkylene glycols were outlined in RS 36-6, Vol II. Results were reported on the syntheses and characterization of some low-molecular weight homologs of the polyoxyalkylene glycols, namely, ethylene glycol (EG), dipropylene glycol (DPG), and tetraoxyethylene glycol (TOEG). Further study now has given additional data on (1) the properties and analyses of the dicarboxylic acids and diamides prepared by the hydrolysis of cyanoethylated EG, DPG, and TOEG; (2) the relative yields of cyanoethylated product from EG, DPG, and TOEG and the influence of selected modifications of the reaction conditions on the yield of cyanoethylated DPG; (3) the relative stability of the cyanoethylated products at room temperature when stored in sealed ampoules under their own vapor pressure versus storage in a closed container at ambient pressure; and (4) the nature of the yellow-colored solid sideproduct formed in many of the cyanoethylation reactions.

*a. Hydrolysis of dinitriles to dicarboxylic acids and diamides.* The acid hydrolysis of cyanoethylated EG, DPG, and TOEG with concentrated hydrochloric acid (Refs 98 to 100) gave the corresponding dicarboxylic acids in yields of 82 to 89%. The diacids 1,8-dicarboxyl-3,6-dioxaoctane and 1,17-dicarboxyl-3,6,9,12,15-pentaoxaheptadecane formed from cyanoethylated EG and TOEG, respectively, were solids, while the diacid 1,11-dicarboxyl-*x,y*-dimethyl-3,6,9-trioxaundecane from cyanoethylated DPG was a liquid. The properties of the three diacids are given in Table 17.

The alkaline hydrolysis of cyanoethylated EG, DPG, and TOEG with hydrogen peroxide in ethanol (Refs 101, 102) gave the corresponding diamides in greater than 87% yield. The diamides 1,8-dicarbamyl-3,6-dioxaoctane and 1,17-dicarbamyl-3,6,9,12,15-pentaoxaheptadecane formed from cyanoethylated EG and TOEG, respectively, were solids, while the diamide 1,11-dicarbamyl-*x,y*-dimethyl-3,6,9-trioxaundecane from cyanoethylated DPG was a viscous liquid which did not crystallize. Attempted purification of the latter material in a molecular still appeared to lead to its decomposition. The properties of the three diamides are given in Table 18.

*b. Cyanoethylation of glycols.* The procedure used for the synthesis of cyanoethylated EG, DPG, and TOEG

Table 17. Properties and analyses of diacids from hydrolysis of dinitriles,  
 $\text{HOOC}-\text{CH}_2\text{CH}_2-\text{O}-\text{R}-\text{O}-\text{CH}_2\text{CH}_2-\text{COOH}$

R	Properties of diacid						Analyses <sup>a</sup>					
	Bp, °C	mp, °C	$n_D^{25}$	$d_4^{20}$	Molar refraction		Acidity, <sup>c</sup> meq/gm		C		H	
					Calc <sup>b</sup>	Found	Calc	Found	Calc	Found	Calc	Found
$-\text{CH}_2\text{CH}_2-$ (from EG) <sup>d</sup>	—	63 to 63.5	—	—	—	—	9.71	9.35	46.60	46.45	6.84	6.78
$\begin{array}{c} \text{H,CH}_3 \quad \text{H,CH}_3 \\   \quad   \\ -\text{CH}-\text{CH}-\text{O}-\text{CH}-\text{CH}- \\   \quad   \\ \text{(from DPG)} \end{array}$	112 to 140 ( $<0.0005$ )	—	1.4556	1.1519	66.16	65.88	7.19	7.04	51.79	51.19	7.97	8.12
$-(\text{CH}_2\text{CH}_2-\text{O})_3-\text{CH}_2\text{CH}_2-$ (from TOEG)	205 to 210 (0.0005 to 0.001)	44.5 to 47	—	—	—	—	5.91	5.71	49.69	48.50	7.75	7.50

<sup>a</sup>Elemental analysis by Elek Microanalytical Laboratories, Los Angeles.  
<sup>b</sup>Structural constants from Ref 99; measured refractive index values were corrected to 20°C.  
<sup>c</sup>The acidity was determined by titration in aqueous solution.  
<sup>d</sup>Reported properties of this diacid: mp 65 to 66°C (Ref 100), mp 66°C (Ref 98).

Table 18. Properties and analyses of diamides from hydrolysis of dinitriles,



R	Properties of diamides						Analyses <sup>a</sup>					
	Bp, °C	mp, °C	$n_D^{25}$	$d_4^{20}$	Molar refraction		N		C		H	
					Calc <sup>b</sup>	Found	Calc	Found	Calc	Found	Calc	Found
$-\text{CH}_2\text{CH}_2-$ (from EG) <sup>b</sup>	—	122 to 123	—	—	—	—	13.72	13.68	47.04	46.95	7.90	7.90
$\begin{array}{c} \text{H,CH}_3 \quad \text{H,CH}_3 \\   \quad   \\ -\text{CH}-\text{CH}-\text{O}-\text{CH}-\text{CH}- \\   \quad   \\ \text{(from DPG)} \end{array}$	—	—	1.4795	1.1576	68.02	69.78	10.14	7.31	—	—	—	—
$-(\text{CH}_2\text{CH}_2-\text{O})_3-\text{CH}_2\text{CH}_2-$ (from TOEG)	—	85.0 to 86.5	—	—	—	—	8.33	8.24	49.99	50.00	8.39	8.35

<sup>a</sup>Elemental analyses by Elek Microanalytical Laboratories, Los Angeles.  
<sup>b</sup>Reported properties of this diamide: mp 123°C (Ref 101), mp 123 to 124°C (Ref 102).  
<sup>c</sup>Properties are for an unpurified product.

was presented previously (RS 36-6). Additional cyanoethylations have been made on EG, DPG, and TOEG on a larger scale (1000 gm) in order to obtain reliable yield data and sufficient material for use in subsequent reactions and stability experiments. The catalyst for the reactions was sodium dissolved in the glycol, with the  $[\text{Na}]/[\text{OH}]$  ratio at 0.0052. The crude products from these reactions contained hydroxyl groups. For the calculation of the percentage yields, these groups were assumed to be present only as the monocynoethylated material. Thus, the yields of dicyanoethylated EG, DPG, and TOEG in the crude product from the large-scale runs were 91, 80, and 86%, respectively. This result indicates a somewhat lower yield for DPG and is in agreement with previous observations on the comparative yields from primary and secondary alcohols (Refs 98, 103).

For the high molecular weight polyoxypropylene glycols, a quantitative cyanoethylation reaction would be desirable, since the separation of unreacted glycol and monocynoethylated material from the dicyanoethylated product will be difficult. Therefore, a more detailed study of a model system, the cyanoethylation of DPG, was undertaken as a means of improving the quantitative nature of the reaction. In the cyanoethylation of DPG, three methods of preparation have been compared. In Method A, the procedure used in the 1000-gm run, the acrylonitrile was added dropwise to an equivalent amount of DPG containing the catalyst, and the temperature was maintained below 30°C. In Method B, the equivalent amount of acrylonitrile was added in the usual manner, and then an additional amount (50% excess) was quickly added with the object of driving the reaction toward

complete cyanoethylation of the hydroxyl groups. In Method C, equivalent amounts of DPG and acrylonitrile were quickly mixed together, resulting in a noticeable exothermic reaction in which the temperature was maintained below 60°C. Analyses of the products indicated a 94% yield of dinitrile from Method B compared to 80% for Methods A and C—all based on the amount of DPG used.

The greatest amount of solid sideproduct was formed in Method B, with a lesser amount from A and only a trace amount in C. In Method B, the isolated weight of dinitrile and yellow-colored solid sideproduct was larger than the theoretical amount of dinitrile and, therefore, some of the excess of acrylonitrile had to be involved in the formation of the yellow-colored solid sideproduct.

*c. Storage stability of cyanoethylated glycols.* It had been observed that cyanoethylated EG, DPG, and TOEG underwent a change when stored at room temperature in closed glass containers. This change was evidenced by an increased infrared absorptance in the 2.85  $\mu$  and 6.15  $\mu$  regions. To obtain additional information on the extent and nature of these changes, distilled samples of cyanoethylated EG, DPG, and TOEG were sealed in glass ampoules under their own vapor pressure. No significant changes were noted for any of the samples during storage periods of 8 or 12 weeks while stored by this method [water = 0.01% wt (Karl Fischer method), and extinction coefficients (neat) at both 2.85  $\mu$  and 6.15  $\mu$  were 0.2  $\text{mm}^{-1}$ ]. When samples were removed from the sealed tubes and stored in closed glass bottles at ambient pressure, however, increases in the water content from 0.01 to 0.23% and in the extinction coefficients from 0.2 to 2.1 and 0.2 to 1.4  $\text{mm}^{-1}$ , respectively, occurred after 4 weeks. The addition of a small amount of water to one of the cyanoethylated EG samples stored in air resulted in an increase in absorbance at only the 2.85 and 6.15  $\mu$  regions of the spectrum. The data for the cyanoethylated EG are typical also of the DPG and TOEG products. These results show that the cyanoethylated products are stable at room temperature when stored in sealed glass ampoules under their own vapor pressure. Furthermore, the changes observed on storage in air have been due to the appearance of water in these samples.

*d. Nature of sideproducts formed in cyanoethylation of glycols.* To determine the nature of the yellow-colored solid sideproduct, the intrinsic viscosities, infrared absorption spectra, and elemental analyses of these materials were compared with those of two samples of polyacrylonitrile (PAN). One of the PAN polymers was a commercial material (American Cyanamid Co., New York), while the other was obtained from the spontaneous polymerization

of a previously distilled sample of acrylonitrile. Contrary to a previously reported result (RS 36-6), solutions in *N,N*-dimethylacetamide (DMA) of the solid sideproduct at 4 gm/100 ml had appreciable viscosities compared to the solvent. The intrinsic viscosities at  $25.00 \pm 0.02^\circ\text{C}$  for the solid sideproducts formed from the cyanoethylation of DPG and polyethylene glycol (PEG 600) were 0.04 and 0.08 dl/gm, respectively. The intrinsic viscosity of the laboratory prepared PAN in DMA was 6.5 dl/gm, indicating that the solid sideproducts have a low molecular weight. The infrared spectra of the cyanoethylation byproducts determined as Nujol mulls were characterized by the expected nitrile peak at 4.45  $\mu$  and also by a broad peak at about 9  $\mu$ , a region usually attributed to the ether structure (Ref 104). This latter peak was not present in the spectrum of either sample of PAN. The elemental analyses of the yellow solid obtained from the cyanoethylation of DPG (Method B) indicate that this material contains six acrylonitriles per DPG unit. These results suggest that the glycol anion is an initiator for the anionic polymerization of acrylonitrile leading, in the case of the PEG 600, to a block copolymer of polyoxyethylene and acrylonitrile units. Such a product has been described recently by Furukawa and co-workers (Ref 105).

## B. Secondary Injection for Thrust Vector Control

J. Newton

An experimental program is in progress on the injection of a secondary fluid into the expansion cone of a conventional rocket nozzle to provide thrust vector control. This program in the field of secondary injection was initiated as the result of a comprehensive study of the various methods being used or proposed for thrust vector control of solid propellant rockets (RS 36-2). Considerable work in the field of secondary injection is being done by other agencies. After surveying this work, it was shown that a need existed for defining the basic mechanisms associated with secondary injection.

The objectives of the secondary injection program are to obtain engineering data pertinent to the design of spacecraft rocket propulsion systems and, secondarily, to gain insight into the pressure profiles of the exhaust during injection. The main areas of interest are operation

at low motor chamber pressures (about 300 psia) and at high expansion ratios (about 25:1) under near-vacuum conditions.

### 1. Initial Feasibility Tests

Feasibility tests were conducted to determine some of the operational techniques and problems associated with secondary injection systems. Motors containing approximately 50 pounds of polysulfide propellant with a thrust level of 1500 pounds and a burning time of 7 seconds were used for this series of tests. The feasibility tests were conducted on the two-component stand shown in Figure 88. A heavyweight 12-degree conical nozzle with a molybdenum throat and interchangeable injection orifice was used for these firings. The repeatability of the data and stand calibrations indicated a nominal error of 5% in the side-force measurements. Table 19 lists the nomenclature used, and Table 20 gives the pertinent data for this series of firings. The values

Table 19. Notation

$D_o$	Injection orifice diameter, in.
$F$	Thrust, lb
$I_s$	Specific impulse, sec
$P$	Pressure, psia
$W$	Flow rate, lb/sec
$T_o$	Stagnation temperature, °F
$X$	Axial distance downstream from nozzle throat, in.
$\theta$	Angle of element of cone measured from injection plane, deg
$E$	Expansion ratio of nozzle
Subscripts	
$c$	Motor chamber
$i$	Injectant
$s$	Side (90 deg to motor axis)
$M$	Motor

Table 20. Two-component stand test results

Run	Injectant	$F_s/F_m$	$W_s/W_m$	$P_i/P_c$	$D_o$ , in.	$I_{s_i}$ , sec	$T_{o_i}$ , °F
9773-2	Water	0.010	0.058	0.65	0.08	34	—
23	Freon-12	0.017	0.047	0.63	0.08	67	—
55	Freon-12	0.018	0.069	0.94	0.11	47	—
129	Freon-12	0.017	0.076	0.31	0.127	48	—
169	Decomposed hydrazine	0.051	0.044	0.81	0.380 <sup>a</sup>	237	1200
171	Decomposed hydrazine	0.041	0.035	0.73	0.380 <sup>a</sup>	236	1014
172	Decomposed hydrazine	0.027	0.024	0.43	0.380 <sup>a</sup>	238	975

<sup>a</sup>Sonic orifice.

of decomposed hydrazine stagnation temperatures listed are the averages for the injection portion of the runs. The side force ratios vs the flow rate ratios are plotted in Figure 89. The low values for the delivered side forces with Freon-12 as the injectant may be attributed to the nonoptimized system. The injection station was close to the exit plane of the nozzle, thereby limiting the area over which the pressure field acts.

### 2. Secondary Injection Program

The first phase of this continuing program has determined the nozzle wall pressure profiles and the thrust generated for various diameter injectors and flow rates. Freon-12 was selected as the injectant because of its favorable properties and its extensive use by other

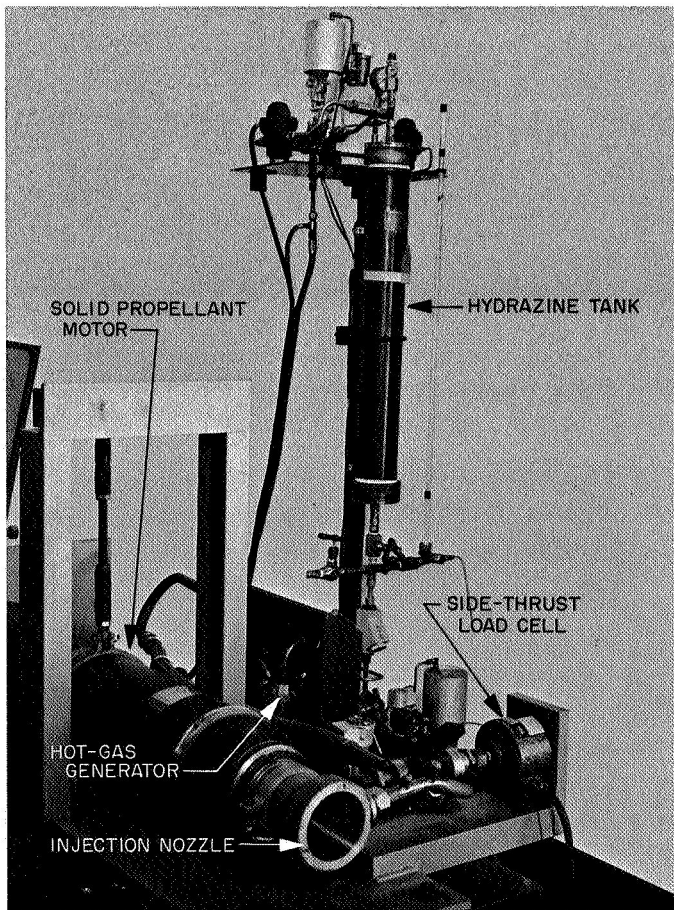


Figure 88. Two-component test stand and hot gas injection apparatus

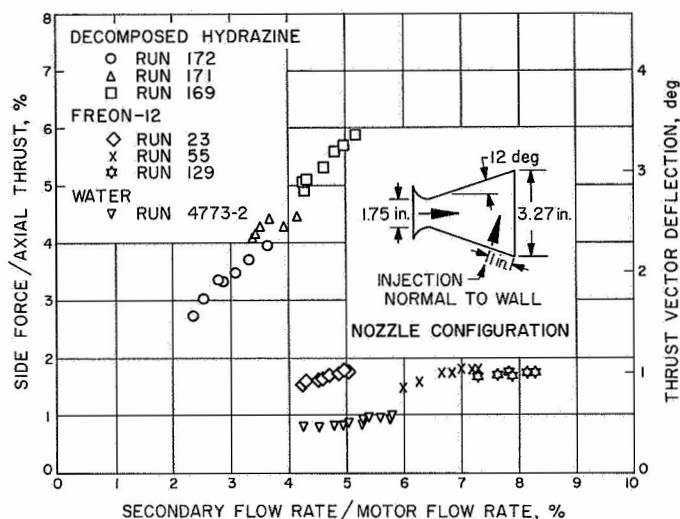


Figure 89. Secondary injection test results with two-compartment test stand

agencies. This facilitates the correlation of the data resulting from other work with secondary injection. The hardware configurations used for these tests are not optimized for the particular nozzle configuration but should provide adequate results for determining the side force generation mechanisms.

**a. Nozzle wall pressure tap diffuser.** A 25:1 expansion ratio nozzle and diffuser assembly was designed and constructed to measure the pressure profiles associated with secondary injection. Two nozzle configurations (Figs 90, 91) were used to measure the pressure profiles. The nozzle geometry and design details for the fully pressure-tapped nozzle are shown in Figure 92, and details for the injector-area pressure-tapped nozzle, in Figure 93. Both nozzles are 15-degree conical nozzles with molybdenum throat inserts. The system is pumped down to approximately 15 mm Hg prior to firing. A blow-off plate on the end of the diffuser tube is ejected with motor ignition. Resulting pressure profiles were measured with a 36-tube open-leg manometer, which was designed and fabricated at JPL. The manometer readings were recorded with a 70-mm still-framing camera. The shutter action of the camera was recorded on the oscillograph record to provide the necessary time correlation. Accuracy of the manometer data acquisition system was checked with that of conventional pressure transducers, and the results were in good agreement during the steady-state portions of the run.

**b. Six-component test stand diffuser assembly.** The six-component 3000-pound-thrust capacity stand utilized for the *Sergeant* program has been modified for use with

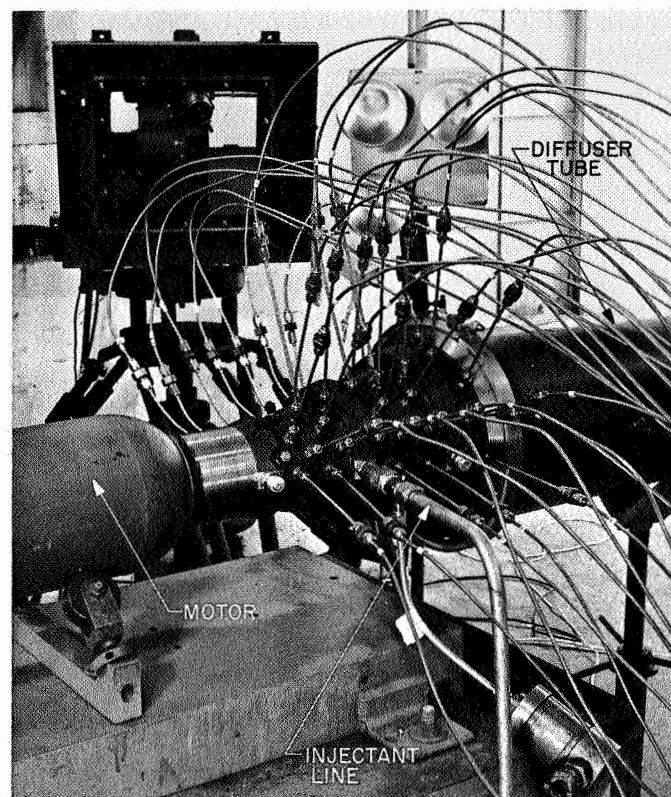


Figure 90. Pressure tap nozzle assembly

the 50-pound RTV polyurethane-propellant motor which develops 1500 pounds of thrust for 8 seconds. An enclosure and diffuser assembly has been constructed to provide the necessary altitude simulation. Test system configuration and nomenclature are shown in Figure 94. The thrust stand is described in detail in Reference 106.

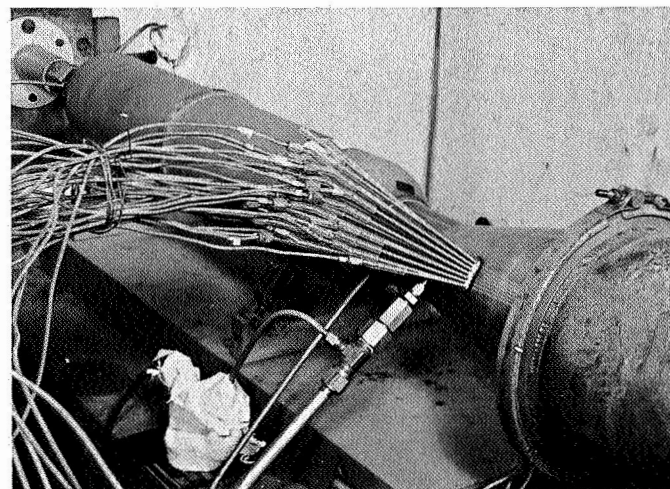


Figure 91. Dense pressure tap assembly

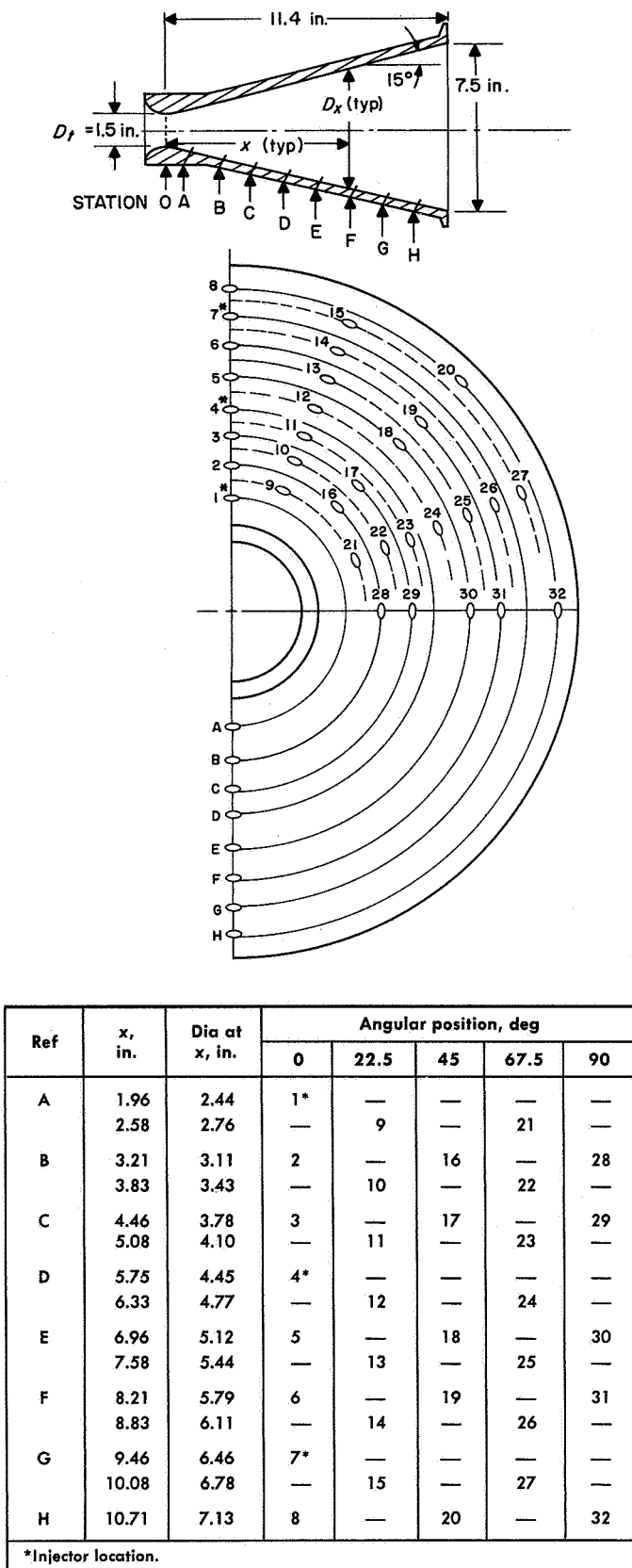


Figure 92. Nozzle pressure tap nomenclature

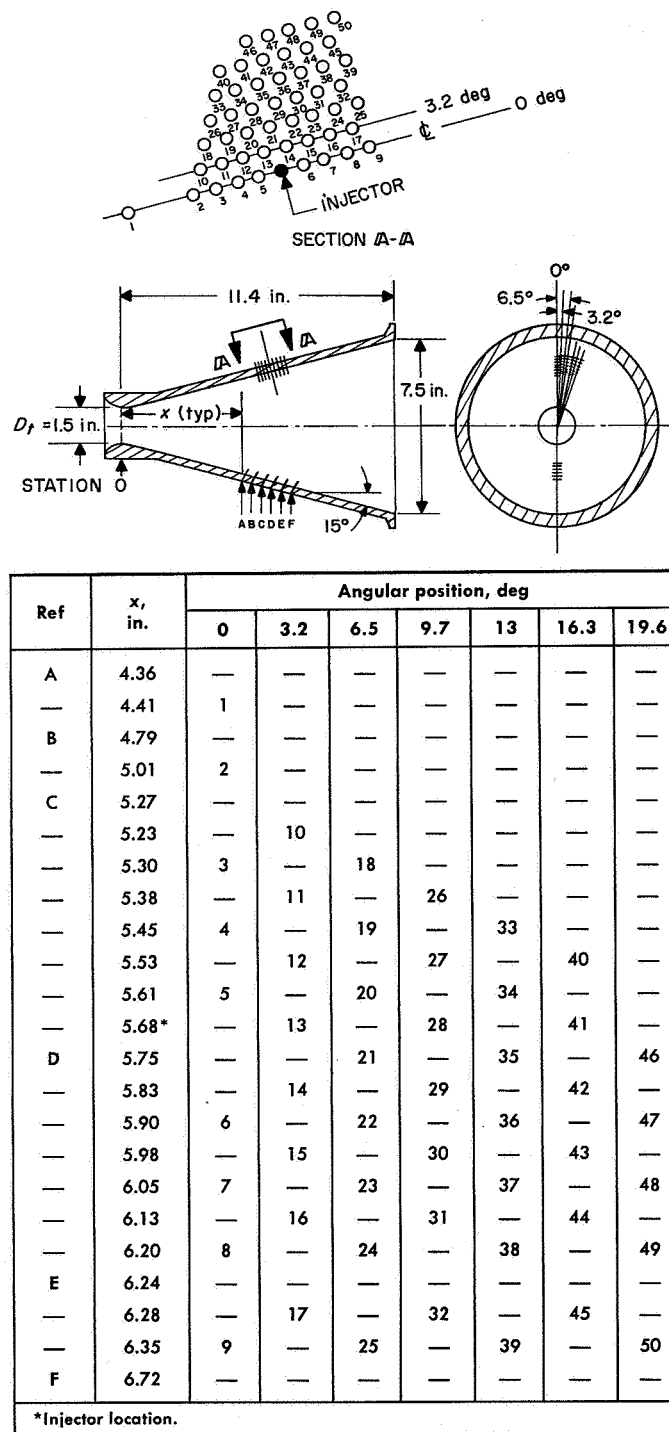


Figure 93. Dense pressure tap nomenclature

A nitrogen gas purge system is used for limiting the amount of exhaust back-flow during tailoff, thereby minimizing heat and corrosion damage to the stand. The diffuser assembly that encloses the stand is removable with an integral hoist-caster arrangement to permit access to



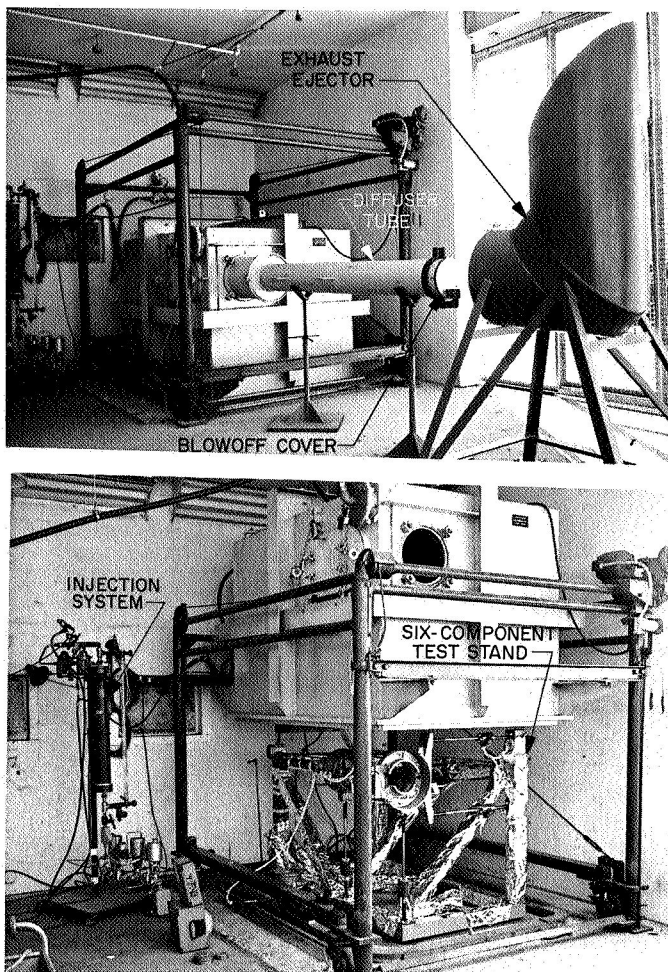


Figure 94. Thrust diffuser assembly, showing test stand and enclosure

the stand and for sea-level motor firings. The exhaust tube is easily modified to accommodate other motor and nozzle configurations.

**c. Fluid injection system.** A breadboard fluid injection system was constructed for use with the nozzle pressure tap diffuser and the thrust diffuser. The system appears in Figure 94b. A valving sequence provided the desired injection pressures with a constant nitrogen-pressurizing gas pressure in the fluid tank. Remote control was provided for pressurizing and venting the system. A mechanical timer was used for sequencing the injection system.

### 3. Test Results

Preliminary test results have been included in this report for the various injectant flow conditions and hardware systems utilized in this phase of the program. The nozzle wall pressure profile acquired for a typical run is

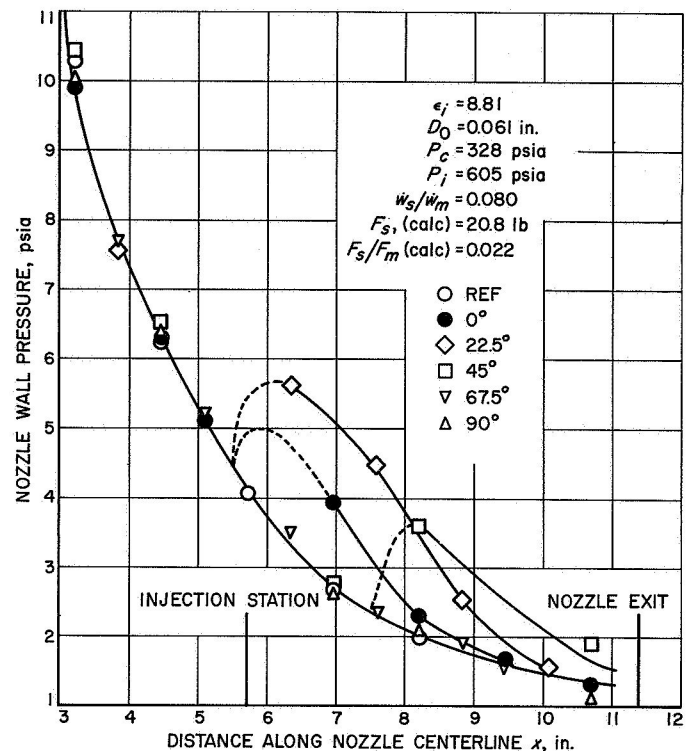


Figure 95. Nozzle wall pressure profile with Freon-12 injectant

shown in Figure 95. The associated nozzle geometry and nomenclature are given in Figure 92. One 90-degree quadrant of the nozzle expansion cone was pressure-tapped. Injection was in the zero-degree plane at an axial distance of 5.75 inches from the throat. The reference pressure taps are located 180 degrees from the injectant station. Nozzle separation occurred near the nozzle exit, as indicated by the rise in exit pressure. A cross plot of the pressure rise attributable to the secondary flow is shown in Figure 96. This pressure field aft of the injector is due to the mass addition of the vaporizing Freon. The spacing of the pressure taps was necessarily limited by the hardware configuration, but the tests have been conducted over a fairly wide range of flow parameters with consistent results.

The pressure profile obtained in the vicinity of the injector is shown in Figure 97. The associated geometry and nomenclature are given in Figure 93, and the reference pressure taps (numbered alphabetically in Figure 97), denote the undisturbed wall pressure at the indicated locations. The maximum pressure rise forward of the injector is approximately three times the local wall pressure at that point. This value is much less than that associated with a normal shock. The pressure rise

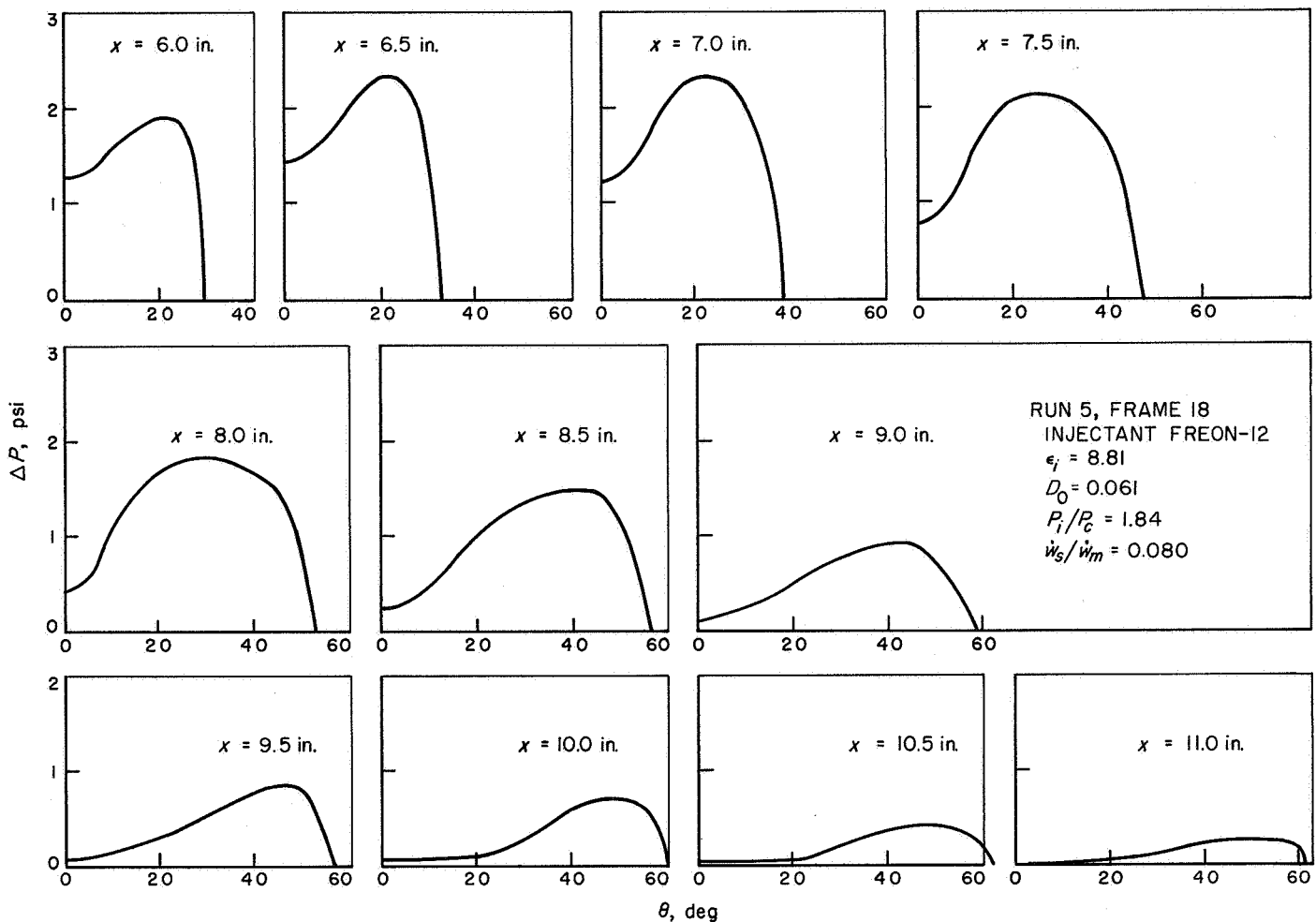


Figure 96. Cross section of pressure profile

aft of the injector corresponds quite well with that obtained with the overall profile as shown in Figure 95. (See Table 19 for nomenclature.)

Table 21. Summary of thrust diffuser firings

Run	$F_s/F_m$	$W_s/W_m$	$P_i/P_c$	$D_0$ , in.	$I_{sp}$ , sec	$F_m$ , lb	$P_{c_i}$ , psia	$\epsilon_i$
747-3	0.019	0.056	2.12	0.061	84.1	1375	445	2.65
	0.016	0.051	1.74	0.061	83.4	1431	465	2.65
	0.014	0.044	1.33	0.061	79.3	1473	490	2.65
758-4	0.017	0.039	2.23	0.048	115.0	1386	450	8.81
	0.014	0.032	1.65	0.048	120.0	1432	468	8.81
783-6	0.025	0.072	2.22	0.061	96.5	1520	451	8.81
	0.022	0.064	1.82	0.061	95.0	1580	467	8.81
	0.017	0.044	0.87	0.061	107.6	1620	471	8.81
786-7	0.038	0.239	1.81	0.080	83.1	1413	445	8.81
	0.030	0.198	1.32	0.080	82.5	1467	461	8.81
	0.029	0.175	1.08	0.080	84.9	1518	484	8.81

The results of the motor firings conducted with the six-component test stand diffuser assembly are listed in Table 21. All of these runs used the same nozzle and injector geometry as the pressure tap diffuser runs to facilitate correlation of the thrust and nozzle pressure measurements. The side force values listed for Run 747-3 are noticeably low because of the upstream injector location. The shock in the nozzle intercepted the nozzle wall, thereby degrading the delivered side force. Run 786-7 was low in delivered side impulse because of the high secondary flow rate. The nozzle flowed fully expanded for all the runs listed in Table 21.

The nozzle wall shock interface was recorded photographically and measured after each run with the thrust diffuser. A typical interface is illustrated in Figure 98. The interface measured from the nozzle agreed quite well with that determined from the nozzle wall pressure profiles. The pressure profiles such as illustrated in Figure 95 were integrated under the curves indicated.



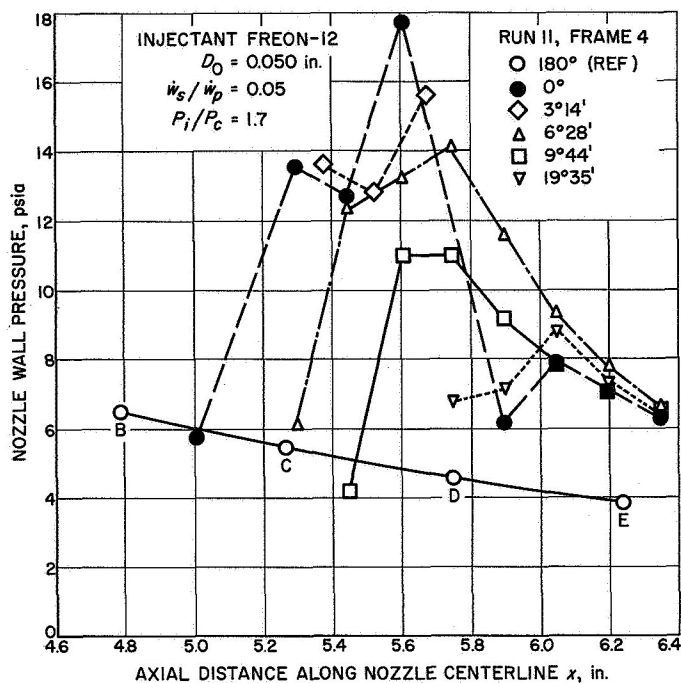


Figure 97. Injector area pressure profile

A typical result is listed in Figure 95 as the calculated value. Only the area downstream of the injector was considered for this integration. The calculated side force agreed very closely to the value measured with a similar nozzle in the six-component thrust diffuser.

#### 4. Conclusions

The results of this series of tests illustrated that the integrated measured nozzle wall pressure profile side

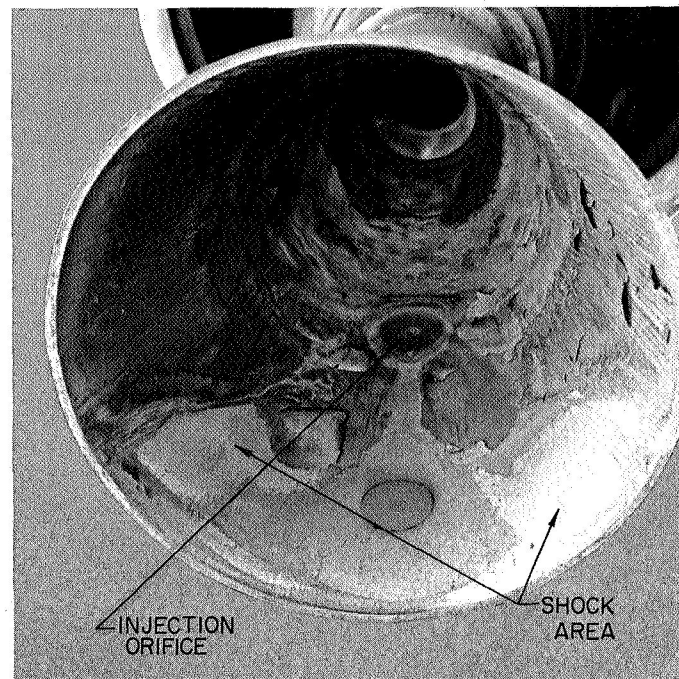


Figure 98. Nozzle wall shock interface

force agrees with that determined from thrust measurements. The pressure profile contributes approximately 90% of the side force with the secondary fluid momentum adding another 10%. The contribution to the side force of the area forward to the injector appears to be less than 5% of the total side force in the tests injecting perpendicular to the nozzle wall. As other agencies have reported, the results show that the relative efficiency of the injectant is strongly dependent on the injectant flow rate, the injector location, and the injecting angle.

## References

1. "First Field-Effect Transistor Now Available," *Electronic Design*, 9 (No. 7): 66, March 29, 1961.
2. Bergman, R. H., "Tunnel Diode Logic Circuit," *IRE Transactions on Electronic Computers*, EC-9 (No. 4): 430-438, December 1960.
3. Chow, W. F., "Tunnel Diode Digital Circuitry," Presented at *International Solid-State Conference*, Philadelphia, 1960.
4. Neff, G. W., Butler, S. A., and Critchlow, D. L., "Esaki Diode Logic Circuits," *IRE Transactions on Electronic Computers*, EC-9 (No. 4): 423-429, December 1960.
5. Sims, R. C., Beck, E. R., and Kamm, V. C., "A Survey of Tunnel-Diode Digital Techniques," *Proceedings of the IRE*, 49 (No. 1): 136-146, January 1961.
6. Sommers, H. S., "Tunnel Diodes as High-Frequency Devices," *Proceedings of the IRE*, 47 (No. 7): 1201-1206, July 1959.
7. Clarke, V. C., *Sourcebook on Interplanetary Trajectories*, Technical Report No. 32-77, Jet Propulsion Laboratory, Pasadena, to be published November 1961.
8. Kozai, Y., "The Motion of a Close Earth Satellite," *Astronomical Journal*, 64 (No. 9): 367-377, November 1959.
9. Aseltine, J. A., Mancini, A. R., and Sarture, C. W., "A Survey of Adaptive Control Systems," *IRE Transactions on Automatic Controls*, AC-3: 102-108, December 1958.
10. Bellman, R. E., *Adaptive Control Processes: A Guided Tour*, Princeton University Press, Princeton, New Jersey, 1961.
11. Chandaket, P., and Leondes, C. T., *Extensions in the Synthesis of Time Optimal or 'Bang-Bang' Nonlinear Control Systems, Part I: The Synthesis of Quasi-Stationary Optimum Nonlinear Control Systems, Part II: Synthesis and Analytic Studies of Optimum Type II Nonlinear Control Systems with Complex Roots*, Report Nos. 60-45, 47, University of California, Los Angeles, June 1960.
12. Del Toro, V., and Parker, S. R., *Principles of Control Systems Engineering*, McGraw-Hill Book Co., New York, 1960.
13. Dorf, R., Farrin, M., and Phillips, C., "Adaptive Sampling Frequency for Sampled Data Control Systems," *IRE 7th Regional Conference*, Phoenix, Arizona, April 1961.
14. Freimer, M., "A Dynamic Programming Approach to Adaptive Control Processes," *IRE Transactions on Automatic Control*, AC-4:10-15, November 1959.
15. Gibson, J. E., "Generalizing the Adaptive Principle," *Control Engineering*, 7 (No. 12): 93-96, December 1960.
16. Hay, J., *Mark I Perceptron Operator's Manual (Project PARA)*, Report VG-1196-G-5, Cornell University, February 15, 1960.
17. Hung, J. C., "Sampled-Data Control Systems with Two Digital Processing Units," *AIEE, Appl and Ind*, 50: 292-298, September 1960.
18. Mattson, R., *An Approach to Pattern Recognition Using Linear Threshold Devices*, LMSD-702680, Lockheed, Sunnyvale, September 1960.
19. Minsky, M., "A Selected Descriptor-Indexed Bibliography to the Literature on Artificial Intelligence," *IRE Transactions on Human Factors in Electronics*, HFE-2 (No. 1): 39-55, March 1961.
20. Mishkin, E., and Braun, L., Editors, *Adaptive Control Systems*, McGraw-Hill Book Co., New York, 1961.
21. "Extending Man's Intellect," *Proceedings of the Western Joint Computer Conference*, Los Angeles, Sponsored by IRE, AIEE, ACM, May 1961.
22. Sweitzer, D., *Biological and Artificial Intelligence*, Literature Search No. 254, Jet Propulsion Laboratory, Pasadena, December 1960.
23. Widrow, B., An Adaptive "Adaline" Neuron Using Chemical "Memistors," Report No. 1553-2, Stanford Electronics Laboratories, Palo Alto, October 17, 1960.
24. Laub, J. H., McGinness, H. D., *Gas-Floated Spinning Spheres*, Technical Report No. 32-61, Jet Propulsion Laboratory, Pasadena, February 28, 1961.
25. *Development of a Gas-Supported Rotating Sphere for Use As a Stable Element*, ASTIA Report ATI 65473, Curtiss-Wright Corp., June 2, 1949.
26. Laub, J. H., McGinness, H. D., *A Closed-Cycle System for Gas Bearings*, Technical Release No. 34-174, Jet Propulsion Laboratory, January 19, 1961.
27. Golomb, S. W., *Sequences with Randomness Properties*, Terminal Progress Report, Contract Reg. No. 639498, Glenn L. Martin Company, Baltimore, June 1955.
28. Carson, J. R., "Frequency-Modulation: Theory of the Feedback Receiver Circuit," *Bell System Technical Journal*, XVIII (No. 3): 395-403, July 1939.
29. Chaffee, J. G., "The Application of Negative Feedback to Frequency-Modulation Systems," *Bell System Technical Journal*, XVIII (No. 3): 404-437, July 1939.
30. Choate, R. L., *Analysis of a Phase Modulation Communications System*, Progress Report No. 30-21, Jet Propulsion Laboratory, Pasadena, October 8, 1959.
31. Wells, W. H., "Quantum Formalism Adapted to Radiation in a Coherent Field," *Annals of Physics*, 12 (No. 1): 1-40, 1961.
32. Foldes, P., and Komlos, S., "Theoretical and Experimental Study of Wide-Band Paraboloid Antenna with Central Reflector Feed," *RCA Review*, XXI (No. 1): 94-116, March 1960.
33. Hannon, P. W., "Microwave Antennas Derived from the Cassegrain Telescope," *IRE Transactions on Antennas and Propagation*, AP-9 (No. 2): 140-153, March 1961.
34. Cutler, C. C., "Parabolic-Antenna Design for Microwaves," *Proceedings of the IRE*, 35 (No. 11): 1284-1294, November 1947.
35. Raburn, L. E., "The Calculation of Reflector Antenna Polarized Radiation," *IRE Transactions on Antennas and Propagation*, AP-8 (No. 1): 43-49, January 1960.
36. De Grasse, R. W., Hogg, D. C., Ohm, E. A., and Scovil, H. E., "Ultra-Low-Noise Measurements Using a Horn Reflector Antenna and a Traveling-Wave Maser," *Journal of Applied Physics*, 30: 2013, 1959.
37. Hogg, D. C., "Effective Antenna Temperatures Due to Oxygen and Water Vapor in the Atmosphere," *Journal of Applied Physics*, 30 (No. 9): 1417-1419, 1959.

38. Liebmann, G., "A Unified Representation of Magnetic Electron Lens Properties," *Proceedings of the Physical Society*, B 68: 737-745, 1955.
39. Haine, M. E., and Einstein, P. A., *British Journal of Applied Physics*, 3: 40, 1952.
40. Rechten, E., *Design of Phase Lock Oscillator Circuits*, Section Report No. 8-566, Jet Propulsion Laboratory, Pasadena, February 1957.
41. Viterbi, A. J., *Acquisition and Tracking Behavior of Phase-Locked Loops*, External Publication No. 673, Jet Propulsion Laboratory, July 14, 1959.
42. Roberts, J. D., *Nuclear Magnetic Resonance: Applications to Organic Chemistry*, pp 42-60, McGraw-Hill Book Co., New York, 1959.
43. Unpublished work of S. L. Manatt and W. S. Johnson done at the University of Wisconsin.
44. Cram, D. J., and Hammond, G. S., *Organic Chemistry*, pp 122-127, McGraw-Hill Book Co., New York, 1959.
45. Barton, D. H. R., Lewis, D. A., and McGhie, J. F., "Conformational Anomalies in Some Triterpenoid Bromoketones," *Journal of the Chemical Society (London)*, 2907-2915, 1957.
46. Karplus, M., "Contact Electron-Spin Coupling of Nuclear Magnetic Moments," *Journal of Chemical Physics*, 30: 11-15, 1959.
47. Pople, J. A., Schneider, W. G., and Bernstein, H. J., *High-Resolution Nuclear Magnetic Resonance*, Chapter 14, McGraw-Hill Book Co., New York, 1959.
48. "Reaction of Atomic Oxygen with Nitrogen," *Research Summary No. 36-3*, Vol I, Part 2, Jet Propulsion Laboratory, Pasadena, June 15, 1960.
49. Stearns, A. E., and Eyring, H., "Nonadiabatic Reactions. The Decomposition of  $N_2O$ ," *Journal of Chemical Physics*, 3:778, 1935.
50. Bloom, A. L., and Shoolery, J. N., "Effects of Perturbing Radiofrequency Fields on Nuclear Spin Coupling," *Physical Review*, 97: 1261-1265, 1955.
51. Anderson, W. A., "Nuclear Magnetic Resonance Spectra of Some Hydrocarbons," *Physical Review*, 102: 151-167, 1956.
52. Meghreblian, R. V., *Gaseous Fission Reactors for Spacecraft Propulsion*, Technical Report No. 32-42, Jet Propulsion Laboratory, Pasadena, July 6, 1960.
53. Stumpf, H. J., *Vortex Tube and Regenerative Tube Parameters for Gaseous Fission Reactors*, Technical Memorandum No. 33-50 (in preparation), Jet Propulsion Laboratory, Pasadena.
54. Kerrebrock, J. L., and Meghreblian, R. V., "Vortex Containment for the Gaseous Fission Rocket," *Journal of Aero-Space Sciences*, 1961 (in press).
55. Meghreblian, R. V., *Prospects for Advanced Nuclear Systems*, Technical Memorandum No. 33-40, Jet Propulsion Laboratory, Pasadena, March 8, 1961.
56. von Roos, O., "Plasma Theory of Electron-Phonon Interaction in Metals," *Physical Review*, 120: 1641, 1960.
57. Bardeen, J., and Pines, D., "Electron-Phonon Interaction in Metals," *Physical Review*, 99: 1140-1150, 1955.
58. Kistiakowsky, G. B., and Volpi, G. G., "Reactions of Nitrogen Atoms. I. Oxygen and Oxides of Nitrogen; II.  $H_2$ , CO,  $NH_3$ , and  $NO_2$ ," *Journal of Chemical Physics*, 27: 1141-1149, 1957.
59. Kaufman, F., "Structure of the Methylamine Molecule. II. Internal Motions of  $CD_3ND_2$ ," *Journal of Chemical Physics*, 28: 352, 1958.
60. Harteck, P., Reeves, R. R., and Mannella, G., "Rate of Recombination of Nitrogen Atoms," *Journal of Chemical Physics*, 29: 608, 1958.
61. Herron, J. F., Franklin, J. L., Bradt, P., and Dibeler, V. H., "Kinetics of Nitrogen Atom Recombination," *Journal of Chemical Physics*, 30: 879, 1959.
62. Reeves, R. R., Mannella, G., and Harteck, P., *Journal of Chemical Physics*, 32: 632, 1960.
63. Krongelb, S., and Strandberg, M. W. P., "Use of Paramagnetic Resonance Techniques," *Journal of Chemical Physics*, 31: 1196, 1959.
64. Benson, S. W., and Axworthy, A. E., *Journal of Chemical Physics*, 26: 1718, 1957.
65. Ford, H. W., and Endow, N., "Rate Constants at Low Concentrations," *Journal of Chemical Physics*, 27: 1156, 1957.
66. Berkowitz, J., Chupka, W. A., and Kistiakowsky, G. B., *Journal of Chemical Physics*, 25: 457, 1956.
67. Barth, C. A., Schade, W. J., and Kaplan, J., "Blue Nitric Oxide Afterglow," *Journal of Chemical Physics*, 30: 347, 1959.
68. The author is indebted to Dr. C. S. Wu for the solution of the differential equation resulting in Equation (4).
69. Kirzhnits, D. A., *Soviet Physics-JETP*, 32(5): 65, 1957.
70. Kompaneets, A. S., and Pavlovskii, E. S., *Soviet Physics-JETP*, 31(4): 328, 1957.
71. Alfred, I. C. R., "Quantum-Corrected Statistical Method for Many-Particle Systems: The Density Matrix," *Physical Review*, 121: 1275, 1961.
72. Baraff, G. A., and Borowitz, S., "Green's Function Method for Quantum Corrections," *Physical Review*, 121: 1704, 1961.
73. von Roos, O., "Boltzmann-Vlasov Equation for a Quantum Plasma," *Physical Review*, 119: 1174, 1960.
74. Wigner, E., "On the Quantum Correction for Thermodynamic Equilibrium," *Physical Review*, 40: 749, 1932.
75. *Research Summary No. 36-3*, Vol I, Part Two, Sect VI-A, Jet Propulsion Laboratory, Pasadena, June 15, 1960.
76. Schultz-Grunow, F., "Der Reibungswiderstand rotierender Scheiben in Gehäusen," *Zeitschrift für angewandte Mathematik und Mechanik*, 15: 191, 1935.
77. Taylor, G. I., "The Boundary Layer in the Converging Nozzle of a Swirl Atomizer," *Quarterly Journal of Mechanics and Applied Mathematics*, 3: 129-139, 1950.
78. Cooke, J. C., "On Pohlhausen's Method with Application to a Swirl Problem of Taylor," *Journal of the Aeronautical Sciences*, 19: 486-490, 1952.
79. von Kármán, T., "Über laminare und turbulente Reibung," *Zeitschrift für angewandte Mathematik und Mechanik*, 1: 233-252, 1921.
80. Stewartson, K., "On Rotating Laminar Boundary Layers," *Symposium Freiburg*, pp 59-70, Springer-Verlag, Berlin, 1958.
81. Debye, P., *Papers on the Kinetic Theory of Matter and Electricity*, Teubner, Berlin, 1914.

82. Peierls, R., "Kinetic Theory of Thermal Conductivity," *Annalen der Physik*, 3: 1055, 1929.
83. Charvat, F., and Kingery, W. D., "Thermal Conductivity: VIII, Effect of Microstructure on Conductivity of Single-Phase Ceramics," *Journal of the American Ceramic Society*, 40(10): 306, 1957.
84. McQuarrie, M., "Thermal Conductivity: VII, Analysis of Variation of Conductivity with Temperature for  $\text{Al}_2\text{O}_3$ ,  $\text{BeO}$ , and  $\text{MgO}$ ," *Journal of the American Ceramic Society*, 37(2): Part 2, 91, 1954.
85. Kingery, W. D., and Lee, D. W., "Radiation Energy Transfer and Thermal Conductivity of Ceramic Oxides," *Journal of the American Ceramic Society*, 43(11): 594, 1960.
86. Grant, E. L., *Statistical Quality Control*, 2nd Ed., p 512, McGraw-Hill Book Co., New York, 1952.
87. Packard, K., "When is a Solid not a Solid," *Proceedings of the IRE*, February 1959.
88. Jensen, N., "Vapor Pressure of Plastic Materials," *Journal of Applied Physics*, 27(12): 1460-1462, December 1956.
89. Madoršky, S. L., Hart, V. E., Straus, S., and Sedlak, V. A., "Thermal Degradation of Tetrafluorethylene and Hydrofluoroethylene Polymers in a Vacuum," *Journal of Research NBS*, 51(6): 327-333, RP 2461, December 1953.
90. Spencer, D. F., *The Plasma Core Reactor*, Technical Report No. 32-104, Jet Propulsion Laboratory, Pasadena, April 24, 1961.
91. Van de Verg, N., and De Vorkin, H., *An Investigation of the Influence of Rocket-Chamber Configuration on Performance*, Progress Report No. 1-82, Jet Propulsion Laboratory, Pasadena, June 4, 1952.
92. Crandall, S. H., et al, *Random Vibration*, Massachusetts Institute of Technology, Cambridge, 1958.
93. Welsh, W. E., and Witte, A. B., *Comparison of Analytical and Experimental Local Heat Fluxes in Liquid Propellant Rocket Thrust Chambers*, ASME Publication No. GI-AV-59, presented at ASME Aviation Conference, March 13, 1961.
94. Welsh, W. E., and Witte, A. B., *Comparison of Analytical and Experimental Local Heat Fluxes in Liquid Propellant Rocket Thrust Chambers*, Technical Report No. 32-43, Jet Propulsion Laboratory, Pasadena, February 1, 1961.
95. Bartz, D. R., "A Simple Equation for Rapid Estimation of Rocket Nozzle Convective Heat Transfer Coefficients," *Jet Propulsion*, 27 (No. 1): 49, January 1957.
96. Eckert, E. R. G., *Survey on Heat Transfer at High Speeds*, TR 54-70, Wright Air Development Command, Dayton, April 1954.
97. Howell, G., "Transient Heat-Transfer Thermocouple-Fabrication and Installation," Process Specification No. 15006, Jet Propulsion Laboratory, Pasadena, March 20, 1958.
98. Christian, R. V., and Hixon, R. M., "The Hydrolysis of Some  $\beta$ -Alkoxypropionitriles," *Journal of the American Chemical Society*, 70: 1333-1336, 1948.
99. Vogel, A. I., *A Textbook of Practical Organic Chemistry*, 3rd Ed. p 1035, Longmans, Green and Co., London, 1957.
100. Nazarov, I. N., Shvekhgeimer, G. A., and Rudenko, V. A., "Hydrolysis, Alcoholysis and Hydrogenation of 2-Cyanoethyl Glycol Ethers," *Chemical Abstracts*, 49: 4514, 1955; *Zhurnal Obshchei Khim*, 24: 329-337, 1954.
101. Terent'ev, A. P., Kost, A. N., and Berlin, A. M., "Syntheses with the Aid of Acrylonitrile. XXVI. Synthesis of Some  $\beta$ -Alkoxy Propionamides," *Chemical Abstracts*, 50: 14586, 1956; *Zhurnal Obshchei Khim*, 26: 719-723, 1956.
102. Bruson, H. A., "Aliphatic Polyether Polyamides." U.S. Patent No. 2,359,708, October 3, 1944.
103. Untermohlen, W. P., "Preparation of  $\gamma$ -alkoxy-n-Propylamines," *Journal of the American Chemical Society*, 67: 1505-1506, 1945.
104. Bellamy, L. J., *The Infrared Spectra of Complex Molecules*, p 101, John Wiley and Sons, New York, 1954.
105. Furukawa, J., Saegusa, T., and Mise, N., "Synthesis of Block-Copolymer of Ethylene Oxide and Acrylonitrile," *Makromolecular Chemistry*, 38: 244-247, 1960.
106. Earnest, J. E., *Six-Component Thrust-Measuring System for Accurate Determination of Specific Impulse*, Technical Memorandum No. 33-23, Jet Propulsion Laboratory, Pasadena, August 19, 1960.